

Some pages of this thesis may have been removed for copyright restrictions.

If you have discovered material in Aston Research Explorer which is unlawful e.g. breaches copyright, (either yours or that of a third party) or any other law, including but not limited to those relating to patent, trademark, confidentiality, data protection, obscenity, defamation, libel, then please read our [Takedown policy](#) and contact the service immediately (openaccess@aston.ac.uk)

**NOVEL ALKALI-FREE OF LAYERED DOUBLE HYDROXIDES
AND SOLID BASE CATALYSTS FOR
TRANSESTERIFICATION OF C₄-C₁₈ TRIGLYCERIDES**

NAZRIZAWATI AHMAD TAJUDDIN

Doctor of Philosophy

ASTON UNIVERSITY

March 2017

© Nazrizawati Ahmad Tajuddin, 2017

Nazrizawati Ahmad Tajuddin asserts her moral right to be
identified as the author of this thesis

This copy of the thesis has been supplied on condition that anyone
who consults it is understood to recognise that its copyright rests
with its author and that no quotation from the thesis and no
information derived from it may be published without appropriate
permission or acknowledgement.

ASTON UNIVERSITY

NOVEL ALKALI-FREE OF LAYERED DOUBLE HYDROXIDES AND
SOLID BASE CATALYSTS FOR TRANSESTERIFICATION OF C4-
C18 TRIGLYCERIDES

NAZRIZAWATI AHMAD TAJUDDIN

Doctor of Philosophy

March 2017

THESIS SUMMARY

This study explores the possibilities of using solid base catalysts, mainly hydrotalcites, for the transesterification of triglycerides (TAG) possessing alkyl groups in the range of C4-C18. The aim of the research is to design various types of layered double hydroxides (LDHs) formulated with different atomic ratio of M^{2+}/Al^{3+} ($M = Zn^{2+}, Ni^{2+}$ and Mg^{2+}), spanning from 1.5-4.0 via an alkali-free method. To enhance the physicochemical properties of the LDH, catalysts were calcined-rehydrated via gas-phase (GP), liquid-phase (LP), and hydrothermal (HTM) pathways. Extensive characterisation of both structural and base properties of these materials was conducted to provide a greater insight into the role of base sites for heterogeneously catalysed transesterification. Results showed HTM reconstructed method enhances the LDH reconstruction purity, surface area and basicity. A positive trend in initial rates was observed as $GP < LP < HTM$ with reconstruction on conventional ZnAl LDH. Following this, the HTM reconstruction method was consequently applied in conventional NiAl and MgAl LDH and further underwent transesterification reaction. However, the diffusion rates of C18 was still hampered by the bulky chains and narrow pores, which the turnover frequency (TOF) in a range of 0.46 min^{-1} for all prepared conventional LDH materials. This was due to the steric limitation of bulkier TAG to access the Bronsted basic sites within the interlayer and edges of LDHs. To overcome this, catalysts possessing a macroporous framework have been synthesised on Zn/Al, Mg/Al and Ni/Al LDH using the polystyrene template and reconstructed under HTM method. Preliminary studies on macroporous Ni/Al LDH found that reconstruction is impossible at ratio 4:1, thus it was discontinued. Macroporous Zn/Al and Mg/Al LDH were further characterised and tested in the transesterification reaction. The TOF was increased nearly ~20 folds in both macroporous LDH, simultaneously overcoming the above issue. Additionally, a comparison on commercial solid based catalysts such as dolomite and NanoMgO were also carried out. A remarkable catalytic performance was observed on commercial catalysts compared to the conventional and macroporous LDH materials which mainly attributed from the enhanced basicity of the catalyst.

Keywords: layered double hydroxide (LDH), hydrothermal, macroporous, solid base catalyst and transesterification

DEDICATION

This thesis is specially bound to the most precious persons in my life. Without them, I would not be who I am today. Hey guys, this is for you....

To my husband and son

Mohd Hafiz Mohd Halil

Haris Rifqi Mohd Hafiz

To my mum, family and in-laws

Hindon Haji Ali

To my late father

Ahmad Tajuddin Saad

I know you are smiling from there...☺

On the top of that, this work is dedicated to The Most Merciful Allah.

ACKNOWLEDGEMENTS

To pursue study in overseas was my childhood dream. I would say it was not an easy job to finally be here, in the United Kingdom one of my dreamlands. PhD is not a single journey of mine; it does involve many parties and I would like to take this opportunity to thank each one of them. First and foremost, the highest award dedicated to my supervisors, **Professor Karen Wilson, Professor Adam F. Lee and Dr Amin Osatiashtiani**, who are my idols in Catalysis field. I could not thank them enough for their advice, guidance, and support throughout my study years. To be working with the cream of the cream in my Catalysis Group was a tremendous experience for me. This, of course, creates most valuable and unforgettable memories in my life.

To my husband, **Mohd Hafiz Mohd Halil**, your endlessly supports and sacrifices always meant the world to me. To relinquish your dream career isn't an easy matter to deal with, and turn out to be impossible to the most of the people, but you did it effortlessly for me. What more could I ask for? I am so grateful to have a great companion like you, who always put me first instead of others. The sweat, tears, sacrifices now all gone and this small token of appreciation is dedicated to you and our beloved son, **Haris Rifqi Mohd Hafiz**. To my mum, **Hindon Haji Ali**; you are my biggest influence of success. You made me believe nothing is impossible with hard works and faith. Thank you for all your prayers for me, I am nobody without you. What have you done for me since I was born, were so priceless. I knew I could not trade the world for you, but this tiny yet significant award, I presenting for you. May Jannah be yours. To my **families**, thank you so much for all your support and keeps believing in me.

Special thanks to **Dr Jinesh Cherakkattu Manayil** who continuously gives me guidance and support on my work starting from my 1st year up to now. Informal but fruitful scientific discussions were possible on a daily basis. **Dr Mark Isaacs**- Thank you for your effortless help and guidance on XRD, XPS, TEM and ICP analysis. **Dr Chris Parlett** and **Dr Lee Durndell**, thank you for TEM analysing. **To my present and past lab mates**, thank you for everything. This journey becomes more meaningful with you guys.

Finally, I would like to convey my heartfelt gratitude to my sponsors; **Malaysian Ministry of Higher Education (MOHE)** and **University of Technology MARA (UiTM)** who offered me this golden opportunity and fully funded my study. To all my **Malaysian friends**; you guys rock my world. Thank you for always being there for me, a shoulder to cry on.

TABLE OF CONTENT

THESIS SUMMARY	II
DEDICATION	III
ACKNOWLEDGEMENTS	IV
TABLE OF CONTENT	V
LIST OF FIGURES	XII
LIST OF TABLES	XIX
LIST OF SCHEMES	XXI
ABBREVIATIONS	XXII
CHAPTER 1: INTRODUCTION	1
1.0 Introduction	2
1.1 Problem statement and research motivation.....	2
1.1.1 Oil depletion issues	2
1.1.2 Problems of homogeneously catalysed biodiesel production	3
1.2 General background to biodiesel	4
1.2.1 Biodiesel as an alternative fuel	4
1.2.2 The Biodiesel production process.....	7
1.2.3 The transesterification reaction.....	7
1.2.4 Oil feedstocks for biodiesel production	11
1.2.4.1 1st and 2nd generation biodiesel fuels.....	11
1.3 Recent robust technology in biodiesel catalysis.....	12
1.3.1 Homogeneous vs heterogeneous catalysis.....	12
1.3.2 Heterogeneous solid acid catalysts.....	14
1.3.3 Heterogeneous solid base catalysts	17
1.4 Hydrotalcite: The uniqueness solid base catalyst	20
1.4.1 Past and current perspectives of hydrotalcite	20
1.4.2 Structural and physicochemical properties of hydrotalcites.....	22
1.4.3 LDH synthesis routes	24
1.4.3.1 Entrained sodium in LDHs	25
1.4.3.2 The x ratio of synthesise hydrotalcite	27
1.4.3.3 Hydrotalcite Reconstruction System	27
1.4.4 Catalytic activity of LDH.....	28
1.5 Hierarchical mesoporous-macroporous LDH materials.....	30
1.6 Other heterogeneous solid base catalyst (Dolomite and NanoMgo)	32
1.7 Research objectives	34
1.8 References.....	34

2.5 References.....	67
CHAPTER 3: ALKALI-FREE ZNAl HYDROTHERMAL RECONSTRUCTED LAYERED DOUBLE HYDROXIDES	69
3.1 Introduction	70
3.2 Novelty and contribution to knowledge	72
3.3 Aim.....	72
3.4 Results and discussion.....	72
3.4.1 Characterisation of ZnAl precursor	73
3.4.1.1 Energy dispersive X-Ray spectroscopy.....	73
3.4.1.2 Thermogravimetric analysis-mass spectrometry	74
3.4.1.3 Powder X-ray diffraction of ZnAl LDH series	77
3.4.1.4 Diffuse reflectance infrared Fourier transform spectroscopy of ZnAl LDH series	80
3.4.2 Characterisation of ZnAl calcined samples	81
3.4.2.1 Powder X-ray diffraction	81
3.4.2.2 Nitrogen porosimetry of ZnAl series	83
3.4.2.3 Scanning electron microscopy of ZnAl LDH	84
3.4.3 Comparison of gas-phase, liquid-phase and hydrothermal ZnAl reconstructed materials	85
3.4.3.1 Scanning electron microscopy of reconstructed ZnAl LDH	85
3.4.3.2 High-resolution scanning transmission electron microscopy of reconstructed ZnAl LDH	87
3.4.3.3 Powder X-ray diffraction	88
a) Gas-phase ZnAl reconstructed.....	88
b) Liquid-phase ZnAl reconstructed.....	90
c) Hydrothermal ZnAl reconstructed	91
3.4.3.4 Nitrogen porosimetry of GP, LP and HTM ZnAl LDH	94
3.4.3.5 Temperature-programmed desorption of CO ₂ of GP, LP and HTM ZnAl LDH	97
3.4.3.6 Al-MAS Nuclear magnetic resonance spectroscopy of ZnAl LDH series	98
3.4.3.7 X-ray photoelectron spectroscopy of ZnAl HTM.....	99
3.4.3.8 Diffuse reflectance infrared Fourier transform spectroscopy of ZnAl HTM	101
3.4.4 Transesterification of tributyrin over reconstructed ZnAl LDH	102

3.4.4.1 Effect of Rehydration/Reconstruction Approaches on GP,LP and HTM ZnAL LDH	102
3.4.4.2 Effect of ratio on ZnAl HTM.....	104
3.4.4.3 Effect of temperature on ZnAl HTM	105
3.4.4.4 Effect of catalyst mass on ZnAl HTM	107
3.4.4.5 Effect of co-solvent on ZnAl HTM	108
3.4.5 Transesterification of Model Triglycerides on ZnAl HTM	110
3.4.5.1 C ₄ -C ₁₈ TAG	110
3.4.6 Leaching Test of ZnAl HTM	112
3.4.7 Reusability Study of ZnAl HTM	114
3.5 Conclusion	115
3.6 References.....	116
CHAPTER 4 : ALKALI-FREE NIAL HYDROTHERMALLY RECONSTRUCTED LAYER DOUBLE HYDROXIDE.....	119
4.1 Introduction	120
4.2 Novelty and contribution to knowledge	121
4.3 Aim.....	121
4.4 Results and discussion.....	121
4.4.1 NiAl LDH Materials Characterisation.....	122
4.4.1.1 Energy dispersive X-Ray spectroscopy of NiAl LDH	122
4.4.1.2 Thermogravimetric analysis-Mass spectrometry of NiAl LDH ..	123
4.4.1.3 Powder X-ray diffraction of NiAl LDH	127
4.4.1.4 Nitrogen porosimetry of NiAl AS and NiAl HTM	130
4.4.1.5 Scanning electron microscopy of NiAl LDH.....	132
4.4.1.6 High-resolution scanning transmission electron microscopy of NiAl LDH	133
4.4.1.7 Solid-state Al-NMR of NiAl LDH.....	134
4.4.1.8 Diffuse reflectance infrared Fourier transform spectroscopy of NiAl AS and NiAl HTM	135
4.4.1.9 Temperature-programme desorption of CO ₂ of NiAl HTM	136
4.4.1.10 X-ray photoelectron spectroscopy of NiAl HTM.....	137
4.4.2 Kinetic transesterification of tributyrin over NiAl HTM.....	140
4.4.2.1 Effect of ratio on NiAl HTM	140
4.4.2.2 Effect of temperature on NiAl HTM	141
4.4.2.3 Effect of catalyst weight on NiAl HTM	142
4.4.3 Transesterification of model compound triglycerides.....	143

4.4.3.1 C ₄ -C ₁₈ TAG reactions.....	143
4.4.4 Leaching study of NiAl HTM	146
4.4.5 Reusability study of NiAl HTM	147
4.5 Conclusion	148
4.6 References.....	149
CHAPTER 5 : CONVENTIONAL VERSUS MACROPOROUS OF MGAL LDH AND ZNAL LDH	152
5.1 Introduction	153
5.2 Novelty and contribution to knowledge	155
5.3 Aim.....	155
5.4 Results and discussion.....	155
5.4.1 Characterisation of Conventional MgAl HTs	155
5.4.1.1 Energy dispersive X-Ray spectroscopy of ConvMgAl LDH	155
5.4.1.2 Thermogravimetric analysis mass spectrometry of ConvMgAl HT	156
5.4.1.3 Scanning electron microscopy of ConvMgAl HT	160
5.4.1.4 Powder X-ray diffraction of ConvMgAl LDH	160
5.4.1.5 Temperature-programmed desorption of CO ₂ of ConvMgAl LDH	163
5.4.1.6 X-ray photoelectron spectroscopy of ConvMgAl LDH	164
5.4.2 Characterisation of polystyrene spheres.....	166
5.4.2.1 Scanning electron microscopy of polystyrene beads.....	166
5.4.3.1 Characterisation of conventional and macroporous reconstructed MgAl and ZnAl LDH.....	167
5.4.1.1 Elemental analysis of ConvLDH and MacroLDH.....	168
5.4.1.2 Powder X-ray diffraction of ConvLDH and MacroLDH.....	168
5.4.1.3 Nitrogen porosimetry of ConvLDH and MacroLDH	171
5.4.1.4 Scanning electron microscopy of ConvLDH and MacroLDH	172
5.4.1.5 High-resolution scanning transmission electron microscopy of MacroLDH	174
5.4.1.7 Diffuse reflectance infrared Fourier transform spectroscopy of ConvLDH and MacroLDH	175
5.4.1.8 Thermogravimetric analysis mass spectrometry of ConvLDH and MacroLDH	177
5.4.1.9 Temperature-programme desorption of CO ₂ of ConvLDH and MacroLDH	181

5.4.1.10 X-ray photoelectron spectroscopy of ConvLDH and MacroLDH	182
5.4.4 Catalytic activity of ConvLDH versus MacroLDH	185
5.4.4.1 C ₄ -C ₁₈ TAG reactions.....	185
5.5 Conclusion	189
5.7 References.....	189
CHAPTER 6 : COMMERCIAL CATALYSTS (DOLOMITE AND NANOMGO)	
FOR TRANSESTERIFICATION REACTION.....	191
6.1 Introduction: Dolomite and nanocrystalline MgO.....	192
6.3 Aims	194
6.4 Results and discussion.....	194
6.4.1 Characterisation of the catalysts	194
6.4.1.1 Energy dispersive X-Ray spectroscopy of Dolomite and NanoMgO	194
6.4.1.2 Thermogravimetric analysis-Mass spectrometry of Dolomite and NanoMgO	196
6.4.1.3 Powder X-ray diffraction of Dolomite and NanoMgO.....	198
6.4.1.4 Nitrogen porosimetry of Dolomite and NanoMgO.....	200
6.4.1.5 Scanning electron microscopy of Dolomite and NanoMgO	203
6.2.1.6 High-resolution scanning transmission electron microscopy of Dolomite and NanoMgO	205
6.2.1.7 Temperature-programme desorption of CO ₂ of Dolomite and NanoMgO	207
6.2.1.8 Diffuse reflectance infrared Fourier transform spectroscopy	209
6.2.1.8 X-ray photoelectron spectroscopy of Dolomite and NanoMgO ..	210
6.3 Catalytic Transesterification reactions of Dolomite and NanoMgO.....	213
6.3.1 C ₄ -C ₈ TAG	213
6.4 Leaching and reusability study of Dolomite and NanoMgO.....	217
6.5 Conclusion	220
6.6 References.....	220
CHAPTER 7 : CONCLUSION AND FUTURE WORK.....	222
7.1 Conclusions.....	223
7.2 Recommendation / Future works.....	225
7.3 References.....	225

APPENDICES	227
Appendix 1: Figure 1.1- Copyright permission from Elsevier.	226
Appendix 2: Table 1.1 Copyright permission from Elsevier.	226
Appendix 3 and 4: Figure 1.5 and 1.6- Copyright permission from Elsevier. ..	227
Appendix 5: Table 1.2- Copyright permission from Elsevier.	229
Appendix 6: Figure 1.8- Copyright permission from Elsevier.	230
Appendix 7: Figure 1.11- Copyright permission from Elsevier.	231
Appendix 8: Figure 1.12- Copyright permission from Elsevier.	232
Appendix 9: Figure 1.13- Copyright permission from Royal Society of Chemistry.	233
Appendix 10: Figure 1.14- Copyright permission from Royal Society of Chemistry.	234
Appendix 11a: Figure 1.15- Copyright permission from Elsevier.	235
Appendix 11b: Figure 1.15- Copyright permission from Royal Society of Chemistry.	236

LIST OF FIGURES

Figure 1.1	The peak oil discovery and the peak oil production for the past hundred years. Adapted from Tsoskounoglou <i>et al.</i> ⁷ with permission from Elsevier (Appendix 1).....	3
Figure 1.2	Formation of unwanted side products during saponification reaction	4
Figure 1.3	General equations of the transesterification reaction.....	7
Figure 1.4	The overall transesterification reaction of triglycerides.....	8
Figure 1.5	Mechanism reaction of transesterification by using a base catalyst. Reprinted from Meher <i>et al.</i> ³⁸ with permission from Elsevier (Appendix 3)	9
Figure 1.6	Mechanism reaction of esterification by using an acid catalyst. Reproduced from Meher <i>et al.</i> ³⁸ with permission from Elsevier (Appendix 4)	9
Figure 1.7	Classification of catalysts adapted from Chouhan and Sarma ⁵³ , copyright 2011 Elsevier (Appendix 6)	14
Figure 1.8	Illustration of layered double hydroxides (LDHs) with the different M^{2+}/M^{3+} ratio.....	21
Figure 1.9	Effect of calcination and rehydration on layered double hydroxide.....	23
Figure 1.10	Impact of MgAl HT surface basicity on their activity towards tributyrin transesterification. Adapted from Cantrell <i>et al.</i> ¹³¹ with permission from Elsevier (Appendix 7).....	29
Figure 1.11	Dual templating route approaches towards hierarchical macroporous-mesoporous silica. Adapted from Lee <i>et al.</i> ¹⁶ with permission from Elsevier (Appendix 8).....	30
Figure 1.12	Nano-engineered macroporous MgAl hydrotalcite impact on surface basicity on their activity towards tributyrin transesterification. Adapted from Woodford <i>et al.</i> ¹³³ with permission from The Royal Society of Chemistry (Appendix 9).....	31
Figure 1.13	(Top) SEM of fresh and 900 °C calcined dolomite with scheme showing corresponding structures. (Bottom) The catalytic activity of calcined Dolomite for the transesterification of short and long chain TAGs with methanol benchmarked against literature solid acid and base catalysts. Reproduced from Wilson <i>et al.</i> ⁸⁷ with permission from The Royal Society of Chemistry (Appendix 10)....	32
Figure 1.14	(Top) Fresh NanoMgO TEM images showing well-defined 3 nm cubic (100) oriented NanoMgO in an amorphous matrix. Following 500 °C annealing, these are converted into ~13 nm. (Bottom) The relationship between NanoMgO particle size and surface polarisability (ΔE_k) and Auger parameter (left) and the surface area normalised by turnover frequency for transesterification reaction (right). Adapted from Montero <i>et al.</i> ²¹⁴ and Montero <i>et al.</i> ²¹⁵ with permission from Elsevier and The Royal Society of Chemistry accordingly (Appendix 11a-b).....	33
Figure 2.1	Preparation one of the hydrotalcite catalyst in a large Radley reactor. Left: Preparation of ZnAl HTH; Right: Preparation of NiAl HTH. MgAl LDH was prepared using the same manners.....	42
Figure 2.2	Preparation one of macroporous hydrotalcite catalyst in four-neck round-bottom flask.....	45

Figure 2.3	Schematic presentation of X-ray tube (above) and simplified incident and reflection in a solid and its relation to a lattice spacing d . The image was obtained from Krumeick ⁶	46
Figure 2.4	The diffraction pattern of hydrotalcite material ¹⁰	47
Figure 2.5	The gas sorption process that occurs in four stages before 100 % saturation on pore. Retrived from http://www.quantachrome.com/gassorption/nova_series.html ¹⁶ (accessed Sep 23, 2014)	49
Figure 2.6	New IUPAC classification of physisorption isotherms, published in IUPAC Technical Report on physisorption of gases, with evaluation of surface area and pore size distribution, 2015 ¹⁵	51
Figure 2.7	IUPAC new classification of hysteresis loop types adapted from IUPAC Technical Report on physisorption of gases, with evaluation of surface area and pore size distribution, 2015 ¹⁵	52
Figure 2.8	Different contact angle applied on mercury (above) and the external pressure applied by the capillary action to force the mercury into the pores (bottom). The image was obtained from https://www.intechopen.com/books/high-performance-concrete-technology-and-applications/microstructure-of-concrete , accessed on Jan 12, 2017.....	54
Figure 2.9	The difference between Light Microscopes (LM), Transmission Electron Microscopy (TEM) and Scanning Electron Microscopy (SEM). The image was obtained from http://www.vcbio.science.ru.nl/en/fesem/info/fesemfaq/ , accessed on Jan 12,2017.....	55
Figure 2.10	The schematic principle of how a DRIFTS instrument works. The image was taken from Chen <i>et al.</i> ²²	57
Figure 2.11	Schematic diagram of how ICP operates. Source: http://www.spectroscopyonline.com/approaches-maximize-performance-and-reduce-frequency-routine-maintenance-icp-ms , retrieved on Jan 12, 2017.....	60
Figure 2.12	Schematic depiction of photoionisation involved in XPS. Accessed on Jan 27, 2017 from http://wikiwand.com/en/X-ray_photoelectron_spectroscopy	62
Figure 2.13	Illustration of how Auger electron is exhibited from the inner shell hole created by the left excited binding energy. The image was obtained from https://wiki.utep.edu/pages/viewpage.action?pagelId=39194437 , accessed on Jan 26, 2017.....	62
Figure 3.1	EDX spectrum of Zn:Al ₃ :1 LDH precursor prepared at pH10.....	74
Figure 3.2	TGA/DSC with MS profiles during decomposition of Zn:Al ₃ .33:1 LDH in N ₂ at 10 °C min from 40-800 °C. Figure A represents ZnAl LDH synthesised at pH 9 and B represent pH 10	75
Figure 3.3	Stacked XRD patterns of Zn:Al ₃ .31:1 LDH prepared at pH 9 (a) and 10 (b). i, ii, iii and iv are represented the atomic ratio of each catalyst from lower to higher ratio (0.89:1-3.20:1 at pH 9 and 1.59:1-3.33:1 at pH 10).....	77
Figure 3.4	Effect of cation distance and interlayer distance as a function of Al content (x value), synthesised at pH 9 (a) and 10(b).....	79
Figure 3.5	DRIFT spectra of ZnAl LDH precursor with Zn:Al ratio of; (a) Zn:Al 1.59:1, (b) Zn:Al 2.00:1, (c) Zn:Al 2.97:1 and (d) Zn:Al 3.33:1. On the right: Cartoon depicted assignments of the functional group involved in ZnAl LDH precursor DRIFTS bands	80

Figure 3.6	XRD pattern of calcined LDH from 250-500 °C (a-d) and its comparison at different temperature using Zn:Al _{3.33} :1 catalyst (e).	82
Figure 3.7	N ₂ adsorption-desorption isotherms of ZnAl LDH precursor and calcined series, where i-iv indicating increasing ratio from 1.59-3.33	84
Figure 3.8	SEM images of ZnAl LDH catalyst showing changes of the morphology for as-synthesised (A) versus calcined (B)	84
Figure 3.9	SEM images of rehydration ZnAl LDH (ratio 3.33:1) through achieved gas-phase (A), liquid phase (B) and hydrothermal (C), respectively	86
Figure 3.10	HRTEM images of rehydration ZnAl LDH (ratio 3.33:1) achieved through gas-phase (A), liquid-phase (B) and hydrothermal (C), respectively.....	87
Figure 3.11	Effect of temperature and ratio on ZnAl LDH. The intensity ratio of ZnAl HT/ZnO is denoted in percentage value.....	88
Figure 3.12	Effect of Zn:Al atomic ratio on reconstructed ratio ($y\text{ZnAl} / (y\text{ZnAl} + y\text{ZnO})$) and crystallite size via gas-phase rehydrated ZnAl LDH	89
Figure 3.13	XRD patterns of ZnAl LP and its dependent on calcined temperature and ratio. The intensity ratio of ZnAl HT/ZnO is denoted in percentage value	90
Figure 3.14	Effect of Zn:Al atomic ratio on the reconstructed ratio ($y\text{ZnAl} / (y\text{ZnAl} + y\text{ZnO})$) and crystallite size via liquid-phase rehydration of ZnAl LDH.....	91
Figure 3.15	XRD patterns of hydrothermal reconstructed ZnAl LDH. The intensity ratio of ZnAl HT/ZnO is denoted in percentage value.....	92
Figure 3.16	Effect of ZnAl LDH/ZnO formation and crystallinity over ZnAl HTM ratio.....	93
Figure 3.17	(a) XRD patterns of comparison between different rehydration routes, gas-phase(i), liquid-phase (ii) and hydrothermal (iii) using Zn:Al _{3.33} :1 catalyst. Cartoon depiction shows lattice parameter changes as the reconstruction method changed (b)	94
Figure 3.18	Left: N ₂ adsorption-desorption isotherms of ZnAl GP, LP and HTM series (a-c) where samples i-iv indicating increasing ratio from 1.59-3.33. Effect of rehydration routes on surface area is shown in (d) on Zn:Al _{3.33} :1 catalyst. All catalysts were calcined at 300 °C ...	95
Figure 3.19	Pore size distribution and fitting plots for ZnAl HTM.	96
Figure 3.20	Basicity desorption showing bicarbonate, bidentate carbonate and unidentate determined by CO ₂ -TPD of different rehydration/reconstruction approaches (a) and ZnAl hydrothermal series spanning from 1.59:1 to 3.33:1 (i-iv) (b)	97
Figure 3.21	Inter-correlations between lattice parameter, crystallite size, surface area and basicity of different reconstructed approached in ZnAl LDH	98
Figure 3.22	²⁷ Al MAS NMR spectra of Zn:Al 3.33:1 hydrotalcite obtained at different rehydration approaches using 9.4 T magnet spectrometer with 14 kHz spin rates	99
Figure 3.23	The C 1s, Zn 2p, Al 2p and O1s spectra (a-d) of ZnAl HTM spectra with i-iv are the increasing ratio from 1.59 to 3.33 accordingly	100
Figure 3.24	Zn surface to bulk ratios determined by XPS and EDX analysis for ZnAl HTM LDH	101

Figure 3.25	DRIFTS spectra of hydrothermal reconstructed ZnAl LDH in different ratio; i) 1.59:1, ii) 2.00:1. iii) 2.97:1 and iv) 3.33:1	102
Figure 3.26	(a) Tributyrin conversion of reconstructed ZnAl through gas-phase, liquid-phase and hydrothermal approaches using Zn:Al3.33:1 catalyst. (b) Effect of rehydration method on conversion, selectivity, and TOF using the same catalyst Conditions: 65 °C, 100 mg catalyst and 6 h reactions. MB is denoted for methyl butyrate	104
Figure 3.27	Tributyrin conversion of hydrothermal ZnAl at a different ratio (a). conversion and selectivity of tributyrin using ZnAl HTM and its catalytic performance (b). The reaction involved 50 mg catalyst, at 65 °C, 30:1 methanol: tributyrin ratio, 650 rpm for 24 hours.....	105
Figure 3.28	Dependence of rate on temperature; (a) Conversion profiles of tributyrin using Zn:Al3.33:1HTM at a different temperature, (b) Effect of temperature on TOF and selectivity and (c) Arrhenius plot for transesterification of tributyrin	107
Figure 3.29	Tributyrin conversion of hydrothermal Zn:Al3.33:1HTM at different catalyst weight (a). Effect of conversion, selectivity, and TOF by ranging the catalyst amount (b). Conditions: 110 °C in pressure flask, different catalyst weight, no co-solvent, 650 rpm and 24 h reaction	108
Figure 3.30	Influence of solvent and co-solvent (a) and TOF of tributyrin transesterification (b) on Zn:Al3.33:1HTM catalyst	109
Figure 3.31	GC chromatogram from transesterification of tributyrin using Zn:Al3.33:1 HTM catalyst.	109
Figure 3.32	Conversion profiles of C ₄ -C ₁₈ TAG on Zn:Al3.33:1HTM (a-e) and TOF (f). (f)	111
Figure 3.33	Leaching profile of for transesterification of tributyrin with methanol using ZnAl HTM catalyst (ratio 3.33:1) (a). DRIFT spectra of biodiesel solution taken at T ₀ , T _{3h} and T _{24h} (b). Reaction conditions: 100 mg catalyst, 4.98 ml tributyrin, 24.4 ml methanol and 1.18 ml dihexyl ether	113
Figure 3.34	Catalyst recyclability study involved Zn:Al3.33:1HTM for three cycles involved fresh, and spent catalysts (2nd and 3rd cycle)	115
Figure 3.35	PXRD patterns of fresh and spent catalysts (2nd and 3rd cycle). The intensity ratio of ZnAl HT/ZnO is denoted in percentage value.	115
Figure 4.1	EDX spectra of Ni:Al3.85:1 LDH precursor	123
Figure 4.2i	TGA/DSC with MS profiles during thermal decomposition of NiAl LDH from 40-800 °C on Ni:Al1.72:1 (A) and Ni:Al2.37:1 (B)	124
Figure 4.2ii	TGA/DSC with MS profiles during thermal decomposition of NiAl LDH from 40-800 °C on Ni:Al2.64:1 (C) and Ni:Al3.85:1 (D)	125
Figure 4.3	Offset wide-angle XRD patterns of as-synthesised NiAl LDH (a), calcined (b), comparison on as-synthesised, calcined, gas-phase, liquid-phase and hydrothermal reconstructed method on ratio 3.85:1 (c) and NiAl LDH hydrothermal series (d). Ni:Al1.72:1, Ni:Al2.37:1, Ni:Al2.64:1 and Ni:Al3.85:1 are denoted as i, ii, iii and iv respectively. The intensity ratio of NiAl HT/NiO is denoted in percentage value	127
Figure 4.4	Effect of Al content on basal spacing d(003), crystallite size and lattice parameter (a and c)	129

Figure 4.5	Stacked adsorption-desorption isotherms of NiAl LDH precursor and hydrothermal series. i-iv are the ratio of Ni:Al synthesised from 1.72:1, 2.37:1, 2.65:1 and 3.85:1	130
Figure 4.6	Pore size distribution and fitting plot for NiAl LDH.....	131
Figure 4.7	SEM images NiAl LDH (ratio 3.85:1) at different stages; the precursor (A) undergone calcined (B) and hydrothermal reconstruction (C) respectively	132
Figure 4.8	HR-STEM images of NiAl LDH with comparison with as-synthesised (A) and after hydrothermal (B) reconstruction techniques on Ni:Al3.85:1 catalyst	133
Figure 4.9	²⁷ Al MAS NMR spectra of Ni:Al3.85:1 hydrotalcite obtained at different stages approaches using 9.4 T magnet spectrometer with 14 kHz spin rates	134
Figure 4.10	Stacked DRIFTS spectra of NiAl AS (a) and NiAl HTM (b) where i-iv represents the Ni:Al ratio from 1.72:1 to 3.85:1 respectively	135
Figure 4.11	CO ₂ -TPD profile of NiAl hydrothermal reconstructed hydrotalcite series from 1.72-3.85 (i-iv)	136
Figure 4.12	XPS spectra of NiAl HTM represents (a) Ni 2p, (b) Al 2p and (c) O 1s. The lower to a higher ratio of Ni:Al is denoted as i-iv	139
Figure 4.13	Ni surface to bulk ratios determined by XPS and EDX analysis for NiAl HTM LDH	140
Figure 4.14	Tributyrin conversion using NiAl HTM at different ratios (a). Effect of catalytic activity on Ni:Al ratio of hydrothermal reconstructed hydrotalcite. (b). The reaction involved 100 mg catalyst, at 110 °C, 30:1 methanol: tributyrin ratio, 650 rpm for 24 hours	141
Figure 4.15	Dependence of rate on temperature using Ni:Al3.85:1 catalyst; (a) Conversion profiles of tributyrin using NiAl HTM at a different temperature, (b) Effect of temperature on TOF and selectivity and (c) Arrhenius plot for transesterification of tributyrin	142
Figure 4.16	Tributyrin conversion using NiAl hydrothermal at different catalyst weight (a). Effect of conversion, selectivity, and initial rates by ranging the catalyst amount (b). Conditions: 110 °C in pressure flask, different catalyst weight, 650 rpm and 24 h reaction	145
Figure 4.17	GC chromatogram from transesterification of tributyrin using NiAl HTM catalyst with C ₄ triglycerides at 110 °C	144
Figure 4.18	Comparison of conversion, selectivity and TOF from C ₄ -C ₁₈ using Ni:Al3.85:1 catalyst. Conditions: 110 °C in pressure flask, 650 rpm, and 24 h reaction	145
Figure 4.19	Leaching profile of for transesterification of tributyrin with methanol using Ni:Al3.85:1 HTM catalyst (a). FTIR spectra of biodiesel solution taken at T ₀ , T _{3h} , and T _{24h} (b). Reaction conditions: 100 mg catalyst, 4.98 ml tributyrin, 24.4 ml methanol and 1.18 ml dihexyl ether	146
Figure 4.20	Catalyst recyclability study involving Ni:Al3.85:1 HTM for three cycles. Conditions: 110 °C in pressure flask, 650 rpm, and 24 h reaction	147
Figure 4.21	PXRD patterns of fresh and spent catalysts (third cycle)	148
Figure 5.1i	TGA-MS patterns of thermal ConvMgAl LDH of ratio 1.83 (A) and 2.06 (B)	157
Figure 5.1ii	TGA-MS patterns of thermal ConvMgAl LDH of ratio 2.17 (A) and 3.31 (B)	158

Figure 5.2	SEM micrograph of parent ConvMgAl LDH	160
Figure 5.3	XRD patterns of the precursor, calcined, hydrothermal rehydrated and comparison of the as-synthesised (AS), calcined (CAL), hydrothermal (HTM) MgAl HTs, and comparison of all (d). a-d denoted for ConvMgAl HT ratio spanning from 1.83:1, 2.06:1, 2.17:1 and 3.31:1	161
Figure 5.4	CO ₂ -TPD profile of ConvMgAl HT series from 1.83:1, 2.06:1, 2.17:1 and 3.31:1 (i-iv)	163
Figure 5.5	Stacked Mg 2s XP (a), Al 2p XP (b) and O 1S XP (c) on ConvMgAl HT series spanning from 1.83:1 to 3.31:1 (i-iv in each series)	165
Figure 5.6	Mg surface wt % as a function of Mg:Al atomic ratio determined by XPS and EDX analysis respectively for ConvMgAl HT series	166
Figure 5.7	Representative SEM image of polystyrene spheres and associated particle size distribution	167
Figure 5.8	XRD diffraction patterns of conventional and macroporous MgAl and ZnAl LDH. The intensity ratio of HT over mixed oxide is denoted by the percentage values	169
Figure 5.9	Stacked adsorption-desorption isotherms of conventional (a) and macroporous (b) MgAl, and ZnAl LDH	171
Figure 5.10	The pore size distribution of ConvLDH and MacroLDH on MgAl HT (left) and ZnAl HT (right) obtained from mercury intrusion porosimetry	172
Figure 5.11	SEM images of conventional (left) and macroporous (right) MgAl LDH(A) and ZnAl LDH (B)	173
Figure 5.12	Calcined (left) and rehydrated (right) MacroMgAl LDH (A) and MacroZnAl LDH (B)	174
Figure 5.13	HR-STEM images of the MacroMgAl HT (A) and MacroZnAl HT (B).....	175
Figure 5.14	DRIFTS spectra of MgAl LDH and ZnAl LDH with indicates spectra for ConvLDH and MacroLDH respectively	176
Figure 5.15	TGA-MS patterns of thermal conventional (A) and macroporous (B) MgAl LDH	178
Figure 5.16	TGA-MS patterns of thermal conventional (A) and macroporous (B) ZnAl LDH	179
Figure 5.17	Theoretical and experimental weight loss of water and carbonates over ConvLDH and MacroLDH MgAl and ZnAl	180
Figure 5.18	Stacked CO ₂ -TPD profiles of conventional and macroporous of MgAl LDH (A) and ZnAl LDH	181
Figure 5.19	a-d) XPS spectra ConvLDH and MacroLDH of MgAl for C1s, Mg 2s, Al 2p and O 1s XP	183
	e-h) XPS spectra ConvLDHLDH and MacroHT of ZnAl for C1s, Zn 2p, Al 2p and O 1s XP	184
Figure 5.20	Reaction profile C ₄ -C ₁₈ for conventional and macroporous of MgAl LDH (left) and ZnAl LDH (right)	185
Figure 5.21	Reaction profile of ConvLDH and MacroLDH for both MgAl and ZnAl LDH in transesterification over C ₄ . Reaction conditions: 110 °C, 650 rpm for 24 h reactions	187
Figure 5.22	TOF profile C ₄ -C ₁₈ for conventional and macroporous of MgAl LDH (a) and ZnAl LDH.....	188

Figure 6.1	EDX spectra of commercial dolomite (a), ex-gasifier dolomite(b) and NanoMgO(c).....	195
Figure 6.2	TGA/DSC with MS profiles during thermal decomposition of commercial dolomite (A), ex-gasifier dolomite (B) and NanoMgO (C) in N ₂ at 10 °C min from 40-900 °C (for both dolomite) and from 40-800 °C (for NanoMgO)	197
Figure 6.3	XRD patterns of commercial dolomite, ex-gasifier dolomite and NanoMgO. Dolomite samples were calcined at 900 °C, meanwhile, NanoMgO was calcined at 500 °C	199
Figure 6.4	A stack of adsorption-desorption isotherms of commercial dolomite (a), ex-gasifier dolomite (b) and Nano MgO (c)	201
Figure 6.5	BJH pore size distribution (left) and DFT pore size distribution (right) of commercial dolomite (A), ex-gasifier dolomite (B) and Nano MgO (C)	202
Figure 6.6	SEM images of commercial dolomite (A), ex-gasifier dolomite (B) and NanoMgO (C)	204
Figure 6.7	Representative bright STEM images of commercial dolomite (A), ex-gasifier dolomite (B) and NanoMgO (C)	206
Figure 6.8	CO ₂ desorption profiles of precursor and calcined dolomites, spent dolomite and NanoMgO	208
Figure 6.9	DRIFTS spectra of commercial dolomites, ex-gasifier dolomites and NanoMgO. a and b are denoted for fresh and calcined catalysts respectively	209
Figure 6.10	C1s (a), Ca 2p (b), Mg 2p (c) and O1s (d) obtained from fresh and calcined of commercial dolomite (i) and ex-gasifier dolomite (ii)	211
Figure 6.11	C1s (a), Mg 2p (b) and O1s(c) spectra obtained from fresh and calcined NanoMgO sample	212
Figure 6.12	C ₄ -C ₁₈ conversion and yield profiles of calcined commercial dolomite (a), ex-gasifier dolomite (b) and NanoMgO (c)	215
Figure 6.13	Reactant and product profiles of tributyrin (C ₄) on commercial dolomite (a), ex-gasifier dolomite (b) and NanoMgO (c). TB, MB, DB and MoB are denoted for tributyrin, methyl butyrate, dibutyryn and monobutyryn respectively	216
Figure 6.14	Comparison of TOF obtained from C ₄ -C ₁₈ using the commercial dolomite, ex-gasifier dolomite and NanoMgO.....	217
Figure 6.15	Leaching profile (a-c) and reusability (d) of solid base catalyst for transesterification of tributyrin with methanol using commercial dolomite, ex-gasifier dolomite and NanoMgO	219
Figure 7.1	Comparison of TOF values in varying chain length triglyceride (C ₄ , C ₈ , C ₁₂ and C ₁₈) transesterification reactions using methanol for the best-performing catalysts from each chapter	224
Figure 7.2	Effect of basicity on the solid base catalysts used in this study.....	224

LIST OF TABLES

Table 1.1	Comparison of petrol diesel and biodiesel fuel property. Adapted from Joshi and Pegg ³⁰ with permission from Elsevier (Appendix 2).....	5
Table 1.2	Comparison of petroleum fuel, first and second generation of biodiesel. Adapted from Naik <i>et al.</i> ⁴⁵ with permission from Elsevier (Appendix 5)	12
Table 1.3	Drawbacks of homogeneous catalysts and the advantages of heterogeneous catalysts.....	13
Table 1.4	Recent heterogeneous solid acid catalysts for biodiesel production.....	15
Table 1.5	Recent heterogeneous solid base catalytic transesterification.....	17
Table 1.6	Past and recent evolution of layered double hydroxides catalysts.....	21
Table 1.7	Common methods of hydrotalcite synthesis.....	24
Table 1.8	The range optimum value of x for obtaining pure HT.....	27
Table 2.1	Comparison of Light Microscope (LM) with Scanning Electron Microscopy (SEM)	55
Table 2.2	Comparison of Scanning Electron Microscopy (SEM) with Transmission Electron Microscopy (TEM).....	56
Table 2.3	Relative sensitivity factor (R.S.F) and the main peak value for the element used in this study.....	61
Table 3.1	The nominal and actual bulk of ZnAl HT atomic ratio synthesised at pH 9 and 10	73
Table 3.2	Experimental and theoretical weight loss and the ZnAl LDH formula as obtained from TGA-MS and EDX	76
Table 3.3	Comparison of the textural parameters of ZnAl LDHs synthesised at different pH	79
Table 3.4	BET surface area (S_{BET}) for ZnAl LDH precursor and calcined at 300 °C	83
Table 3.5	The textural parameter of ZnAl LDH reconstructed through gas-phase, liquid- phase and hydrothermal approaches	93
Table 3.6	BET surface area (S_{BET}) for ZnAl GP, LP and HTM.....	96
Table 3.7	The amounts of basic sites in ZnAl LDH samples	98
Table 3.8	Triglycerides chain length used in this study ($\text{C}_4\text{-C}_{18}$)	110
Table 3.9	Band wavelength of biodiesel reaction of C_4 obtained by DRIFTS..	113
Table 3.10	The concentration of Zn and Al (3.33:1) in leaching tests as determined by ICP-OES	113
Table 3.11	The atomic weight of Zn and Al on fresh and third cycles determined by ICP-OES and the carbon content from CHNS on Zn:Al3.33:1HTM catalyst	114
Table 4.1	The nominal and actual bulk of NiAl LDH atomic ratio.....	122
Table 4.2	Comparison of water and carbonates in experimental and theoretical weight loss of NiAl LDH.....	126

Table 4.3	The textural parameter of basal spacing $d(003)$, lattice parameter and crystallite size of NiAl LDH precursor and hydrothermal	129
Table 4.4	BET surface area (S_{BET}) for NiAl precursor and hydrothermal LDH.....	131
Table 4.5	The amounts of basic sites in NiAl LDH samples.....	137
Table 4.6	The atomic weight of Ni and Al on first and third cycles determined by ICP-OES.	148
Table 5.1	Collection of methodologies implemented for the synthesis of macroporous LDH materials	154
Table 5.2	The nominal and actual bulk of MgAl HT atomic ratio.....	156
Table 5.3	Comparison of water and carbonate in experimental and theoretical weight loss of ConvMgAl HT as obtained from TGA-MS and EDX....	159
Table 5.4	The textural parameter of basal spacing $d(003)$, lattice parameter and crystallite size for MgAl HT	162
Table 5.5	The amounts of basic sites in ConvMgAl HT samples.....	164
Table 5.6	Bulk M^{2+} : Al^{3+} ratio determined by EDX and XPS for conventional and macroporous LDH	168
Table 5.7	The textural parameter of conventional and macroporous MgAl and ZnAl LDH including the basal spacing $d(003)$, lattice parameter and crystallite size.	170
Table 5.8	BET surface area (S_{BET}) and mercury intrusion pore diameter for conventional and macroporous MgAl and ZnAl LDH.....	171
Table 5.9	Experimental, theoretical weight loss and the LDH formula obtained from TGA-MS and EDX	180
Table 5.10	Base site characterisation obtained via CO_2 chemisorption/TPD.....	181
Table 5.11	Comparison of catalytic performance on transesterification using MacroMgAl LDH	188
Table 6.1	Elemental analysis of commercial dolomite and ex-gasifier dolomite NanoMgO determined by EDX	195
Table 6.2	Elemental analysis of NanoMgO determined by EDX.....	195
Table 6.3	Carbon dioxide weight loss from dolomite and NanoMgO obtained from EDX	198
Table 6.4	Comparison of crystallite size of commercial dolomite, ex-gasifier dolomite and NanoMgO.....	200
Table 6.5	The textural parameter of surface area, pore volume and pore diameter of the precursor and calcined dolomite and NanoMgO.....	201
Table 6.6	The amounts of basic sites in dolomites (commercial and ex-gasifier) and NanoMgO	208
Table 6.7	Elemental and surface analysis of commercial dolomite, ex-gasifier dolomite and NanoMgO	213
Table 6.8	Before and after filtered mass concentration of the catalysts to evaluate the leaching test as determined by ICP-OES	219

LIST OF SCHEMES

Scheme 1.1	Twelve principles of Green Chemistry introduced by Paul Anastas in 1998 ¹⁸⁸	26
Scheme 3.1	The scope of this study involving different layer alterations via different Zn^{2+}/Al^{3+} ratio which involved in calcination, hydrothermal reconstruction and later being adopted in transesterification reaction of triglycerides.....	71
Scheme 3.2	Rehydration approaches on ZnAl LDH synthesised via the alkali-free method	72
Scheme 3.3	The schematic view showing the basal spacing, layer thickness and interlayer thickness of a layer double hydroxide ⁴¹	78
Scheme 3.4	Illustration of calcination process taking place at desired temperature.....	81
Scheme 4.1	Illustration of hydrothermally reconstructed NiAl layered double hydroxides (LDHs) applied in a transesterification reaction of triglycerides spanning from C_4 to C_{18}	121
Scheme 4.2	Comparison of NiO and $Ni(OH)_2$ spectra obtained from http://xpssimplified.com/elements/nickel.php	137
Scheme 5.1	Polystyrene templating route to transform ordinary layered double hydroxide into a macropore network	153
Scheme 6.1	Calcite hexagonal unit cell superimposed onto rhombohedral unit cell (a) and dolomite hexagonal unit cell superimposed onto rhombohedral unit cell (b). Figure adapted from Gregg <i>et al.</i> ⁴	192
Scheme 6.2	Cationic defect on the solid base catalyst of $Mg^{2+}-O^{2-}$ and how crystal facet termination increased the base strength from $(100) < (110) < (111)$ (a), adapted from Ref ³ and the application of mixed oxide from different facet (b), adapted from Kuang <i>et al.</i> ⁷	193
Scheme 6.3	The (100) , (110) and (111) facets of MgO. Source: ²²	205
Scheme 7.1	Solid base catalysts used in this research for transesterification reaction of model chain TAG.	223

ABBREVIATIONS

AS	As-synthesised
ASTM	American Society for Testing and Materials
BE	Binding energy
BET	Brunauer, Emmett and Teller
BJH	Barrett, Joyner and Halenda
CAL	Calcined
Co-ppt	Co-precipitation
DRIFTS	Diffuse reflectance infrared Fourier transform
FAME	Fatty acid methyl ester
FFA	Free fatty acid
GP	Gas-phase
HT	Hydrotalcite
HC	Hydrocarbon
HRTEM	High-resolution transmission electron microscopy
HTM	Hydrothermal
HTLC	Hydrotalcite-like compound
ICP-OES	Inductively coupled plasma optical emission spectroscopy
LDH	Layered double hydroxide
LP	Liquid-phase
MacroHT	Macroporous hydrotalcite
MS	Mass-spectroscopy
TAG	Triacylglycerol
TPD	Temperature-programmed desorption
TOF	Turnover frequency
PSD	Particle size distribution
SEM	Scanning Electron Microscopy
XPS	X-ray photoelectron spectroscopy
XRD	X-ray powder Diffraction

Chapter 1

Introduction

Published in¹:

“Chapter 6-Production of biodiesel via catalytic upgrading & refining of sustainable
oleageneous feedstocks.”

Handbook of Biofuels Production (Second Edition)
Processes and Technologies

2016, Pages 121–164

<http://dx.doi.org/10.1016/B978-0-08-100455-5.00006-0>

1.0 Introduction

This chapter provides an overview of the current status of biodiesel production using heterogeneous solid acid and base catalysts¹ which can offer significant process advantages of improved product separation, decreased waste and also opportunities to work in continuous operation. A particular focus of the review will be on recent robust catalysis technology which seeks to overcome mass transfer limitation in bulk by designing tailored hierarchical macroporous-mesoporous frameworks.

1.1 Problem statement and research motivation

In this topic, two major research problems have been identified. The first issue is related to the fossil oil depletion and the second issue is on how homogeneous catalysts are not suitable to use in biodiesel transesterification reactions will be explained in following sub-topic.

1.1.1 Oil depletion issues

The World Energy Forum has predicted that fossil-based oil, coal and gas reserves will be exhausted in less than ten decades²⁻⁴. Exxon Mobil has developed an annual outlook on future trends in energy supply, demand and technology⁵. According to this report, the world's population will rise 25 % from 2010 to 2040, equating to a growth of nearly nine billion. Along with this urban growth, energy consumption and fuel usage also will be increased. Whilst demand keeps increasing across the years, consumption of oil is faster than discoveries, thus petroleum production is decreasing and will be depleted.

These predictions are described by *Hubbert* peak theory, which says that when the peak production is passed, production rates enter an exponential decline⁶. The depletion or decline process is a natural phenomenon that accompanies the development of all non-renewable resources. **Figure 1.1** illustrates the global peak oil discoveries and production over the past centuries. This issue has brought a renewed interest in the use of bio-based materials.

The desire to replace the petroleum-based material with environmentally friendly and sustainable alternatives has stimulated the development of oil-based materials such as biodiesel. The development of renewable, biodegradable, and environmentally friendly industrial fluids on biodiesel has resulted in the widespread use of natural oils and fats from non-edible feedstocks.

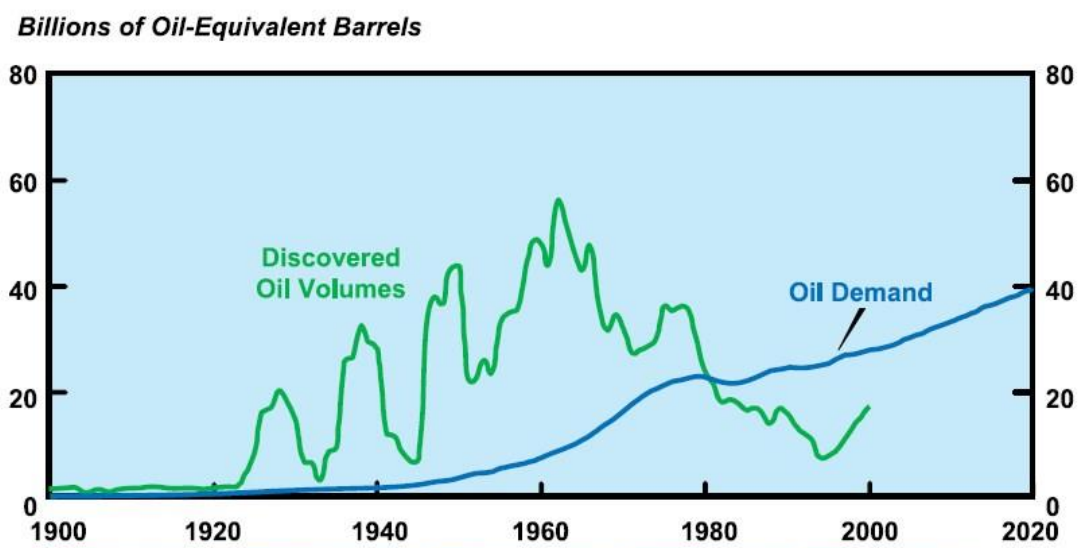


Figure 1.1 The peak oil discovery and the peak oil production for the past hundred years. Adapted from Tsoskounoglou *et al.*⁷ with permission from Elsevier (Appendix 1).

1.1.2 Problems of homogeneously catalysed biodiesel production

Biodiesel is defined as an alternative fuel that being produce from a transesterification process using oils or fats from vegetable oil, tallows or waste cooking oil. Conventionally, the most frequent method used to produce biodiesel is using a homogeneous acid-base catalyst. Homogeneous base catalysts such as sodium and potassium hydroxides, for instance, have been reported to yield high conversion of vegetable oil to methyl ester^{8,9}. However, there are many drawbacks, in particular, catalyst recovery is almost impossible and saponification occurs with results in separation and purification problems^{8–12}. Thus, biodiesel and glycerol by-product have to undergo extensive washing, which is energy intensive, generating vast quantities of waste, as well as being a time-consuming process.

Homogeneous catalysts are also often very sensitive towards free fatty acid (FFA) and water content in triglycerides (TAG)¹³. If the feedstock contains more than 3 wt% FFA, typical homogeneous catalysts such as sodium hydroxide (NaOH), potassium hydroxide (KOH) or methoxide have tendencies to form soap and water (or methanol if using methoxide ions) through the saponification process^{12,14} (**Figure 1.2**). This leads to quenching steps which render separation of the catalyst become almost impossible¹⁵. Complete removal of the catalyst is essential as several researchers reported residual homogeneous catalyst can corrode engine components^{12,16}.

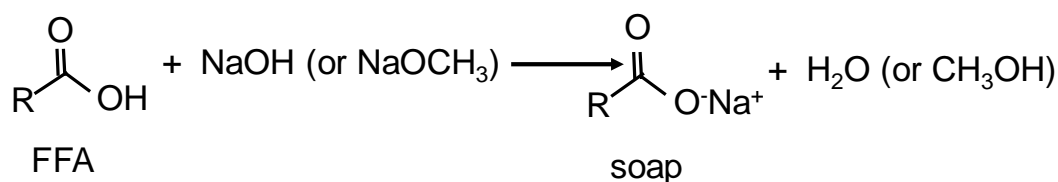


Figure 1.2 Formation of unwanted side products during saponification reaction.

In view of the limitations associated with homogeneous catalysts, suitable heterogeneous catalysts are needed as a matter of urgency for green chemistry, as emphasised by Dhakshinamoorthy *et al.*¹⁷ with the advantages of heterogeneous catalysts widely reported^{8,12,16,18}. Apart than that, the potential to exploit the simplified downstream operation of a heterogeneously catalysed process, along with improved economics process and probability for producing higher purity biodiesel are more pronounced⁸. It is important that the catalyst does not exhibit any leaching of the active phase during the reaction in order to have more productive catalyst and to avoid contaminating product at the same time. In both cases discussed above, urgent alternatives oil sources are needed in order to meet the current demand. This has motivated scientists and researchers to work hard in order to accomplish this goal.

1.2 General background to biodiesel

1.2.1 Biodiesel as an alternative fuel

There many research initiatives aimed at developing alternative renewable biodiesels and energy resources^{19–21}. However, alternate resources of first and second generation biodiesels derived from terrestrial crops and non-edible crops contribute to water shortages and destruction of the world's forests¹⁰. Therefore, biodiesels specifically derived via transesterification reaction of oil feedstock using heterogeneous solid base and solid acid catalysts are considered to be a technically viable alternative energy resource that is devoid of the major drawbacks of first-generation biodiesels.

The urge to find sustainable replacements for transport fuel has led to a drive to find renewable, non-toxic and carbon-neutral biofuels. Biodiesel is a fuel composed of a mono-alkyl ester derived from vegetable oil or fats oil, which is proven to contribute to reductions in the world's dependence on fossil oils²². The most significant advantages of biodiesel usage over fossil fuel are:

- a) Biodiesel can be produced from plant, algae or waste oil, including sunflower, soybean, palm, canola oil, jatropha oil and many more^{10,23,24}. This factor contributes to the reduction of greenhouse gas (GHG) emission simultaneously²⁵. However, care must be taken to ensure land use issues do not arise when using such feedstocks.
- b) Biodiesel is biodegradable, non-toxic, safe and produces less contamination towards environments compared to fossil fuels which release greenhouse gases that lead to the global warming²⁶.
- c) Biodiesel has the remarkable potential to lessen the world's dependency on petroleum-based oil. The transportation sector is the most dependent on petroleum-based fuel such as diesel, gasoline and liquid petroleum gas (LPG) and compressed natural gas (CNG)²⁷. Sharma *et al.*²⁵ reported that biodiesel produces non-toxic emissions due to it having less carcinogenic components and a low sulphur content. In addition, biodiesel significantly reduces exhaust emissions such as unburnt hydrogen, carbon monoxides and particulate matters.
- d) Biodiesel is also a safer fuel which gives better engine performance due to the higher cetane number (CN) and flash point compared to petrol diesel (**Table 1.1**). The essential property of diesel performance is the ability to auto ignite, which is determined by the cetane number²⁸. The higher the cetane number, the better performance of the engine.
- e) Biodiesel improves the energy security of nations, particularly developing nations without fossil fuel reserves, with the potential to play an important role in world primary energy. Producing biodiesel can help a country lessen their reliance on imported fuel or reduce the impact of volatile foreign markets. Biodiesel can also help support local economies where it creates new infrastructure jobs for people²⁹.

Table 1.1 Comparison of petrol diesel and biodiesel fuel property. Adapted from Joshi and Pegg³⁰ with permission from Elsevier (Appendix 2).

Fuel property	Diesel	Biodiesel
Fuel standard	ASTM D975	ASTM PS 121
Fuel composition	C ₁₀ – C ₂₁ HC	C ₁₂ -C ₂₂ FAME
Lower heating value (MJ/m ³)	36.6 × 10 ³	32.6 × 10 ³
Kinematic viscosity @ 40 °C (mm ² /s)	1.3–4.1	1.9–6.0
Specific gravity @ 15.5 °C	0.85	0.88
Density @ 15 °C (kg/m ³)	848	878

Water (ppm by wt.)	161	0.05 % max
Carbon (wt%)	87	77
Hydrogen (wt%)	13	12
Oxygen (by diff.) (wt%)	0	11
Sulfur (wt%)	0.05 max	0.0–0.0024
Boiling point (°C)	188–343	182–338
Flash point (°C)	60–80	100–170
Cloud point (°C)	–15 to 5	–3 to 12
Pour point (°C)	–35 to –15	–15 to 10
Cetane number	40–55	48–65
Stoichiometric air/fuel ratio (wt./wt.)	15	13.8

Even though biodiesel comprises advantages over diesel fuels as mentioned above, it also has limitations. Among the disadvantages of biodiesel or direct use of oils as a fuel are:

- a) Production of biodiesel from edible oils (first generation of biodiesel) has led to many issues such as competition over land usage for crops agricultural and biofuel production. In conjunction with this, food shortage, raised food prices and destruction of biodiversity as deforestation occurred²⁹ are major causes for concern. The production of biodiesel from second generation feedstocks should be encouraged to make these more viable/profitable.
- b) Incomplete combustion is a frequent problem associated with the direct use of vegetable oil as a fuels³¹. While polyunsaturated fatty acids are very vulnerable to polymerisation and gum formation at a higher temperature, this can be improved by blending vegetable oil with diesel.
- c) Other problems include carbon deposits, coking and trumpet formation in injectors, oil ring sticking and thickening and lubricating oil gelling^{8,32,33}. Atadashi *et al.*⁸ addressed the above problems and also suggested few potential solutions such as preheating engines prior to starting, adjusting injection timing and use of higher compressor engines.

1.2.2 The Biodiesel production process

Commercially, there are four different techniques to produce biofuel from triglycerides; direct use and blending, microemulsions, thermal cracking (pyrolysis) or transesterification²³. Out of these methods, transesterification is the most energy efficient due to the mild conditions that can be employed for conversion of the triglyceride to the fatty acid methyl ester (FAME) which is the fuel widely referred to as biodiesel¹¹. Transesterification is a process of converting triglycerides (TAG) from vegetable oil or fats to fatty acid methyl ester (FAME) in the addition of an alcohol such as methanol in the presence of acid, base or enzyme catalyst (**Figure 1.3**).

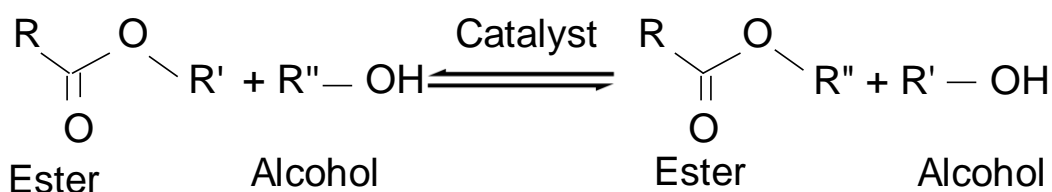


Figure 1.3 General equation of the transesterification reaction.

1.2.3 The transesterification reaction

Transesterification is a reversible reaction in which there is an exchange of the alkyl group of an ester with an alkyl group of an alcohol as shown above, and can be catalysed by acid or base catalyst^{26,34}. This reaction also can be accomplished by addition of enzymes (biocatalysts) particularly lipases^{35–37}. Biodiesel is commonly composed of fatty acid methyl ester (FAME) and can be produced by triglycerides from vegetable oils by transesterification with methanol as illustrated in **Figure 1.4**. The reaction of triglycerides with methanol proceeds in a stepwise manner to produce the intermediates of diglyceride and monoglyceride, with subsequent reactions with methanol producing glycerol and biodiesel.

The mechanisms for base and acid catalysed transesterification are shown in **Figure 1.5** and **Figure 1.6**³⁸ respectively. In the basic conditions, the nucleophilic of alkoxide ion (RO^-) attacks the carbonyl group of triglycerides ions and forming a tetrahedral intermediate. This process is followed by the rearrangement of the intermediate producing one molecule of methyl ester and diglyceride ion, with a further nucleophilic attack on the electrophile producing glycerol and FAME (biodiesel).

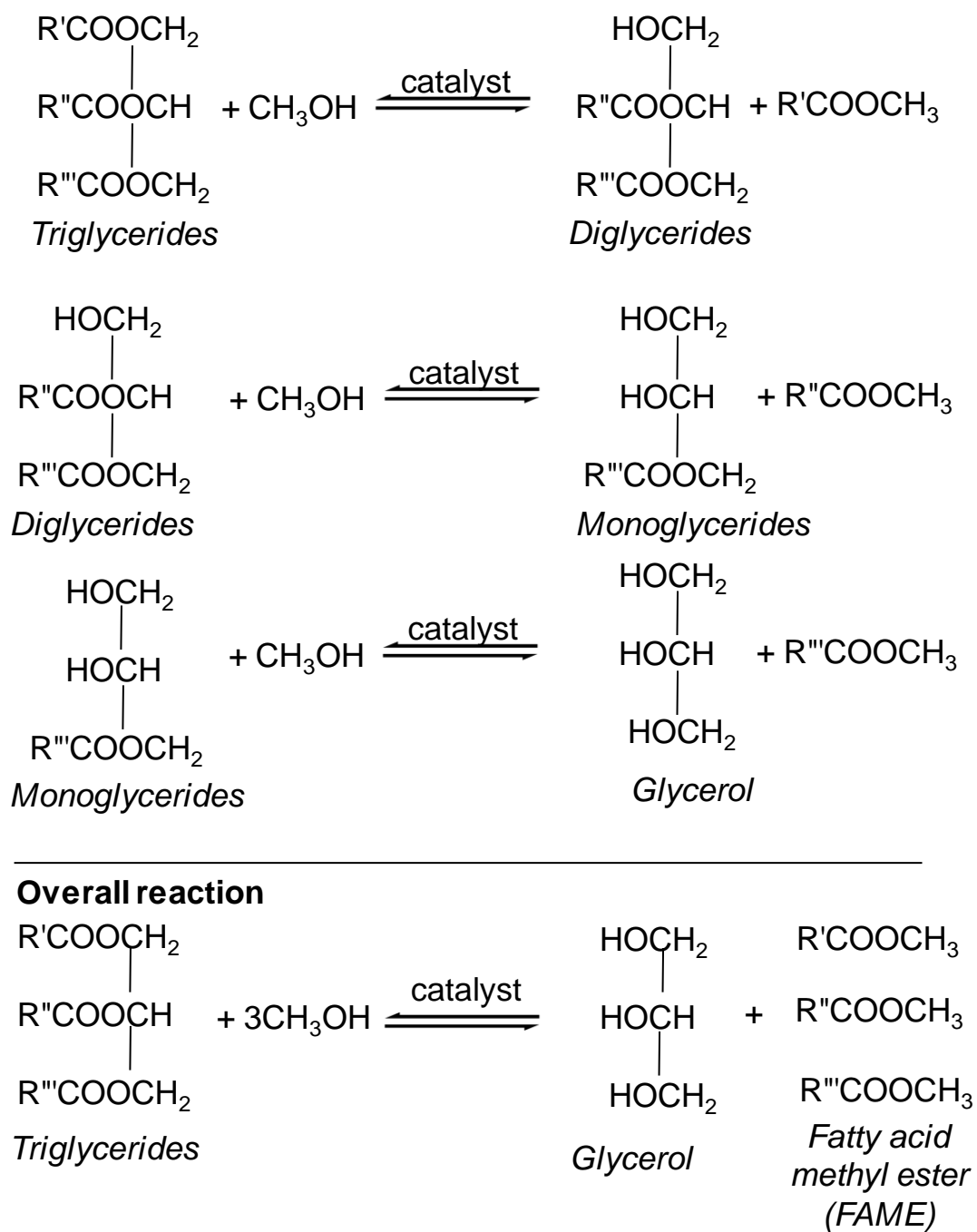


Figure 1.4 The overall transesterification reaction of triglycerides.

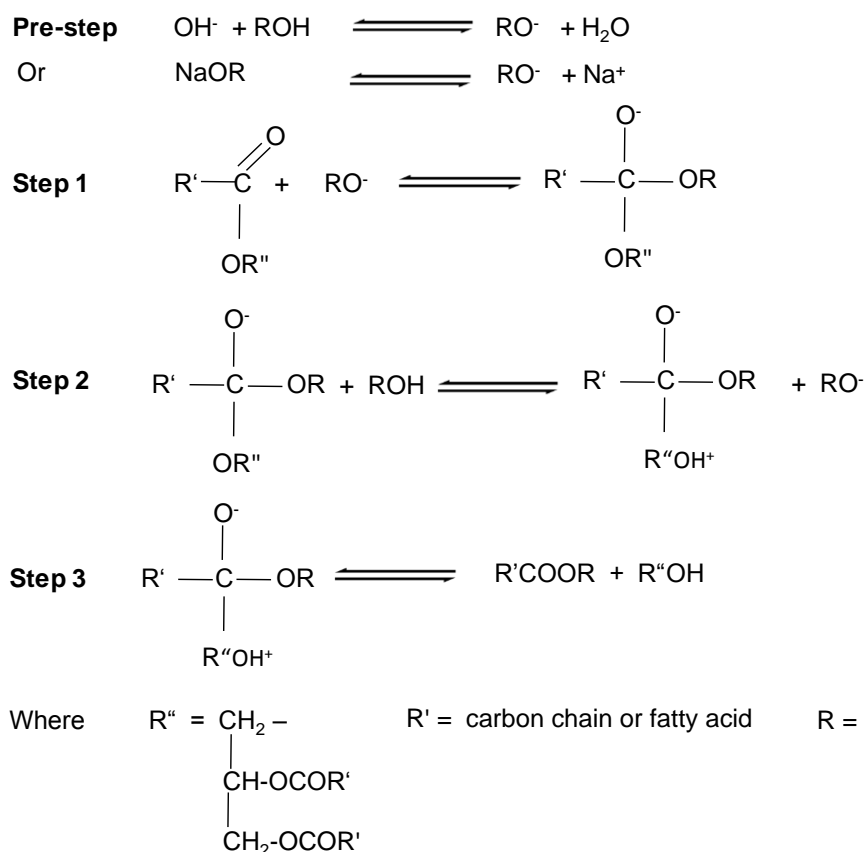


Figure 1.5 Mechanism reaction of transesterification by using a base catalyst. Reprinted from Meher *et al.*³⁸ with permission from Elsevier (Appendix 3).

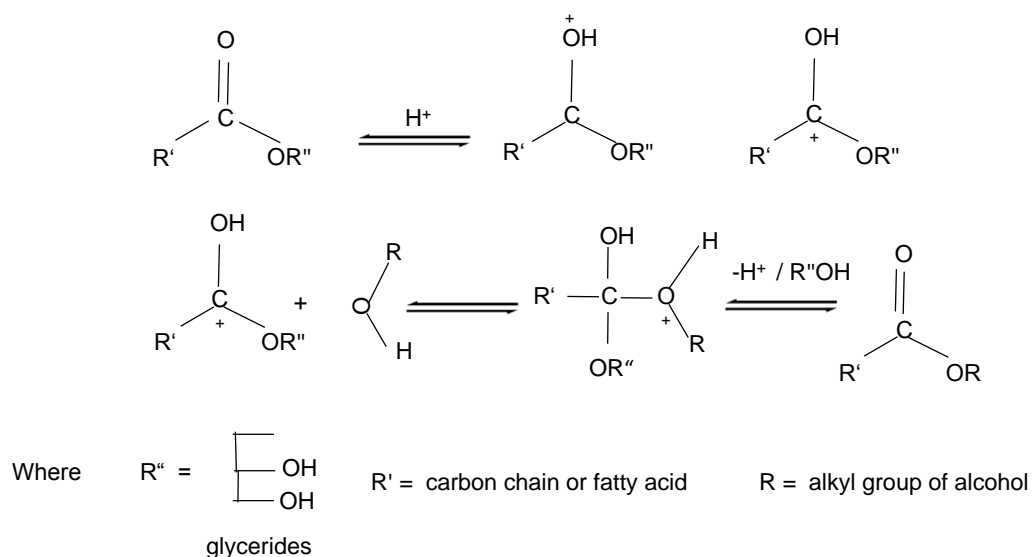


Figure 1.6 Mechanism reaction of esterification by using an acid catalyst. Reproduced from Meher *et al.*³⁸ with permission from Elsevier (Appendix 4).

For the acid catalysed -reaction, the carbonyl group is activated toward nucleophilic attacks by protonation of H^+ . Principally, carbonyl is protonated first before OH due to the carbonyl group being more nucleophilic compared to OH. The net effect of protonation leads to a weakening of the carbon-oxygen π bond thus makes carbonyl carbon a stronger electrophile. The weakly nucleophilic alcohol is then able to attack the carbonyl carbon forming an intermediate which possesses two equivalent hydroxyl groups. Intramolecular proton transfer ultimately leads to the loss of water and a proton as the ester is formed.

Hydrotalcite, a common solid base catalyst has been received an enormous attention in the transesterification of biodiesel³⁹. The first systematic study of transesterification mechanism using ZnAl hydrotalcite was reported by Liu *et al.* in 2014⁴⁰. To be active in transesterification, the catalyst must adsorb the substrate to produce intermediate products and further reacts to produce the final products. Interestingly, they reported methanol can absorb on OH group of triglycerides and form both bridging and terminal methoxy group if the reaction temperature is at 423 K. They also stated transesterification is more favourable on terminal methoxy due to it being more ionic^{40,41}. Meanwhile, bridging methoxy may re-associate to methanol henceforth do not contribute in the transesterification.

Another recent systematic study on transesterification mechanism of MgAl hydrotalcite has been done by Ma *et al.*⁴² in 2016 aligned with details reported by Liu *et al.*⁴⁰. In general, to activate the reaction, methanol is catalytically absorbing on the surface to form the nucleophilic methoxy (CH_3O^-) species. Then, the methoxy group attacks the carbonyl carbon to form tetrahedral intermediates. Rearrangement of intermediates happens if the surface of the catalysts has sufficient methoxy coverage, then transesterification will occur sequentially, leading to diglycerides, monoglycerides, and ultimately glycerol⁴⁰.

1.2.4 Oil feedstocks for biodiesel production

1.2.4.1 1st and 2nd generation biodiesel fuels

Conventionally, biodiesel is produced from a chemical reaction called transesterification as explained earlier. Biodiesel can be classified into two types: first generation and second generation biodiesel. The first generation of biodiesel is derived from edible feedstock such as soybean oil, rapeseed oil, palm oil, sunflower oil and linseed^{1,26}, however, these sources of biodiesel provoked much concern over the competition of land use for agriculture versus energy crop cultivation^{12,26,43}. These oils also have different fuel properties when compared to diesel fuel, most notably higher density, viscosity and flash point, as well as lower cetane number and heating values, which raised environmental issues relating to incomplete combustion and production of higher levels of emissions¹¹.

Then, so-called second generation biodiesel feedstocks are derived from non-food oil sources and have been developed to reduce the dependency on edible oils⁴⁴. *Jatropha curcas*, jojoba oil, tobacco seed and sea mango are among the second generation biodiesel⁴⁵. In addition to increased use of waste cooking oils, restaurant grease and animal fats, such as beef tallow and pork lard, which are also considered as second generation feedstocks. **Table 1.2** shows the comparison of petroleum fuel, first and second generation of biodiesel as well as other biofuels derived from sugars and lignocellulose that form part of the renewable fuels landscape.

Biodiesel production from algae is another perspective avenue that is receiving increased attention from biodiesel researchers²⁷. While there is a strong view among industry professionals that algae represent the most optimal feedstock for biofuel production in the long run, there are concerns over the cost of production and nutrient requirement which needs to be carefully managed. These second generation biofuels will help to reduce the demand on land as algal cultivation can be conducted in large scale pond facilities which do not place a demand on agricultural land⁴⁶. Algae is claimed to be the only feedstock that can be produced on a scale large enough to meet targets for biofuel production in a short time^{47–49}.

Table 1.2 Comparison of petroleum fuel, first and second generation of biodiesel. Adapted from Naik *et al.*⁴⁵ with permission from Elsevier (Appendix 5).

Criteria/Type	Petroleum refinery	First generation	Second generation
Feedstock	Crude petroleum	Edible vegetable oils, corn sugar, etc.	Non-edible crops, waste biomass i.e cellulose, lignin etc. and aquatic biomass (algae)
Products	Compressed natural gas (CNG), liquefied petroleum gas(LPG), diesel, petrol, kerosene, jet fuel	Fatty acid methyl ester (FAME) or biodiesel, corn ethanol, sugar alcohol	Bio oil, hydrotreating oil, lignocellulosic ethanol, butanol, mixed alcohols
Problem	Depletion of petroleum reserve, environmental pollution, economic and ecological problems	Limited feedstock (food vs fuel), blended partly with conventional fuel	Still under development to reduce the cost (advance technology)
Advantages	-	Environmental friendly, economic and social security	No food competition Environmentally friendly

1.3 *Recent robust technology in biodiesel catalysis*

. Catalysis is a vital technology in today's world.. In reality, most of the industrial sectors are relying on the catalyst for their economic growth. The catalyst is the substance that alters the rate of a reaction without itself undergoing any permanent chemical change. The catalyst is not a new phenomenon, although its wide-scale application by mankind has only really begun in the last century.

Nowadays, the term of catalyst encompasses both catalyst precursor and the catalytically active species. The catalyst precursor is a substance added to the reaction but may undergo loss of a ligand before it is available as catalytically active species. Some reactions are tending to internally catalyse (autocatalysis) during the reaction take places, where one of the products is able to catalyse the reaction itself.

1.3.1 *Homogeneous vs heterogeneous catalysis*

In Section 1.1.2, the undesirable homogeneous catalysts used in biodiesel have been discussed in detail. Although transesterification using a homogeneous alkali-catalysed process gives high conversion levels of triglycerides to their corresponding

methyl esters in short times, the reaction has several drawbacks. **Table 1.3** summaries the drawbacks of homogeneous catalysts and the advantages of heterogeneous catalysts.

Table 1.3 Drawbacks of homogeneous catalysts and the advantages of heterogeneous catalysts.

Drawbacks of homogeneous catalysts	Advantage of heterogeneous catalysts
Difficult to separate the catalysts from product	Easily separated for recycling
Technically difficult to recycle the catalyst	Possible for reusability
Catalyst needs to be removed or washed by a large amount of hot water	Minimise the product separation and purification costs
Produce large amount of industrial wastewater	Economically viable to compete with commercial petro-base diesel fuel
Homogeneous acid catalysts are corrosive to equipment	Non-corrosive and non-toxic catalysts

Owing to these disadvantages, research on the transesterification reaction using heterogeneous catalysts for biodiesel production has increased over the past decade¹⁶. **Figure 1.7** summarises the classification of catalysts. Zhang *et al.*⁵⁰ argued there is a considerable incentive for the substitution of the liquid base by the solid base for the following reasons: (a) energy intensive product/catalyst separation, (b) corrosiveness and (c) the costs associated with the disposal of spent or neutralised caustics.

In other words, the use of heterogeneous catalysts allows an environmental friendly process to be used for biodiesel production. Furthermore, McNeff *et al.*⁵¹ agreed the use of heterogeneous catalysts could enable the design of an efficient, continuous process and improve the economics of biodiesel production. Furthermore, the use of heterogeneous catalysts will reduce the production of soaps through free fatty acid neutralisation as reported by Guo *et al.*⁵², which simplifies the post-treatment (i.e. separation and purification) processes.

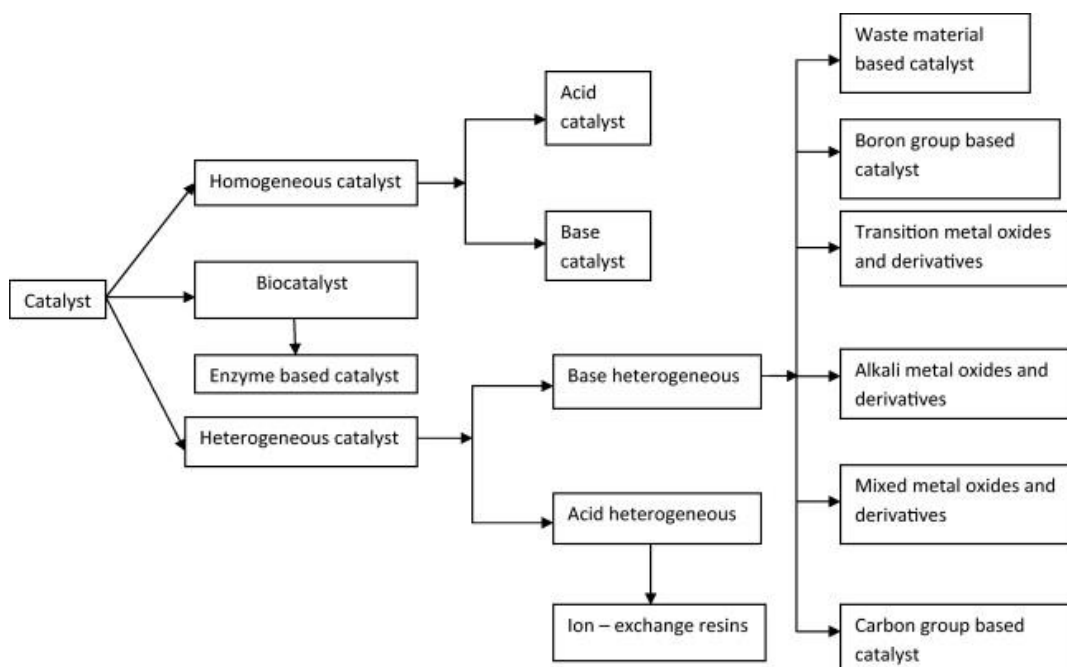


Figure 1.7 Classification of catalysts adapted from Chouhan and Sarma⁵³, copyright 2011 Elsevier (Appendix 6).

Porosity and surface basicity are among important factors to be considered prior to selection of a good heterogeneous transesterification catalyst⁵³. Additionally, base strength will determine the catalytic activity of a catalyst. According to Lee *et al.*¹⁶, solid base catalysts are preferable for the transesterification of high purity oil with low FFA as they are more active compared to solid acids. Numerous studies have been undertaken on heterogeneous biodiesel catalysts ranging from alkali metal oxides^{54,55}, alkaline metal oxides^{56–60}, mixed metal oxides^{61–64}, transition metal oxides^{65–68}, ion-exchange resins^{69–71}, sulphated oxides^{72,73}, boron group^{74–76}, carbon groups^{77–79} and enzymes^{80–82}.

Waste material is another promising avenue in the solid heterogeneous catalyst. It has been claimed to be effective in transesterification reaction especially involving egg shells^{83,84}, clams⁸⁵ and cockle⁸⁶. While natural dolomite also has been adapted by in biodiesel reaction⁸⁷.

1.3.2 Heterogeneous solid acid catalysts

A wide range of inorganic and polymeric solid acids are commercially available, however, their application for the transesterification of oils into biodiesel is less frequently explored, in part reflecting their lower activity compared with base-catalysed routes, in turn necessitating higher reaction temperatures to deliver suitable conversions. Solid acids have the advantage however over solid bases in that they are less sensitive to FFA contaminants than their solid base analogues and hence can operate with unrefined or

waste oil feedstocks containing FFA content³⁰. Solid acids can either be used to remove fatty acid impurities by esterification as a pretreatment, or at higher temperatures, to simultaneously esterify FFA and transesterify major triglycerides components, without soap formation, and thus reduce the number of processing steps to biodiesel^{36–38}.

Solid acid catalysts have advantages over the solid base in term of them being less sensitive to FFA contaminants thus they can be operated in unrefined or waste oil feedstocks⁸⁸. Solid acids can also be used to remove impurities by pre-treatment of esterification^{88–90}.

Numerous studies have reported on solid acid catalysed biodiesel production using sulfated metal oxides (e.g. $\text{SO}_4^{2-}/\text{ZnO}$ ⁹¹, $\text{SO}_4^{2-}/\text{ZrO}_2$ ^{92,93}, $\text{SO}_4^{2-}/\text{Nb}_2\text{O}_5$ and $\text{SO}_4^{2-}/\text{TiO}_2$ ⁹⁴, H-form zeolites⁹⁵, sulfonic ion-exchange resins⁹⁶, sulfonic modified mesostructured silica^{97,98}, sulfonated carbon-based catalyst⁹⁹, heteropolyacids (HPAs)¹⁰⁰ and acidic ionic liquids (ILs)^{101,102}. The results from recent publications on solid acid transesterification for biodiesel are summarised in **Table 1.4**. The ideal solid acid for esterification and transesterification should have a characteristic such as strong Brönsted and/or Lewis properties to promote biodiesel reaction with significant rates, unique porosity or textural properties to minimise diffusional problem between long chain molecules, and hydrophobic surfaces to promote absorption of oily hydrophobic species on catalyst surface^{26,103,104}.

Table 1.4 Recent heterogeneous solid acid catalysts for biodiesel production.

Catalysts	Preparation method /remarks	Oil sources and solvent used	Conversion or yield obtained	Ref
Mixed oxide				
$\text{Fe}_2\text{O}_3\text{-MnO-SO}_4^{2-}/\text{ZrO}_2$	Impregnation reaction followed by calcination at 600 °C for 3 h	Waste cooking oil containing 17.5.% free fatty acids added to methanol and oil	Yield of 96.5 ± 0.02 %	92
$\text{S}_2\text{O}_8^{2-}/\text{ZrO}_2\text{-TiO}_2\text{-Fe}_3\text{O}_4$	Co-ppt and impregnation methods	Cottonseed oil with various volumes of methyl acetate	98.5 % in Zr/Ti molar ratio of 3:1 calcined at 550 °C	105
WO_3/ZrO_2	Impregnation of $\text{Zr}(\text{OH})_4$ with an ammonium	Soybean oil with 4 wt% oleic acid,	93 % conv.	106

	metatungstate, WO ₃ is calcined at 800 °C	oil and methanol ratio 1:9		
SO ₄ ²⁻ /SnO ₂ , SO ₄ ²⁻ /SnO ₂ -SiO ₂ , SO ₄ ²⁻ /SnO ₂ -Al ₂ O ₃	Impregnation method, calcined at 200, 300, 400, 500 °C	Waste cooking oil in methanol	Yield of 92.3 %	107
Sulfonic acid				
Macroporous cation exchange resin	Suspension polymerization method using styrene and divinyl benzene	10 wt% catalyst loading, 40 wt% methanol (mol ratio of MeOH/FFAs = 10:1, acid value = 64.9 mg KOH g ⁻¹)	30 % and 50 % CLD resins exhibited 32.4 % and 68.7 % FFA conv.	96
SO ₄ ²⁻ /ZrO ₂	Add NH ₃ aqueous solution in ZrOCl ₂ ·8H ₂ O up to pH 8.5.	Oleic acid with methanol	90 % conv.	108
Carbon-mesoporous silica (CS) composite functionalized with sulfonic acid	Carbonisation of sucrose impregnated in SBA-15 mesoporous silica and its subsequent sulfonation	Esterification of palmitic acid and methanol, palmitic acid and TE of soybean oil and methanol	Esterification conv. = 98 % TE yield: 99 %:	77
Heteropoly acids and polyoxometalates aqueous				
PA/NaY (PA = organic phosphonic acid)	Immersion method: 50 % PA and NaY were added in 20 ml of water	Free fatty oil oleic acid with ethanol	77.62 % conversion	109
HPWO and CsHPWO supported on SiO ₂ , MCM-41 and ZrO ₂	sol-gel hydrothermal method and two-step	Crude palm oil is called palm fatty acid distillate or PFAD)	Up to 92 % FAME	110

	impregnation method			
Zr supported HPA	Suspension method	Sunflower oil with methanol	97 % conversion	111

*TE: transesterification, co-ppt: co-precipitation

1.3.3 Heterogeneous solid base catalysts

Solid base catalysts exhibit excellent activity for transesterification of triglycerides and would be the favoured choice for conversion of oils with low free fatty acid content. Numerous solid base catalysts have been explored for the transesterification of triglycerides, spanning oxides of group IIA elements; CaO ^{84,112–114}, Mg ^{115–118}, SrO ¹¹⁹, BaO ¹²⁰, carbonates of group IA and IIA elements; CaCO_3 ¹²¹, MgCO_3 ¹²², SrCO_3 ^{123,124}, BaCO_3 ¹²³, transition metal oxides^{125,126}, basic zeolites^{127–129}, hydrotalcites^{62,130–133}. **Table 1.5** tabulates the most recent heterogeneous solid base catalysts used in biodiesel synthesis.

Table 1.5 Recent heterogeneous solid base catalytic transesterification reactions.

Catalysts	Preparation method	Oil sources and solvent used	Conversion or yield obtained	Ref
Mixed oxides				
Mg-Zn mixed oxides	Co-ppt, impregnation and urea hydrolysis method	Soybean oil in methanol ratio 12:1 to 24:1	Yield: Mg ₃ Zn ₁ :90 %	134
CaFeAl	co-ppt, calcined at 750 °C for 3h	Soybean oil in methanol ratio 6:1, 9:1, 12:1 and 15:1	Yield: 90 % at 12:1 ratio	135
MgAl mixed oxide (Mg ₁ Zn ₂ Al ₁ , Mg ₁ Co ₂ Al ₁ , Mg ₃ Al _{0.6} Fe _{0.4} and Mg ₃ Al _{0.6} La _{0.4})	Co-ppt, calcined at 773K for 8h	Soybean oil in methanol	Yield: Mg ₁ Zn ₂ Al ₁ : 64.7 %, Mg ₁ Co ₂ Al ₁ :66.4 %, Mg ₃ Al _{0.6} Fe _{0.4} :95.7 % Mg ₃ Al _{0.6} La _{0.4} :98.3 %	136

CaO–La ₂ O ₃	co-ppt, calcined at 800 °C for 6 h	<i>Jatropha</i> oil in methanol ratio 24:1	Yield: 86.51 %	137
Carbonates				
SrCO ₃	Modified sol–gel and co-ppt method. Calcined at 900 °C for 1 h	Soybean oil in methanol (ratio 12:1)	Conversion:98 %	138
Ca(C ₃ H ₇ O ₃) ₂ / CaCO ₃	Calcined CaCO ₃ in a He at 900 °C for 1.5h	Soybean oil, canola oil and sunflower oil in methanol ratio 30:1	Yield: Soybean oil:75 % Sunflower oil:70 % Canola oil: 63 %	121
Dolomites (CaMg(CO ₃) ₂)	Calcined between 600–900 °C for 2 h	Palm kernel oil (PKO) in methanol (ratio 30:1).	Methyl ester content: > 98 % with calcined dolomite at 800 °C	139
Transition metal oxides				
Ferric-manganese doped tungstated/ Molybdenana nanoparticle	Impregnation reaction followed by calcination at 600 °C for 3 h	Waste cooking oil in methanol (ratio 25:1)	Yield: 92.3 % ±1.12	140
Sr ₃ Al ₂ O ₆	Sol–gel method, calcined in air at 900 °C	Soybean oil in methanol (ratio 25:1)	Yield: 95.7 ± 0.5 %	124
SrO, CaO, ZnO, TiO ₂ and ZrO ₂	Calcination of zinc hydroxide at 800 °C for 5 h	Rapeseed oil in methanol	Yield: 95 % at 250 °C	141
Tungsten zirconia (WZ) oxide	Calcined at 800 °C for 3h	Triacetin in methanol		142
Hydrotalcites @ LDH				
MgCaAl HT	co-ppt, calcined at 450 °C for 4 h	<i>Jatropha</i> oil in methanol ratio 6:1	Conversion: 90% for Mg/Ca = 1	143

CaAl HT	co-ppt, calcined at 550 °C for 5 h	Soybean oil in methanol	Yield: 87.4 %	130
ZrZnAl HT	co-ppt, calcined at 140 °C and 200 °C	Soybean oil in methanol	Yield: 91.71 % at 140 °C	144
Mg/Al–CO ₃ HT	urea method(urea/NO ₃ [–] molar ratio of 3.0) calcined at 500 °C for 4 h	Refined microalgae oil in methanol	Conversion: 90.3 %	122
Metallic (Fecralloy®) monoliths based on Mg–Al HT	co-ppt, calcined at 500 °C	Sunflower oil in methanol	62–77 % oil conversion after 10 h	145
MM MgAl HT	Free-alkali co-ppt, template with polystyrene	Triglycerides (C ₄ -C ₁₈)	C ₄ TAG is 2–3 times faster than that of the C ₁₈ TAG	133

Basic Zeolites

Zeolite X and A from flyash	Alkaline fusion method through ion exchange and calcined at 900 (±10) °C for 2 h	Refined mustard oil in methanol (ratio 18:1).	Conversion: 84.6 %	146
Hierarchical ZSM-5(h-ZSM-5) and Beta (h-Beta) zeolites	functionalised zeolitic with organosilanes, calcined in air at 550°C for 5h	Algae oil in methanol	Yield/conversion value is not stated. A recovered production phase around 50 wt%	129
Zeolites of mordenite, beta and X	Impregnation with sodium acetate then calcined at 550 °C for 15 h	Refined sunflower oil in methanol (ratio 6:1)	Zeolite 3NazX FAME wt% : 95.1 %	147

*TE: transesterification, co-ppt: co-precipitation method

1.4 Hydrotalcite: The uniqueness solid base catalyst

1.4.1 Past and current perspectives of hydrotalcite

Layered nanomaterial, as a new hybrid solid base catalyst, started to gain much attention due to their unique properties such as the ability to reconstruct the lamellar structure, provides a distinctive effect on catalyst architecture. The importance of this application has driven significant interest in layered materials. It has been scientifically and technologically proven important in many applications such as in environmental benign and energy application including in waste water treatment^{148,149}, biomass conversion^{150–154}, photocatalytic activities^{155–157,157,158} and much more. In conjunction with this positive trend, this sub-chapter intentionally reviews the literature available on the use of hydrotalcites as solid base catalysts in the production of biodiesel.

Hydrotalcites (HTs) or layered double hydroxides (LDHs) (**Figure 1.8**) is an interesting class of layered nanomaterial which has been extensively explored in recent decades. The evolution of hydrotalcite begins in early 1842 (in Sweden) where it was first discovered as mineral-like talc which contains hydrocarbonates of Mg and Al^{159,160}. Seventy-three years later, Prof. Manase determined the chemical formula of hydrotalcite (HT); $[\text{Mg}_6\text{Al}_2 (\text{CO}_3) (\text{OH})_{16} \cdot 4(\text{H}_2\text{O})]$ for the first time¹⁶¹. Two polytypes of hydrotalcite specifically rhombohedral and hexagonal symmetry were discovered in 1931¹⁶². Eleven years later, through a number of investigations, a double sheet structure in hydrotalcite phases was discovered¹⁵⁹. **Table 1.6** summaries the discoveries of hydrotalcite from the earlier years until now.

Hydrotalcite-like compounds (HTLCs) started to be introduced in 1970 as a precursor to hydrogenation catalyst which later being patterned¹⁶³. A decade has passed, and the role of HTLC as a basic catalyst has been expanded and tentatively endeavours in many solid bases reactions¹⁶⁴. By looking at the trends in **Table 1.6**, it shows robust enhancement has been developed and achieved on hydrotalcite architecture.

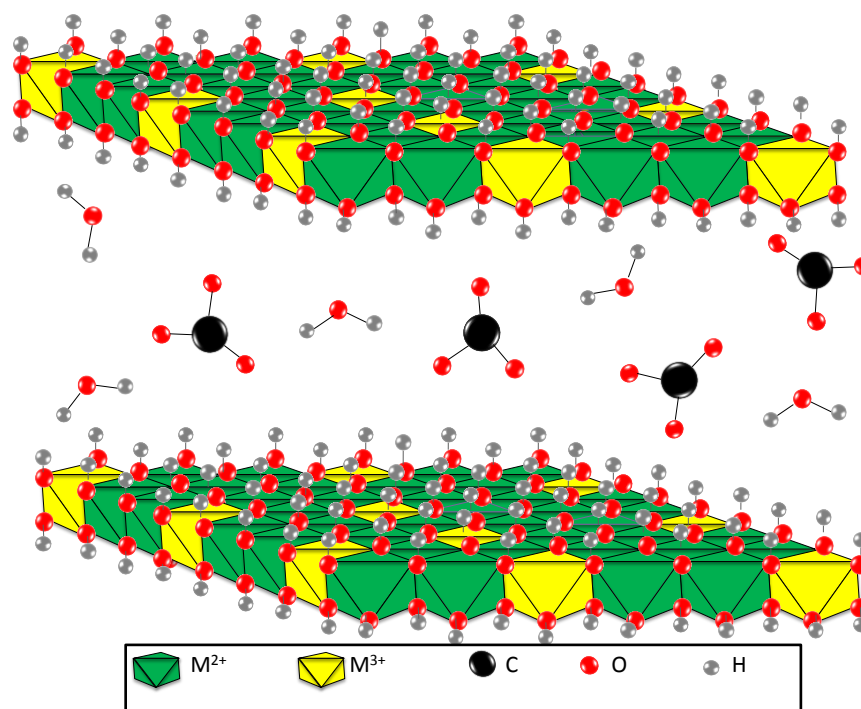


Figure 1.8 Illustration of layered double hydroxides (LDHs) with the different M^{2+}/M^{3+} ratio.

Table 1.6 Past and recent evolution of layered double hydroxide catalysts.

Year	Material synthesised	Remarks	Ref
1842	Mineral like talc (hydroxycarbonate of Mg and Al)	First discovered in Sweden	160
1915	$Mg_6Al_2(CO_3)(OH)_{16} \cdot 4(H_2O)$	First HTs formula discovered	161
1942	HTs like structure	Introduced double sheet structure	159
1970	First German patent on HTLC	Precursor in hydrogenation catalysts	165
1971	$[Mg_{1-x}Al_x(OH)_2]^{x+} [A_{x/2}^{2-} \cdot mH_2O]^{x-}$, where A^{2-} is SO_4^{2-} or CrO_4^{2-}	Solid acid and base catalysts	163
1990	Novel heterogeneous catalyst Patent on synthetic hydrotalcite	Solid bases catalyst Heating from 500-900 °C to form activated magnesia	166 167
2000	Mg–Al–O–t-Bu hydrotalcite	Novel hydrotalcite used in transesterification reaction	168
2005	MgAl HYDROTALCITE	Novel alkali-free co-precipitation (ppt) route	131
2006	Calcined MgAl HT	Transesterification of soybean oil & cottonseed oil	169,170
2012	Macroporous-mesoporous MgAl	Alkali-free co-ppt method	133
2015	HT HTs coated MM-SBA-15	Stepwise growth of conformal alumina	171
2016	Pt/Mg(Sn)(Al)O/Al ₂ O ₃	Pt and Sn induced in LDH	172

Nowadays, HTs have engendered much attention as solid bases due to these four factors:

- (i) Possessing a good anion-exchange capability which can be used as ion-exchangers¹⁷³, absorbent¹⁷⁴ or in sensor applications¹⁷⁵.
- (ii) HTs have great basic properties which are suitable not only to be applied in transesterification reaction but also in aldol-condensation, Knoevenagel condensation, Claisen-Schmidt condensation, Micheal addition and alkylation¹⁷⁶.
- (iii) Tunable base strength for the transesterification reaction leading to convenience preparation of bivalent (Ni, Cu, Co) and trivalent (Fe, Cr) cations¹⁷⁷.
- (iv) Ability to reconstruct the lamellar structure through calcined rehydration hydrotalcite which then allows co-operating with any kind anions¹⁷⁷.

The hydrotalcite (HT) family is one class of solid base catalyst which has attracted much attention in a solid base catalysed biodiesel production due to it possessing good anion-exchange properties^{173,176} and tuneable base strength for the transesterification reaction¹⁶.

1.4.2 Structural and physicochemical properties of hydrotalcites

Hydrotalcite-like compounds are a family of anionic clays which are also known as layered double hydroxides¹⁷⁸. They are represented by the general formula $M^{2+}_{1-x}M^{3+}_x(OH)_2A^{n-}_{x/n}\cdot yH_2O$ where M^{2+} are divalent anions (e.g., $Mg^{2+}, Zn^{2+}, Mn^{2+}, Ni^{2+}, Co^{2+}, Fe^{2+}$), M^{3+} are trivalent metal ions (e.g., $Al^{3+}, Cr^{3+}, Fe^{3+}, Co^{3+}, Ga^{3+}$) and A^{n-} is the interlayer anion^{179,180}.

Tuning HTs morphology is feasible and becomes fascinating as it can be modified in a range of ways. HTs can be distinguished in three different morphologies; as-synthesized, calcined and reconstructed (**Figure 1.9**). As-synthesized hydrotalcite, also known as fresh hydrotalcite normally obtained from the variation of synthesis methods which will be discussed in Section 1.4.3. Commonly synthesised HT is Mg-Al compound which has of CO_3^{2-} group in the interlayer.

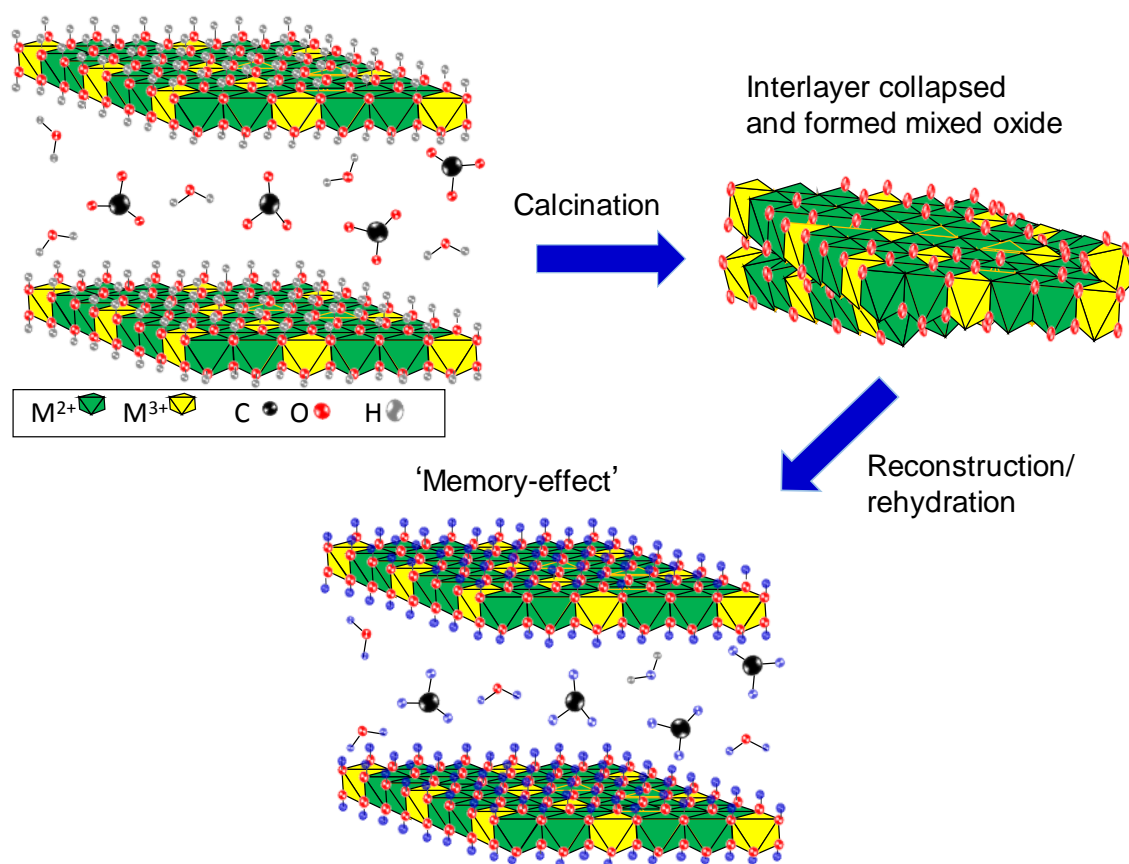


Figure 1.9 Effect of calcination and rehydration on layered double hydroxide.

Calcination at a certain temperature will significantly enhance the surface area due to the MgAl HT morphology converting to MgO or Mg(Al)O mixed oxide with a higher surface area, and well dispersed mixed oxides. Xie *et al.*,¹⁸¹ reported calcination of MgAl HT at high temperature (773 K) produced the significant catalytic activities in the transesterification of soybean oil (66 % conversion) while calcination beyond that resulted in lower basicity due to the formation of spinel phase. Through rehydration with suitable anions with water, the interlayer of OH⁻ will be reconstructed. This unique characteristic is known as the retro-topotactical effect or as commonly called a '*Memory Effect*', which means HT interlayer is regained through the calcination-rehydration process¹⁸². Nishimura *et.al*¹⁷⁹ observed that reconstructed HT has a higher Brönsted basicity due to the high-density of OH⁻ anions compared to CO₃²⁻ ions in as-synthesized HT. The easily tailored properties, made possible with economical reagents, marks HTs with special merit, giving rise to the potential for exploitation in many technological applications.

1.4.3 LDH synthesis routes

There are various ways to prepare HTs which are presented in **Table 1.7**. Among all, co-precipitation (co-ppt) is the most commonly used method. Co-ppt can be performed by three different methods; titration, precipitation at low supersaturation and/or precipitation at higher supersaturation^{160,164,182}. The most common and least expensive method is co-precipitation with the base such as, NaOH and/or NaHCO₃. This method is somewhat is not advisable because it is believed to be difficult to precipitate pure HTs as they tend to precipitate divalent and trivalent cation at lower pH (Mg²⁺/Al³⁺ at pH 7.7-8.5 while AlOH₃ at pH 4-4.5)¹⁶⁰. In addition, it is reported precipitation method using NaOH contributed to leaching due to entrained of sodium ion or sodium salts in LDH¹⁸³.

Table 1.7 Common methods of hydrotalcite synthesis.

Techniques apply	Advantages	Disadvantages	Ref
Co-precipitation			
<ul style="list-style-type: none"> Precipitate at variable or constant pH At high or low supersaturation 	<ul style="list-style-type: none"> Most common method Inexpensive, simple and no specific apparatus required Careful control of the charge density (M²⁺/M³⁺ ratio) by regulating the solution pH 	<ul style="list-style-type: none"> Small amounts of carbonates are always present Homogeneous of pH during precipitation process Wide distribution of crystallite and particle sizes 	157,179
Urea hydrolysis			
<ul style="list-style-type: none"> Utilises urea as its precipitating agent 	<ul style="list-style-type: none"> Progresses slowly, leads to a low degree of supersaturation during precipitation. More homogeneous nucleation and growth compared to co-ppt method No intense washing needed 	<ul style="list-style-type: none"> Not suitable for the preparation of LDHs with low charge density 	184
Sol-gel method			
<ul style="list-style-type: none"> The reaction between monomers (Al-tri-sec-butoxide) into a colloidal solution of MgAl 	<ul style="list-style-type: none"> HT exhibits higher thermal stability than co-ppt Higher surface area than co-ppt method 	<ul style="list-style-type: none"> Catalyst tends to deactivate after few cycles. 	185

(sol). Sample allowed to gelling through precipitation			
Ion-exchange method			
<ul style="list-style-type: none"> Modification from poly (ethylene terephthalate) / aspartic acid on LDH 	<ul style="list-style-type: none"> Useful for the preparation of noncarbonated LDHs. Good dispersion morphology 	<ul style="list-style-type: none"> Rapid saturation occurred 	186
Hydrothermal on alkali source			
<ul style="list-style-type: none"> Combination of co-ppt and followed by hydrothermal ageing treatment Then only undergone thermal treatment 	<ul style="list-style-type: none"> Faster nucleation and uniform growth Large particle size could be obtaining (50-300 nm) High surface area (up to 300 m²/g) 	<ul style="list-style-type: none"> Promising entrained of sodium into the LDH framework 	179
Alkali-free and hydrothermal reconstruction			
<ul style="list-style-type: none"> Alkali-free co ppt method Calcine at desired temperature (depending on decarbonation of catalyst Rehydrate/reconstruct under hydrothermal conditions 	<ul style="list-style-type: none"> No sources of alkali involved in the synthesis Leaching of basic species is avoidable Versatile, easy and environmental-friendly approach Serves high surface area via hydrothermal reconstruction/rehydration 	<ul style="list-style-type: none"> - Time-consuming to prepare the catalysts 	Our study

1.4.3.1 Entrained sodium in LDHs

In particular, the use of alkali as precipitating agents in the co-precipitation method is problematic especially during transesterification, due to the possibility of Na⁺ contamination -in the hydrotalcite lattice as NaOH can act as base catalysts. The NaOH from the lattice can leach out under reaction conditions. This makes hydrotalcite synthesis through alkali co-precipitation route more active and makes it difficult to determine the true activity of the homogeneous catalyst.

A previous study¹⁸⁷ proved addition of alkali in LDH precursor synthesis lowering down the surface area compared to alkali-free LDH, consequently reducing the rate of reaction. Addition of alkali during the synthesis of hydrotalcite results in high levels of residual alkali metal ions, which later requires an extensive of washing and also

contributes to leach of basicity. Finally, it will affect the catalysis performance, especially in the transesterification reaction.

Hence, promoting alkali-free synthesis of HT is crucial steps for transesterification reaction. Further, existing chemistries employed in the synthesis of HTs have significant environmental drawbacks and we aim to overcome these issues by following the principles of green chemistry¹⁸⁸ (**Scheme 1.1**).

Among the related principles that we want to achieve are:

1) Waste prevention

-Prioritise the prevention of waste rather than cleaning up and treating waste after it been created.

2) Design less hazardous chemical synthesis

- By designing a safer route of synthesis including the potential hazards towards human health and environment

3) Catalysis

-Use catalyst instead of stoichiometric reaction to enhance selectivity, minimise waste and safer energy.

Green Chemistry
Everyone's Doing It!

The 12 Principles of Green Chemistry
A framework for designing or improving materials, products, processes and systems.

1. Prevent Waste
2. Atom Economy
3. Less Hazardous Synthesis
4. Design Benign Chemicals
5. Benign Solvents & Auxiliaries
6. Design for Energy Efficiency
7. Use of Renewable Feedstocks
8. Reduce Derivatives
9. Catalysis (vs. Stoichiometric)
10. Design for Degradation
11. Real-Time Analysis for Pollution Prevention
12. Inherently Benign Chemistry for Accident Prevention

*Anastas, P. T.; Warner, J. C. Green Chemistry: Theory and Practice, Oxford University Press: New York, 1998, p.30. By permission of Oxford University Press.

www.acs.org/greenchemistry

A New Kind of Chemistry

Green Chemistry is based on a set of principles that when used in the design, development and implementation of chemical products and processes, enables scientists to protect and benefit the economy, people and the planet.

Green Chemistry uses renewable, biodegradable materials which do not persist in the environment.

Green Chemistry is using catalysis and biocatalysis to improve efficiency and conduct reactions at low or ambient temperatures.

Green Chemistry is a proven systems approach.

Green Chemistry reduces the use and generation of hazardous substances.

Green Chemistry offers a strategic path way to build a sustainable future.

© 2014 ACS Green Chemistry Institute®
To catalyze and enable the implementation of green chemistry and engineering throughout the global chemical enterprise

Scheme 1.1 Twelve principles of Green Chemistry introduced by Paul Anastas in 1998¹⁸⁸.

1.4.3.2 The x ratio of synthesise hydrotalcite

It has been reported elsewhere, in order to obtain a pure hydrotalcite, the x ratio ($\text{Al}^{3+} / \text{Al}^{3+} + \text{M}^{2+}$) must be in the range of $0.2 < x < 0.33$ ¹⁶⁰. If the value is outside the limits, the metal hydroxides could be formed. Below 0.20, normally divalent metal hydroxides will be formed and when x higher than 0.33, amorphous trivalent metal hydroxides (i.e $\text{Al}(\text{OH})_3$) tend to form¹⁸⁹. Contrary to that, lowering the x value under 0.2 will increase the metal density (such as Mg^{2+} or Zn^{2+} octahedral sites) in brucite layer hence, forming metal hydroxide such as $\text{Mg}(\text{OH})_2$.

Several papers reported LDH can be prepared outside the range of $0.22 < x < 0.33$. Cantrell *et al.*¹³¹, for example, have reported MgAl LDHs were prepared between a range of $0.25 < x < 0.55$. They have reported a similar conclusion as above; x value outside the limits of $0.25 < x < 0.44$ were formed $\text{Mg}(\text{OH})_2$ and $\text{Al}(\text{OH})_3$. ZnNiFe-LDH has been prepared by Touahra *et al.*¹⁸⁹ in the range of $0.2 < x < 0.66$. Above 0.5 to 0.66, they noticed the formation of NiFe_2O_4 . Some of the reports are tabulated in **Table 1.8**. In conjunction with that, to obtain a pure hydrotalcite, a certain pH has been suggested as listed below. This pH is subjected to change depending on the metal cation used in the synthesis process. For example, MgAl HT is favourable to be synthesised at pH 8.5, pH 9.5 in NiAl HT, meanwhile ZnAl HT favours at pH 9-10.

Table 1.8 The range optimum value of x for obtaining pure HT.

pH prepared	Results finding	References
Lower pH (8 and lower)	<ul style="list-style-type: none"> No HT formed, complex pathway, not completed Metal hydroxide impurities will be formed 	
Suggested pH	<ul style="list-style-type: none"> A pH range of 8.5–10 can be used to prepare most anionic clays 	160,182,190
Higher pH	<ul style="list-style-type: none"> At pH 11: Unexpected peaks associated to $\text{Al}(\text{OH})_3$ and sodium nitrate At pH 13-14: mixed oxide will be formed 	

1.4.3.3 Hydrotalcite Reconstruction System

The structure of hydrotalcite formed by rehydration of mixed metal oxide is affected by the rehydration conditions, such as the $\text{M}^{2+}/\text{Al}^{3+}$ ratio and pH, parent's HTs

calcination temperature and the stirring speed^{191–193}. Valente *et al.*¹⁹⁴ have reported that the calcination-rehydration process played enormous roles in changes of morphology, crystallinity and particles size in MgAl hydrotalcite. Traditionally, there are two rehydration techniques applied to hydrotalcites: gas-phase and liquid-phase¹⁹¹. In gas-phase, calcined catalysts were rehydrated by exposing them under N₂ or argon passed through a water bubbler. Meanwhile, in the liquid-phase method, samples were treated in decarbonated water at room temperature for at least 5 h. Abello *et al.*¹⁷⁴ have reported liquid-phase rehydration promised a better physicochemical and catalytic performance compared to gas-phase. Liquid-phase rehydration leads to increased surface area of the LDH up to 270 m²/g and also materials that exhibited higher basicity, the latter enhancing the catalytic activity in aldol condensation. Somehow, these methods have their own drawbacks where there is a tendency to produce an incomplete reconstruction of the lamellar structure¹⁹⁵. Generally, successful reconstruction depends on several conditions such as:

- i) Nature of the cation involved; reconstruction becomes more difficult if more than two cations involved. For example, the addition of Ni²⁺ on MgAl compounds deficit the ability of metal oxide to be severe covered under rehydration. Reconstruction becomes challenging if larger cationic atom involved (e.g. Zn²⁺ is harder to reconstruct compare to Mg²⁺).
- ii) Temperature, time and ramping rate of the parent calcination.
- iii) Rehydration techniques (e.g. gas-phase, liquid-phase, microwave assisted or hydrothermal). NiAl LDH has been reported managed to be reconstructed by microwave assisted but not through non-assisted gas-phase or liquid-phase¹⁹².
- iv) Length and temperature of rehydration process.

Recently, hydrothermal treatment has been adapted in hydrotalcite synthesis and results revealed a desirably greater surface area (up to 340 m²/g) with narrow pore size distribution¹⁹⁶ and higher crystallinity^{195–197}. Apart than that, particle size, morphology and consistency of composition also are feasible and easy to adjust in hydrothermal synthesis method¹⁹⁵. Yet no study has been done on the hydrothermal reconstruction of alkali-free LDH, thus extended knowledge on this approach is essentially required.

1.4.4 Catalytic activity of LDH

It is reported elsewhere, as-synthesised LDH materials are less catalytically active in transesterification reactions compared to calcined and rehydrated LDH¹⁶⁴. .

Nevertheless, as-synthesised catalysts are found to be active in some reactions particularly in Micheal addition¹⁶⁸ and isomerisation of alkenes^{198,199}. Recently, as-synthesised CoMgAl has been adapted in selective oxidation of benzyl alcohol to benzaldehyde²⁰⁰. The addition of Mg^{2+} into the system has enhanced the catalytic performance. Calcined MgAl HTs found not only to be active in transesterification^{201,202} but also in aldol condensation^{203,204}, Knoevenagel condensation^{205,206}, esterification reaction^{207–209} and Cannizzaro reaction²¹⁰. Reconstructed hydrotalcite also exhibits superior catalytic performance in transesterification reactions¹²² and base-catalysed reaction such as aldol condensation²¹¹ compared to parent HTs.

MgAl HTs have been applied for TAG transesterification of poor and high-quality oil feeds. The alkali-free route has been applied to prepare HTs which employ NH_3OH and NH_3CO_3 solutions for the precipitation, thereby overcoming leaching issues related to residual Na and K^{131} . Increasing Mg:Al ratio is found to increase the surface charge in the layers, which correlates with base strength and rate of C_4 transesterification¹³¹ (Figure 1.10).

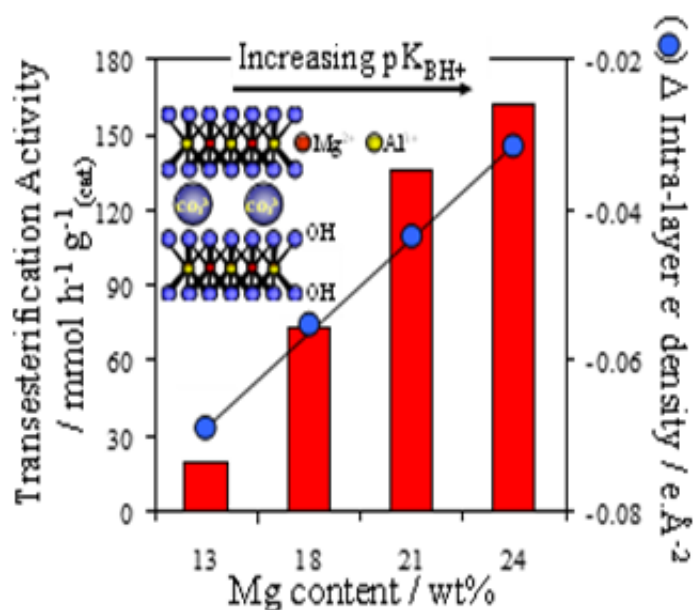


Figure 1.10 Impact of MgAl HT surface basicity on their activity towards tributyrin transesterification. Adapted from Cantrell *et al.*¹³¹ with permission from Elsevier (Appendix 7).

1.5 Hierarchical mesoporous-macroporous LDH materials

Formation of hierarchical macroporous-mesoporous support materials has started to gain attention recently. Previously, the hierarchical macroporous-mesoporous silica SBA-15 has been developed in order to promote better diffusion in bulk and viscous C₁₆-C₁₈ TAGs and to boost up their catalytic performance²¹². SBA-15 has been synthesised by a dual-templating hierarchical method using a soft liquid crystalline surfactant and hard polystyrene nano sphere template (**Figure 1.11**). The resulting sulfonic acid derivatised bi-modal PrSO₃H-MM-SBA-15 material is a macroporous-mesoporous hierarchical catalyst offering high surface area and increased rate of reaction of both esterification and transesterification²¹².

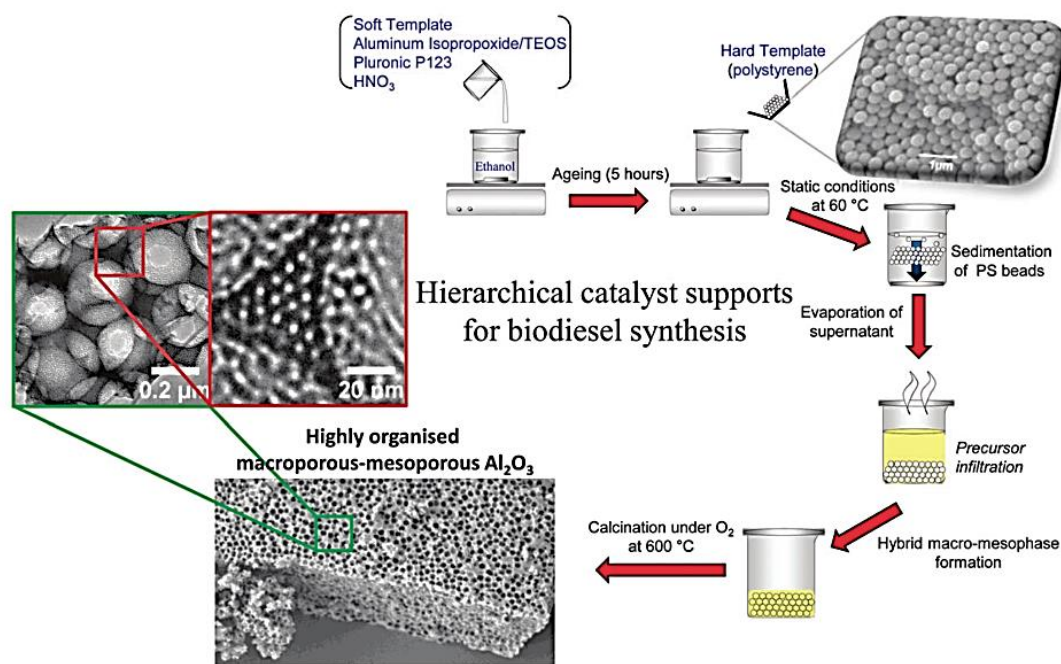


Figure 1.11 Dual templating route towards hierarchical macroporous-mesoporous silica. Adapted from Lee *et al.*¹⁶ with permission from Elsevier (Appendix 8).

The increased activity of PrSO₃H-MM-SBA-15 is attributed to a higher accessibility of sulfonic group towards mesopores as macropores act as rapid transport conduits to the active sites and hence increase the mass transport in both transesterifications of tricapyrin and esterification of palmitic acid²¹². This fascinating synthesis method also has successfully used to form highly structured macroporous-mesoporous alumina²¹³ with mesopores diameter of 200-500 nm and 5-20 nm respectively. This will tremendously lessen the diffusion problem in bulky oil.

The bulky nature of oil triglycerides causes serious mass-transport limitations and poor accessibility of base sites in bulk hydrotalcite. Woodford *et al.*¹³³ addressed this issue through the synthesis of Mg-Al macroporous-mesoporous hydrotalcite (MM-HT). The catalysts were prepared via an alkali-free method, in which size controlled polystyrene nano spheres were used as a physical template to introduce macropores. MM-HT was found to exhibit a 10-fold enhancement in the transesterification of long-chain triglycerides (C_{12} and C_{18}) when compared to conventional HT (**Figure 1.12**), which was attributed to increased accessibility of the base sites in macropores.

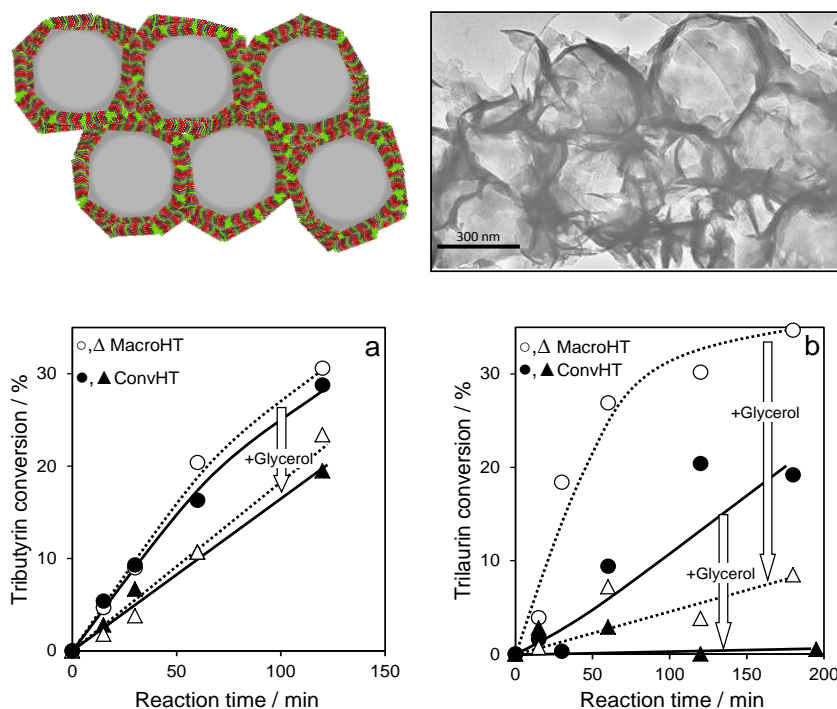


Figure 1.12 Nano-engineered macroporous MgAl hydrotalcite impact on surface basicity on their activity towards tributyrin transesterification with scheme showing macroporous features. Adapted from Woodford *et al.*¹³³ with permission from The Royal Society of Chemistry (Appendix 9).

Shorter chain C_4 triglycerides showed less accessibility problem due to the smaller size and better diffusion of this reactant. It was interesting to note that in both cases (low or bulkier triglycerides) spiking the reaction with glycerol has a significant detrimental impact on reaction rate, suggesting strongly bound glycerol may be implicated in catalyst deactivation.

1.6 Other heterogeneous solid base catalyst (Dolomite and NanoMgo)

Dolomite is a naturally abundant material, used widely for construction applications, which comprises $\text{Mg}(\text{CO}_3)\text{-Ca}(\text{CO}_3)$ layers in an arrangement very similar to calcite (CaCO_3) and is an interesting precursor to generate solid base catalysts. As in carbonate form, dolomite is relatively inactive, however, upon calcination dolomite forms an intermixed MgO-CaO composite which shows excellent activity for biodiesel production. A study of transesterification reactivity using short and long chains over dolomite catalyst has been established by Wilson *et al.*⁸⁷ (**Figure 1.13**).

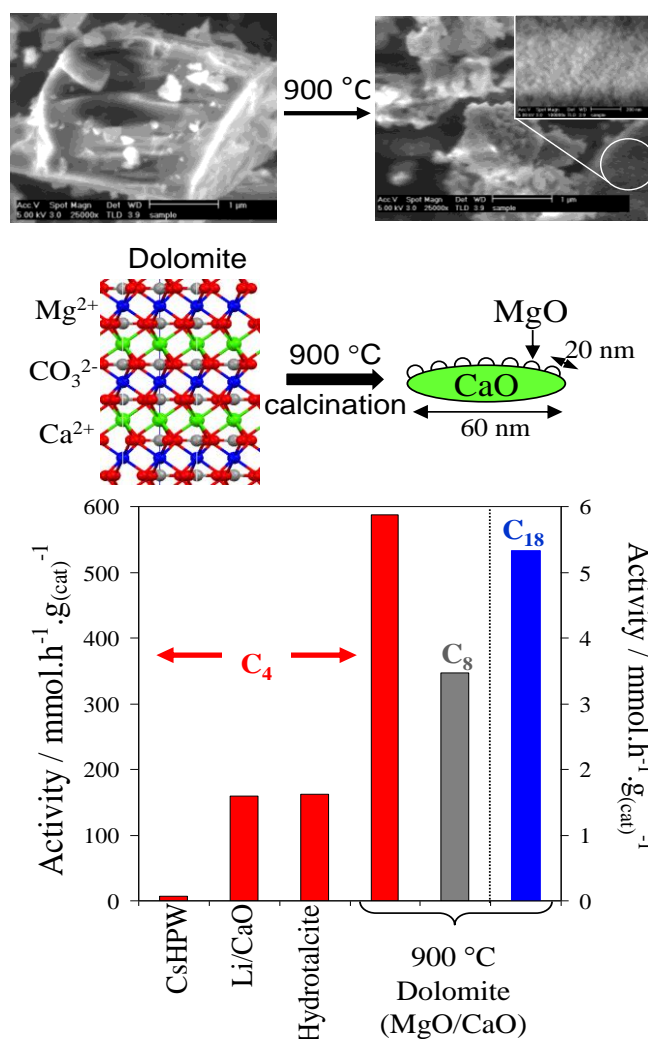


Figure 1.7 (Top) SEM of fresh and 900 °C calcined dolomite with scheme showing corresponding structures. (Bottom) The catalytic activity of calcined dolomite for the transesterification of short and long chain TAGs with methanol benchmarked against literature solid acid and base catalysts. Reproduced from Wilson *et al.*⁸⁷ with permission from The Royal Society of Chemistry (Appendix 10).

This research demonstrated that uncalcined dolomite was inactive for transesterification, due to a lack of base sites as proven by CO₂-TPD⁸⁷. After calcination at 900 °C, dolomite exhibited remarkable activity in the transesterification of C₄-C₈ as well as in higher bulkier triglycerides (C₁₆-C₁₈). Exceptional consequences also have been obtained in the transesterification of olive oil where promising outstanding conversion of more than 90 % within 3 h reaction is observed⁸⁷.

NanoMgO is another interesting solid base catalyst for transesterification that has also attracted much interest. Montero *et al.*²¹⁴ successfully employed NanoMgO for the transesterification of tributyrin with methanol (**Figure 1.14**), producing conversions between 60 and 80 % after 24 h.

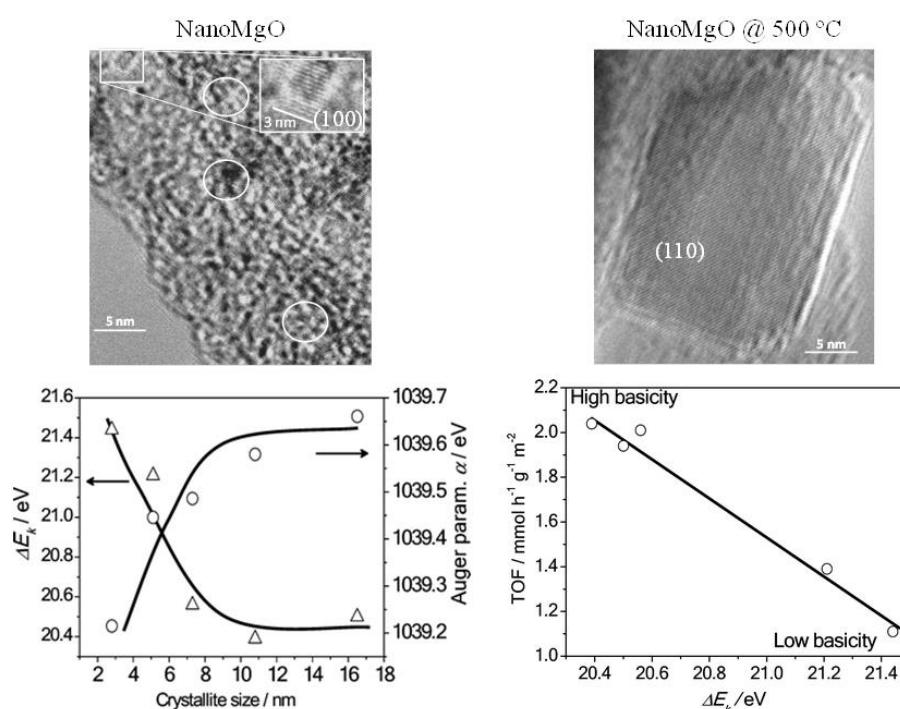


Figure 1.8 (Top) Fresh NanoMgO TEM images showing well-defined 3 nm cubic (100) oriented NanoMgO in an amorphous matrix. Following 500 °C annealing, these are converted into ~13 nm. (Bottom) The relationship between NanoMgO particle size and surface polarisability (ΔE_k) and Auger parameter (left) and the surface area normalised by turnover frequency for transesterification reaction (right). Adapted from Montero *et al.*²¹⁴ and Montero *et al.*²¹⁵ with permission from Elsevier and The Royal Society of Chemistry accordingly (Appendix 11a-b).

In their study (Montero *et al.*²¹⁴), NanoMgO were synthesised through a sol-gel method using supercritical drying to form a precursor with ~3 nm cubic MgO nanocrystals. Results have demonstrated the catalytic activity of calcined NanoMgO in transesterification is depending on size evolution of surface electronic structure where in this case (110) and (111) facet is much more active in tributyrin reaction. TEM and XPS both have proven MgO with low coordination surface attributes more activity in mild transesterification reaction of tributyrin²¹⁵.

1.7 Research objectives

The principle aims of these investigations are:

- (i) To synthesise and characterise solid base ZnAl LDH prepared via the alkali-free method and its reconstruction under hydrothermal condition. The major question concerns whether hydrothermal reconstruction method is better to compare to gas-phase and liquid-phase rehydration approaches in term of its structural physiochemical properties and towards catalytic performance in the transesterification reaction.
- (ii) To synthesise, characterise and evaluate alkali-free NiAl LDH prepared by the similar method as mentioned in Objective (i). Catalyst will be examined in a similar reaction as above.
- (iii) To prepare and compare macroporous LDH (MacroLDH) mainly MgAl LDH, ZnAl LDH with conventional MgAl and ZnAl LDH. A further understanding of its reactivity to overcome mass-transform limitation will be gained from this study.
- (iv) To characterise and compare of solid base heterogeneous catalyst (Dolomite and NanoMgO) catalysts for simultaneous transesterification reactions in triglycerides model compound.

1.8 References

- (1) Ahmad Tajuddin, N.; Lee, A. F.; Wilson, K. In *Handbook of Biofuels Production*; Woodhead Publishing, 2016; pp. 121–164.
- (2) Bauer, N.; Hilaire, J.; Brecha, R. J.; Edmonds, J.; Jiang, K.; Kriegler, E.; Rogner, H.-H.; Sferra, F. *Energy* **2016**, *111*, 580–592.
- (3) Hallett, D.; Clark-Lowes, D.; Hallett, D.; Clark-Lowes, D. In *Petroleum Geology of Libya*; 2016; pp. 1–33.
- (4) van Moerkerk, M.; Crijns-Graus, W. *Energy Policy* **2016**, *88*, 148–158.
- (5) Mobile, E. *2012 the Outlook for Energy: A View to 2040*; 2011.
- (6) Hubbert, M. K. *Nucl. Energy Foss. Fuels* **1956**, *95*, 1–57.
- (7) Tsoskounoglou, M.; Ayerides, G.; Tritopoulou, E. *Energy Policy* **2008**, *36*, 3797–3806.
- (8) Atadashi, I. M.; Aroua, M. K.; Aziz, a. A. *Renew. Energy* **2011**, *36*, 437–443.
- (9) Sandesh, S.; Kristachar, P. K. R.; Manjunathan, P.; Halgeri, A. B.; Shanbhag, G. V. *Appl. Catal. A Gen.* **2016**, *523*, 1–11.
- (10) Anuar, M. R.; Abdullah, A. Z. *Renew. Sustain. Energy Rev.* **2016**, *58*, 208–223.
- (11) Knothe, G. *Prog. Energy Combust. Sci.* **2010**, *36*, 364–373.
- (12) Wilson, K.; Lee, A. F. *Catal. Sci. Technol.* **2012**, *2*, 884–897.
- (13) Sani, Y. M.; Daud, W. M. A. W.; Abdul Aziz, A. R. *Appl. Catal. A Gen.* **2014**, *470*, 140–161.
- (14) Moser, B. R. *Biofuels* **2011**, 285–347.
- (15) Yan, S.; DiMaggio, C.; Mohan, S.; Kim, M.; Salley, S. O.; Ng, K. Y. S. *Top. Catal.* **2010**, *53*, 721–736.
- (16) Lee, A. F.; Wilson, K. *Catal. Today* **2015**, *242*, Part, 3–18.
- (17) Dhakshinamoorthy, A.; Alvaro, M.; Corma, A.; Garcia, H. *Dalt. Trans.* **2011**, *40*, 6344–6360.
- (18) Borges, M. E.; Díaz, L. *Renew. Sustain. Energy Rev.* **2012**, *16*, 2839–2849.

- (19) Ramkumar, S.; Kirubakaran, V. *Energy Convers. Manag.* **2016**, *118*, 155–169.
- (20) Mardhiah, H. H.; Ong, H. C.; Masjuki, H. H.; Lim, S.; Lee, H. V. *Renew. Sustain. Energy Rev.* **2017**, *67*, 1225–1236.
- (21) Verma, P.; Sharma, M. P. *Renew. Sustain. Energy Rev.* **2016**, *62*, 1063–1071.
- (22) Knothe, G.; Razon, L. F. *Prog. Energy Combust. Sci.* **2017**, *58*, 36–59.
- (23) Baskar, G.; Aiswarya, R. *Renew. Sustain. Energy Rev.* **2016**, *57*, 496–504.
- (24) Wilson, K.; Lee, A. F. *Philos. Trans. A. Math. Phys. Eng. Sci.* **2016**, *374*, 20150081-.
- (25) Sharma, Y. C.; Singh, B. *Renew. Sustain. Energy Rev.* **2009**, *13*, 1646–1651.
- (26) Santacesaria, E.; Vicente, G. M.; Di Serio, M.; Tesser, R. *Catal. Today* **2012**, *195*, 2–13.
- (27) Sharma, Y. C.; Singh, V. *Renew. Sustain. Energy Rev.* **2017**, *67*, 72–88.
- (28) Nada B. Nakkash and Sarah R. Al-Karkhi. *Iraqi J. Chem. Pet. Eng.* **2012**, *13*, 13–25.
- (29) Lin, L.; Cunshan, Z.; Vittayapadung, S.; Xiangqian, S.; Mingdong, D. *Appl. Energy* **2011**, *88*, 1020–1031.
- (30) Joshi, R. M.; Pegg, M. J. *Fuel* **2007**, *86*, 143–151.
- (31) Lam, M. K.; Lee, K. T.; Mohamed, A. R. *Biotechnol. Adv.* **2010**, *28*, 500–518.
- (32) Leung, D. Y. C.; Wu, X.; Leung, M. K. H. *Appl. Energy* **2010**, *87*, 1083–1095.
- (33) Bergthorson, J. M.; Thomson, M. J. *Renew. Sustain. Energy Rev.* **2015**, *42*, 1393–1417.
- (34) Santana, H. S.; Tortola, D. S.; Reis, É. M.; Silva, J. L.; Taranto, O. P. *Chem. Eng. J.* **2016**, *302*, 752–762.
- (35) Peñarrubia Fernandez, I. A.; Liu, D.-H.; Zhao, J. *Resour. Conserv. Recycl.* **2016**.
- (36) Tian, K.; Li, Z. *Biochem. Eng. J.* **2016**, *115*, 30–37.
- (37) Guldhe, A.; Singh, P.; Ansari, F. A.; Singh, B.; Bux, F. *Fuel* **2017**, *187*, 180–188.
- (38) Meher, L.; Vidyasagar, D.; Naik, S. *Renew. Sustain. Energy Rev.* **2006**, *10*, 248–268.
- (39) Helwani, Z.; Othman, M. R.; Aziz, N.; Fernando, W. J. N.; Kim, J. *Fuel Process. Technol.* **2009**, *90*, 1502–1514.
- (40) Liu, Q.; Wang, B.; Wang, C.; Tian, Z.; Qu, W.; Ma, H.; Xu, R. *Green Chem.* **2014**, *16*, 2604.
- (41) Montanari, T.; Sisani, M.; Nocchetti, M.; Vivani, R.; Concepcion Herrera Delgado, M.; Ramis, G.; Busca, G.; Costantino, U. *Catal. Today* **2010**, *152*, 104–109.
- (42) Ma, Y.; Wang, Q.; Zheng, L.; Gao, Z.; Wang, Q.; Ma, Y. *Energy* **2016**, *107*, 523–531.
- (43) Naik, S. N.; Goud, V. V.; Rout, P. K.; Dalai, A. K. *Renew. Sustain. Energy Rev.* **2010**, *14*, 578–597.
- (44) Lee, R. A.; Lavoie, J. M. *Anim. Front.* **2013**, *3*, 6–11.
- (45) Naik, S. N.; Goud, V. V.; Rout, P. K.; Dalai, A. K. *Renew. Sustain. Energy Rev.* **2010**, *14*, 578–597.
- (46) Mata, T. M.; Martins, A. a.; Caetano, N. S. *Renew. Sustain. Energy Rev.* **2010**, *14*, 217–232.
- (47) Fasahati, P.; Liu, J. J. *Fuel Process. Technol.* **2016**, *144*, 262–273.
- (48) Noraini, M. Y.; Ong, H. C.; Badrul, M. J.; Chong, W. T. *Renew. Sustain. Energy Rev.* **2014**, *39*, 24–34.
- (49) Adenle, A. A.; Haslam, G. E.; Lee, L. *Energy Policy* **2013**, *61*, 182–195.
- (50) Zhang, Y. al; Dube, M. A.; McLean, Dd.; Kates, M. *Bioresour. Technol.* **2003**, *89*, 1–16.
- (51) McNeff, C. V.; McNeff, L. C.; Yan, B.; Nowlan, D. T.; Rasmussen, M.; Gyberg, A. E.; Krohn, B. J.; Fedie, R. L.; Hoyer, T. R. *Appl. Catal. A Gen.* **2008**, *343*, 39–48.
- (52) Guo, F.; Fang, Z. In *Biodiesel Feedstocks and Processing Technologies*; 2011; pp. 1–21.
- (53) Chouhan, A. P. S.; Sarma, A. K. *Renew. Sustain. Energy Rev.* **2011**, *15*, 4378–

- 4399.
- (54) Ebiura, T.; Echizen, T.; Ishikawa, A.; Murai, K.; Baba, T. *Appl. Catal. A Gen.* **2005**, 283, 111–116.
 - (55) Arzamendi, G.; Campo, I.; Arguiñarena, E.; Sánchez, M.; Montes, M.; Gandía, L. M. *Chem. Eng. J.* **2007**, 134, 123–130.
 - (56) Tittabut, T.; Trakarnpruk, W. *Ind. Eng. Chem. Res.* **2008**, 47, 2176–2181.
 - (57) Mootabadi, H.; Salamatinia, B.; Bhatia, S.; Abdullah, A. Z. *Fuel* **2010**, 89, 1818–1825.
 - (58) Serio, M. Di; Ledda, M.; Cozzolino, M.; Minutillo, G.; Tesser, R.; Santacesaria, E.; Li, F.; Angelo, M. S.; Cintia, V.; B, S. S. N. P. S.; Na, V. **2006**, 3009–3014.
 - (59) Vujicic, D.; Comic, D.; Zarubica, A.; Micic, R.; Boskovic, G. *Fuel* **2010**, 89, 2054–2061.
 - (60) Su, M.; Yang, R.; Li, M. *Fuel* **2013**, 103, 398–407.
 - (61) Xie, W.; Zhao, L. *Energy Convers. Manag.* **2014**, 79, 34–42.
 - (62) Teng, G.; Gao, L.; Xiao, G.; Liu, H.; Lv, J. *Appl. Biochem. Biotechnol.* **2010**, 162, 1725–1736.
 - (63) Gao, L.; Teng, G.; Xiao, G.; Wei, R. *Biomass Bioenergy* **2010**, 34, 1283–1288.
 - (64) Umdu, E. S.; Tuncer, M.; Seker, E. *Bioresour. Technol.* **2009**, 100, 2828–2831.
 - (65) Jitputti, J.; Kitiyanan, B.; Rangsunvigit, P.; K, B.; Attanatho, L.; Jenvanitpanjakul, P. *Chem. Eng. J.* **2006**, 116, 61–66.
 - (66) Yang, Z.; Xie, W. *Fuel Process. Technol.* **2007**, 88, 631–638.
 - (67) Madhuvilakku, R.; Piraman, S. *Bioresour. Technol.* **2013**, 150, 55–59.
 - (68) Wen, Z.; Yu, X.; Tu, S.-T.; Yan, J.; Dahlquist, E. *Bioresour. Technol.* **2010**, 101, 9570–9576.
 - (69) Alsalmé, A.; Kozhevnikova, E. F.; Kozhevnikov, I. V. *Appl. Catal. A Gen.* **2008**, 349, 170–176.
 - (70) Li, J.; Fu, Y.-J.; Qu, X.-J.; Wang, W.; Luo, M.; Zhao, C.-J.; Zu, Y.-G. *Bioresour. Technol.* **2012**, 108, 112–118.
 - (71) Shibasaki-Kitakawa, N.; Kanagawa, K.; Nakashima, K.; Yonemoto, T. *Bioresour. Technol.* **2013**, 142, 732–736.
 - (72) Rattanaphra, D.; Harvey, A. P.; Thanapimmetha, A.; Srinophakun, P. *Fuel* **2012**, 97, 467–475.
 - (73) Boffito, D. C.; Crocellà, V.; Pirola, C.; Neppolian, B.; Cerrato, G.; Ashokkumar, M.; Bianchi, C. L. *J. Catal.* **2013**, 297, 17–26.
 - (74) Tormin, T. F.; Gimenes, D. T.; Richter, E. M.; Munoz, R. A. A. *Talanta* **2011**, 85, 1274–1278.
 - (75) Wang, W.; Yang, H.; Liu, Y.; Cui, H.; Chen, J. *Hydrometallurgy* **2011**, 109, 47–53.
 - (76) Shajaratun Nur, Z. A.; Taufiq-Yap, Y. H.; Rabiah Nizah, M. F.; Teo, S. H.; Syazwani, O. N.; Islam, A. *Energy Convers. Manag.* **2014**, 78, 738–744.
 - (77) Fang, L.; Zhang, K.; Li, X.; Wu, H.; Wu, P. *Chinese J. Catal.* **2012**, 33, 114–122.
 - (78) Fu, X.; Li, D.; Chen, J.; Zhang, Y.; Huang, W.; Zhu, Y.; Yang, J.; Zhang, C. *Bioresour. Technol.* **2013**, 146, 767–770.
 - (79) Shu, Q.; Gao, J.; Nawaz, Z.; Liao, Y.; Wang, D.; Wang, J. *Appl. Energy* **2010**, 87, 2589–2596.
 - (80) Yun, H.; Wang, M.; Feng, W.; Tan, T. *Energy* **2013**, 54, 84–96.
 - (81) Taher, H.; Al-Zuhair, S.; Al-Marzouqi, A. H.; Haik, Y.; Farid, M. *Biochem. Eng. J.* **2014**, 90, 103–113.
 - (82) Zhao, T.; No, D. S.; Kim, Y.; Kim, Y. S.; Kim, I.-H. *J. Mol. Catal. B Enzym.* **2014**, 107, 17–22.
 - (83) Joshi, G.; Rawat, D. S.; Lamba, B. Y.; Bisht, K. K.; Kumar, P.; Kumar, N.; Kumar, S. *Energy Convers. Manag.* **2015**, 96, 258–267.
 - (84) Boro, J.; Konwar, L. J.; Deka, D. *Fuel Process. Technol.* **2014**, 122, 72–78.
 - (85) Girish, N.; Niju, S. P.; Meera Sheriffa Begum, K. M.; Anantharaman, N. *Fuel* **2013**, 111, 653–658.

- (86) Boey, P.-L.; Maniam, G. P.; Hamid, S. A.; Ali, D. M. H. *Fuel* **2011**, *90*, 2353–2358.
- (87) Wilson, K.; Hardacre, C.; Lee, A. F.; Montero, J. M.; Shellard, L. *Green Chem.* **2008**, *10*, 654.
- (88) Lotero, E.; Liu, Y.; Lopez, D. E.; Suwannakarn, K.; Bruce, D. A.; Goodwin, J. G. *Ind. Eng. Chem. Res.* **2005**, *44*, 5353–5363.
- (89) Narasimharao, K.; Brown, D.; Lee, A.; Newman, A.; Siril, P.; Tavaner, S.; Wilson, K. *J. Catal.* **2007**, *248*, 226–234.
- (90) Kouzu, M.; Nakagaito, A.; Hidaka, J. *Appl. Catal. A Gen.* **2011**, *405*, 36–44.
- (91) Istadi, I.; Anggoro, D. D.; Buchori, L.; Rahmawati, D. A.; Intaningrum, D. *Procedia Environ. Sci.* **2015**, *23*, 385–393.
- (92) Alhassan, F. H.; Rashid, U.; Taufiq-Yap, Y. H. *Fuel* **2015**, *142*, 38–45.
- (93) Yi, Q.; Zhang, J.; Zhang, X.; Feng, J.; Li, W. *Fuel* **2015**, *143*, 390–398.
- (94) Xie, W.; Wang, T. *Fuel Process. Technol.* **2013**, *109*, 150–155.
- (95) Wang, Y.-Y.; Lee, D.-J.; Chen, B.-H. *Energy Procedia* **2014**, *61*, 918–921.
- (96) Fu, J.; Chen, L.; Lv, P.; Yang, L.; Yuan, Z. *Fuel* **2015**, *154*, 1–8.
- (97) Melero, J. A.; Bautista, L. F.; Morales, G.; Iglesias, J.; Sánchez-Vázquez, R. *Chem. Eng. J.* **2010**, *161*, 323–331.
- (98) Shao, G. N.; Sheikh, R.; Hilonga, A.; Lee, J. E.; Park, Y.-H.; Kim, H. T. *Chem. Eng. J.* **2013**, *215–216*, 600–607.
- (99) Poonjarernsilp, C.; Sano, N.; Tamon, H. *Appl. Catal. A Gen.* **2015**, *497*, 145–152.
- (100) Alcañiz-Monge, J.; Trautwein, G.; Marco-Lozar, J. P. *Appl. Catal. A Gen.* **2013**, *468*, 432–441.
- (101) Ullah, Z.; Bustam, M. A.; Man, Z. *Renew. Energy* **2015**, *77*, 521–526.
- (102) Muhammad, N.; Elsheikh, Y. A.; Mutalib, M. I. A.; Bazmi, A. A.; Khan, R. A.; Khan, H.; Rafiq, S.; Man, Z.; Khan, I. *J. Ind. Eng. Chem.* **2015**, *21*, 1–10.
- (103) Su, F.; Guo, Y. *Green Chem.* **2014**, *16*, 2934–2957.
- (104) Melero, J. a.; Iglesias, J.; Morales, G. *Green Chem.* **2009**, *11*, 1285.
- (105) Wu, H.; Liu, Y.; Zhang, J.; Li, G. *Bioresour. Technol.* **2014**, *174*, 182–189.
- (106) Park, Y.-M.; Lee, J. Y.; Chung, S.-H.; Park, I. S.; Lee, S.-Y.; Kim, D.-K.; Lee, J.-S.; Lee, K.-Y. *Bioresour. Technol.* **2010**, *101 Suppl*, S59–61.
- (107) Lam, M. K.; Lee, K. T. *Fuel Process. Technol.* **2011**, *92*, 1639–1645.
- (108) Patel, A.; Brahmkhatri, V.; Singh, N. *Renew. Energy* **2013**, *51*, 227–233.
- (109) Liu, W.; Yin, P.; Zhang, J.; Tang, Q.; Qu, R. *Energy Convers. Manag.* **2014**, *82*, 83–91.
- (110) Trakarnpruk, W. *Mendeleev Commun.* **2013**, *23*, 46–48.
- (111) Sunita, G.; Devassy, B. M.; Vinu, A.; Sawant, D. P.; Balasubramanian, V. V.; Halligudi, S. B. *Catal. Commun.* **2008**, *9*, 696–702.
- (112) Liu, F.; Zhang, Y. *Ceram. Int.* **2012**, *38*, 3473–3482.
- (113) Hu, S.; Guan, Y.; Wang, Y.; Han, H. *Appl. Energy* **2011**, *88*, 2685–2690.
- (114) Istadi, I.; Prasetyo, S. A.; Nugroho, T. S. *Procedia Environ. Sci.* **2015**, *23*, 394–399.
- (115) Mahdavi, V.; Monajemi, A. *J. Taiwan Inst. Chem. Eng.* **2014**, *45*, 2286–2292.
- (116) Jeon, H.; Kim, D. J.; Kim, S. J.; Kim, J. H. *Fuel Process. Technol.* **2013**, *116*, 325–331.
- (117) Manríquez-Ramírez, M.; Gómez, R.; Hernández-Cortez, J. G.; Zúñiga-Moreno, A.; Reza-San Germán, C. M.; Flores-Valle, S. O. *Catal. Today* **2013**, *212*, 23–30.
- (118) Teixeira, A. P. C.; Santos, E. M.; Vieira, A. F. P.; Lago, R. M. *Chem. Eng. J.* **2013**, *232*, 104–110.
- (119) Dias, A. P. S.; Bernardo, J.; Felizardo, P.; Correia, M. J. N. *Fuel Process. Technol.* **2012**, *102*, 146–155.
- (120) Zhang, X.; Ma, Q.; Cheng, B.; Wang, J.; Li, J.; Nie, F. *J. Nat. Gas Chem.* **2012**, *21*, 774–779.

- (121) Hsieh, L.-S.; Kumar, U.; Wu, J. C. S. *Chem. Eng. J.* **2010**, *158*, 250–256.
- (122) Zeng, H.-Y.; Xu, S.; Liao, M.-C.; Zhang, Z.-Q.; Zhao, C. *Appl. Clay Sci.* **2014**, *91–92*, 16–24.
- (123) Sirisomboonchai, S.; Abuduwayiti, M.; Guan, G.; Samart, C.; Abliz, S.; Hao, X.; Kusakabe, K.; Abudula, A. *Energy Convers. Manag.* **2015**, *95*, 242–247.
- (124) Rashtizadeh, E.; Farzaneh, F.; Talebpour, Z. *Bioresour. Technol.* **2014**, *154*, 32–37.
- (125) Wang, S.-H.; Wang, Y.-B.; Dai, Y.-M.; Jehng, J.-M. *Appl. Catal. A Gen.* **2012**, *439–440*, 135–141.
- (126) Lee, H. V.; Taufiq-Yap, Y. H. *Process Saf. Environ. Prot.* **2015**, *94*, 430–440.
- (127) Shu, Q.; Yang, B.; Yuan, H.; Qing, S.; Zhu, G. *Catal. Commun.* **2007**, *8*, 2159–2165.
- (128) Wu, H.; Zhang, J.; Wei, Q.; Zheng, J.; Zhang, J. *Fuel Process. Technol.* **2013**, *109*, 13–18.
- (129) Carrero, A.; Vicente, G.; Rodríguez, R.; Linares, M.; del Peso, G. L. *Catal. Today* **2011**, *167*, 148–153.
- (130) Sun, C.; Qiu, F.; Yang, D.; Ye, B. *Fuel Process. Technol.* **2014**, *126*, 383–391.
- (131) Cantrell, D. G.; Gillie, L. J.; Lee, A. F.; Wilson, K. *Appl. Catal. A Gen.* **2005**, *287*, 183–190.
- (132) Trakarnpruk, W.; Porntangjitlikit, S. *Renew. ENERGY* **2008**, *33*, 1558–1563.
- (133) Woodford, J. J.; Dacquin, J.-P.; Wilson, K.; Lee, A. F. *Energy Environ. Sci.* **2012**, *5*, 6145.
- (134) Pasupulety, N.; Rempel, G. L.; Ng, F. T. T. *Appl. Catal. A Gen.* **2015**, *489*, 77–85.
- (135) Lu, Y.; Zhang, Z.; Xu, Y.; Liu, Q.; Qian, G. *Bioresour. Technol.* **2015**, *10–13*.
- (136) Sun, J.; Yang, J.; Li, S.; Xu, X. *Catal. Commun.* **2014**, *52*, 1–4.
- (137) Taufiq-Yap, Y. H.; Teo, S. H.; Rashid, U.; Islam, A.; Hussien, M. Z.; Lee, K. T. *Energy Convers. Manag.* **2014**, *88*, 1290–1296.
- (138) Lima, J. R. de O.; Ghani, Y. A.; da Silva, R. B.; Batista, F. M. C.; Bini, R. A.; Varanda, L. C.; de Oliveira, J. E. *Appl. Catal. A Gen.* **2012**, *445–446*, 76–82.
- (139) Ngamcharussrivichai, C.; Nunthasanti, P.; Tanachai, S.; Bunyakiat, K. *Fuel Process. Technol.* **2010**, *91*, 1409–1415.
- (140) Alhassan, F. H.; Rashid, U.; Taufiq-Yap, Y. H. *J. Oleo Sci.* **2015**, *64*, 91–99.
- (141) Yoo, S. J.; Lee, H.-S.; Veriansyah, B.; Kim, J.; Kim, J.-D.; Lee, Y.-W. *Bioresour. Technol.* **2010**, *101*, 8686–8689.
- (142) Lopez, D.; Suwannakarn, K.; Bruce, D.; Goodwinjr, J. J. *Catal.* **2007**, *247*, 43–50.
- (143) Guzmán-Vargas, A.; Santos-Gutiérrez, T.; Lima, E.; Flores-Moreno, J. L.; Oliver-Tolentino, M. A.; Martínez-Ortiz, M. de J. *J. Alloys Compd.* **2015**.
- (144) Liu, Q.; Wang, C.; Qu, W.; Wang, B.; Tian, Z.; Ma, H.; Xu, R. *Catal. Today* **2014**, *234*, 161–166.
- (145) Reyero, I.; Velasco, I.; Sanz, O.; Montes, M.; Arzamendi, G.; Gandía, L. M. *Catal. Today* **2013**, *216*, 211–219.
- (146) Volli, V.; Purkait, M. K. *J. Hazard. Mater.* **2015**.
- (147) Ramos, M. J.; Casas, A.; Rodríguez, L.; Romero, R.; Pérez, Á. *Appl. Catal. A Gen.* **2008**, *346*, 79–85.
- (148) Rodríguez-Chiang, L.; Llorca, J.; Dahl, O. *Bioresour. Technol.* **2016**, *218*, 84–91.
- (149) Zhang, J.; Li, Y.; Zhou, J.; Chen, D.; Qian, G. *J. Hazard. Mater.* **2012**, *205–206*, 111–117.
- (150) Bhanja, P.; Bhaumik, A. *Fuel* **2016**, *185*, 432–441.
- (151) Li, D.; Lu, M.; Aragaki, K.; Koike, M.; Nakagawa, Y.; Tomishige, K. *Appl. Catal. B Environ.* **2016**, *192*, 171–181.
- (152) Hu, Q.; Yang, L.; Fan, G.; Li, F. *J. Catal.* **2016**, *340*, 184–195.
- (153) Zhang, X.; Yang, S.; Xie, X.; Chen, L.; Sun, L.; Zhao, B.; Si, H. *J. Anal. Appl. Pyrolysis* **2016**, *120*, 371–378.

- (154) Manikandan, M.; Venugopal, A. K.; Prabu, K.; Jha, R. K.; Thirumalaiswamy, R. *J. Mol. Catal. A Chem.* **2016**, 417, 153–162.
- (155) Carja, G.; Husanu, E.; Gherasim, C.; Iovu, H. *Appl. Catal. B Environ.* **2011**, 107, 253–259.
- (156) Hallett-Tapley, G. L.; Crites, C.-O. L.; González-Béjar, M.; McGilvray, K. L.; Netto-Ferreira, J. C.; Scaiano, J. C. *J. Photochem. Photobiol. A Chem.* **2011**, 224, 8–15.
- (157) Theiss, F. L.; Ayoko, G. A.; Frost, R. L. *Appl. Surf. Sci.* **2016**, 383, 200–213.
- (158) Carriazo, D.; Arco, M.; García-lópez, E.; Marci, G.; Martín, C.; Palmisano, L.; Rives, V. *Journal Mol. Catal. A, Chem.* **2011**, 342–343, 83–90.
- (159) Feitknecht, W.; Gerben, M. *Helv. Chim. Acta* **25** **1942**, 131–137.
- (160) F. Cavani, F. Trifiro, A. V. *Catal. Today* **1991**, 2, 173–301.
- (161) E. Manasse. No Title. *Atti. Soc. Toscana Sc. Nat., Proc. Verb.* 1915, 24, 92.
- (162) G. aminoff and B. Broome. *Contribution to knowledge of pyroaurite.*; Kungl. Svenska. Vetenskaps Handl., 1931; Vol. 9.
- (163) S. Miyata, T. Kumura, H. H. and K. T. *Solid Acids and Bases*; 1971; Vol. 92.
- (164) Y. Ono, H. H. *Solid Base Catalysis*; 2011.
- (165) F. J. Brocker and L. Kainer. Catalysts and Catalysts Carrier Having Very Finely Divided Active Components and Their Preparation (German Patent), 1970.
- (166) Evans, J. *J. Electroanal. Chem. Interfacial Electrochem.* **1991**, 305, 329–330.
- (167) Misra, C.; Boro, P.; Double, A.; Mawasseite, H.; Mineralosist, T. A.; Properties, P. C.; Minerologist, A.; Cited, R. Synthetic Hydrotalcite, 1990.
- (168) Choudary, B. .; Lakshmi Kantam, M.; Venkat Reddy, C.; Aranganathan, S.; Lakshmi Santhi, P.; Figueras, F. *J. Mol. Catal. A Chem.* **2000**, 159, 411–416.
- (169) Xie, W.; Peng, H.; Chen, L. *J. Mol. Catal. A Chem.* **2006**, 246, 24–32.
- (170) Chen, H.; Wang, J.-F. *Biodiesel from Transesterification of Cottonseed Oil by Heterogeneous catalysis*; Studies in Surface Science and Catalysis; Elsevier, 2006; Vol. 159.
- (171) Creasey, J. J.; Parlett, C. M. A.; Manayil, J. C.; Isaacs, M. A.; Wilson, K.; Lee, A. F. *Green Chem.* **2015**, 17, 2398–2405.
- (172) Zhu, Y.; An, Z.; He, J. *J. Catal.* **2016**, 341, 44–54.
- (173) Allada Rk, Navrotsky A, Berbeco HT, C. W. *Science (80-)*. **2002**, 296, 721–723.
- (174) Abelló, S.; Medina, F.; Tichit, D.; Pérez-Ramírez, J.; Groen, J. C.; Sueiras, J. E.; Salagre, P.; Cesteros, Y. *Chem. – A Eur. J.* **2005**, 11, 728–739.
- (175) Morandi, S.; Prinetto, F.; Di Martino, M.; Ghiotti, G.; Lorret, O.; Tichit, D.; Malagù, C.; Vendemiati, B.; Carotta, M. C. *Sensors Actuators B Chem.* **2006**, 118, 215–220.
- (176) B. F. Sels, D. E. De Vos, P. A. J. *Catal. Rev. Sci. Eng* **2001**, 43, 443.
- (177) Debecker, D. P.; Gaigneaux, E. M.; Busca, G. *Chem. – A Eur. J.* **2009**, 15, 3920–3935.
- (178) Wang, Y.-B.; Jehng, J.-M. *Chem. Eng. J.* **2011**, 175, 548–554.
- (179) Nishimura, S.; Takagaki, A.; Ebitani, K. *Green Chem.* **2013**, 15, 2026.
- (180) Jairo Tronto, Ana Cláudia Bordonal, Z. N. and J. B.; Valim. In *Materials Science - Advanced Topics*; Intech, 2013.
- (181) Xie, W.; Peng, H.; Chen, L. *J. Mol. Catal. A Chem.* **2006**, 246, 24–32.
- (182) Othman, M. R.; Helwani, Z.; Martunus; Fernando, W. J. N. *Appl. Organomet. Chem.* **2009**, 23, 335–346.
- (183) Fraile, J. M.; García, N.; Mayoral, J. a.; Pires, E.; Roldán, L. *Appl. Catal. A Gen.* **2009**, 364, 87–94.
- (184) Baskaran, T.; Christopher, J.; Sakthivel, A. *RSC Adv.* **2015**, 5, 98853–98875.
- (185) Helwani, Z.; Aziz, N.; Kim, J.; Othman, M. R. *Renew. Energy* **2016**, 86, 68–74.
- (186) Bunekar, N.; Tsai, T.-Y.; Yu, Y.-Z. *Mater. Today Proc.* **2016**, 3, 1415–1422.
- (187) Diana Iruretagoyena Ferrer. *Supported Layered Double Hydroxides as CO₂ Adsorbents for Sorption-enhanced H₂ production*; Springer, 2016.
- (188) Anastas, P. T.; Warner, J. C., O. *Green Chemistry: Theory and Practice*; Oxford

- University Press, new York, 1998.
- (189) Touahra, F.; Sehailia, M.; Ketir, W.; Bachari, K.; Chebout, R.; Trari, M.; Cherifi, O.; Halliche, D. *Appl. Petrochemical Res.* **2015**.
 - (190) Klopogge, J. T.; Hickey, L.; Frost, R. L. *J. Solid State Chem.* **2004**, *177*, 4047–4057.
 - (191) Xu, C.; Gao, Y.; Liu, X.; Xin, R.; Wang, Z. *RSC Adv.* **2013**, *3*, 793–801.
 - (192) Benito, P.; Guinea, I.; Labajos, F. M.; Rives, V. *J. Solid State Chem.* **2008**, *181*, 987–996.
 - (193) Pavel, O. D.; Zăvoianu, R.; Bîrjega, R.; Angelescu, E.; Costentin, G.; Che, M. *Appl. Clay Sci.* **2015**, *104*, 59–65.
 - (194) Valente, J. S.; Lima, E.; Toledo-antonio, J. A.; Cortes-jacome, M. A.; Lartundo-rojas, L.; Montiel, R.; Prince, J. **2010**, 2089–2099.
 - (195) Bankauskaite, A.; Baltakys, K. *J. Therm. Anal. Calorim.* **2015**, *121*, 227–233.
 - (196) Zawadzki, M.; Wrzyszczy, J. *Mater. Res. Bull.* **2000**, *35*, 109–114.
 - (197) Fahami, A.; Al-Hazmi, F. S.; Al-Ghamdi, A. A.; Mahmoud, W. E.; Beall, G. W. *J. Alloys Compd.* **2016**, *683*, 100–107.
 - (198) Winter, F.; Xia, X.; Herejggers, B. P. C.; Bitter, J. H.; Jos Van Dillen, a.; Muhler, M.; De Jong, K. P. *J. Phys. Chem. B* **2006**, *110*, 9211–9218.
 - (199) Baskaran, T.; Christopher, J.; Ajithkumar, T. G.; Sakthivel, A. *Appl. Catal. A Gen.* **2014**, *488*, 119–127.
 - (200) Zhou, W.; Liu, J.; Pan, J.; Sun, F.; He, M.; Chen, Q. *Effect of Mg²⁺ on the catalytic activities of CoMgAl hydrotalcites in the selective oxidation of benzyl alcohol to benzaldehyde*; 2015; Vol. 69.
 - (201) Córdova Reyes, I.; Salmones, J.; Zeifert, B.; Contreras, J. L.; Rojas, F. *Chem. Eng. Sci.* **2014**, *119*, 174–181.
 - (202) Liu, X.; Fan, B.; Gao, S.; Li, R. *Fuel Process. Technol.* **2013**, *106*, 761–768.
 - (203) Hora, L.; Kikhtyanin, O.; Čapek, L.; Bortnovskiy, O.; Kubička, D. *Catal. Today* **2015**, *241*, 221–230.
 - (204) Kikhtyanin, O.; Hora, L.; Kubička, D. *Unprecedented selectivities in aldol condensation over Mg–Al hydrotalcite in a fixed bed reactor setup*; 2015; Vol. 58.
 - (205) Dumbre, D. K.; Mozammel, T.; Selvakannan, P.; Hamid, S. B. A.; Choudhary, V. R.; Bhargava, S. K. *J. Colloid Interface Sci.* **2015**, *441*, 52–58.
 - (206) Khan, F. A.; Dash, J.; Satapathy, R.; Upadhyay, S. K. *Hydrotalcite catalysis in ionic liquid medium: a recyclable reaction system for heterogeneous Knoevenagel and nitroaldol condensation*; 2004; Vol. 45.
 - (207) Kocík, J.; Samikannu, A.; Bourajoini, H.; Pham, T. N.; Mikkola, J.-P.; Hájek, M.; Čapek, L. *J. Clean. Prod.* **2016**.
 - (208) Bacilla, A. C. C.; de Freitas, M. R.; Bail, A.; dos Santos, V. C.; Nagata, N.; Silva, Â.; Marçal, L.; Ciuffi, K. J.; Nakagaki, S. *J. Mol. Catal. A Chem.* **2016**, *422*, 221–233.
 - (209) Yan, W.; Hao, W.; ZHONG, T.; ZHAO, W.; ZHAI, Y. *J. Fuel Chem. Technol.* **2011**, *39*, 831–837.
 - (210) Kikhtyanin, O.; Lesnik, E.; Kubička, D. *Appl. Catal. A Gen.* **2016**, *525*, 215–225.
 - (211) Wang, Z.; Fongarland, P.; Lu, G.; Essayem, N. *J. Catal.* **2014**, *318*, 108–118.
 - (212) Dhainaut, J.; Dacquín, J.-P.; Lee, A. F.; Wilson, K. *Green Chem.* **2010**, *12*, 296.
 - (213) Dacquín, J.-P.; Dhainaut, J.; Duprez, D.; Royer, S.; Lee, A. F.; Wilson, K. *J. Am. Chem. Soc.* **2009**, *131*, 12896–12897.
 - (214) Montero, J. M.; Brown, D. R.; Gai, P. L.; Lee, A. F.; Wilson, K. *Chem. Eng. J.* **2010**, *161*, 332–339.
 - (215) Montero, J. M.; Gai, P.; Wilson, K.; Lee, A. F. *Green Chem.* **2009**, *11*, 265–268.

Chapter 2

Experimental

2.1 Catalyst preparation

In this chapter, the methods used to prepare solid base hydrotalcite, its characterisation and catalytic reactions involved will be described.

2.1.1 Hydrotalcite synthesis

Novel metal hydrotalcites have been prepared via the alkali-free method adapted from Cantrell and co-workers¹ except the element ratio of metal was altered; Zn, Ni and Mg to Al were changed to 4:1, 3:1, 2:1 and 1.5:1. MgAl hydrotalcites (HTs) have been prepared as a benchmark catalyst. Metal nitrate hexahydrate ($(M(NO_3)_2 \cdot 6H_2O)$ where M = Zn, Ni and Mg) aqueous solution ($x \text{ cm}^3$ 1.5 M) and aluminum nitrate nonahydrate ($(Al(NO_3)_3 \cdot 9H_2O)$ aqueous solution ($y \text{ cm}^3$, 1.5 M) were mixed together so that $x + y = 100 \text{ cm}^3$. Ammonium carbonate is used as the alkali-free precipitating agent. The mixed metal nitrate solutions are added dropwise (1 ml min^{-1}) simultaneously with ammonium carbonate (2 M, 100 cm^3) using an automated pump syringe into a Radley reactor (Figure 2.1).



Figure 2.1 Preparation one of the hydrotalcite catalyst in a large Radley reactor. Left: Preparation of ZnAl HTH; Right: Preparation of NiAl HTH. MgAl LDH was prepared using the same manners.

Ammonia solution was added in order to keep the pH constant for each synthesis involved; pH 9-10 for Zn, 9.5 for Ni and 8.5 for Mg. After the precursor addition was completed and the mixture was aged at 65 °C for overnight. The precipitate was isolated by filtration and washed several times until neutral pH 7 is obtained. The powder was then calcined over different temperature ranges 300 - 500 °C for 5 hours under O₂ (20 mL min⁻¹), at a ramp rate of 1 °C min⁻¹. The calcined hydrotalcites were cooled and rehydrated under flowing water based on different methods as described in Section 2.1.1.2. Different approaches have been tried to ensure pure hydrotalcites has been synthesised.

2.1.1.1 Calcination of hydrotalcites

Hydrotalcite samples have been calcined at different temperatures according to their metal precursor which the decomposition temperature has been determined by TGA. ZnAl LDH has been calcined at 300 °C, NiAl LDH was calcined at 350 °C and MgAl LDH at 450 °C.

2.1.1.2 Rehydration of hydrotalcites

In order to determine the best rehydration method for hydrotalcite, samples have been rehydrated through three different ways; gas-phase (GP), liquid-phase (LP) and hydrothermal (HTM) method.

a) Gas-phase

In gas-phase, the calcined samples (300-500 °C) were rehydrated following Woodford's² method with some modification. Samples were rehydrated under nitrogen saturated with water at 30 ml / min⁻¹ for 48 hours, before being stored in a desiccator and subsequently subject to characterisation analysis.

b) Liquid-phase method

In a round bottom flask, the calcined sample was immersed in deionised water at room temperature overnight. The sample then was centrifuged, isolated by filtration and placed in drying oven at 80 °C.

c) Hydrothermal method

The calcined catalyst was stirred in a beaker until it has dispersed completely in water and then placed in a hydrothermal flask at 110 and 150 °C overnight. The sample

then was centrifuged, isolated by filtration and washed with deionised water before dried in an oven at 80 °C.

2.1.2 Polystyrene beads synthesis for macroporous LDH

Polystyrene beads were prepared using emulsifier-free emulsion polymerisation method following Vaudreuil *et al.*³. 0.35 g of potassium persulfate was dissolved in 20 ml distilled water at 80 °C. In a round bottom flask, 1500 ml water was purged under N₂ overnight. In the mean time styrene (140 ml) and divinyl benzene (27 ml) were washed with sodium hydroxide: water (0.1 M, 1:1 ratio) followed by three more times washing with distilled water in order to remove polymerization inhibitors. The styrene and divinyl benzene were then added to the round-bottom flask with water followed by dropwise addition of potassium persulfate solution. The mixture was left for overnight under stirring. The sample was isolated by filtration and washed with deionized water and ethanol prior to dry in the oven at 70 °C.

2.1.3 Macroporous hydrotalcite synthesis

Macroporous hydrotalcite (MacroLDH) (Mg/Al, Ni/Al and Zn/Al LDH) were prepared according to the method of Géraud *et al.*⁴ and Woodford *et al.*² method's with modification on rehydration via gas-phase, liquid-phase and hydrothermal methods. In this study, we synthesised alkali-free MacroNiAl LDH and MacroZnAl LDH for the first time and to be compared with MacroMgAl LDH. 1 M M²⁺ salts (Mg²⁺, Ni²⁺ and Zn²⁺) and 1 M Al³⁺ salts were both dissolved in 100 ml deionised water prior to preparation of ratio 4:1. 2 M ammonium carbonate was prepared by dissolved in 100 ml deionised water as alkali-free precipitating agent. In a four-neck round bottom flask, 6 g of polystyrene beads were immersed in ethanol: water (1:1) solution with stirring at 65 °C (**Figure 2.2**). The M²⁺: Al³⁺ and ammonium carbonate solution were added dropwise using an automated pump (1 ml/min). The mixture was maintained at the desired pH as mentioned above with the addition of ammonium hydroxide solution. The mixture was aged at 65 °C overnight followed by filtration and washed with deionised water until pH drops to 7. The samples were calcined according to their calcination temperature as mentioned before. Rehydration was undertaken following hydrothermal method.



Figure 2.2 Preparation one of macroporous hydrotalcite catalyst in four-neck round-bottom flask.

2.1.4 Commercial catalysts: Dolomite and NanoMgO

In Chapter 6, three commercial catalysts have been used in this study; commercial dolomite, ex-gasifier dolomite (both obtained from EBRI pyroformer reactor, one was fresh and later obtained from the waste collector) and NanoMgO (99.6 %, Nanoactive Magnesium Oxide Plus, NanoScale Corporation). Samples were calcined at the desired temperature (900 °C for dolomite and 500 °C for Nano MgO) at 5 °C min⁻¹ under Helium flow of 10 ml/min⁻¹.

2.2 Characterisation methods

This section will be describing the main techniques engaging in characterising layered double hydroxides and the commercial catalysts. In each technique, the basic concepts on how the instruments works, how the samples are prepared and how samples analysed are thoroughly discussed.

2.2.1 Powder X-ray diffraction

Bruker D8 Advance Powder X-Ray Diffraction (PXRD) fitted with LYNX eye high-speed detector has been used to measure the crystal structure of powder or thin film materials. The wide-angle patterns were recorded over a range of $2\theta = 5 - 80$ °C (step

size 0.02° with scan speed $0.020^\circ \text{ s}^{-1}$). Typically, Cu K_α X-ray photons radiation (0.1541 nm) is used in XRD due to it is more intense compared to Co and give better resolution.

In this study, PXRD is a convenient technique to examine the layered ordering of HTs. Crystallite information such as ordered or less ordered layers, unit-cell dimension, and basal spacing of the layers are among the valuable information that can be obtained from PXRD⁵. PXRD helps to confirm the formation of hydrotalcite with all known characteristic peaks.

X-ray beams are passing through an evacuated tube similar to cathode ray tube (**Figure 2.3**). Simultaneously, the tungsten filament will heat up by current and releases electrons. The electrons are accelerating by a high voltage and hit a copper target hence generates the copper x-rays. The x-ray emitted and an incident radiation occurs upon interacts with solid. The beams passed through a slit that determines the width of the angular beam. A wider slit will give a strong energy and wider peaks but smaller slit will give a less energy with better resolution.



Figure 2.3 Schematic presentation of X-ray tube (above) and simplified incident and reflection in a solid and its relation to a lattice spacing d . The image was obtained from Krumeick⁶.

X-ray at angle theta is diffracted from internal crystal plane separated by a distance. The diffraction is equalised with the distance of constructive interference which produces a set of refraction angles or distance known as spacing, d . This angle depends on two factors; the wavelength of the X-ray source and the distance between lattice planes, as given by the Bragg's equation in **Equation 2.1**.

$$n\lambda = 2d\sin \theta \quad \text{-----} \quad \text{Equation 2.1}$$

where n = order of the interference (integer), λ = the wavelength of the incident X-rays, d = distance between two lattice planes and θ = diffraction angle between the incident X-ray and the reflective lattice plane.

In term of the prepared samples, it is important to have well-defined polycrystalline materials which the particle size should not exceed 45 microns. The sample should be enough to be packed on a sample holder so that when a beam hits at a particular angle, the Bragg equation is satisfied and good diffraction patterns appeared. The sample has been analysed using Diffrac. Eva license software, Copyright© Bruker AXS Version 3.0.

The XRD pattern of a typical hydrotalcite is definite and the example of diffraction patterns can be seen in **Figure 2.4**. The intense peaks basal plane at $d(003)$ indicates the formation of a well-structured crystalline arrangement, attributed to the formation of a 3-dimensional sheet of hydrotalcite⁷.

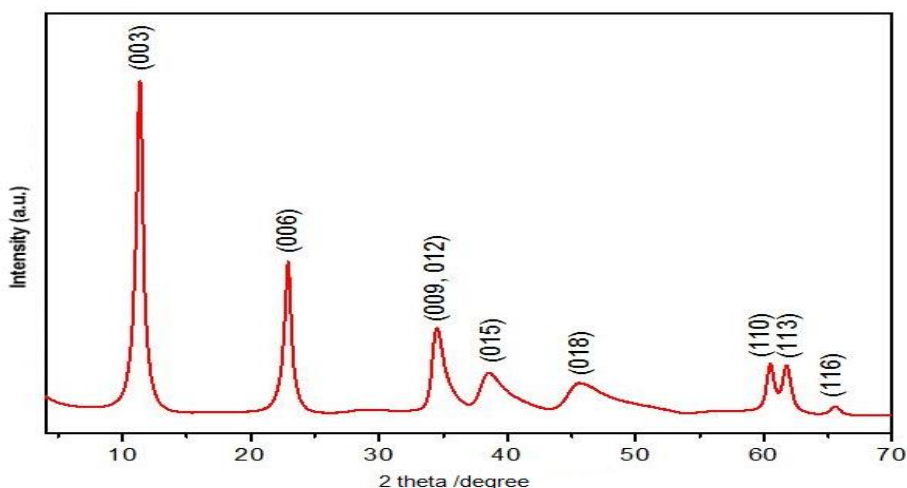


Figure 2.4 The diffraction pattern of hydrotalcite material¹⁰.

The reflection of $d(110)$ has been indexed with respect to lattice parameter a , related to the unit cell, can be calculated by using **Equation 2.2**⁹. Parameter a also indicates the average cation-cation distance in the layers¹¹.

$$a = 2d_{110} \text{ ----- Equation 2.2}$$

The lattice parameter c which relates to the thickness of a unit cell¹¹ and can be calculated by using $d(003)$, $d(006)$ and $d(009)$ ⁹ in **Equation 2.3**. The thickness of the brucite layer is normally controlled by the size and orientation of interlayer anions¹².

$$c = d_{003} + 2d_{006} + 3d_{009} \text{ ----- Equation 2.3}$$

The Scherrer Equation is used to determine the particle size of crystals in the form of powder as can be seen in **Equation 2.4**.

$$PS_{av} = \frac{k\lambda}{\sqrt{(\beta^2 + S^2)} \cos \theta} \text{ ----- Equation 2.4}$$

where PS_{av} = average particle size (Å), k = dimension of shape factor, value is 0.9 (constant), λ is wavelength of X-ray (0.154 nm), β = Full Width at Half Maximum (FWHM) of diffraction peak, S = 0.15 (systematic broadening caused by diffractometer) and θ is diffraction of Bragg angle (in °)¹³.

2.2.2 Nitrogen adsorption

N₂ porosimetry was undertaken on a Quantachrome Instrument Nova 4200e to determine surface area, pore size diameter, and pore volume¹⁴. The surface area and pore size analysis by gas adsorption were achieved by preparing the sample in the glass cell tube and heating under vacuum (degassing)¹⁵. Samples were degassed using an inert gas at 120 °C for 3 h or longer (for macroporous) to remove moisture and other contaminants¹⁶. Adsorption/desorption isotherms were recorded at -196 °C (77 K). The actual measurement begins by exposing the samples to a very low pressure of 'adsorptive' gas. **Figure 2.5** demonstrates the gas sorption process that occurs in four stages.

The amount of gas absorbed at the surfaces are correlated with the pressure of gas rises. As the small amount of the gas (adsorbate) is stick to the surface of the solid (adsorbent), a thin layer or monolayer is formed which is later been used to calculate the Brunauer, Emmett, and Teller (BET) surface area (**Equation 2.5**). Additional molecules will absorb on the monolayer to form a multilayer. As the pressure of the gas is further increased, mesopore filling begins, which is often referred to 'capillary condensation'. Once the equilibrium adsorbate approaches saturation, the pores become completely filled with adsorbate.



Figure 2.5 The gas sorption process that occurs in four stages before 100 % saturation on pore. Retrieved from http://www.quantachrome.com/gassorption/nova_series.html¹⁶ (accessed Sep 23, 2014).

$$\frac{P}{Va(P_o - P)} = \frac{1}{VmC} + \frac{C-1}{VmC} \left(\frac{P}{P_o} \right) \text{----- Equation 2.5}$$

$$Vm = \frac{1}{\text{Gradient} + \text{intercept}}$$

$$C = \left(\frac{\text{Gradient}}{\text{Intercept}} \right) + 1$$

$$Sa = \frac{Vm\sigma Na}{mv} \text{----- Equation 2.6}$$

where P = pressure, P_o = saturation pressure, Va = volume absorbed, Vm = monolayer volume, C = multilayer adsorption parameter, Sa = surface area, σ = N₂ area (0.162 nm²), N_a = Avogadro number, m = sample mass, v = gas molar volume.

On the other hand, Barrett, Joyner, Halenda (BJH) surface area is calculated from Kelvin equation (**Equation 2.7**). This equation foresees the pressure at which the adsorbate will spontaneously evaporate for a given pore diameter. The equation is as follow:

$$\ln \left(\frac{P}{P_o} \right) = - \left(\frac{2\gamma v \cos \theta}{RT rm} \right) \text{----- Equation 2.7}$$

where P/P_o relative pressure of vapor in equilibrium with condensed gas meniscus; γ = liquid surface tension; v = condense adsorbate molar volume; cos θ = adsorbate surface contact angle (0 for N₂ thus cos θ = 1), R = gas constant; T = temperature and rm = mean radius of condensed gas meniscus.

After 30 years, IUPAC has recently reviewed and renewed the IUPAC manual on the evaluation of surface area and pore size distribution¹⁵. In **Figure 2.6**, the eight new IUPAC classifications of sorption and six hysteresis loops are represented instead of six sorptions and four hysteresis loops¹⁷ that have been used all these while. Detailed explanation about adsorption-desorption isotherms can be found in Thommes *et al.*¹⁵ with the brief explanations are as follows:

Type I: Represents the microporous solid with fairly small external surfaces which normally found in some activated carbon, zeolites or certain porous oxides. *Type I* occurs due to limiting uptake of accessible micropores resulting very low P/P_o micropores filling. *Type Ia* is mainly for narrow micropores (<~1 nm), meanwhile *Type Ib* is basically for a range of pore including wider micropores to possibly narrow mesopores (<~2.5 nm). This type normally found on activated carbon, molecular size zeolites and certain porous oxides).

Type II: Mostly accommodates nonporous or macroporous absorbents resulting from unrestricted monolayer-multilayer adsorption (high P/P_o). The sharp knee at point

B indicates the completion of monolayer coverage. If the shape is more curved (less than point B), this indicates the overlap between monolayer coverage and multilayer adsorption.

Type III: Showing a weak adsorbent-adsorbate interaction, thus no point B is observed. The amount of absorbed is finite at saturation pressure $P/P_0 = 1$. Normally this type is applicable for nonporous or macroporous solid.

Type IV: Resembles the mesoporous adsorbent with the typical type of final saturation plateau. *Type IVa* represents the capillary condensation with hysteresis with pore wider than 4 nm. On the other hand, *Type IVb* is the opposite to *Type IVa* with no hysteresis observed. Somehow the conical and step stairs features are remaining.

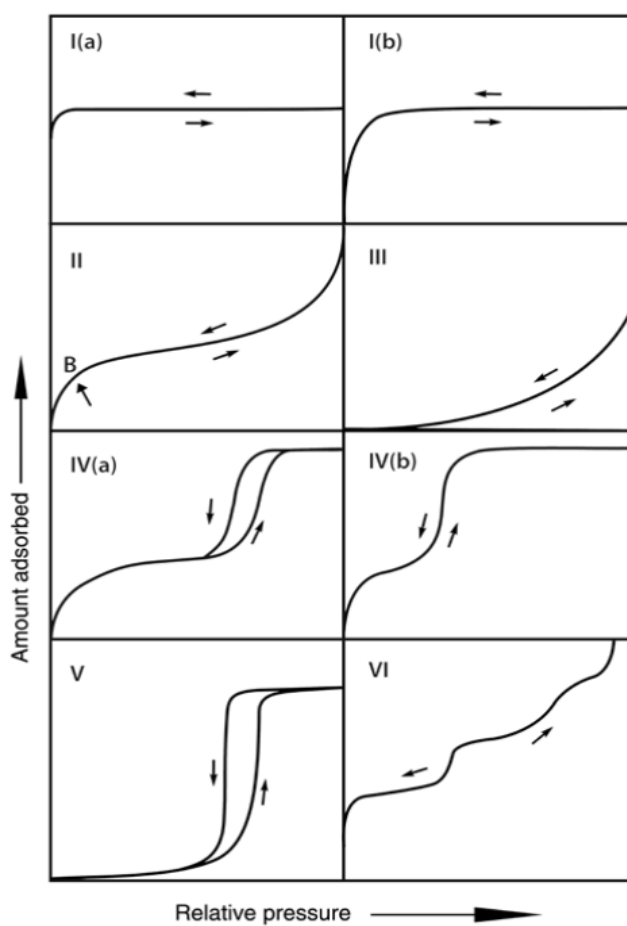


Figure 2.6 New IUPAC classification of physisorption isotherms, published in IUPAC Technical Report on physisorption of gases, with evaluation of surface area and pore size distribution, 2015¹⁵.

Type V: Indicates a weak-fluid wall-interaction which is less common occurred (low P/P_0), but observed in certain porous absorbents¹⁴. At higher P/P_0 , pore filling

happens during molecular clustering. This type is mainly found in water adsorption on hydrophobic micro/mesoporous adsorbents.

Type VI: Represents the layer-by-layer adsorption on highly uniform nonporous surface such as on argon or krypton at low temperature on graphitised carbon blacks. Each absorbed layer capacity is depending on the step-height, meanwhile, the temperature and the systems determined the sharpness of the peak.

Hysteresis loops reference also has been renewed and compiled in the new IUPAC Technical Report, 2015¹⁵ as shown in **Figure 2.7**. The similar types H1, H2(a), H3 and H4 were used and adapted from the original IUPAC Technical Report 1985. New classification involves the addition of H2(b) and H(5). The identification is as follows:

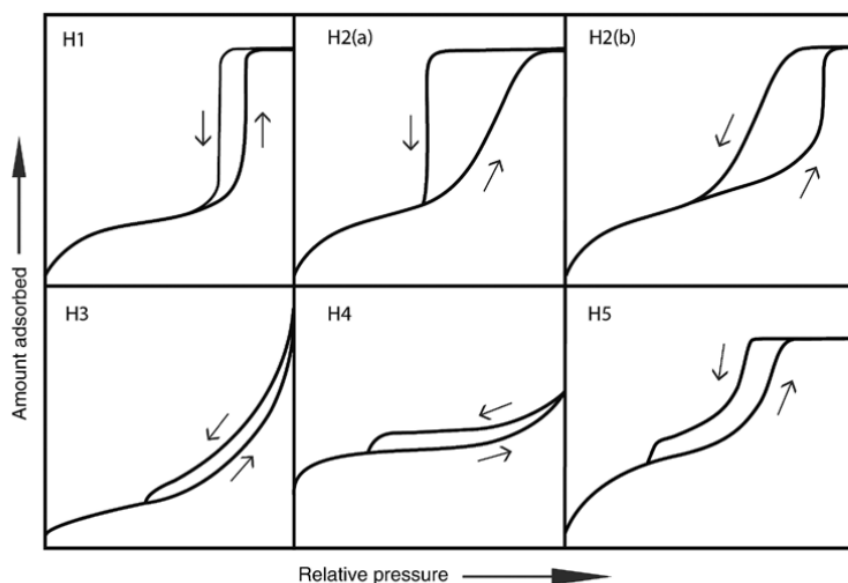


Figure 2.7 IUPAC new classification of hysteresis loop types adapted from IUPAC Technical Report on physisorption of gases, with evaluation of surface area and pore size distribution, 2015¹⁵.

Type H1: Represents the narrow uniform mesopores, indicates the delayed condensation on adsorption branch. It is having similar width size distribution between neck size and pore/ cavity size distribution. This type normally can be found in templated silica, controlled pore glass or mesopores carbons.

Type H2: The steep desorption shape indicates either pore blocking/ percolation in narrow pore necks or to cavitation-induced evaporation.

Type H3: Represents the non-rigid aggregates of plate-like particles or if the pore contains incomplete macropores.

Type H4: Nearly similar to H3 but more in a combination of types I and II, with more uptake P/P_0 associated to micropores filling. This loops normally found in aggregates zeolites and microporous carbon.

Type H5: Unusual loops due to consist both open and partially blocked mesopores.

Pore diameters and pore volumes were further analysed by using DFT method by using the fitting model for N_2 at 77 K on carbon (slit pores, QSDFT equilibrium mode). This fitting model has been chosen because it gave the best fitting with experimental data.

2.2.3 Mercury intrusion

More accurate pore volume and pore diameter analyses were undertaken using Mercury Intrusion Porosimetry with a PoreMaster-60 instrument which generates pressure to 60,000 psia for pore size from >950 microns to 0.0036-micron pore diameter. This instrument is mainly used for pore size and pore volume where it capable to analyse from micropore to macropore size. Apart than that, it also often used to measure distribution, density and other porosity-related analysis¹⁸.

The principle of this analysis is based on the contact angle of mercury which is physically a non-wetting liquid (**Figure 2.8**). Hence, an external pressure needs to be applied in order to force the mercury into the pore. The relationship between the applied pressure and pore diameter is given by the Washburn equation (**Equation 2.8**) as follows:

$$D = (-4\gamma \cos \theta)/P \text{ ----- Equation 2.8}$$

where P is applied pressure, γ is surface tension of the mercury, θ is the contact angle between mercury and solid surface, and D the pore diameter.

Prior to the analysis, samples were evacuated for an hour to remove air and residual moisture¹⁸. Samples were then filled with mercury and voids/pores will be slowly filled by pressure. Each pressure change will reflect the volume of mercury intrudes into the sample, and by that, the volume of mercury is measured by mercury penetrometer. This also will generate the pore size/volume distribution from Weshburn equation.



Figure 2.8 Different contact angle applied on mercury (above) and the external pressure applied by the capillary action to force the mercury into the pores (bottom). The image was obtained from <https://www.intechopen.com/books/high-performance-concrete-technology-and-applications/microstructure-of-concrete>, accessed on Jan 12, 2017.

2.2.4 Electron microscopy

Electron microscopes were developed due to the limitation of light microscopes which only capable for 500x to 2000x magnification. Electron Microscopy (EM) is a remarkably powerful scanning of sample's morphology, especially on nanomaterials¹⁹. By using this electron beam, samples are magnified to 500,000 times, thus revealing the details and complexity of the morphology. This becomes one of the advantages of EM over traditional light microscope (LM) (**Figure 2.9**). The others advantages of EM are listed in **Table 2.1**. EM is a useful technique that provides information such as size, morphology, the texture of material and element composition.



Figure 2.9 The difference between Light Microscopes (LM), Transmission Electron Microscopy (TEM) and Scanning Electron Microscopy (SEM). The image was obtained from <http://www.vcbio.science.ru.nl/en/fesem/info/fesemfaq/>, accessed on Jan 12, 2017.

Table 2.1 Comparison of Light Microscope (LM) with Scanning Electron Microscopy (SEM).

Criteria	Light Microscopy (LM)	Electron Microscopy (EM)
Radiation	Visible light	Electron beams
Magnification	x 2000	x 500 000
Approx. radiation wavelength	400-700 nm	< 1nm
Radiation focus by	Lenses (glass lenses)	Electromagnets
Resolution	200nm	0.2 nm
Preparation of material	Quick and simple	Time consuming
Cost	Relatively cheap	Very expensive

SEM images were recorded at Leeds Electron Microscopy and Spectroscopy Centre using a HITACHI SU8230, a high-performance cold field emission (CFE) SEM with Oxford Instruments Aztec Energy EDX system with 80mm X-Max SDD detector. The electron is recorded using secondary electron (SE) and backscattered electron (BSE) with high resolution as well as nanoscale EDX capabilities. Samples were mounted on aluminum stubs using a thin layer of conductive carbon tape or gold sputter coated to reduce charging. Images were analysed by using ImageJ 1.50d software.

Electron gun will induce the beam towards sample using a thermionic electron to heat up. Once the electron beams hit up the specimen, two types of electron normally come off which known as a secondary electron (SE) and backscattered electron (BSE). In SE mode, atoms absorb energy and give off their own electrons. These electrons mainly covered on shallow surface. They will be captured by a detector in a filament cage that having a positive charge around 300V. The detector will transfer the

information to a computer and translate it into the image. On the other hand, BSE comes from the surface and deeper down of the specimen which then is detected by the second detector.

EDX was used for elemental analysis of the composition of the specimen. In principle, all elements from atomic number 4 (Be) to 92 (U) can be detected under this instrument²⁰. EDX analysis software linked to the SEM with a 30 mm two light element attached to two light elements atmospheric twin window (ATW) detector. Electron beam fired an X-ray radiation on the sample. Energy penetration depth is about 10 μm . Simultaneously, electron beams excited from the ground state and ejected from the atom. Each excited and emitted electron will occupy at different level of energy. The difference between these energy levels will released as an X-ray. Further analysis on this emitted X-ray will provides information on atomic structure of the elements.

Transmission Electron Microscopy (TEM) analysis was carried out using a JEOL 2100F FEG STEM operating (200 keV) at the University of Birmingham. Samples were set by dispersing in methanol and then drop cast onto a copper grid coated with a holey carbon support film (Agar Scientific Ltd). Typically, TEM has an almost similar concept like LM, except TEM incorporates with more lenses and uses electron beams as the main energy source. TEM allows penetration up to the atomic level meanwhile SEM distinguish features a few nanometers in size (further differences between SEM and TEM can be seen in **Table 2.2**).

Table 2.2 Comparison of Scanning Electron Microscopy (SEM) with Transmission Electron Microscopy (TEM).

SEM	TEM
Based on scattered electron	Based on transmitted electrons
Sample can be of any thickness and is mounted on aluminum stub	Specially prepared thin samples are supported on TEM grid
Electron beam scans over surface of specimen	Electron beams passes through thin sample
Focus on surfaces and its composition	Focus on what inside and beyond the surface
2D image	3D image
Max level of magnification = 2 million	Max level of magnification = 50 million

In TEM electron beams are transmitted through the thin sample from a cathode. The beams are then accelerated towards the specimen by the positive anode. Only a small energy range can pass through a thin disk with a small circular through-hole (2-100 μm) so that a well-defined energy is created. Differences in thickness, atomic mass and density are responsible towards the degree of interaction between beam and

samples. The image is generated from the morphology of the specimen, thus also produces the 3D images result.

2.2.5 Diffuse reflectance infrared Fourier transform spectroscopy

The Diffuse Reflectance Infrared Fourier Transform Spectroscopy (DRIFTS) experiments were carried out using a Thermo Scientific Nicolet iS50 FT-IR instrument with Smart Collector accessory. The infrared source of ever-glo mid/near is used and mercury cadmium telluride (MCT-A) photon was cooled by liquid N₂ at -196 °C. Spectra were recorded using OMNIC software. The spectroscopic data provide information about the functional groups at the surface and possible interaction between organic and inorganic parts of the catalysts²¹. A wide wavelength region from 4000 – 400 cm⁻¹ is normally detected by the instrument. Samples are prepared with 10 % of catalyst pressed into dried KBr. The spectra are recorded over a wavelength range from 4000 to 400 cm⁻¹ under 64 scans. Among the advantages of using DRIFTS over conventional transmission (or reflection) FTIR methods are; it involves fast and nondestructive technique, makes it suitable for both powder or as it is sampled and also suitable for strongly absorbing material²¹.

An infrared beam is directed to the sample, it eventually migrates and bounces around the sample before being absorbed and reflected back onto the focusing mirrors (**Figure 2.10**). The spectrum is detected by detector and computer translated it as spectrum results.



Figure 2.10 The schematic principle of how a DRIFTS instrument works. The image was taken from Chen *et al.*²².

2.2.6 Thermal analysis mass spectrometry

Thermal analysis mass spectrometry (TGA-MS) is a powerful approach for the study of the thermal behaviour of solid and liquid samples. A simultaneous TGA/DSC (Differential Scanning Calorimetry) coupled to Mass Spectrometer (MS) was used in this analysis. This interface allows one to characterise and quantify compounds in the off-gas in real-time along with each mass loss²³. Apart than that, it also able to characterise decomposition and thermal stability study, composition studies, to determine purity, humidity, volatile ash and fixed carbon content and also able to identify gasification of carbonaceous sample studies. DSC is used to determine the thermal critical points like melting point, enthalpy specific heat or glass transition temperature of substances. The results of a DSC experiment is presented in a curve of heat flux versus temperature or time. This curve can be used to calculate enthalpies of transition between positive or negative peaks.

The thermoanalytical analysis was undertaken on a Mettler STARe (STA-780 Series) Thermo Gravimetric Analyser in a flowing N₂ atmosphere at a heating rate of 10 °C / min under 30 ml min⁻¹ of N₂ flow. TGA analysis was carried out with the METTLER TOLEDO ultra-micro balance with unique built-in calibration weights to ensure accuracy. To simultaneously follow the evolution of the gaseous decomposition products over the temperature range from room temperature to 800 °C, the thermobalance was connected to Pfeiffer Vacuum high-end mass spectrometer. In this way, the thermogravimetric analysis (TGA) and mass spectrometric (MS) ion intensity curves of the selected ionic species could be recorded simultaneously. The MS quadrupole used is able to measure a wide range of mass or charge ratios (1 to 300).

2.2.7 Temperature-programmed desorption of CO₂

The CO₂ Temperature Programmed Desorption (CO₂-TPD) analysis was performed by using Quantachrome ChemBET 3000. CO₂ pulse chemisorption was run followed by temperature programmed desorption (TPD) analysis to study the basicity of hydrotalcite/solid base samples. To prepare the sample, approximately 50 mg of catalyst was placed into quartz chemisorption cell plugged with quartz wool and was degassed for 1 hour under He gas at 120 °C. The sample was then let cool until the temperature dropped to 40 °C. Then CO₂ was pulse titrated in 50 µL doses until three consecutive saturated same height peaks are obtained. The counts were recorded. The sample then was heated to 700 °C (for hydrotalcite) and up to 900 °C (for commercial catalyst) at 10 °C min⁻¹. The amount of CO₂ absorbed then can be determined.

2.2.8 Solid-state NMR spectroscopy

Solid-state NMR spectra were obtained at the EPSRC UK National Solid-state NMR Service, Durham University. The spectra were recorded on Varian VNMRs spectrometer with a 9.4 T magnet. This is a “three-channel” (HXY) instrument with two magic-angle spinning probes. These differ in rotor size (4 and 6 mm) but are otherwise generally similar: both can operate over a temperature range of around -80 to +180 °C and have three RF channels (but can operate in either double- or triple-resonance mode). The available sample space is 52 or 242 µl for the 4 and 6 mm rotors, respectively. The maximum spin rates are 14 kHz for the 4 mm rotors and 7 kHz for the 6 mm. In the triple-resonance mode, the probes can be configured to work with any XY pair of nuclei providing their resonance frequencies are separated by 20 MHz or more. In the solid-state ^1H is a special case and does not give high-resolution spectra (in the same sense that ^{13}C does, for example). However, it can yield useful physical information through its relaxation behaviour.

2.2.9 Inductive coupled plasma-Optical emission spectrometry

Inductive Coupled Plasma-Optical Emission Spectrometry (ICP-OES) is another multi-elemental analysis technique that used plasma source to dissociate the sample into its constituent atoms or ions, then exciting them to a level where they emit light of a characteristic wavelength. This elemental analysis has been performed on Thermo Scientific iCAP 7000 Series ICP OES Spectrometer. Illustration of ICP schematic diagram is shown in **Figure 2.11**.

The sample was prepared according to the Environmental Protecting Agency (EPA) Standard Operating Procedure²⁴. In order to digest the solid sample, 10 mg of the catalyst was mixed with 100 mg of ammonium fluoride with precaution taken. Then the mixture was diluted with 5 ml of HNO_3 , 1 ml of H_2SO_4 and 4 ml of deionised water (Solution 1). Once this solution was completely dissolved, 1 ml of boric acid has been added to remove hydrogen fluoride that formed from the reaction of ammonium fluoride with acid. Then, in an autosampler tube, 1ml of this solution 1 was added with 9 ml of deionised water.

A series of calibration standards were prepared as follows:

- 1) Nitric acid solution was prepared by adding nitric acid to water (1:1 ratio) (Solution 2).

- 2) 9ml of Solution 2 was added to 1 ml of Zn standard solution to make up a 1000 ppm of stock solution
- 3) An acid digestion solution was prepared by adding nitric acid, boric acid, and sulphuric acid to water.
- 4) To dilute the stock solution to 100 ppm, the mixture was added with 1ml of Ni standard, 1 ml of Al standard solution, 1 ml of Mg standard and 6ml of stock solution in an autosampler tube.
- 5) This solution then was further diluted to 50 ppm, 10 ppm, 5 ppm and 1 ppm respectively.

Using the autosampler, sample (in liquid form) is delivered to the nebuliser via a peristaltic pump. On approaching nebuliser, the sample is converted to a mist or finely droplet called aerosol. The sample is sucked into the capillary tube by a high-pressure stream of Argon gas flowing around the tip of the tube. This pressure breaks the liquid into fine droplets in various sizes in the spray chamber. The spray chamber is prompt to select the finest droplet of mist and the large droplets must be pumped away. Technically, around 3 % of the droplets are allowed to reach the plasma and the remaining samples went to waste bottle²⁵. Simultaneously, the mist will be dried by heat from the torch and been induced by plasma. Decomposition happened and excitation of elements will take place. The excited atom leads to photon emission and ionisation. The emitted radiation from the plasma is then transmitted to the spectrometer and data output will be interpreted by a computer.



Figure 2.11 Schematic diagram of how ICP operates. Source: <http://www.spectroscopyonline.com/approaches-maximize-performance-and-reduce-frequency-routine-maintenance-icp-ms>, retrieved on Jan 12, 2017.

2.2.10 X-ray photoelectron spectroscopy

Surface compositions were investigated using X-ray photoelectron spectroscopy (XPS) using a Kratos Axis Hsi X-ray photoelectron spectrometer. This instrument is fitted with charge neutraliser and magnetic focusing lens employing Al K α monochromated radiation (1486.6 eV). Spectra were processed in CasaXPS version 2.3.15 software. Binding energies were corrected using adventitious carbon at 284.6 eV. The X-ray source of MgK α (1253.6 eV) or AlK α (1486.3 eV) anode is routinely employed on due to their low kinetic energy roughly in a range of 0-1 keV²⁶. A set of relative sensitivity factors (R.S.F) is necessary for all elements, where the sensitivity factors are designed to scale in the measured areas using CasaXPS so that meaningful atomic concentrations can be obtained, regardless of the peak chosen. **Table 2.3** summarised the R.S.F value used in this study.

Table 2.3 Relative sensitivity factor (R.S.F) and the main peak value for the element used in this study.

Spectra	Relative sensitivity factor (R.S.F)	Corrected area / main peak value (eV)
C 1s	0.318	284.6
Al 2p	0.257	74.5
O 1s	0.736	532
Mg 2p	0.168	50.0
Mg 2s	0.525	90.1
Ni 2p	3.845	854.6, 873
Zn 2p	4.81	1022, 1045
Ca 2p	1.95	347

XPS is a sensitive surface spectroscopy technique used to investigate the elemental composition, chemical state, electronic state and an empirical formula of the element²⁶. XPS mainly used to study the surface chemistry of material either at the precursor or after treatment state. XPS can detect most elements in periodic table but is not easily able to detect H₂ and He. Principally, XPS is a photoelectric energy based technique. XPS detects only those electrons that have actually escaped from the sample into the vacuum of the instrument, and reach the detector. As an X-ray electron is absorbed with binding energy onto the core or a valence energy, the photoelectron is emitted with kinetic energy, as can be seen in **Figure 2.12** and calculated using the following **Equation 2.9** below.

$$E_k = h\nu - E_b - \phi \text{ ----- Equation 2.9}$$

where E_k is the kinetic energy of photoelectron, h is Planck's constant, ν is frequency of the exciting radiation, E_b is the binding energy of photoelectrons with respect to the Fermi level and ϕ is the work function of the spectrometer.



Figure 2.12 Schematic depiction of photoionisation involved in XPS. Accessed on Jan 27, 2017 from http://wikiwand.com/en/X-ray_photoelectron_spectroscopy.

Photoelectron exhibits the spectrum due to it being highly ejected after leaving the core level with created a hole in the outer shell by the binding energy²⁶. This phenomenon creates a transition excited state. The second level electron will fill up the hole and creates another hole on that level and this process will continue up to the most inner shell which in the end produces Auger electron. The Auger electron can easily be recognised by comparing between two energies; i.e the same binding energy can be expected from the XPS peak, but not from the Auger electron. Auger peaks are reported to be shifted to binding energy scale²⁶. Further information about Auger electron is illustrated in **Figure 2.13**.



Figure 2.13 Illustration of how Auger electron is exhibited from the inner shell hole created by the left excited binding energy. The image was obtained from <https://wiki.utep.edu/pages/viewpage.action?pagelId=39194437>, accessed on Jan 26, 2017.

2.3 Catalytic studies

2.3.1 Transesterification reaction of conventional LDH

2.3.1.1 Tributyrin (C₄)

Transesterification of hydrotalcite base catalysts was carried out with tributyrin (C₄) by using a Radley's Starfish reactor. In a three necks flask, using a micropipette, 10 mmol of tributyrin (2.93 cm³) has been added to 308 mmol (12.5 ml) methanol with 0.0025 mol (0.59 cm³) dihexyl ether. At t=0, 0.15 cm³ samples are withdrawn and analysed by Gas Chromatography-Flame Ionization Detector (GC-FID). Then, 50 mg of the catalyst has been added and the mixture was stirred at 650 rpm, 65 °C for 24 hours. Periodic sampling was done and analysed by offline GC to generate reaction profiles.

In transesterification reaction, triglycerides are converted to fatty acid methyl ester (FAME). The conversion, selectivity, yield and turn of frequency (TOF) are calculated as follows:

Conversion

$$= \frac{\text{Concentration of TAG at } T_0 \text{ (moles)} - \text{Concentration of TAG at } T_1 \text{ (moles)}}{\text{Concentration of TAG at } T_0 \text{ (moles)}} \times 100$$

$$\text{Selectivity} = \frac{\text{Concentration of product formed (moles)}}{\text{Total product concentration (moles)}} \times 100$$

$$\text{Yield} = \text{Selectivity} \times \text{Conversion}$$

$$\text{Turn over frequency (TOF)} = \frac{\text{Initial rates (mmolg}^{-1}\text{min}^{-1})}{\text{Number of active sites (mmolg}^{-1})}$$

2.3.1.2 Transesterification of bulkier triglycerides (C₈-C₁₈) at higher temperature

Bulkier TAG needs the higher temperature in order to avoid mass-transport limitation during transesterification reaction. For this purpose, an ACE® pressure flask has been used (**Figure 2.23**). Condition parameter and stoichiometry of reactant were

maintained as before, except the reaction temperature was increased to 110 °C. 10 mmol of bulkier TAG (C8-C18) was added to an ACE® glass pressure flask, along with methanol (12.5 mL) and 0.0025 mol dihexyl ether (0.59 cm³, Aldrich 97 %) as an internal standard. 20 wt% butanol was added to aid the solubility of triglycerides. The reaction mixture was magnetically stirred at 650 rpm. A t=0 sample (0.15 cm³) was removed before catalyst addition and analysed by GC. To ensure a good series of reaction is obtained, we also tested transesterification reaction under C₄ in the pressure flask bottle.

Trilaurin (C₁₂) is in solid powder form, and normally faces the sampling issue (solidifies after 2-3 sampling). To circumvent this, an autoclave with sampling valve on the hot plate was used where the mixtures are more immersed and sampling will be much convenient. To make sure the autoclave is well tightening, nitrogen and snoop leak test have been beforehand. This test is run each time before reaction takes place until no leaking was found.

2.3.1.3 Transesterification of macroporous LDH

In transesterification reaction of macroporous LDH, most reaction conditions remain the same except reactions have been done at 110 °C in pressure flask (to be standardised for bulkier TAG) with 100 mg of catalyst.

2.3.2 Preparation of calibration standards

As calibration is such a common and important step in any analytical methods, it is essential that analysts have a good understanding of how to set up calibration experiments and how to evaluate the results obtained. There are few things need to be considered when preparing calibration curves such as; the number of calibration standards, the concentration of each of the calibration standards, the number of replicates at each concentration and preparation of the calibration standards²⁷.

Firstly, the concentration of TAG and internal standard (dihexyl ether) is calculated. Then, in 10 ml volumetric flask, a standard Solution 1 contains an absolute concentration of TAG, FAME and glycerol were added. DCM is added to mark up the volume to 10 ml. Solution 2 was prepared by adding an absolute concentration of internal standard (dihexyl ether) and DCM to 100 ml. The concentration of solution 1 is diluted from 100 % to 3.125 % in the different vial (1 to 6). In each vial (except 100 %), 5 ml of solution 1 is added with 5 ml of the Solution 2. This dilution concentration then is injected

to GC-FID. It is necessary to construct calibration curves for each component. The linearity of all calibration curves was determined with satisfactory ($R^2 \geq 0.99$).

2.3.3 Gas chromatography-flame ionisation detector

The TAG conversion and FAME formation were followed by analysis of the aliquots using a Shimadzu Gas Chromatography fitted with a flame ionisation detector (FID). Aliquots were periodically withdrawn from the flask and filtered before being added with dichloromethane (DCM) to 1.6 cm³ in a GC vial. Samples have then been injected to Shimadzu GC-2010 Plus (Japan) equipped with an autosampler and Zb-50 capillary column (30 m x 0.32 mm x 0.25 µm). Conversion, yields, initial rates and turnover frequency (TOF) have been determined from the chromatogram results. Initial rates were calculated from the linear portion of the conversion profile during the first 60 min of the reaction. Turnover frequencies (TOFs) were determined by normalising rates to the base site density.

2.3.4 Gas chromatography-mass spectrometry

Identification of components in the chromatogram has been done using Gas Chromatography-Mass Spectrometry (GC-MS) using FactorFour capillary column VF-5ms (30 m x 0.25 mm x 0.25 µm). The product, molecular weight and retention time obtained from MS were checked and matched with NIST Library. ASTM D-6584 was applied to determine the concentration of monobutylin, dibutylin, tributyrin and glycerol in samples.

2.3.5 On-column gas chromatography for bulkier triglycerides

The TAG conversion and FAME formation were followed by analysis of the aliquots using a Varian 450 GC fitted with a flame ionisation detector (FID) and an 8400 autosampler via on-column injection on a CP-sim disc wide-bore column ZB-1HT (15 m x 0.53 mm i.d. and 0.1 µm) with temperature programmed injector.

2.3.6 Leaching & reusability study of LDH and commercial catalysts

2.3.6.1 Leaching study

Substrates were prepared as usual except the amount has been double up; 4.98 ml tributyrin, 24.28 ml methanol, 1.18 ml dihexyl ether and 100 mg catalyst. Condition parameter of transesterification reaction was kept similar as before. After 180 minutes of reaction, the catalyst was taken out, filtered and washed with methanol. The supernatant liquid continued reacting until 24 hours. The supernatant liquid was measured under ICP at T0 and T24 h after the reaction.

2.3.6.2 Reusability study

In this reusability study, transesterification of tributyrin (C₄) was run by adding the amount of the solvent and catalyst to four times; 9.96 ml tributyrin, 48.6 ml methanol, 2.36 ml dihexyl ether and 200 mg of catalyst. The reaction was done at the same condition parameter as described before. After the 24 hours of reaction, the catalyst was filtered, washed with methanol, and dried at 80 °C. The catalyst was examined under XRD before resumed in the next reaction. The catalyst was calcined at 300 °C and rehydrated under hydrothermal beforehand. The final cycle of catalyst was analysed under XRD, ICP and CO₂-TPD.

2.4 List of chemicals used

Chemicals used	Supplier
Magnesium(II) nitrate hexahydrate	Sigma-Aldrich, ACS reagent, 99 %
Nickel(II) nitrate hexahydrate	Sigma-Aldrich, puriss. p.a., ≥98.5 %
Zinc(II) nitrate hexahydrate	Sigma-Aldrich, reagent grade, 98 %
Aluminium nitrate nonahydrate	Sigma-Aldrich ACS reagent ≥ 98 %
Ammonium carbonate	Sigma-Aldrich ACS reagent ≥ 30 % NH ₃ basis
Ammonium hydroxide solution	Sigma-Aldrich ACS reagent 28.0-30.0 % NH ₃
Dihexyl ether	Sigma-Aldrich, 97 % (Aldrich)
Glyceryl tributyrate (Tributyrin)	Sigma-Aldrich, >99 %
Methyl butyrate	Sigma-Aldrich, 99 %
Monobutyrin	Aldrich
Dibutyrin	Sigma-Aldrich

Glyceryl trioctanoate (Tricaprylin)	Sigma, >99 %
Methyl caprylate	Sigma Aldrich
Monocaprylin	Sigma Aldrich
Dicaprylin	Sigma Aldrich
Trilaurin	Alfa Aesar
Triolein	Alfa Aesar
Monoolein	Sigma-Aldrich, > 99 %
Dichloromethane	Sigma-Aldrich

2.5 References

- (1) Cantrell, D. G.; Gillie, L. J.; Lee, A. F.; Wilson, K. *Appl. Catal. A Gen.* **2005**, 287 (2), 183–190.
- (2) Woodford, J. J.; Dacquin, J.-P.; Wilson, K.; Lee, A. F. *Energy Environ. Sci.* **2012**, 5 (3), 6145.
- (3) Vaudreuil, S.; Bousmina, M.; Kaliaguine, S.; Bonneviot, L. *Adv. Mater.* **2001**, 13, 1310.
- (4) Géraud, E.; Prévot, V.; Leroux, F. *J. Phys. Chem. Solids* **2006**, 67 (5–6), 903–908.
- (5) Debecker, D. P.; Gaigneaux, E. M.; Busca, G. *Chem. – A Eur. J.* **2009**, 15 (16), 3920–3935.
- (6) Krumeick, F. Properties of electrons, their interactions with matter and applications in electron microscopy. www.microscopy.ethz.ch (accessed Jan 13, 2017).
- (7) Pramod K. Sahu, Praveen K. Sahu, S. K. G. and D. D. A. *Catal. Sci. Technol.* **2013**, 3, 1520.
- (8) Hammond, C. *The basics of crystallography and diffraction*, Fourth ed.; Oxford Oxford University Press, 2015.
- (9) F. Cavani, F. Trifiro, A. V. *Catal. Today* **1991**, 2, 173–301.
- (10) Jairo Tronto, Ana Cláudia Bordonal, Z. N. and J. B.; Valim. In *Materials Science - Advanced Topics*; Intech, 2013.
- (11) Guo, X.; Li, S.; Hou, W.; Han, S.; Hu, J.; Li, D. *Chem. Res. Chinese Univ.* **2003**, 19 (2), 211–215.
- (12) J. E. Huheey E. A. Keiter R. L. Keiter. *Inorganic Chemistry: Principles of Structure and Reactivity*, 1993.
- (13) Patterson, A. L. *Phys. Rev.* **1939**, 56 (10), 978–982.
- (14) S. Lowell, Joan E. Shields, Martin A. Thomas, M. T. *Characterization of Porous Solids and Powders: Surface Area, Pore Size and Density*; Springer Netherlands, 2004.
- (15) Thommes, M.; Kaneko, K.; Neimark, A. V.; Olivier, J. P.; Rodriguez-Reinoso, F.; Rouquerol, J.; Sing, K. S. W. *Physisorption of gases, with special reference to the evaluation of surface area and pore size distribution (IUPAC Technical Report)*; 2015; Vol. 87.
- (16) Quantachrome instruments. Nova Series: High-speed surface area and pore size analysers http://www.quantachrome.com/gassorption/nova_series.html (accessed Sep 23, 2014).
- (17) Sing, K. S. W.; Everett, D. H.; Haul, R. a. W.; Moscou, L.; Pierotti, R. a.; Rouquérol, J.; Siemieniowska, T. *Pure Appl. Chem.* **1982**, 54 (11), 2201–2218.
- (18) Giesche, H. *Part. Part. Syst. Charact.* **2006**, 23 (1), 9–19.
- (19) Suga, M.; Asahina, S.; Sakuda, Y.; Kazumori, H.; Nishiyama, H.; Nokuo, T.;

- Alfredsson, V.; Kjellman, T.; Stevens, S. M.; Cho, H. S.; Cho, M.; Han, L.; Che, S.; Anderson, M. W.; Schüth, F.; Deng, H.; Yaghi, O. M.; Liu, Z.; Jeong, H. Y.; Stein, A.; Sakamoto, K.; Ryoo, R.; Terasaki, O. *Prog. Solid State Chem.* **2014**, *42* (1–2), 1–21.
- (20) University of California. *Introduction to Energy Dispersive X-ray Spectrometry (EDS)*; 2015.
- (21) Accardo, G.; Cioffi, R.; Colangelo, F.; d'Angelo, R.; De Stefano, L.; Paglietti, F. *Materials (Basel)*. **2014**, *7* (Lcm), 457–470.
- (22) Chen, Y.; Zou, C.; Mastalerz, M.; Hu, S.; Gasaway, C.; Tao, X. *Int. J. Mol. Sci.* **2015**, *16* (12), 30223–30250.
- (23) Basalik, T. *Am. Lab.* **2005**, *37* (1), 24–27.
- (24) Environmental Protection Agency (EPA). Standard Operating Procedures: Determination of Metals By Inductively Coupled Plasma (ICP). EPA/SW-846 Methods 3015/3050B/6010B, 2006.
- (25) Thermo Elemental. *An elementary overview of elemental analysis*; 2001.
- (26) Chorkendorff, I, Niemantsverdriet, J. *Concepts of Modern Catalysis and Kinetics*, 2nd ed.; WILEY-VCH Verlag, 2015.
- (27) Prichard, L.; Barwick, V. Preparation of Calibration Curves A Guide to Best Practice Contact Point, 2003, *1*, 27.

Chapter 3

***Alkali-Free ZnAl
Hydrothermal
Reconstructed
Layered Double
Hydroxides***

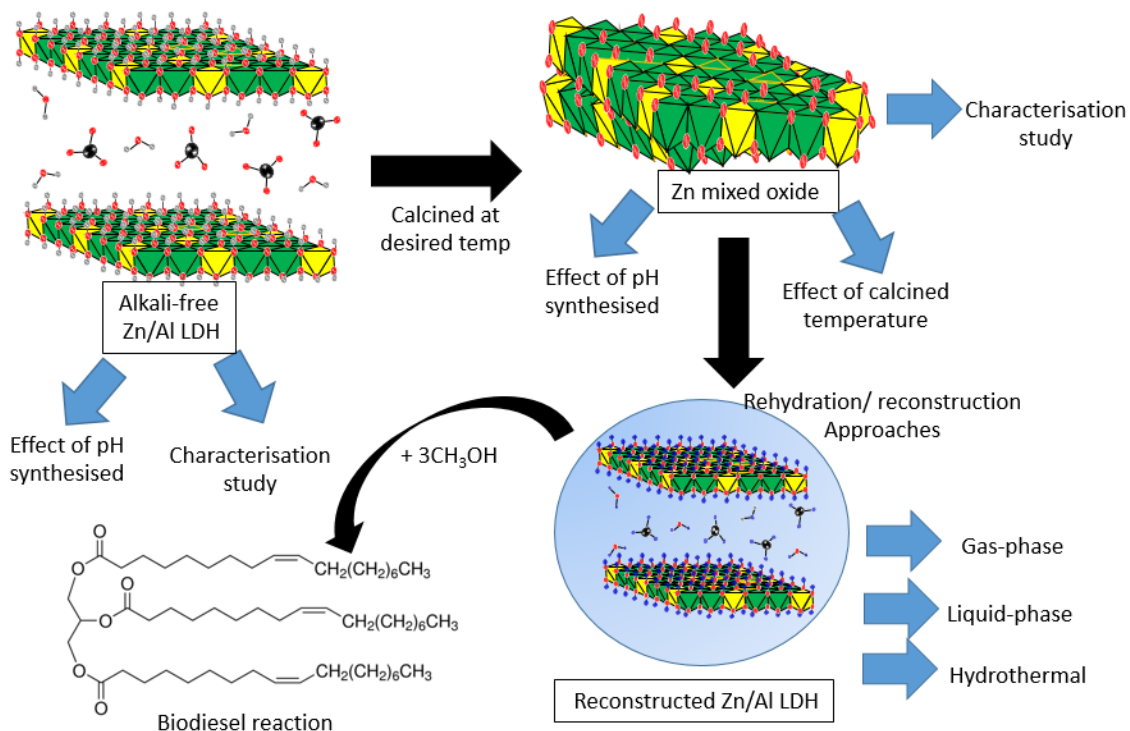
3.1 Introduction

Research on layered double hydroxides has attracted much interest over the years, with the applications have included waste water treatment^{1,2}, biomass conversion^{3–5}, photocatalytic activities^{6–8} and much more. Traditionally, research has focussed on MgAl HT, but recently a great deal of research has been performed into incorporating alternative metals into LDHs, including zinc^{2,8,9}, lithium¹⁰, chromium^{2,9,11,12}, iron¹³, calcium^{14,15}, gallium¹⁶, nickel^{17–19}, cobalt^{20,21}, manganese^{22–25} and copper⁴.

Recently, Liu *et al.*²⁶ reported on the nature strength basic site of calcined ZnAl layered double hydroxides (LDH) which later were applied in the transesterification of soybean oil in a fixed bed reactor. The yield obtained was approximately 76 % with no deactivation found after 150 h. Another study on Zr incorporated ZnAl LDH which was also on the calcined phase,²⁷ demonstrated that incorporation of Zr on the bulk ZnAl LDH surface led to an increased pore diameter up to 10.6 nm. Additionally, the catalyst basicity was also improved which enhanced the performance in soybean transesterification to 91.7 %. These two studies confirmed ZnAl LDH possesses basic properties suitable for transesterification reactions. In another recent publication by Meng *et al.*²⁸ the synthesis of a novel ZnAl LDH material from Zn(OH)₂ was described using a co-precipitation method. The characterisation of the material was however only on the fresh precursor, and no catalytic performance has been reported.

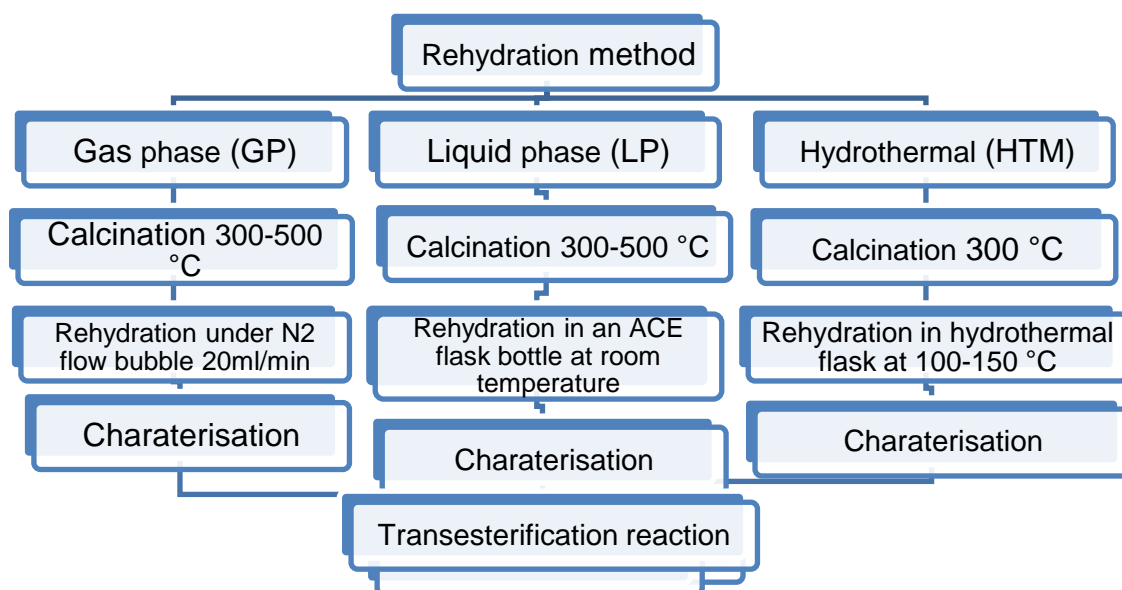
One limitation of the LDH catalysts reported is that they are still prepared using a NaOH precipitation method, which has a severe limitation due to the presence of residual alkali on the catalyst which would leach during liquid phase reactions, potentially contaminating biodiesel and harming the environment at the same time^{26–28}. As explained in sub-chapter 1.4.3.1, traces of sodium must be avoided in hydrotalcite synthesis especially if the catalyst will be applied in the transesterification reaction. To overcome this drawback, in this chapter the synthesis and catalytic application of alkali-free ZnAl LDH is described. To our knowledge, no previous work has been reported on the reconstruction of ZnAl LDH via a green alkali-free co-precipitation method, especially via hydrothermal reconstruction approaches.

A detailed study of the precursor decomposition and reconstruction conditions have been undertaken to explore the effect of precursor to calcination and rehydration conditions via hydrothermal treatment (**Scheme 3.1**). The resulting hydrotalcite was tested in the transesterification of triglycerides (TAGs) with varying chain lengths to form fatty acid methyl ester (FAME).



Scheme 3.1 Scope of this study involving different layer alterations via different $\text{Zn}^{2+}/\text{Al}^{3+}$ ratio which involved in calcination, hydrothermal reconstruction and later being adopted in transesterification reaction of triglycerides.

Three different rehydration/reconstruction routes known as gas-phase (GP), liquid-phase (LP) and hydrothermal phase (HTM) will be investigated (**Scheme 3.2**). In addition, the effect of synthesising the ZnAl LDH precursor at different pH was explored to assess the appropriate pH for the preparation of ZnAl LDH with a high surface area and uniform crystallinity of hydrotalcite. Secondly, the impact of calcination temperature on morphology, crystallinity, surface area and basicity were also thoroughly explored. The effect of rehydration/reconstruction approaches on the final properties of the material and performance in the transesterification of TAGs with C4-C18 alkyl chain lengths is finally investigated.



Scheme 3.2 Rehydration approaches on ZnAl LDH synthesised via the alkali-free method.

3.2 Novelty and contribution to knowledge

Alkali-free ZnAl LDHs were prepared for the first time and later were subject to different rehydration methods; gas-phase, liquid-phase and hydrothermal. A detailed study of the effect of chain length of TAGs on catalytic transesterification activity was undertaken to assess the impact of active site accessibility with increasing bulkiness of the reactant.

3.3 Aim

The major objective of this work is to examine the factors influencing reconstruction of ZnAl LDH. The principal question concerns whether hydrothermal reconstruction methods are feasible or not and how efficient its catalytic performance in application to transesterification of triglycerides chains.

3.4 Results and discussion

A series of conventional layer double hydroxides with nominal Zn:Al ratios varying from 1.5:1 to 4:1 were prepared via an alkali-free co-precipitation method developed by Cantrell and co-workers²⁹ which have to date only been applied to MgAl HT systems. The properties of LDH strictly depend on the synthesis method used,³⁰ hence the effect of synthesised pH, calcination temperature and reconstruction approaches will be discussed thoroughly.

3.4.1 Characterisation of ZnAl precursor

3.4.1.1 Energy dispersive X-Ray spectroscopy

The successful incorporation of Zn and Al within the layered double hydroxides materials of $[\text{Zn}_{(1-x)}\text{Al}_x(\text{OH})_2]^{x+}(\text{CO}_3)_{x/n}^{2-}$ at pH 9 and 10 was first verified by energy dispersive X-Ray (EDX) spectroscopy. The Zn:Al atomic ratio of the hydrotalcites prepared are shown in **Table 3.1**. The results demonstrate there is a progressive increase in Zn:Al ratio across the family of materials, even though the experimentally determined bulk ratio of Zn:Al is slightly lower than the target ratio. This suggests a lower rate of Zn incorporation compared to Al. However as Zn:Al atomic ratio is increased during synthesis, the bulk ratio is decreased³¹. ZnAl LDH prepared at pH 9 showed a lower actual ratio compared to materials prepared at pH 10 suggesting that at pH 10 the incorporation of Zn and Al metal are more favourable and this is correlated with the optimum pH condition³².

Table 3.1 The nominal and actual bulk of ZnAl HT atomic ratio synthesised at pH 9 and 10.

Nominal atomic Zn:Al ratio	Zn wt% bulk (EDX)	Al wt% bulk (EDX)	Bulk atomic Zn:Al ratio	$x=(\text{Al}/\text{Al}+\text{Zn})$
1.5:1 pH 9	22.8	10.6	0.9	0.5
2:1 pH 9	21.9	6.0	1.5	0.4
3:1 pH 9	28.5	15.2	2.1	0.3
4:1 pH 9	66.2	8.6	3.2	0.2
1.5:1 pH 10	30.9	8.0	1.6	0.4
2:1 pH 10	32.3	6.7	2.0	0.3
3:1 pH 10	33.5	4.6	3.0	0.3
4:1 pH 10	44.2	3.5	3.3	0.2

As discussed in sub-chapter 1.4.3.2, the x value must be in a range of $0.2 < x < 0.33$ ³³. Outside these limit, it would trigger the formation of divalent and trivalent metal hydroxides (i.e. $\text{Al}(\text{OH})_3$) for lower and higher x value, respectively, which they are undetectable by XRD³⁴. Results in the table below revealed at the nominal ratio of 1.5:1 (for both synthesised pH), the x value was outside the limit of $0.2 < x < 0.33$. This could be contributing to the less crystalline structure of HT, which will be confirmed and discussed later under XRD characterisation (sub-chapter 3.4.1.3). The EDX spectrum also revealed the existence of Zn, Al, and O atoms as can be seen in **Figure 3.1**. EDX revealed the main elements and in the image presented, no alkali is present in this sample further confirming this method was alkali-free. Most of the elements detected are expected to be in ZnAl LDH except Cu was detected, potentially as an impurity from the

chemicals used, or due to background fitting errors. Nevertheless, this should be disregarded as the amount is negligible.

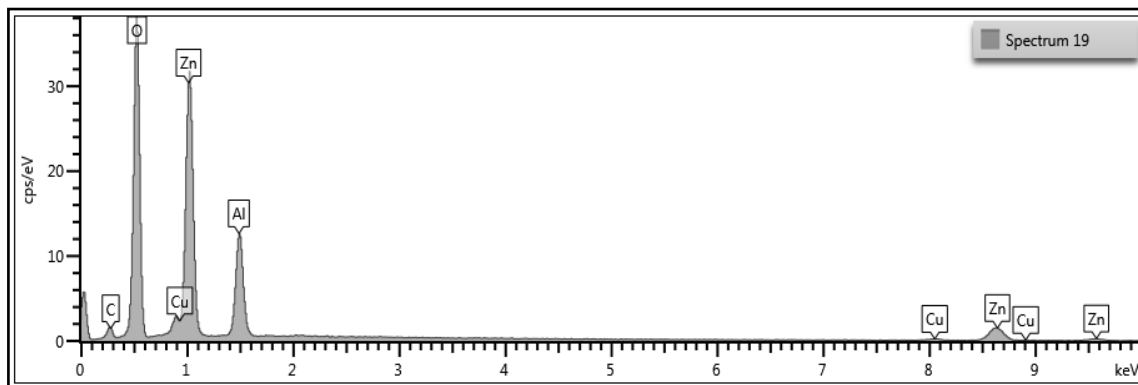


Figure 3.1 EDX spectrum of Zn:Al3:1 LDH precursor prepared at pH10.

3.4.1.2 Thermogravimetric analysis-mass spectrometry

Thermogravimetric Analysis-Mass spectrometry (TGA-MS) of samples was conducted to investigate the thermal decompositions of ZnAl LDH and to quantify the H₂O and CO₃²⁻ present in the materials (**Figure 3.2**). The MS curve of H₂O ($m/z = 18$) confirmed the water is lost in two major steps. The first transition associated with loss of water (dehydration) interlayer occurred up to 185 °C. The second transition is due to loss of remaining water that occurs up to 290 °C, and coincides with the evolution of CO₂. Decomposition and dehydroxylation/decarboxylation occurred over the temperature range 219-340 °C, when the brucite-like layers start to collapse⁸ and interlayer CO₃²⁻ decomposed to yield CO₂. The observed evolution of CO₂ ($m/z = 44$) is in the range 250-300 °C which is in agreement with the literatures^{8,26,27}. The decarboxylation temperature also affected by the amount of CO₂ gas present in the compound³⁵. This finding has important implications for choosing the right calcination temperature before proceeding with rehydration/reconstruction procedures. Effect of basicity and the functional group will be explained later.

The general formula for HTs; $[M(II)_{1-x}M(III)_x(OH)_2]^{x+}(A^{n-})_{x/n} \cdot mH_2O$ where $m = 0.81 - x$, has been applied in order to calculate the theoretical and experimental weight loss³⁶ as can be seen in **Table 3.2**. The ZnAl LDH compositional formula also has been obtained from a combination of this analysis and EDX. Zn, Al, OH and CO₃ composition were calculated from atomic percent from EDX, with the H₂O composition obtained from percentage weight loss obtained from TGA-MS over 49-340 °C attributed to water. As the Zn:Al atomic ratio increases, the amount of H₂O in the interlayer is found to increase.

Meanwhile, the number of carbonates deposited on the interlayer diminishes as the Zn:Al ratio increases. In general, the total weight loss of both pH in experimental and theoretical value are comparable. Apart from that, this also proved the synthesis of pH plays an important role in the chemical composition of the material formed.

Differential Scanning Calorimetry (DSC) profiles of Zn:Al_{3.31}:1 LDH prepared at pH 9 and 10 showed two heat flow steps at 45 °C and 190 °C which are attributed to the absorbed water and dehydroxylation of water in the interlayer. Another heat flow was observed at 250 °C is attributed to the loss of carbon dioxide from the interlayer anion.

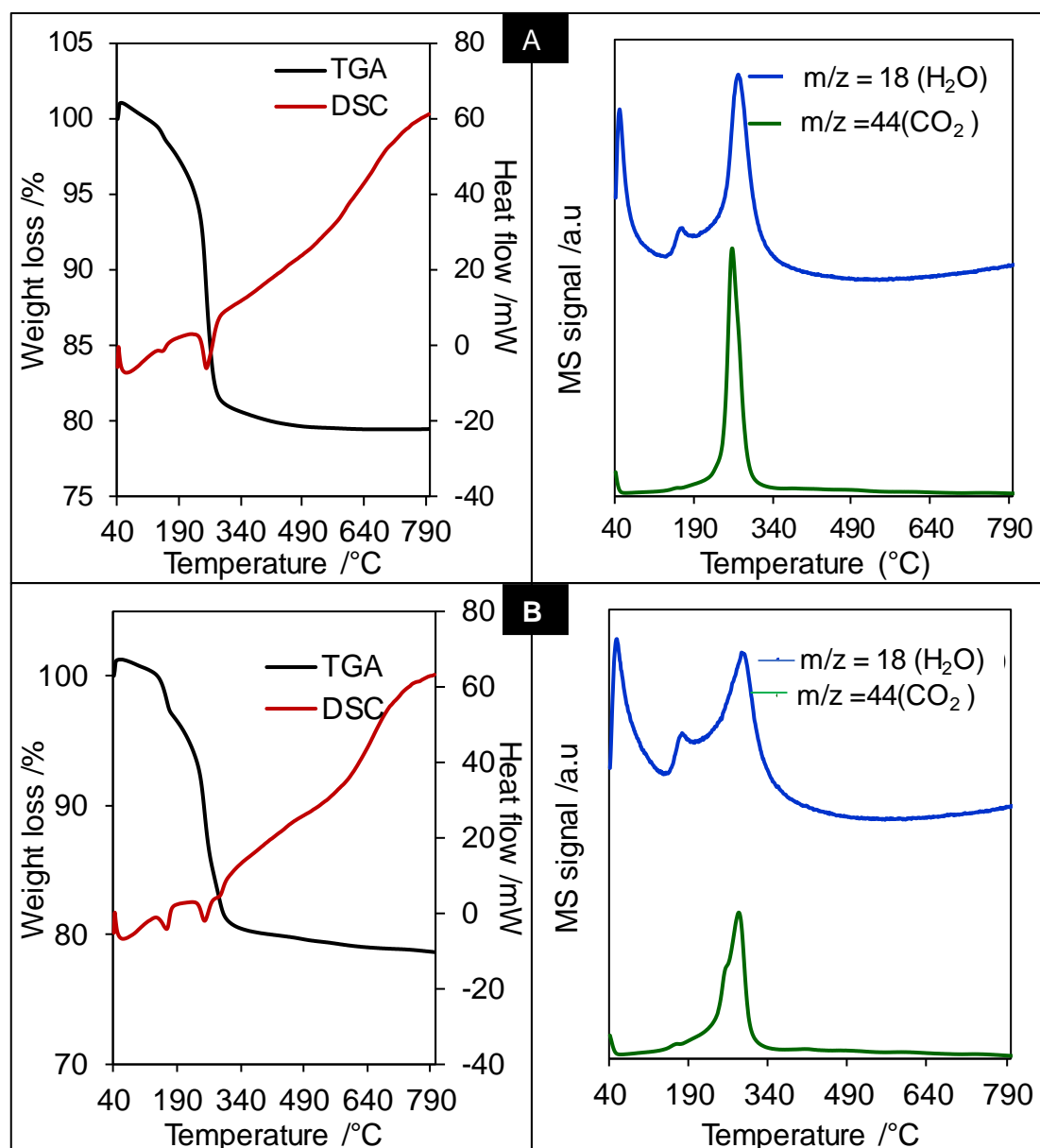


Figure 3.2 TGA/DSC with MS profiles during decomposition of Zn:Al_{3.33}:1 LDH in N₂ at 10 °C min from 40-800 °C. Figure A represents ZnAl LDH synthesised at pH 9 and B represent pH 10.

Table 3.2 Experimental and theoretical weight loss and the ZnAl LDH formula as obtained from TGA-MS and EDX.

Experimental Weight loss / %				Theoretical weight loss / %			ZnAl LDH Formula
LDH catalyst/ weight loss	H ₂ O exp	CO ₃ exp	Total Weight loss/ %	H ₂ O theory	CO ₃ theory	Total Weight loss / %	
<i>pH 9</i>							
Zn:Al0.89:1AS	14.2	10.1	24.3	5.0	16.2	21.2	[Zn _{0.47} Al _{0.53} (OH) ₂].(CO ₃) _{0.27} 0.28H ₂ O
Zn:Al1.50:1AS	13.2	10.1	23.3	7.4	12	19.4	[Zn _{0.60} Al _{0.40} (OH) ₂].(CO ₃) _{0.20} 0.41H ₂ O
Zn:Al2.13:1AS	8.1	12.5	20.6	8.8	9.6	18.4	[Zn _{0.68} Al _{0.32} (OH) ₂].(CO ₃) _{0.16} 0.49H ₂ O
Zn:Al3.20:1AS	10.5	910.0	20.4	10.3	7.2	17.5	[Zn _{0.76} Al _{0.24} (OH) ₂].(CO ₃) _{0.12} 0.57H ₂ O
<i>pH 10</i>							
Zn:Al1.59:1AS	14.4	9.1	23.5	7.6	11.4	119.0	[Zn _{0.61} Al _{0.39} (OH) ₂].(CO ₃) _{0.19} 0.42H ₂ O
Zn:Al2.00:1AS	12.2	10.2	22.4	8.6	10.2	18.8	[Zn _{0.67} Al _{0.33} (OH) ₂].(CO ₃) _{0.17} 0.48H ₂ O
Zn:Al2.97:1AS	10.3	12.5	22.8	10.9	7.8	17.9	[Zn _{0.75} Al _{0.25} (OH) ₂].(CO ₃) _{0.13} 0.56H ₂ O
Zn:Al3.33:1AS	12.1	910.0	22.1	10.5	7.2	17.6	[Zn _{0.77} Al _{0.23} (OH) ₂].(CO ₃) _{0.12} 0.58H ₂ O

AS is denoted for as-synthesised.

3.4.1.3 Powder X-ray diffraction of ZnAl LDH series

The XRD patterns of all ZnAl LDH series synthesised at pH 9 and 10 are summarised in **Figure 3.3a-b**. From the XRD, the system of this material is confirmed as hexagonal with $R\text{-}3m$ space group, which is in excellent agreement with the literature³⁷. Sharp diffraction patterns of as-synthesised ZnAl LDH were observed at basal spacing $d(003)$, $d(006)$, $d(012)$, $d(015)$, $d(018)$, $d(1010)$, $d(1011)$, $d(110)$ and $d(113)$ which confirmed the formation of ZnAl LDH. XRD patterns of as synthesised (AS) ZnAl LDH at pH 9 displayed weak intensities indicating a poorly crystalline structure. By increasing the pH from 9 to 10, better diffraction patterns of ZnAl LDH is observed due to the completion of co-precipitation of ZnAl HT phase. A previous study was done by Melián-Cabrera *et al.*³⁸ which also demonstrated that HTs formation is not favoured at lower pH, and leads to less crystalline materials.

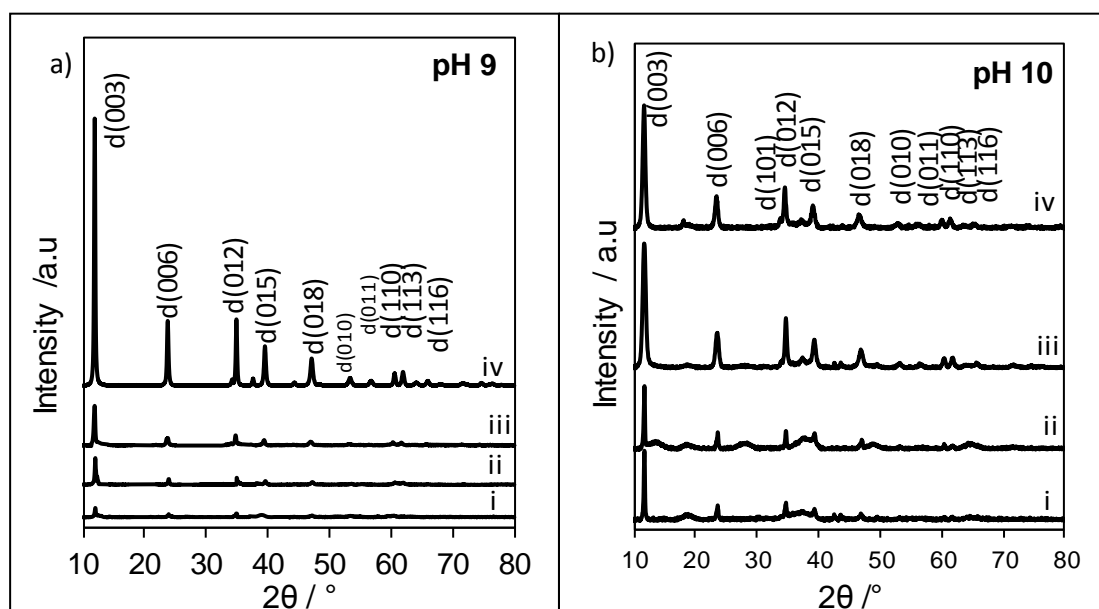
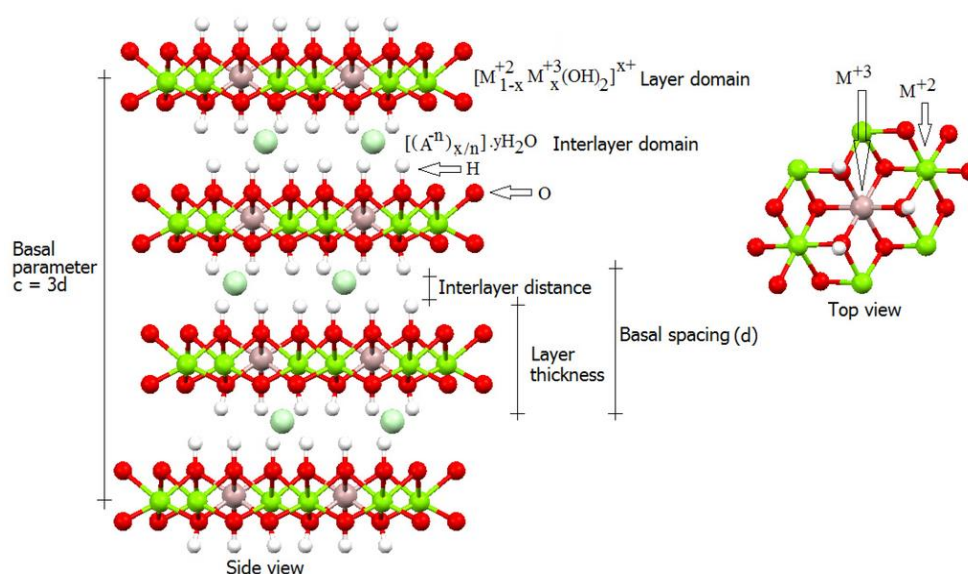


Figure 3.3 Stacked XRD patterns of Zn:Al_{3.31}:1 LDH prepared at pH 9 (a) and 10 (b). i, ii, iii and iv are represented the atomic ratio of each catalyst from lower to higher ratio (0.89:1-3.20:1 at pH 9 and 1.59:1-3.33:1 at pH 10).

Lattice parameter a and c (**Scheme 3.3**) of the catalyst synthesised at both pHs were in agreement with those literature reported by Liu *et al.*²⁷, Kooli *et al.*³⁹ and Thevenot *et al.*⁴⁰ (**Table 3.3**). These values were calculated from d spacing values of d_{003} , d_{006} , $d_{009/012}$ and d_{110} (from Bragg equation). The a parameter corresponds to cation-cation distance in the layer is calculated using a formula of $a = 2d_{110}$. Meanwhile, c is attributed to interlayer distance is calculated using $c = d_{003} + 2d_{006}$ and $3d_{019/012}$ ³³. The value of a and c are in the same range unless there is any substitution between metal hydroxalate or its anions²⁷ are occurred.



Scheme 3.3 The schematic view showing the basal spacing, layer thickness and interlayer thickness of a layer double hydroxide⁴¹.

As mentioned in Chapter 1, the value of x can be used as a guide to the range of compositions over which the HT phase will form, and it is reported that for the formation of a pure hydrotalcite phase, the value of x must lie in the range of $0.2 < x < 0.33$ ³³. In this study, the experimentally determined values were in the range $0.24 > x < 0.53$ at pH 9 and $0.20 > x < 0.39$ at pH 10 (**Figure 3.4a-b**). An increasing trend in the magnitude or in the lattice parameter a and c is observed as the x value is decreased significantly in both synthesised pH. This is due to the lowering Al^{3+} content will decrease the electrostatic attraction between positive cations and negative charge of interlayer anions hence will increase the interlayer distance, c ⁴².

Crystallite size of ZnAl LDH is in the range of 27-43 nm. This also shows crystallite size increases as ratio and pH increase. Thus the x value obtained from these results show pH 10 possess the most significant range as expected in pure hydrotalcite compared to pH 9. Hereby, now it is confirmed that ZnAl LDH synthesised at pH 10 shows better diffraction pattern at basal spacing $d(003)$ and better layer thickness parameter. EDX of fresh samples prepared at pH 10 also shows superior x value ranges compared to those obtained at pH 9. Consequently, the following subtopic will be thoroughly discussing ZnAl LDH synthesised at pH 10 only.

Table 3.3 Comparison of the textural parameters of ZnAl LDHs synthesised at different pH.

Parameter/ catalyst	d_{003} / nm	d_{110} / nm	^a Lattice parameter / nm		^b Crystallite size / nm	$x=(Al/Al+Zn)$
			<i>a</i>	<i>c</i>		
Zn:Al 0.89:1 pH 9	0.73±0.04	0.153±0.003	0.306±0.018	2.24±0.02	35±3	0.53
Zn:Al 1.50:1 pH 9	0.73±0.02	0.153±0.003	0.306±0.015	2.24±0.02	43±5	0.40
Zn:Al 2.13:1 pH 9	0.73±0.02	0.153±0.001	0.306±0.015	2.24±0.02	43±6	0.32
Zn:Al 3.20:1 pH 9	0.73±0.05	0.154±0.006	0.307±0.001	2.25±0.01	51±5	0.24
Zn:Al 1.59:1 pH 10	0.74±0.06	0.153±0.002	0.306±0.013	2.27±0.01	27±6	0.39
Zn:Al 2.00:1 pH 10	0.74±0.02	0.154±0.001	0.307±0.013	2.27±0.01	31±3	0.33
Zn:Al 2.97:1 pH 10	0.74±0.01	0.154±0.002	0.307±0.019	2.27±0.01	36±2	0.25
Zn:Al 3.33:1 pH 10	0.74±0.01	0.154±0.004	0.308±0.009	2.28±0.02	36±1	0.23

^afrom Bragg equation and ^bfrom Scherrer formula

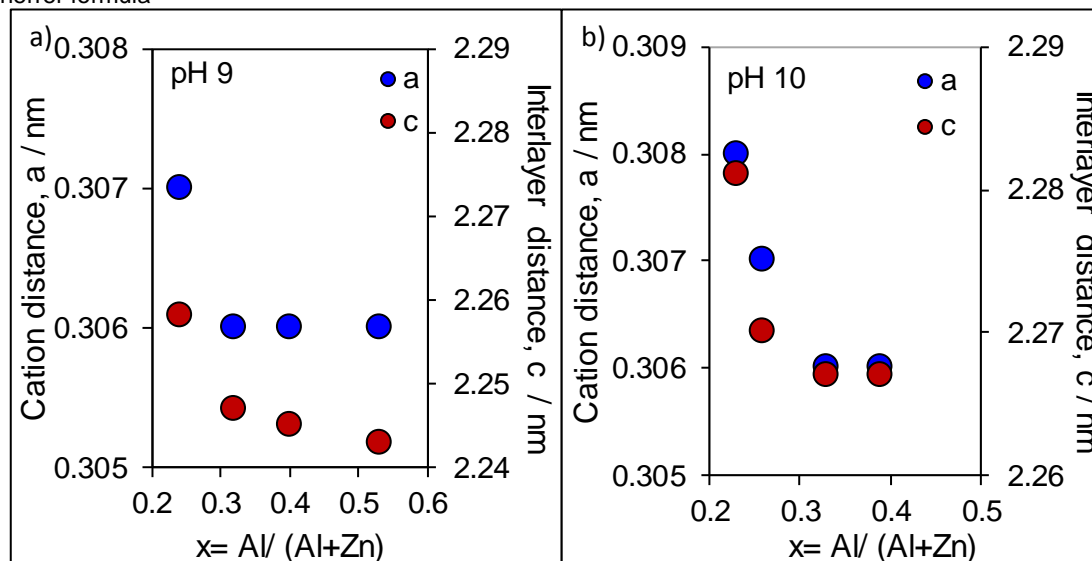


Figure 3.4 Effect of cation distance and interlayer distance as a function of Al content (x value), synthesised at pH 9 (a) and 10(b).

3.4.1.4 Diffuse reflectance infrared Fourier transform spectroscopy of ZnAl LDH series

The functional groups present at the surface were subsequently probed by Diffuse reflectance infrared fourier transform spectroscopy (DRIFTS). **Figure 3.5** shows the evolving surface infrared (IR) spectra of ZnAl LDH series before calcination. IR spectra of hydrotalcite can be differentiated in three distinctive regions⁴³. Theoretically, a broad OH stretching mode $\nu(\text{OH})^-$ and absorbed water molecules are observed around 3360 cm^{-1} from the interlayer region. This region also correlated to hydrogen bonding between water molecules and bidentate carbonates group in the interlayer region³⁸ which later has been detected at 1710 cm^{-1} . Apart than that, vibration at $1560\text{--}1600\text{ cm}^{-1}$ represents H_2O vibration on the surfaces.

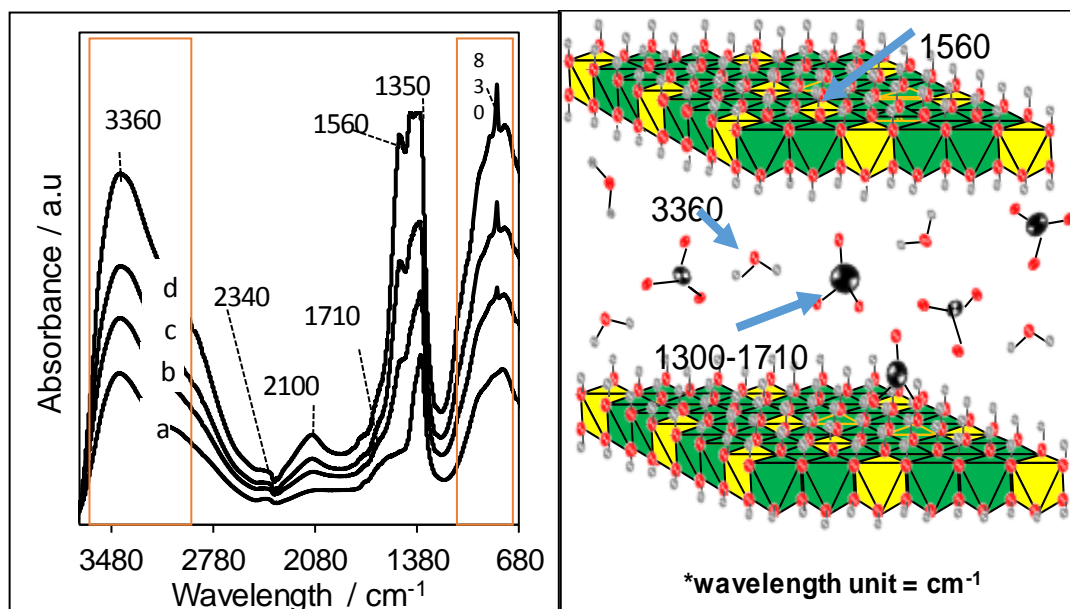
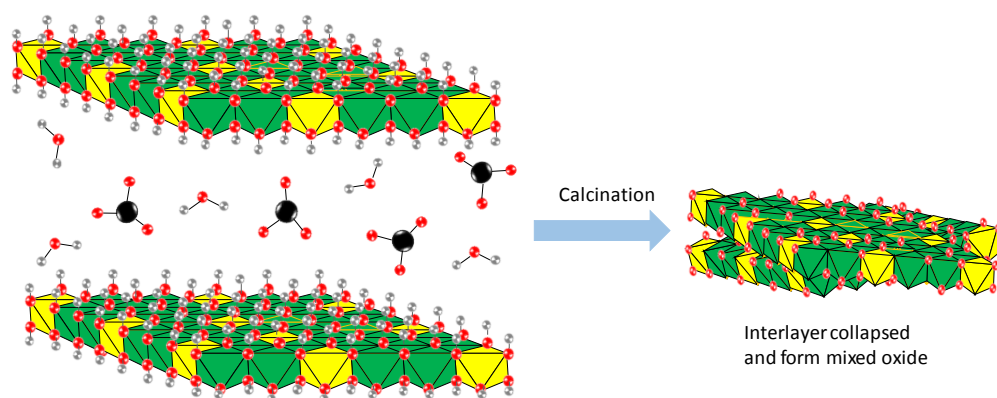


Figure 3.5 DRIFT spectra of ZnAl LDH precursor with Zn:Al ratio of; (a) Zn:Al 1.59:1, (b) Zn:Al 2.00:1, (c) Zn:Al 2.97:1 and (d) Zn:Al 3.33:1. On the right: Cartoon depicted assignments of the functional group involved in ZnAl LDH precursor DRIFTS bands. ● is C, ● is O, ● is H, ▲ is M^{2+} and ▲ is M^{3+} .

A small region of CO_2 absorbed from the atmosphere has been detected around 2300 and 2100 cm^{-1} . Bands of unidentate and bidentate carbonates are overlapping and mostly lies between $1300\text{--}1770\text{ cm}^{-1}$. Zn-Al-O regions were detected around $830\text{--}704\text{ cm}^{-1}$.

3.4.2 Characterisation of ZnAl calcined samples

As-synthesised HTs are normally less active in base catalysed reactions⁴³, thus thermal activation is necessary. During calcination, the interlayer of H_2O and CO_3^{2-} are destroyed and a mixed oxide is formed (**Scheme 3.4**). In this section, the influence of calcination temperatures on the thermal stability of alkali-free ZnAl LDH was investigated for a better understanding of the process involved. In this study, no intention has been made to explore the variation of calcination time on metal oxide sample as Bankauskaite *et al.*³⁰ has proven no pronounced effect was found with changing the calcination time for a MgAl HT study.



Scheme 3.4 Illustration of calcination process taking place at the desired temperature.

3.4.2.1 Powder X-ray diffraction

Based on the results from XRD in sub-chapter 3.4.1.3, hydrotalcite samples prepared at pH 10, which were selected as these gave more crystalline materials with the desired level of Zn incorporation. Calcination temperatures were selected from 250-500 °C⁴⁴ to allow efficient removal of CO_2 and generation of base sites from the decomposition of mixed oxides. ZnAl LDH samples prepared at pH 10 were calcined in a tube furnace at different temperature (250, 300, 400 and 500 °C) for 5 hours, under a flow of 30 ml O_2 , ramp rate 10 °C/min. Offset XRD patterns of the calcined ZnAl LDH series at different temperature are summarised in **Figure 3.6**. Calcination causes a collapse of the brucite sheets and loss of features associated with the layered hydrotalcite structure due to the process of dehydroxylation and decarboxylation of carbonate. From the diffraction patterns, the results confirmed that the re-crystallisation of ZnAl LDH is dependent on the x ratio ($\text{Al}/(\text{Zn} + \text{Al})$) and calcination temperature^{45–47} with lower onset temperatures of 250 °C, ZnO has formed in the sample with a lower Zn:Al atomic ratio (2.00:1).

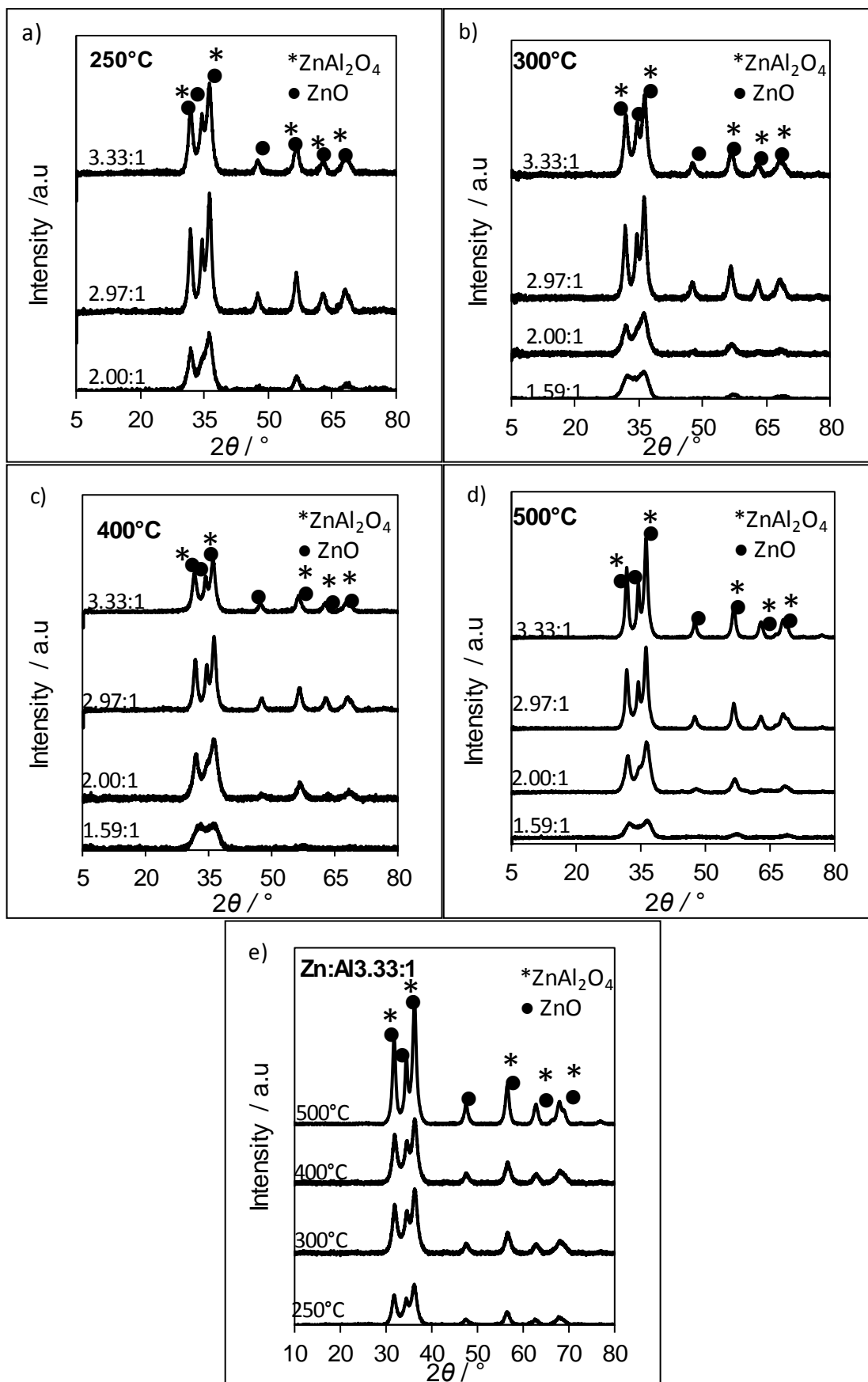


Figure 3.6 XRD pattern of calcined LDH from 250-500 °C (a-d) and its comparison at different temperature using Zn:Al_{3.33}:1 catalyst (e).

Meanwhile, ZnO with ZnAl_2O_4 spinel structure started to form at a higher ratio (2.97:1 and 3.33:1) at the same temperature (250 °C) (Crystallography Open Database (COD) 9011662). After calcination, the $\text{Al}(\text{OH})_3$ phases are not detected in the entire diffraction patterns and these results are in a good agreement with Carriazo *et al.*⁴². Further increasing calcination temperature leads to a sharpening of all peaks, indicating increased crystallinity. The increased crystallinity of ZnO and ZnAl_2O_4 will be shown later in section 3.4.3.3 to be detrimental for reconstruction of calcined LDH materials.

3.4.2.2 Nitrogen porosimetry of ZnAl series

The surface area of calcined and the precursor samples are tabulated in **Table 3.4**. The surface area materials decreased with the formation of mixed oxides. XRD proved that the LDH layer structure has been destroyed and the mixed oxide (ZnO) along with spinel (ZnAl_2O_4) are detected⁴⁸. **Figure 3.7** depicted the adsorption-desorption isotherms of the precursor and calcined ZnAl LDH. It represents the type II according to IUPAC classification with H3 hysteresis loops⁴⁹.

Table 3.4 BET surface area (S_{BET}) for ZnAl LDH precursor and calcined at 300 °C.

Catalyst /Parameter	BET Surface area (m^2/g)
<i>Precursor</i>	
Zn:Al 1.59:1	364 ± 4
Zn:Al 2.00:1	309 ± 17
Zn:Al 2.97:1	445 ± 19
Zn:Al 3.33:1	215 ± 25
<i>Calcined</i>	
Zn:Al 1.59:1	168 ± 10
Zn:Al 2.00:1	170 ± 29
Zn:Al 2.97:1	140 ± 13
Zn:Al 3.33:1	90 ± 41

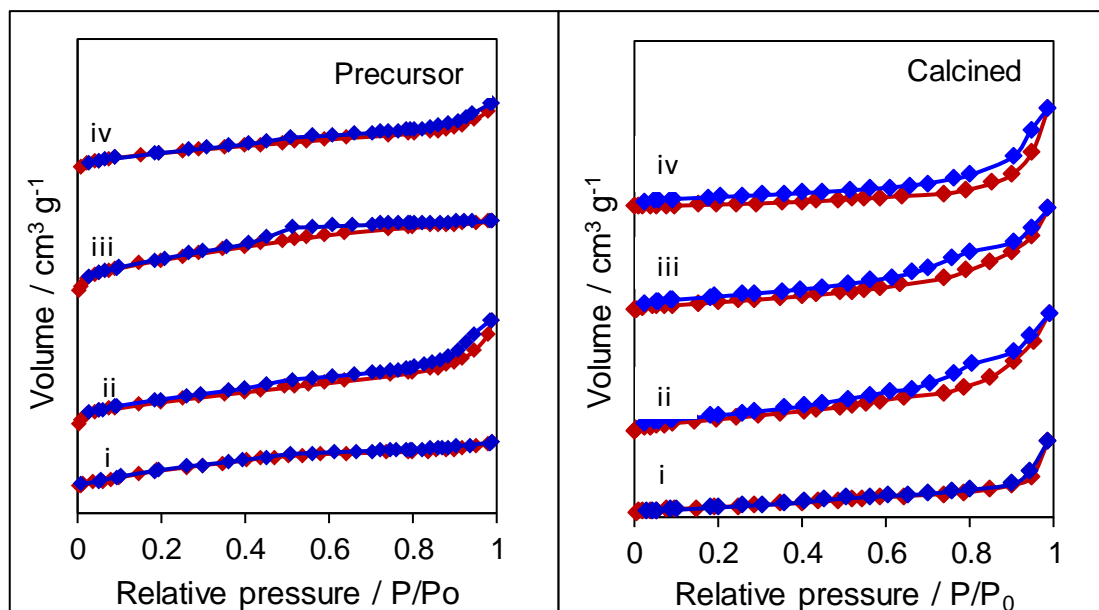


Figure 3.7 N₂ adsorption-desorption isotherms of ZnAl LDH precursor and calcined series, where i-iv indicating increasing ratio from 1.59-3.33.

3.4.2.3 Scanning electron microscopy of ZnAl LDH

Figure 3.8 depicted images of ZnAl LDH obtained from Scanning Electron Microscopy (SEM) imaging. The sand-roses morphology can clearly be seen on the as-synthesised catalyst and indicates the successful synthesis of ZnAl LDH^{48,50}. Meanwhile, during the calcining process, interlayer structures are diminished due to calcination process destroying the CO₃ and H₂O layer, as confirmed by SEM images below.

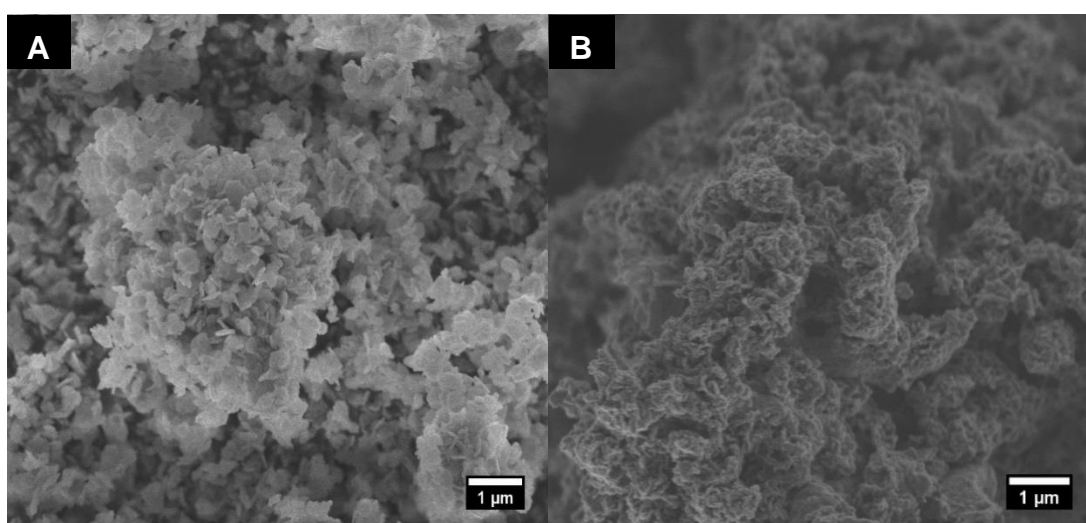


Figure 3.8 SEM images of ZnAl LDH catalyst showing changes of the morphology for as-synthesised (A) versus calcined (B).

3.4.3 Comparison of gas-phase, liquid-phase and hydrothermal ZnAl reconstructed materials

Calcination of ZnAl LDH materials has been shown to generate ZnO and ZnAl₂O₄ which will possess more Lewis base sites but are less favourable for promoting the transesterification reaction⁴². To promote the Brönsted basicity, calcined samples were rehydrated using three different methods; gas-phase (GP), liquid-phase (LP) and hydrothermal (HTM) methods, to assess which is most favourable for fully reconstructing the layered HT structure. The literature on the reconstruction of calcined ZnAl LDH is limited and there are no studies on the use of hydrothermal reconstruction methods using alkali-free parent LDHs. Therefore, this study is vital in order to understand how the textural properties change and resulting impact on catalytic activity in subsequent transesterification reactions.

3.4.3.1 Scanning electron microscopy of reconstructed ZnAl LDH

The morphology of reconstructed ZnAl LDH through gas-phase (GP), liquid-phase (LP) and hydrothermal (HTM) were examined by Scanning electron microscopy (SEM). The ‘*Memory Effect*’ of hydrotalcite should lead to the lamellar structure being regained upon rehydration as is observed commonly for MgAl LDH⁵¹, however, for ZnAl LDH optimum conditions have not previously been demonstrated. A casual look at the low-magnification SEM (**Figure 3.9**) images indicate that images of bar-like structures⁵² following GP treatments. Meanwhile, in LP, bundles of hexagonal flakes with a 3D flake-like morphology can clearly be seen. Following HTM treatments, we observed the overlapping platelets suggesting more extensive re-crystallisation forming a structure⁵².

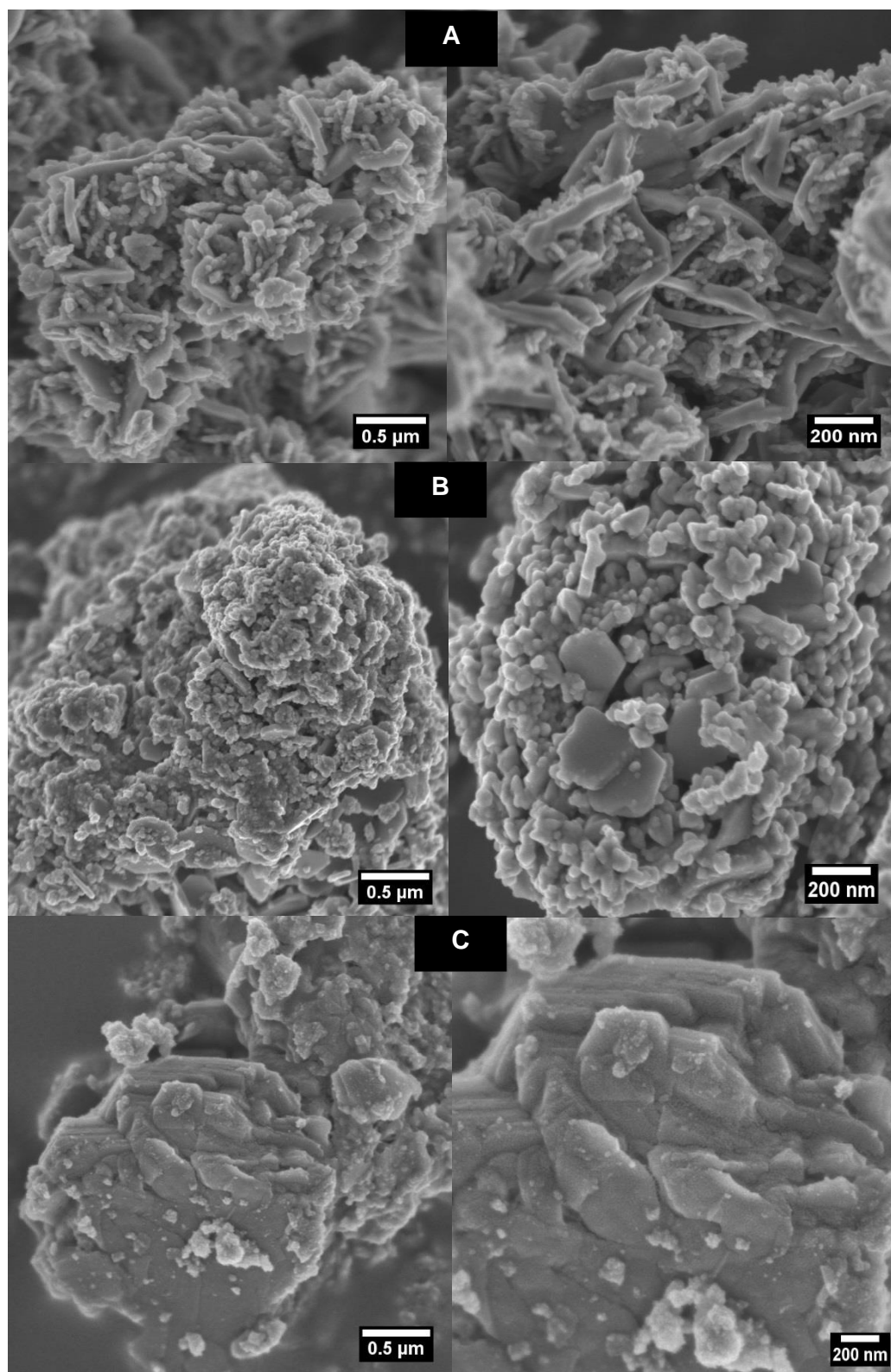


Figure 3.9 SEM images of rehydration ZnAl LDH (ratio 3.33:1) through achieved gas-phase (A), liquid phase (B) and hydrothermal (C), respectively.

3.4.3.2 High-resolution scanning transmission electron microscopy of reconstructed ZnAl LDH

HR-STEM was performed to monitor changes in morphology of differently reconstructed Zn LDH at higher magnification. Micrographs are depicted in **Figure 3.10**.

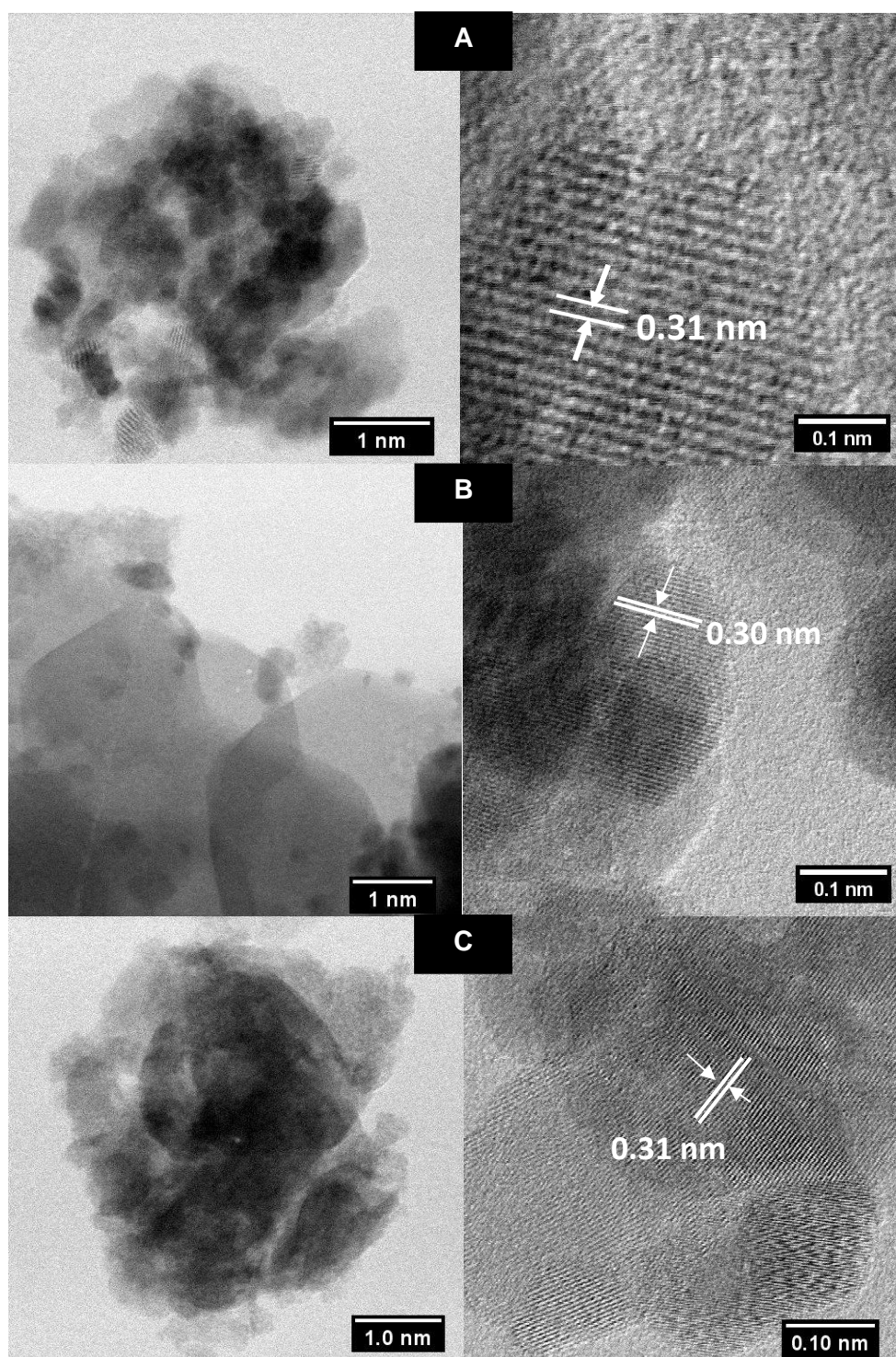


Figure 3.10 HRTEM images of rehydration ZnAl LDH (ratio 3.33:1) achieved through gas-phase (A), liquid-phase (B) and hydrothermal (C), respectively.

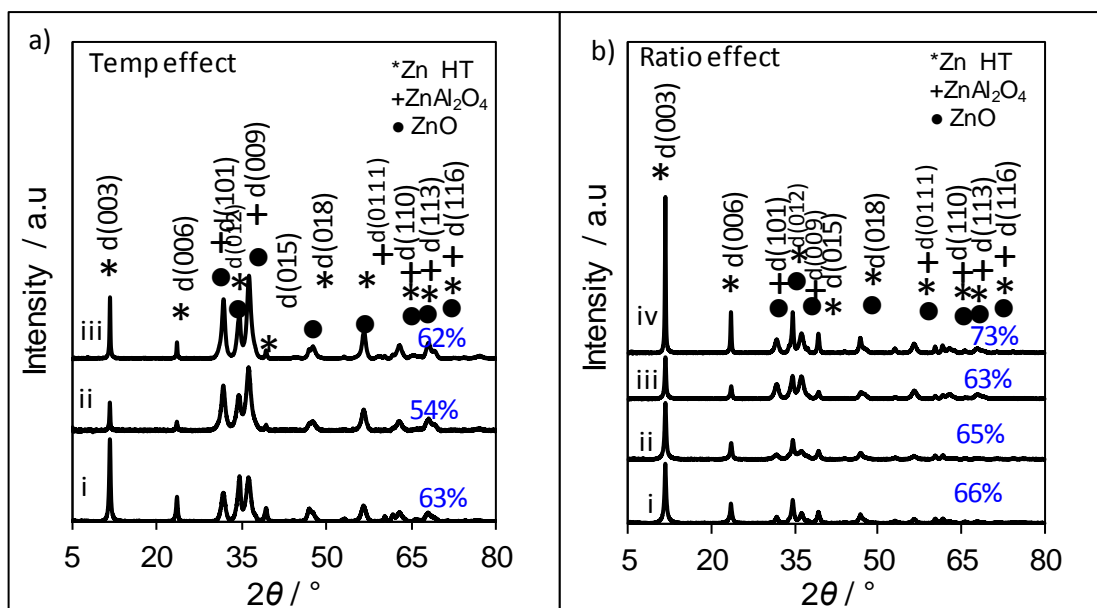
Nanoplatelet sheets of hexagonal structures can clearly be seen in all samples. The lattice fringes obtained in a range of 0.30 ± 0.01 nm corresponds to the lattice parameter, a , in good agreement with values from XRD measurements⁵³.

3.4.3.3 Powder X-ray diffraction

The reconstruction properties were investigated using different rehydration methods under gas-phase (GP), liquid-phase (LP) and hydrothermal (HTM) rehydration method as mentioned before.

a) Gas-phase ZnAl reconstructed

Figure 3.11 shows the diffraction patterns of gas-phase rehydration as a function of calcination temperature for each Zn:Al atomic ratio. Samples were rehydrated under wet nitrogen bubbler at 30 ml/min^{-1} for 48 hours.



a) XRD pattern of rehydrated ZnAl LDH (ratio 2.97:1) prepared via gas-phase at different calcination temperatures; i=300 °C, ii=400 °C) and iii=500 °C at ratio 3.33:1

b) XRD pattern of rehydrated ZnAl LDH prepared via gas-phase at different ratio; i=1.59:1, ii=2.00:1 and iii=2.97:1 and iv=3.33:1 at 300 °C.

Figure 3.11 Effect of temperature and ratio on ZnAl LDH. The intensity ratio of ZnAl HT/ZnO is denoted in percentage value.

To evaluate the purity of the reconstructed calcined ZnAl LDH, the intensity ratio of ZnAlHT (peak 003) over ZnO (peak 012) is calculated. As mentioned in sub-chapter 3.4.1.3, the spinel of ZnAl_2O_4 appears even though at a lower calcination temperature, hence no unique feature of ZnO could be depended on. As these mixed oxides started to form at 250 °C, it is hard to reconstruct the lamellar without formation of these two compounds. For a pure LDH, a ratio of ZnAl HT/ZnO was calculated and represents the limiting value to be targeted. The calculation has been done by applying this formula: $[y\text{ZnAl} / (y\text{ZnAl} + y\text{ZnO})] \times 100 \%$, where y =intensity of y_2 - y_1 . In this case, the intensity of ZnAl from diffraction pattern of d(003) is divided by the sum of ZnAl from d(003) intensity and intensity of ZnO from diffraction pattern of d(012).

Under GP method, when the samples were pre-calcined at 300-500 °C, around 54.2-68 % ZnAl LDH were reconstructed but a significant amount of ZnO and ZnAl_2O_4 remained (Crystallography Open Database (COD)-00-038-0486) (**Figure 3.11a**). Materials calcined at 300 °C give the highest purity of LDH (63.1 %), so it was selected to compare the effect of Zn:Al atomic ratio on reconstruction (**Figure 3.11b**), with the degree of reconstruction, increasing with Zn:Al atomic ratio, varying over the 63.1-73.0 %. The trend in both reconstructed ratio and crystallite size are dependent upon Zn:Al ratio as shown in **Figure 3.12**. Higher Zn content appears to lead to the increased crystallinity of the ZnAl LDH^{39,54}.

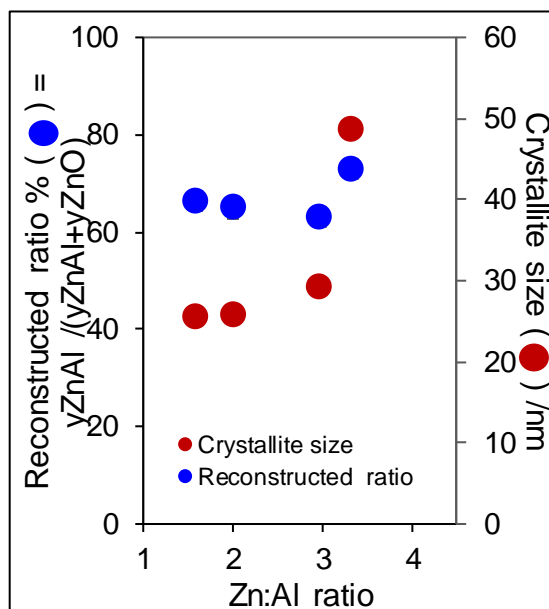
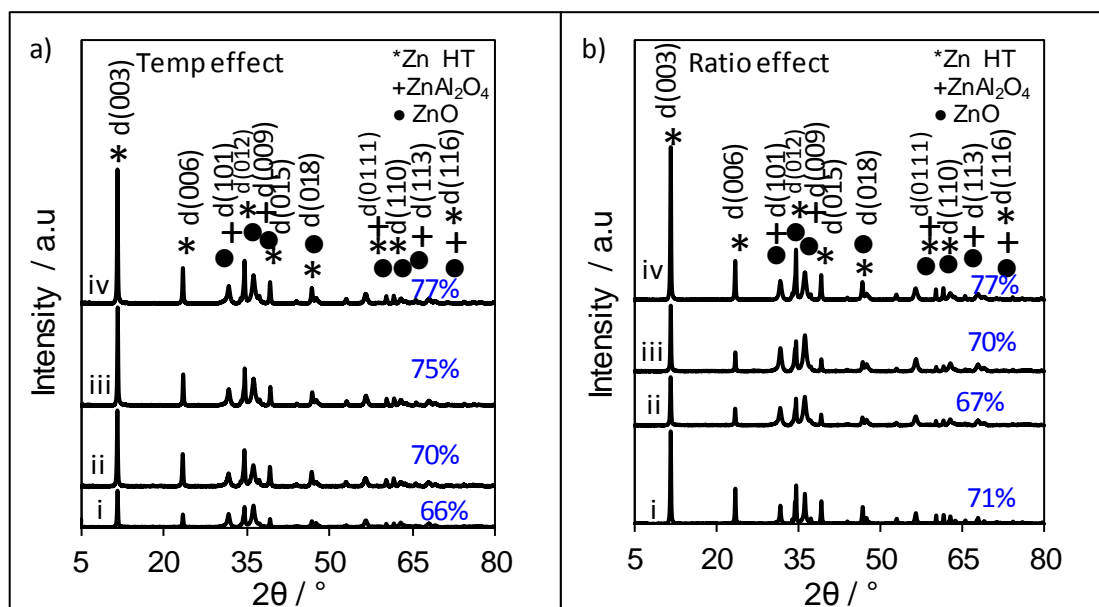


Figure 3.12 Effect of Zn:Al atomic ratio on the reconstructed ratio ($y\text{ZnAl} / (y\text{ZnAl} + y\text{ZnO})$) and crystallite size via gas-phase rehydrated ZnAl LDH.

b) Liquid-phase ZnAl reconstructed

GP rehydration shows the calcined ZnAl LDH is not fully rehydrated after 48h. Hence, rehydration by liquid-phase (LP) (at room temperature, in carbonated water) was explored to enhance the catalyst physiochemical properties. The diffraction patterns of regenerated hydrotalcite structure following LP rehydration are summarised in **Figure 3.13a-b**. Similar to GP method, the presence of ZnO and ZnAl_2O_4 are still detected following LP rehydration. There is an increased crystallite size as the calcination temperature of the parent HT is increased from 250-500 °C. Again, these patterns are matched with Crystallography Open Database (COD) 00-038-0486 which confirmed the reconstruction of ZnAl LDH. The LP method appears to be more effective at reconstructing the ZnAl LDH than the GP approach, with the intensity of the d(003) reflection significantly more intense relative to the ZnO and ZnAl_2O_4 features.



a) XRD pattern of rehydrated ZnAl LDH (ratio 2.97:1) prepared via liquid-phase at different calcination temperatures; i=250°C, ii=300 °C), iii=400°C and iv=500 °C

b) XRD pattern of rehydrated ZnAl LDH prepared via liquid-phase at different ratio; i=1.59:1, ii=2.00:1 and iii=2.97:1 and iv=3.33:1 at 300 °C

Figure 3.13 XRD patterns of ZnAl LP and its dependent on calcined temperature and ratio. The intensity ratio of ZnAl HT/ZnO is denoted in percentage value.

Again the effect of Zn:Al atomic ratio on LP rehydration for 300°C calcined samples was explored **Figure 3.13b** which shows a purity of ZnAl HT/ZnO in a range of 67-77 % is obtained which is a slight improvement on the GP approach. The crystallite size (**Figure 3.14**) was not found to vary with Zn:Al atomic ratio with all having the same limiting value as that obtained following GP reconstruction. This experiment proves the

calcined oxides can be reconstructed to LDH if the parent temperature is not exceeding than 500 °C. Higher parent calcination temperature (700 °C) will inflict a detrimental impact on reconstruction due to potential sintering effects occurring which make reconstruction impossible³⁹.

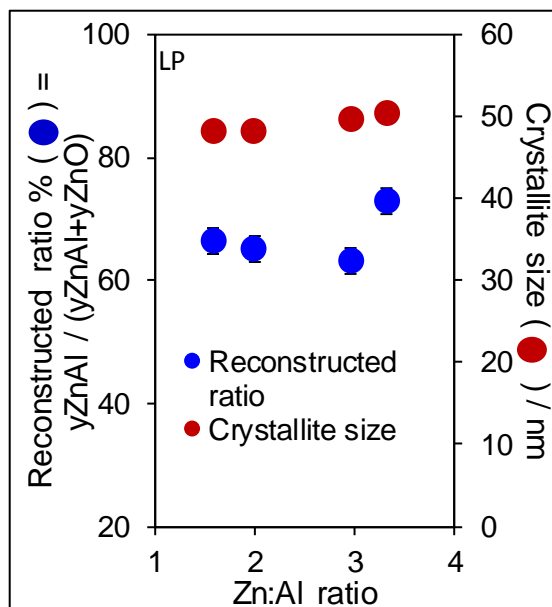


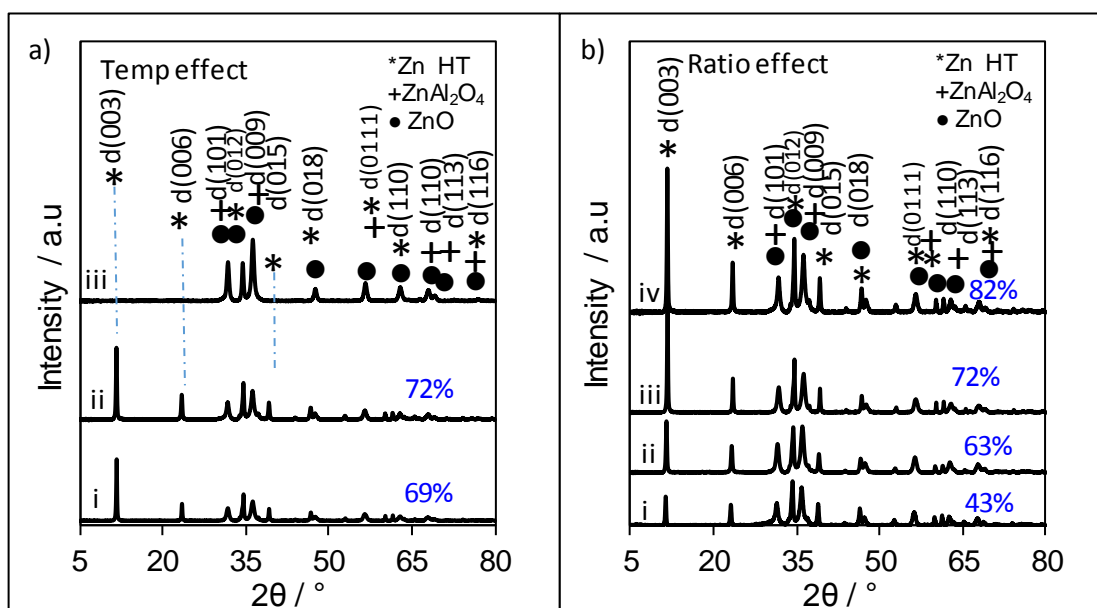
Figure 3.14 Effect of Zn:Al atomic ratio on the reconstructed ratio ($y\text{ZnAl} / (y\text{ZnAl} + y\text{ZnO})$) and crystallite size via liquid-phase rehydration of ZnAl LDH.

c) Hydrothermal ZnAl reconstructed

In the previous discussion, we focus on rehydration of ZnAl LDH via gas and liquid phase. Somehow, rehydration through these methods is promoting the incomplete reconstruction of lamellar³⁰. For this reason, hydrothermal reconstruction was introduced here. As no publication on alkali-free ZnAl LDH reconstructed via hydrothermal has been reported, extended knowledge on this material is essentially required.

Firstly, the effect of introducing different hydrothermal temperature has been tested on different ratios of Zn:Al to establish further understanding on hydrothermal temperature dependency. Two different temperatures have been conducted; 100 and 150 °C. Results in **Figure 3.15a** reveal ZnAl LDH were easily reconstructed at temperature 100 °C with an amount of zinc oxide was detected regardless of its ratio either at 2.00:1 or 2.97:1. The most striking result to emerge is from the XRD diffraction pattern at temperature 150 °C where ZnO and ZnAl_2O_4 have failed to reconstruct the lamellar structure. Data shown reconstructed ZnAl LDH is not favourable at a higher temperature.

This result fulfilled the gap in knowledge left from the work done by Kooli *et al.*³⁹ where they found ZnAl LDH prepared via hydrothermal-alkali co-ppt were able to reconstruct between 80-120 °C under hydrothermal temperature. No higher temperature has been tested. They also observed better LDH were formed as hydrothermal temperatures were increased accordingly. We obtained a higher intensity peak as the ratio was increased from 1.59 to 3.33 as can be seen in **Figure 3.15b**. Interestingly, higher purity (82.2 %) of ZnAl LDH was obtained for samples having higher Zn:Al atomic ratio (3.33:1) as compared to lower one. An increase in crystallite size is also observed at higher Zn:Al atomic ratio (**Figure 3.16**). Together these results provide important insights into a successful reconstruction of hydrothermally treated calcined ZnAl LDH, regardless to if the removal of ZnO is impossible in the lamellar structure after the calcined-rehydration process due to the rigid formation of ZnO spinel. Most importantly, now a clear understanding of how ZnO influences on the purity of reconstructed LDH is clearly answered.



a) Effect of different hydrothermal temperature and ratio.

i=Zn:Al2.00:1HTM100,
ii=Zn:Al2.97:1HTM100 and
iii=Zn:Al2.00:1HTM150.

b) Effect of ranging the ratio at constant hydrothermal temperature (100 °C). i-iv are the increment ratio from 1.59 to 3.33.

Figure 3.15 XRD patterns of hydrothermal reconstructed ZnAl LDH. The intensity ratio of ZnAl HT/ZnO is denoted in percentage value.

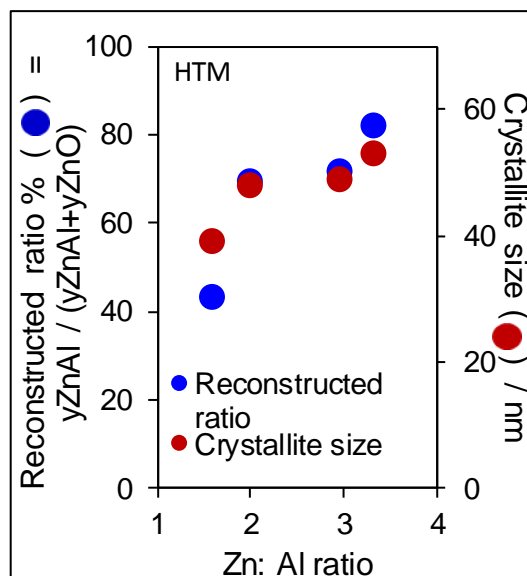


Figure 3.16 Effect of ZnAl LDH/ZnO formation and crystallinity over ZnAl HTM ratio.

Table 3.5 The textural parameter of ZnAl LDH reconstructed through gas-phase, liquid-phase and hydrothermal approaches.

Catalyst /Parameter	^a Lattice parameter / nm		^b Crystallite size/nm	Intensity ratio of ZnAl LDH/ ZnO / %
	<i>a</i>	<i>Cc</i>		
<i>Different rehydration/reconstruction approaches (Zn:Al3.33:1)</i>				
Gas-phase (GP)	0.307±0.009	2.28±0.12	29±7	73 ± 0.1
Liquid-phase (LP)	0.307±0.013	2.28±0.09	49±5	77 ± 0.1
Hydrothermal (HTM)	0.308±0.005	2.28±0.13	53±6	82 ± 0.2
<i>ZnAl hydrothermal series</i>				
Zn:Al 1.59:1 HTM	0.307±0.014	2.28±0.23	39±8	43 ± 0.3
Zn:Al 2.00:1 HTM	0.307±0.008	2.28±0.17	48±1	63 ± 0.2
Zn:Al 2.97:1 HTM	0.307±0.001	2.28±0.16	49±2	71 ± 0.5
Zn:Al 3.33:1 HTM	0.308±0.005	2.28±0.13	53±6	82 ± 0.2

*a were determined by Bragg equation and b were determined by Scherrer equation

The XRD results showed that rehydration under hydrothermal condition improved the rehydration step with the formation of ZnAl LDH with traces of impure ZnO and ZnAl₂O₄ (**Figure 3.17a**). However, hydrothermal route gave more crystalline ZnAl LDH in comparison with gas and liquid phase rehydration. Unit cell parameters (*a* and *c*) calculated (**Table 3.5**) were in a good agreement with literature³⁹ without much change irrespective of the rehydration steps and '*a*' parameter show bigger values than for MgAl hydrotalcite because of the higher octahedral ionic radius of Zn²⁺ over Mg²⁺. The crystallite size of reconstruction steps exhibit crystallite size of 50 ± 5 nm. Among different methods rehydration under hydrothermal conditions gave a ZnAl hydrotalcite with good crystallinity, higher lattice parameter (**Figure 3.17b**), less amount of mixed oxide impurity and better than liquid/gas phase rehydration.

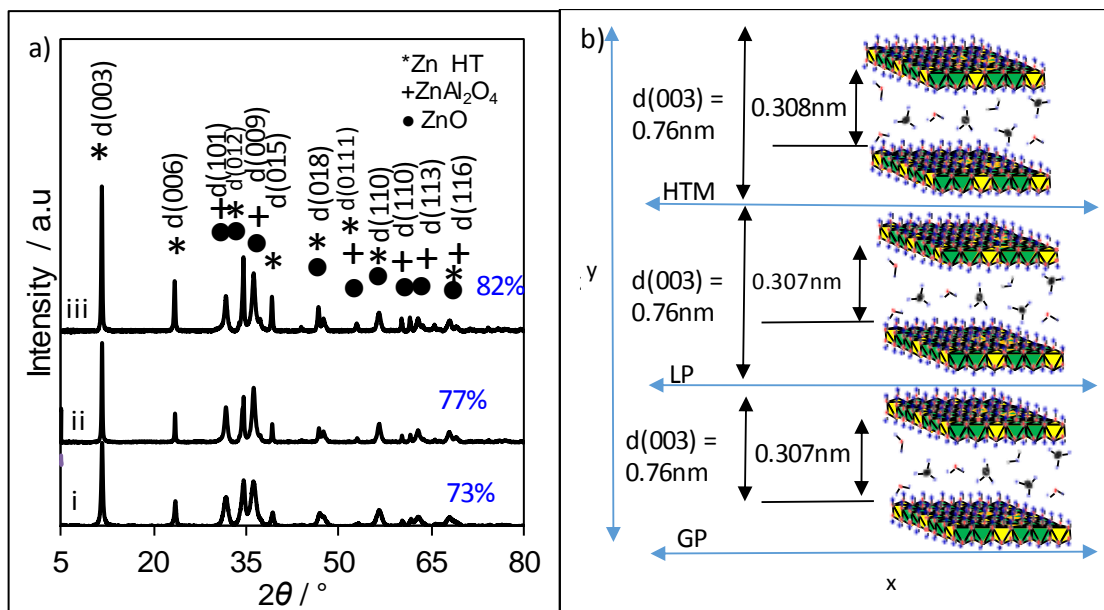


Figure 3.17 (a) XRD patterns of comparison between different rehydration routes, gas-phase(i), liquid-phase (ii) and hydrothermal (iii) using Zn:Al3.33:1 catalyst. Cartoon depiction shows lattice parameter changes as the reconstruction method changed (b).

3.4.3.4 Nitrogen porosimetry of GP, LP and HTM ZnAl LDH

The N₂ adsorption-desorption isotherms of GP, LP and HTM reconstructed LDH are presented in **Figure 3.18 (a-c)** which are consistent with Type II isotherms according to IUPAC classification with a type H3 hysteresis loops⁴⁹. The loop is very narrow and becomes more pronounced for the hydrothermal reconstructed samples, having a tendency to be most vertical and parallel over a wide range of relative pressure⁵⁵ especially at a higher ratio of Zn/Al. This suggests that hydrothermally reconstructed materials tend to have better-developed domains of narrow slit-like pores which are attributes from the lattice distance.

The low surface area in gas-phase rehydration techniques is suspected due to steric hindrance produced by OH⁻ and H₂O molecules in the interlayer space of ZnAl LDH⁵⁶. Highest surfaces area was obtained for reconstructed materials pre-calcined at 300 °C which correlated with XRD results where we found more ZnO and ZnAl₂O₄ formed at a higher temperature.

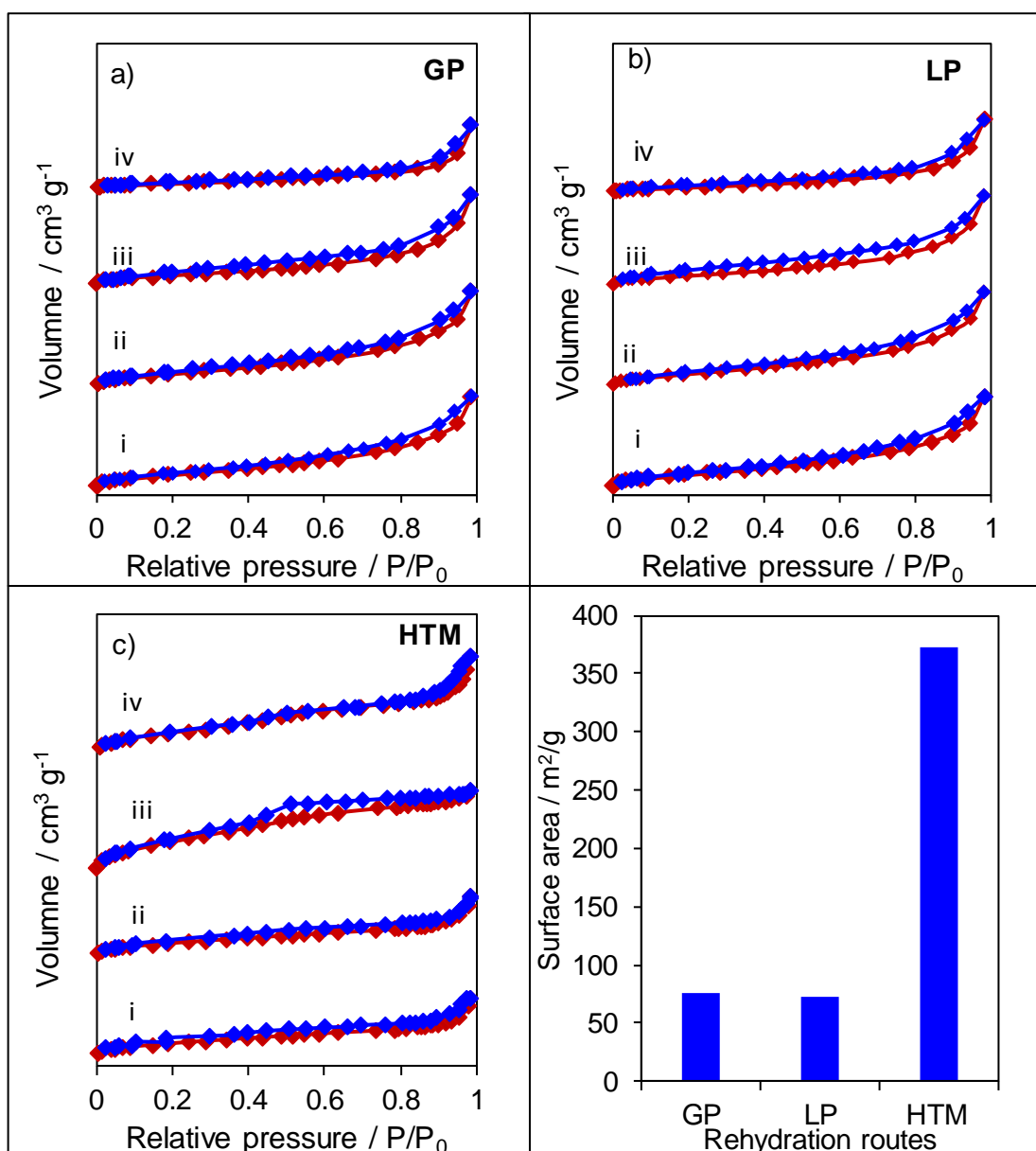


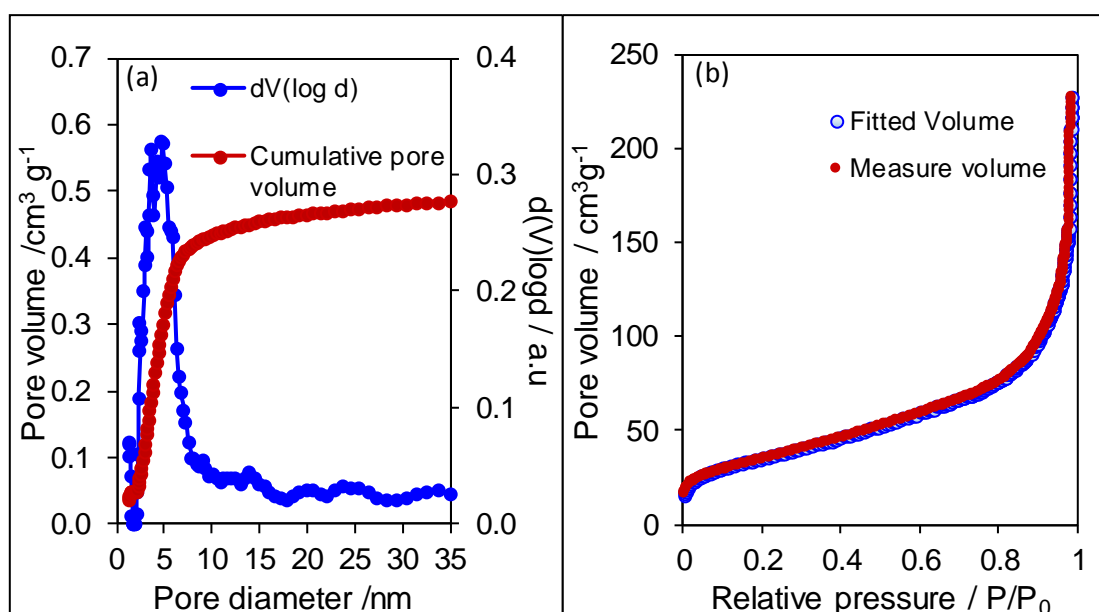
Figure 3.18 Left: N₂ adsorption-desorption isotherms of ZnAl GP, LP and HTM series (a-c) where samples i-iv indicating increasing ratio from 1.59-3.33. Effect of rehydration routes on surface area is shown in (d) on Zn:Al₃.33:1 catalyst. All catalysts were calcined at 300 °C.

Figure 3.18d and **Table 3.6** summarises the effect of rehydration/reconstruction routes on surfaces area. The physiochemical properties of HTM method have a significant impact on the surface area where it enhanced ~5 fold compared to GP and LP. Through rehydration process under hydrothermal heating, the crystallinity of the catalyst has been increased (shown in **Table 3.3** before), thus increased the surface area simultaneously. Apart than that, no significant effect of ratio on the surface area has been observed here. Meanwhile, a very small pore volume has been detected (average 0.32 cm³ g⁻¹), which in the same agreement with the narrow loops shown above.

Table 3.6 BET surface area (S_{BET}) for ZnAl GP, LP and HTM.

Catalyst /Parameter	BET Surface area / m^2/g
<i>Different rehydration/reconstruction approaches (Zn:Al3.33:1)</i>	
Gas-phase (GP)	76±10
Liquid-phase (LP)	71±17
Hydrothermal (HTM)	373±17
<i>ZnAl hydrothermal series</i>	
Zn:Al 1.59:1 HTM	215±31
Zn:Al 2.00:1 HTM	133±22
Zn:Al 2.97:1 HTM	373±17
Zn:Al 3.33:1 HTM	256±23

A pore size distribution has been carried out over HTM reconstructed LDH using a QuantaChrome Autosorb instrument (under N_2 at 77 K) that allows for a more accurate determination of micropore distributions (**Figure 3.19a**). Application of a Density Functional Theory (DFT) equilibrium using a model for slit-like pores in a carbonaceous material (**Figure 3.19b**) reveals a good agreement between the fitted and measured volume experimental data. The average pore diameter determined from this analysis is in the range of 4.9 nm which is attributed to internal voids and interspacing of HTs^{57,58}, with a cumulative pore volume of $0.39 \text{ cm}^3 \text{ g}^{-1} \pm 0.77$. The high surface area and well-defined porous structure of the hydrothermal catalyst may offer improved diffusional properties under reaction⁵⁸ and enhanced catalytic performance in the transesterification reaction.

**Figure 3.19** Pore size distribution and fitting plots for ZnAl HTM.

3.4.3.5 Temperature-programmed desorption of CO₂ of GP, LP and HTM ZnAl LDH

CO₂ chemisorption measurements were undertaken to characterise the basicity of the family of reconstructed ZnAl LDH materials. Fundamentally, the binding of CO₂ on hydrotalcite can be classified into three regions (**Figure 3.20**); bicarbonate (weakly basic), bidentate carbonate (medium basic) and unidentate (strong basic)^{26,59}. ZnAl GP, LP and HTM exhibit a feature characteristic of medium basic sites, with CO₂ desorbing in the range from 176 °C to 450 °C. This peak is correlated to decomposition of bidentate carbonate species, formed from adsorption of CO₂ on Brönsted basic sites⁶⁰.

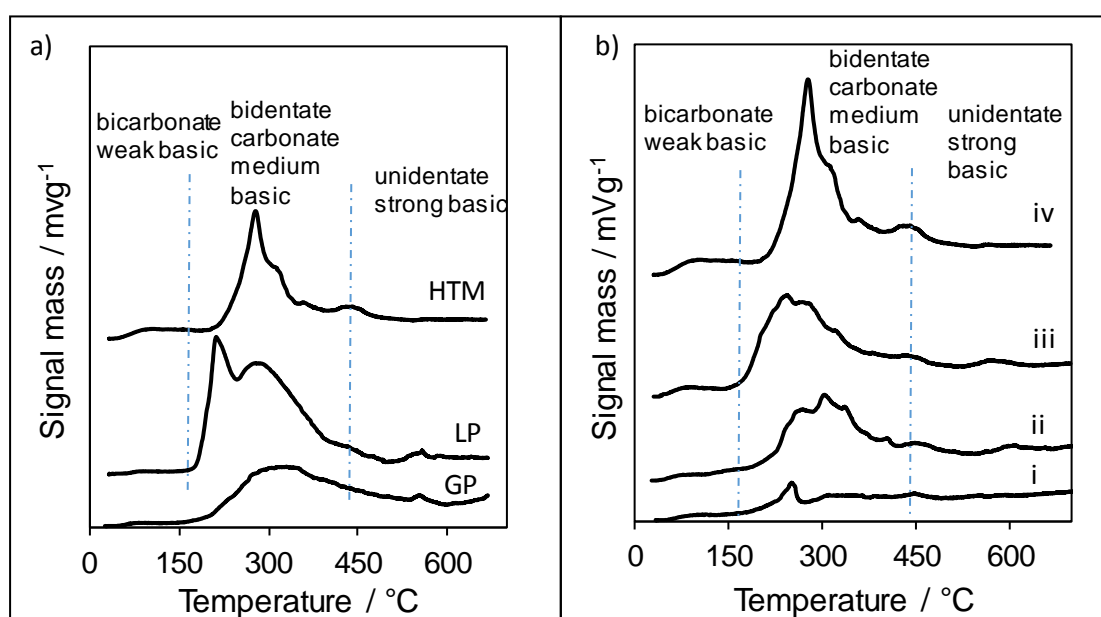


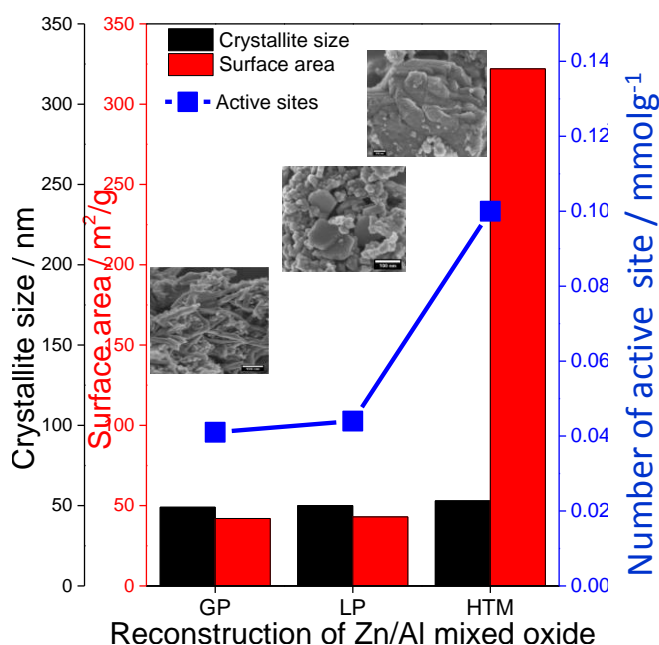
Figure 3.20 Basicity desorption showing bicarbonate, bidentate carbonate and unidentate determined by CO₂-TPD of different rehydration/reconstruction approaches (a) and ZnAl hydrothermal series spanning from 1.59:1 to 3.33:1 (i-iv) (b).

Basic site density increases with rehydration, with hydrothermal treatment offering more basic sites than gas or liquid phase rehydration (**Table 3.7**). A summary of the textural and basic properties of the reconstructed HT materials having Zn:Al ratio of 3.33:1 is shown in **Figure 3.21**, which shows that crystallite size, surface area and base site loading increase in the order GP < LP < HTM.

Table 3.7 The amounts of basic sites in ZnAl LDH samples.

Samples	Number of active sites ^a / mmol g ⁻¹	Base site density ^b / molecules g ⁻¹ (x10 ¹⁹)
<i>Different rehydration/reconstruction approaches (Zn:Al3.33:1)</i>		
Zn:Al GP	0.041 ± 0.005	2.4 ± 0.1
Zn:Al LP	0.044 ± 0.002	2.6 ± 0.1
Zn:Al HTM	0.100 ± 0.054	6.0 ± 1.2
<i>ZnAl hydrothermal series</i>		
Zn:Al 1.59:1 HTM	0.048 ± 0.002	2.9 ± 0.1
Zn:Al 2.00:1 HTM	0.058 ± 0.012	3.5 ± 0.3
Zn:Al 2.97:1 HTM	0.079 ± 0.033	4.7 ± 0.7
Zn:Al 3.33:1 HTM	0.100 ± 0.054	6.0 ± 1.2

^{a,d}determined by CO₂ pulse chemisorption

**Figure 3.21** Inter-correlations between lattice parameter, crystallite size, surface area and basicity of different reconstructed approached in ZnAl LDH.

3.4.3.6 Al-MAS Nuclear magnetic resonance spectroscopy of ZnAl LDH series

²⁷Al MAS NMR (**Figure 3.22**) was undertaken to evaluate the arrangement of Al³⁺ sites in the structure of the hydroxalcite. Octahedrally coordinated Al³⁺ peak present in the brucite-like layers observed at 9 ppm in all phases from as-synthesised to hydrothermal. Meanwhile, a peak at 66 ppm started to rise after calcination, characteristic of tetrahedrally coordinated Al³⁺ in the mixed oxide. These findings are in agreement with Miyazaki *et al.*⁶¹, where two peaks around 6 and 60 ppm attributed to

octahedral and AlO_4 tetrahedral species respectively. Similar observations were reported by Van de Laag *et al.*⁶² who observed the formation of zinc aluminate, ZnAl_2O_4 , a type of mineral gahnite which has formed along with ZnO during calcination and been detected by Al-NMR. Further understanding on how ZnAl_2O_4 (Al_{IV}) incorporated on the surface (alongside with ZnO) after the calcination, regardless of the rehydration step, is now revealed and clearly answered.

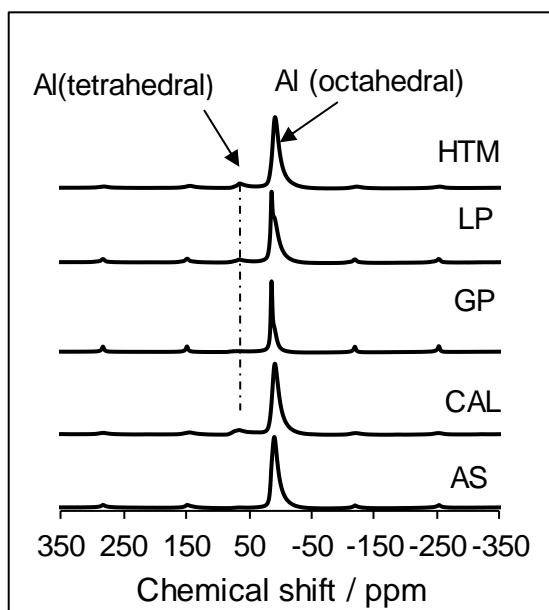


Figure 3.22 ^{27}Al MAS NMR spectra of Zn:Al 3.33:1 hydrotalcite obtained at different rehydration approaches using 9.4 T magnet spectrometer with 14 kHz spin rates.

3.4.3.7 X-ray photoelectron spectroscopy of ZnAl HTM

The surface compositions of the ZnAl HTM series were subsequently analysed by XPS. **Figure 3.23(a-c)** depicts the Zn 2p, Al 2p and O 1s spectra, respectively which were calibrated to the C 1s peak at 284.6 eV corresponding to C-C adventitious carbon. The C=O carbonates are observed at 286.7 eV (**Figure 3.23a**). Binding energies and assignments were made with reference to the NIST standard XPS database⁶³ and all spectra were background subtracted. The Zn 2p for ZnAl HTM (**Figure 3.23b**) exhibited doublet at 1022 and 1044 eV which corresponding to the spin-orbit split Zn $2p_{3/2}$ and $2p_{1/2}$ states respectively.

Al 2p spectra (**Figure 3.23c**) can be two deconvoluted into two peaks at 72.4 and 74.5 eV. These peaks are corresponding to formation of Al in tetrahedral coordination at lower BE and bonded to octahedral Al^{3+} in higher BE. The intensity of Al^{3+} was found to decrease as the Zn: Al ratio increased which is in good agreement with EDX.

The O 1s spectra (**Figure 3.23d**) exhibit two components at 531 and 533 eV which are characteristic of carbonate and hydroxyl environments respectively²⁹. Peak deconvolution of all ZnAl HTM series revealed the surface concentration of O²⁻ correlates well with the incorporation of Zn²⁺ into the lattice.

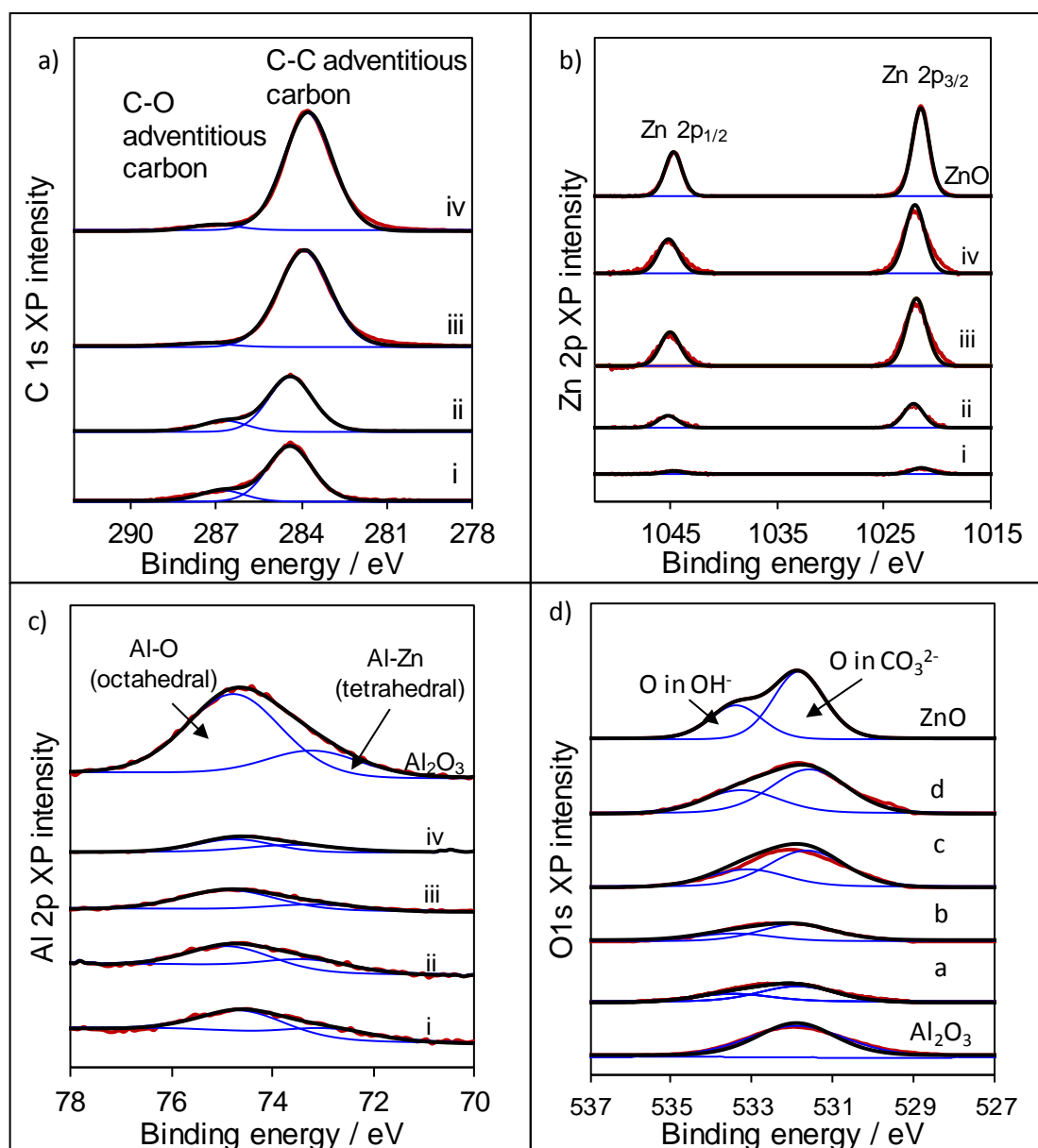


Figure 3.23 The C 1s, Zn 2p, Al 2p and O1s spectra (a-d) of ZnAl HTM spectra with i-iv are the increasing ratio from 1.59 to 3.33 accordingly. — denoted as envelope, — raw data and — HT component.

Relationship of the surface over bulk Zn content can be seen in **Figure 3.24** as analysed by XPS and EDX respectively. Both surface and bulk Zn were increased as

the nominal ratio increased. The total surface ratio is found to be lower than the bulk of Zn.

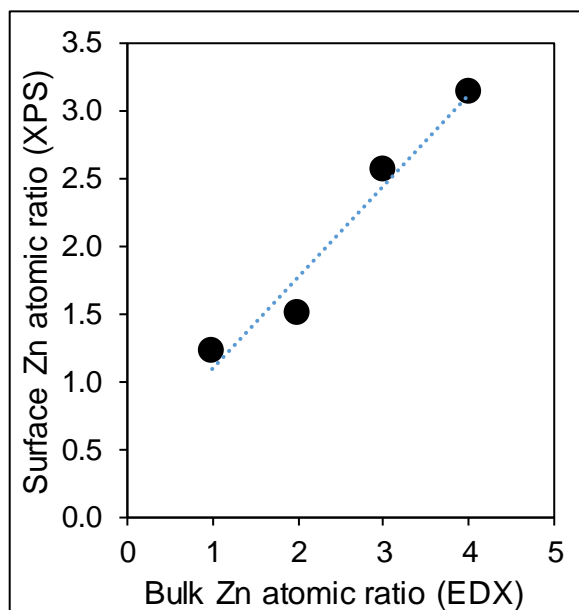


Figure 3.24 Zn surface to bulk ratios determined by XPS and EDX analysis for ZnAl HTM LDH.

3.4.3.8 Diffuse reflectance infrared Fourier transform spectroscopy of ZnAl HTM

Figure 3.25 shows the DRIFTS spectra of ZnAl HTM series confirming the typical profile of reconstructed hydrotalcite^{64,65}. It is known that three main hydroxyl regions are expected in Zn hydrotalcite structure with a weak H₂O bending appear later⁶⁶. A region from 3500-3300 cm⁻¹ is attributed to OH⁻ stretching groups which indicates the successful addition of water after reconstruction process⁵⁹. The band around 3306 cm⁻¹ corresponded to H₂O in the interlayer. Meanwhile, the shoulder appears later at 1660 cm⁻¹ is referred to a very weak H₂O bending vibration.

C-O vibration appeared between 2809-2895 cm⁻¹ from the environment. Unidentate carbonate asymmetric vibration was detected at ~1515 cm⁻¹ ascribed with an interaction of metal (Zn²⁺) as also reported elsewhere⁵⁶. This unidentate region somehow is showing very low-intensity peaks indicating this is not relatively strong basicity site exist in the HT. Al-O deformation and Zn-O translation were found later in the region wavelength at 857 and 719 cm⁻¹ respectively as proven by Klopogge *et al.*⁶⁷.

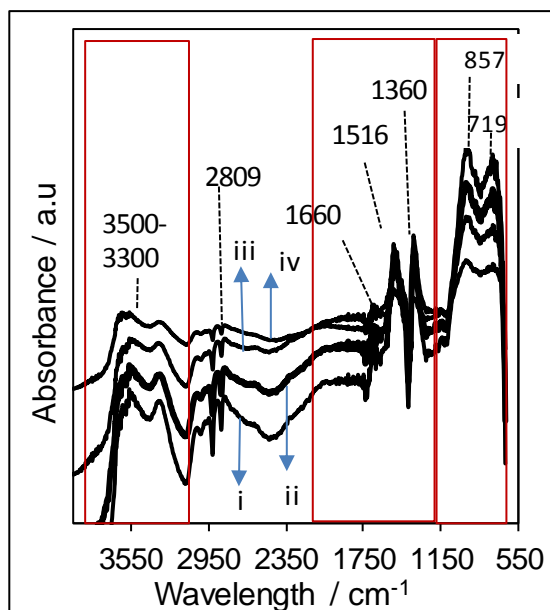


Figure 3.25 DRIFTS spectra of hydrothermal reconstructed ZnAl LDH in different ratio; i) 1.59:1, ii) 2.00:1. iii) 2.97:1 and iv) 3.33:1.

3.4.4 Transesterification of tributyrin over reconstructed ZnAl LDH

The efficiency of the transesterification of TAG with methanol and the catalytic activity affected by many parameters. These include the strength and distribution of basic sites obtained from a different type of rehydration ZnAl LDH and its ratio, the reaction temperature, the catalyst amount and effect of co-solvent in the transesterification reaction. Theoretically, this reaction requires using 3 moles of methanol over 1 mole of glyceride. In actual fact, however, this reaction requires a large excess of methanol. In our studies the methanol to oil molar ratio was adopted 30:1 to allow comparison of results with previous studies of hydrotalcite based materials by Cantrell *et al.*²⁹ and Woodford *et al.*⁶⁸.

3.4.4.1 Effect of Rehydration/Reconstruction

Approaches on GP, LP and HTM ZnAL LDH

The aim of this section is to investigate the effect of gas-phase, liquid-phase and hydrothermal (GP, LP and HTM) rehydration/reconstruction approaches on catalytic activity for TAG transesterification, so as to select the optimum method to explore with longer alkyl length TAGs. The conversion, selectivity and yield are calculated as follows:

Conversion

$$= \frac{\text{Concentration of TAG at } T_0 \text{ (moles)} - \text{Concentration of TAG at } T_1 \text{ (moles)}}{\text{Concentration of TAG at } T_0 \text{ (moles)}} \times 100$$

$$\text{Selectivity} = \frac{\text{Concentration of product formed (moles)}}{\text{Total product concentration (moles)}} \times 100$$

$$\text{Yield} = \text{Selectivity} \times \text{Conversion}$$

TOF was calculated by normalising initial rates derived from the linear portion of reaction profiles during the first hour to the base site loadings obtained from CO₂ chemisorption as following:

$$\text{Turn of frequency (TOF)} = \frac{\text{Initial rates (mmol min}^{-1} \text{ g}^{-1})}{\text{Base site loading (mmol g}^{-1})}$$

Conversion profiles for the transesterification of tributyrin using Zn:Al3.33:1 GP, LP and HTM were plotted in **Figure 3.26a**. Meanwhile, in **Figure 3.26b**, a summary of the conversion, selectivity and TOF are compiled. Clearly, a positive trend of conversion, selectivity and TOF are observed as follows: gas-phase < liquid-phase < hydrothermal approaches. These results are well correlated with their structural parameters. The TOF increases with conversion and selectivity as rehydration improves from GP to HTM. These findings prove ZnAl LDH prepared via rehydration/reconstruction methods prompts better catalytic activity due to the higher Bronsted basic strength. This also shows that HTM rehydration is more accessible in transesterification reaction compared to GP and LP. Conjunction with this, ZnAl LDH reconstructed via HTM techniques will be used in the transesterification of C₄-C₁₈.

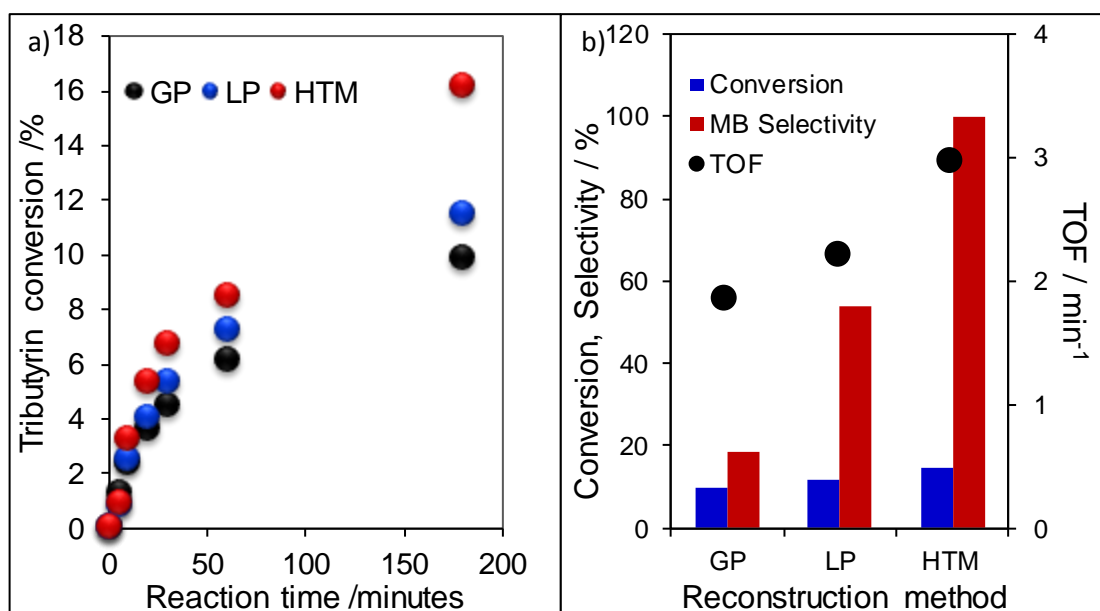


Figure 3.26 (a)Tributyrin conversion of reconstructed ZnAl through gas-phase, liquid-phase and hydrothermal approaches using Zn:Al3.33:1 catalyst. (b) Effect of rehydration method on conversion, selectivity and TOF using the same catalyst Conditions: 65 °C, 100 mg catalyst and 6 h reactions. MB is denoted for methyl butyrate.

In the **sub-chapter 3.4.3**, comparisons of the physicochemical properties of rehydration/reconstruction ZnAl LDH through GP, LP and HTM has been presented and discussed. This finding proven ZnAl LDH prepared via HTM reconstruction approaches is more catalytically active than others due to these three reasons:

- i) ZnAl HTM catalyst (ratio 3.33:1) possesses a high surface area (256 m²/g); allowing better diffusion of TAG during transesterification and enhanced conversion.
- ii) ZnAl HTM catalyst (ratio 3.33:1) possesses a higher number of base sites (6.0 x10¹⁹ molecules g⁻¹), which catalyse the transesterification, as Lewis bases transformed to Brönsted⁶⁰ after rehydration process.
- lii) ZnAl HTM catalyst (ratio 3.33:1) possesses higher crystallite size (53 nm), though not really influencing the transesterification reaction, the effect may influence the exposure of favoured facets for activation of TAG.

3.4.4.2 Effect of ratio on ZnAl HTM

To investigate the effect of Zn:Al atomic ratio on tributyrin conversion, a series of hydrothermally reconstructed ZnAl LDH was prepared with Zn:Al atomic ratio 1.59 to 3.33 were tested for tributyrin transesterification. Conversion profiles and evolution of products of each reconstruction methods are summarised in **Figure 3.27a**.

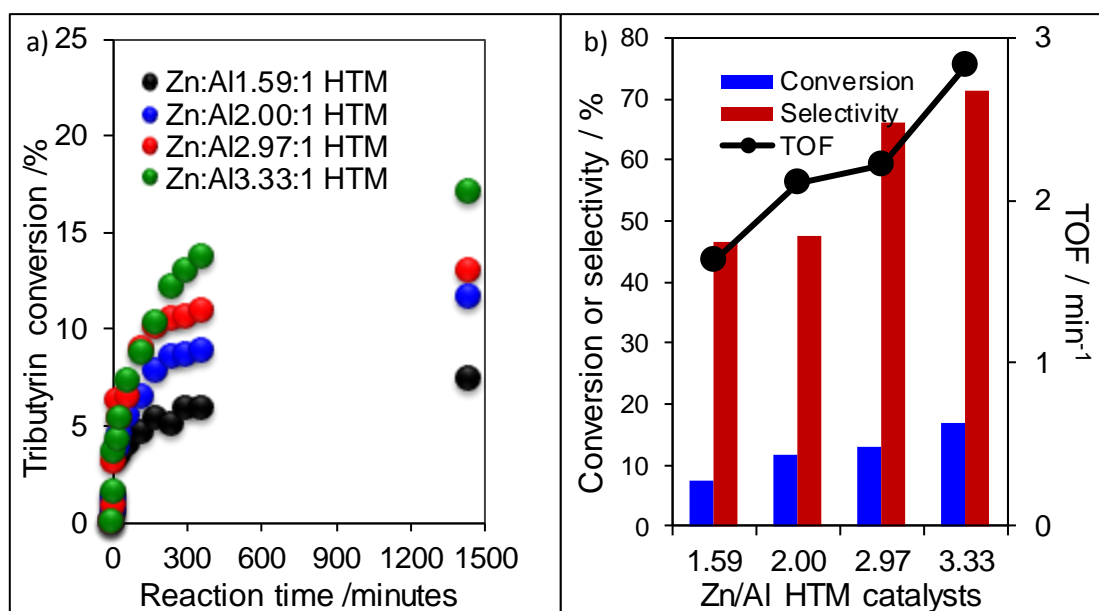


Figure 3.27 Tributyrin conversion of hydrothermal ZnAl at a different ratio (a). conversion and selectivity of tributyrin using ZnAl HTM and its catalytic performance (b). The reaction involved 50 mg catalyst, at 65 °C, 30:1 methanol: tributyrin ratio, 650 rpm for 24 hours.

It is observed that, the TAG conversion and TOF (**Figure 3.27b**) were greatly affected by the increase of Zn content in the following sequence: Zn:Al1.59:1HTM < Zn:Al2.00:1HTM < Zn:Al2.97:1HTM < Zn:Al3.33:1HTM. Apparently, the Zn:Al atomic ratio in hydrotalcite influences the catalytic performances for tributyrin conversion, with initial rate and limiting conversion increasing with Zn content. This trend is similar to that reported by Woodford *et al.*⁶⁸ except they were using rehydrated MgAl instead of ZnAl.

3.4.4.3 Effect of temperature on ZnAl HTM

The effect of varying the reaction temperature for transesterification of tributyrin using hydrothermal reconstructed hydrotalcite was also investigated at 65 °C, 80 °C, 90 °C and 110 °C to calculate the activation energy for the reaction. Firstly, transesterification reaction has been done on C₄ at 65 °C where the conversion observed was only 4.25 % with low selectivity (0.49 %). Also, a reaction on C₈ and C₁₂ has been done at 65 °C using Zn:Al3.33:1HTM catalyst (data not provided). Unfortunately, there was no conversion observed at this temperature. In general, the reaction of bulkier TAG at 65 °C is problematic.

Consequently, the temperature was increased to from 80 to 110 °C, tested using tributyrin in a pressure flask, while other parameters have remained the same. This result is important in order to compare with bulkier TAG which also took place in a pressure

flask. The reaction profiles of tributyrin and related TOF can be seen in **Figures 3.28a-b** respectively, which clearly show that higher reaction temperatures lead to increased conversion and TOF. It was not possible to increase the temperature above 150 °C due to the formation of unwanted species deactivating the catalyst. Another issue is the potential collapse of the LDH phase at a hydrothermal temperature of 150 °C as proven by XRD. Further investigation needs to be performed in order to prove this assumption.

The activation energy was determined by measuring how the initial rates varied with reaction temperature (80 - 110 °C) as shown in the Arrhenius plot of $\ln k$ versus $1/T$ in **Figure 3.28c**. A straight line was obtained indicating no change in the rate-determining step during the experiments and no deactivation was observed^{69,70}. The Activation energy (E_a) obtained from the plot was 33 kJ/mol, which is comparable to values reported by Chantrasa *et al.*⁶⁹ who reported an activation energy of 38 kJ/mol for the transesterification of tricaprylin using MgAl hydrotalcite. Singh and Fernando⁷¹ reported an E_a of 44 kJ/mol using a magnesium methoxide solid catalyst in soybean oil, while the use of MgAl HT in the transesterification of poultry fat⁷⁰. gave an activation energy of 57 kJ/mol. Overall, it can be concluded that the E_a value from our experiment is in the agreement with previous literature as mentioned above.

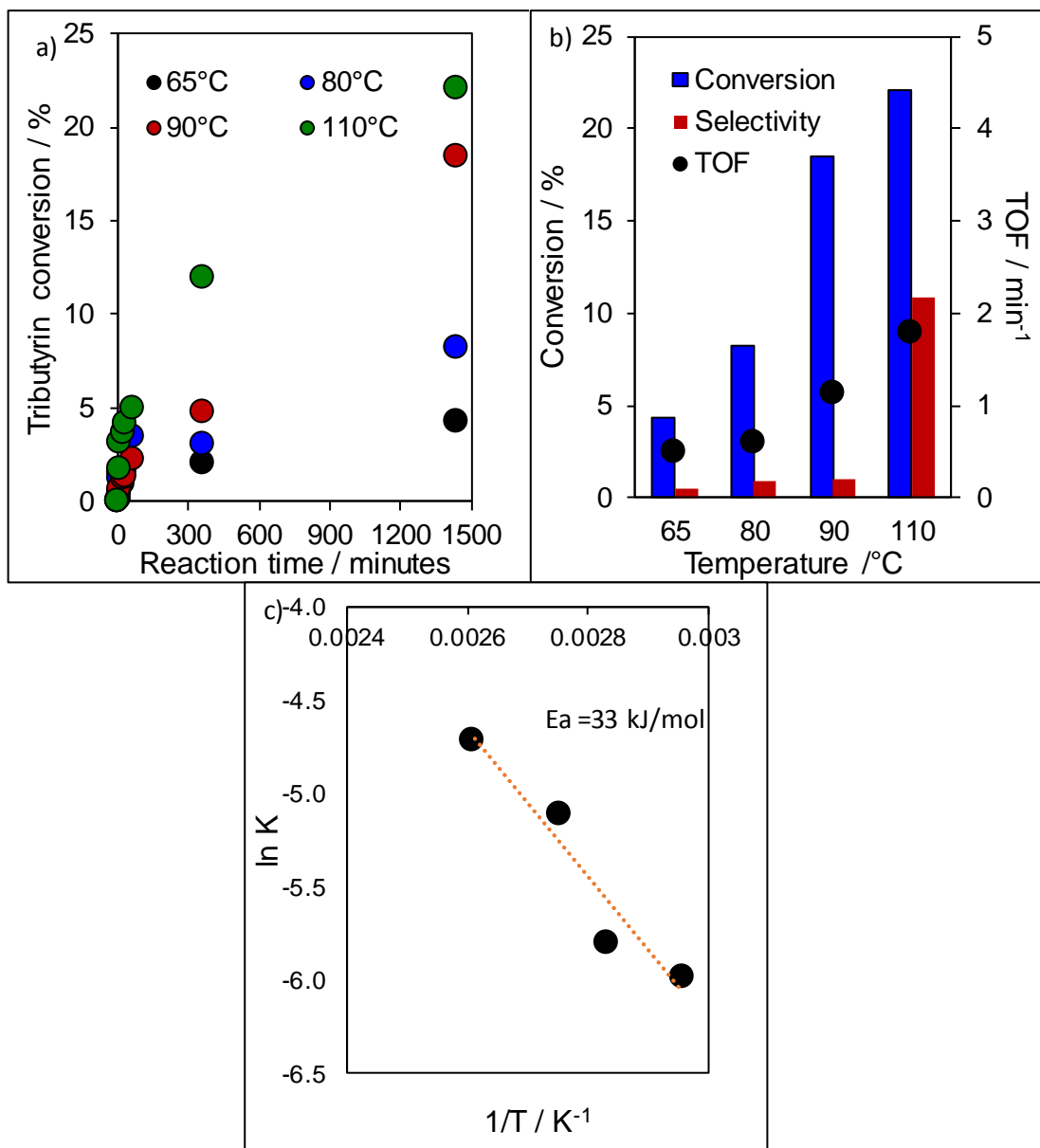


Figure 3.28 Dependence of rate on temperature; (a) Conversion profiles of tributyrin using Zn:Al3.33:1HTM at a different temperature, (b) Effect of temperature on TOF and selectivity and (c) Arrhenius plot for transesterification of tributyrin.

3.4.4.4 Effect of catalyst mass on ZnAl HTM

The masses of ZnAl HTM were employed (0, 25, 50 and 100 mg), compared and displayed in **Figure 3.29a** to assess the activity of the catalyst. The rate of tributyrin conversion is found to increase with catalyst mass, the reaction is proven to be not selective at lower catalyst weight and started to form more FAME as the amount of the catalysts were increased (**Figure 3.29b**). The increasing of rate is expected with an

increase in the amount of catalyst used⁷². This result was due to the increase in the amount of available catalytic active sites as the amount of catalyst increased⁷³.

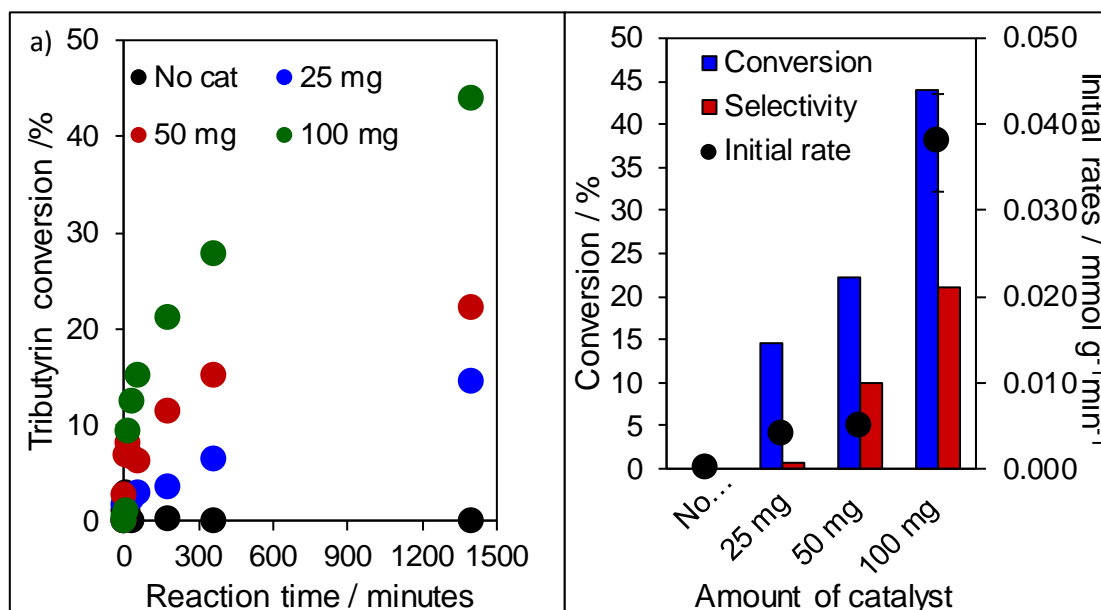


Figure 3.29 Tributyrin conversion of hydrothermal Zn:Al_{3.33}:1HTM at different catalyst weight (a). Effect of conversion, selectivity and TOF by ranging the catalyst amount (b). Conditions: 110 °C in pressure flask, different catalyst weight, no co-solvent, 650 rpm and 24 h reaction.

3.4.4.5 Effect of co-solvent on ZnAl HTM

In order to explore the catalytic performance of higher TAG (C₈, C₁₂ and C₁₈), we need to add butanol as co-solvent to aid solubility of reactant in methanol⁶⁸. Resulting reactions in methanol are compared with reactions in which butanol is added as a co-solvent as shown in **Figure 3.30a**. In all cases, the calculated TOF decreased as more butanol was added (**Figure 3.30b**). The addition of butanol may compete with methanol for adsorption at base sites leading to lower rates of TAG conversion, thus reducing the TOF value significantly.

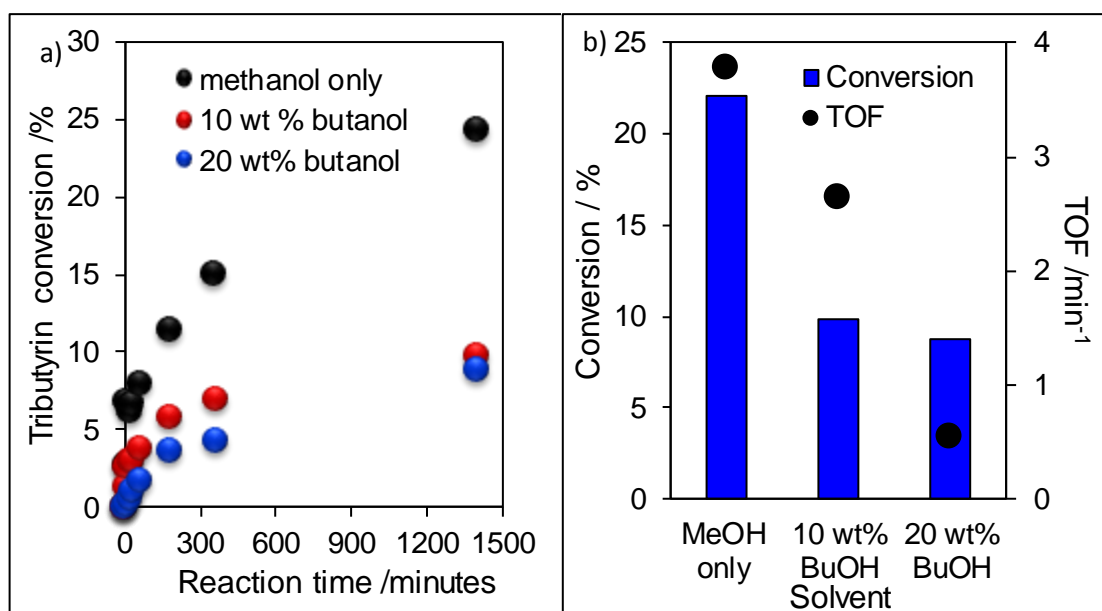


Figure 3.30 Influence of solvent and co-solvent (a) and TOF of tributyrin transesterification (b) on Zn:Al_{3.33}:1HTM catalyst.

The addition of butanol is essential for studying reactions with longer chain TAG to reduce mass transfer limitation so even though the rate of reaction is lower this is an essential baseline. No additional products have been observed attributes to butanol here as can be seen in gas chromatogram of transesterification of TAG (C₄) obtained from GC-FID (**Figure 3.31**). Peak 1-3 correspond to the solvent of methanol, dichloromethane and butanol respectively. An internal standard of dihexyl ether was observed around 5.6 minutes (peak number 5). Meanwhile, the products of methyl butyrate, monobutyrin and dibutyrin appeared at peak number 4, 6 and 7 respectively. Tributyrin was observed around 11 minutes (peak number 8). No formation of butyl butyrate appears here.

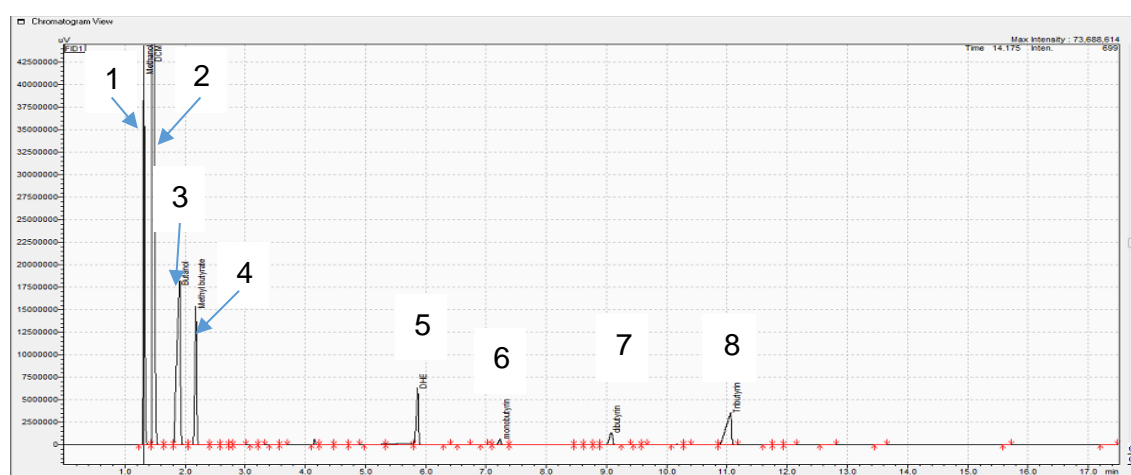


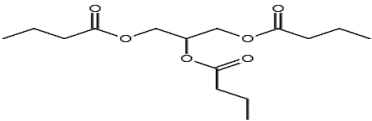
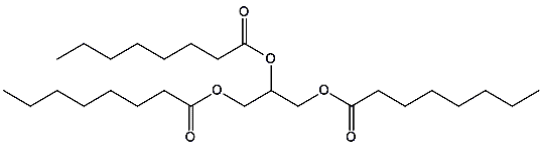
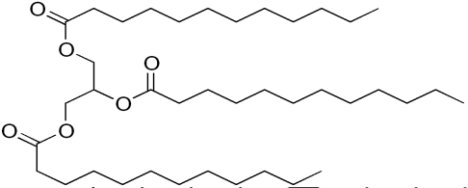
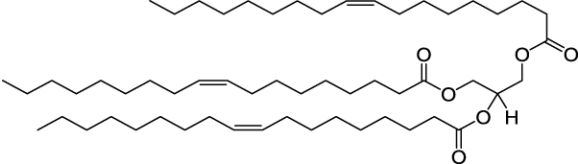
Figure 3.31 GC chromatogram from transesterification of tributyrin using Zn:Al_{3.33}:1 HTM catalyst.

3.4.5 Transesterification of Model Triglycerides on ZnAl HTM

3.4.5.1 C₄-C₁₈ TAG

The ZnAl HTM were tested for the transesterification of TAGs with C₄ to a C₁₈ chain length (**Table 3.8**). Methanol was used both reagent and solvent while butanol is added as a co-solvent in order to assist solubility and mass transfer of bulkier TAGs during the reaction. Based on results presented in **sub-chapter 3.4.3**, Zn:Al3.33:1 HTM was tested for the transesterification of varying chain length triglycerides, from a model C₄ to a C₁₈ chain length as can be seen in **Figure 3.32a-d**. Reactions were performed at 110 °C using 100 mg catalyst with the addition of co-solvent in order to assist solubility of bulkier TAG during reaction⁶⁸. The reaction was performed immediately after the catalysts are ready after the calcined-rehydration process.

Table 3.8 Triglycerides chain length used in this study (C₄-C₁₈)

Triglycerides names	Formula structure
Tributyryn (C ₄)	
Tricaprylin(C ₈)	
Trilaurin (C ₁₂)	
Triolein (C ₁₈)	

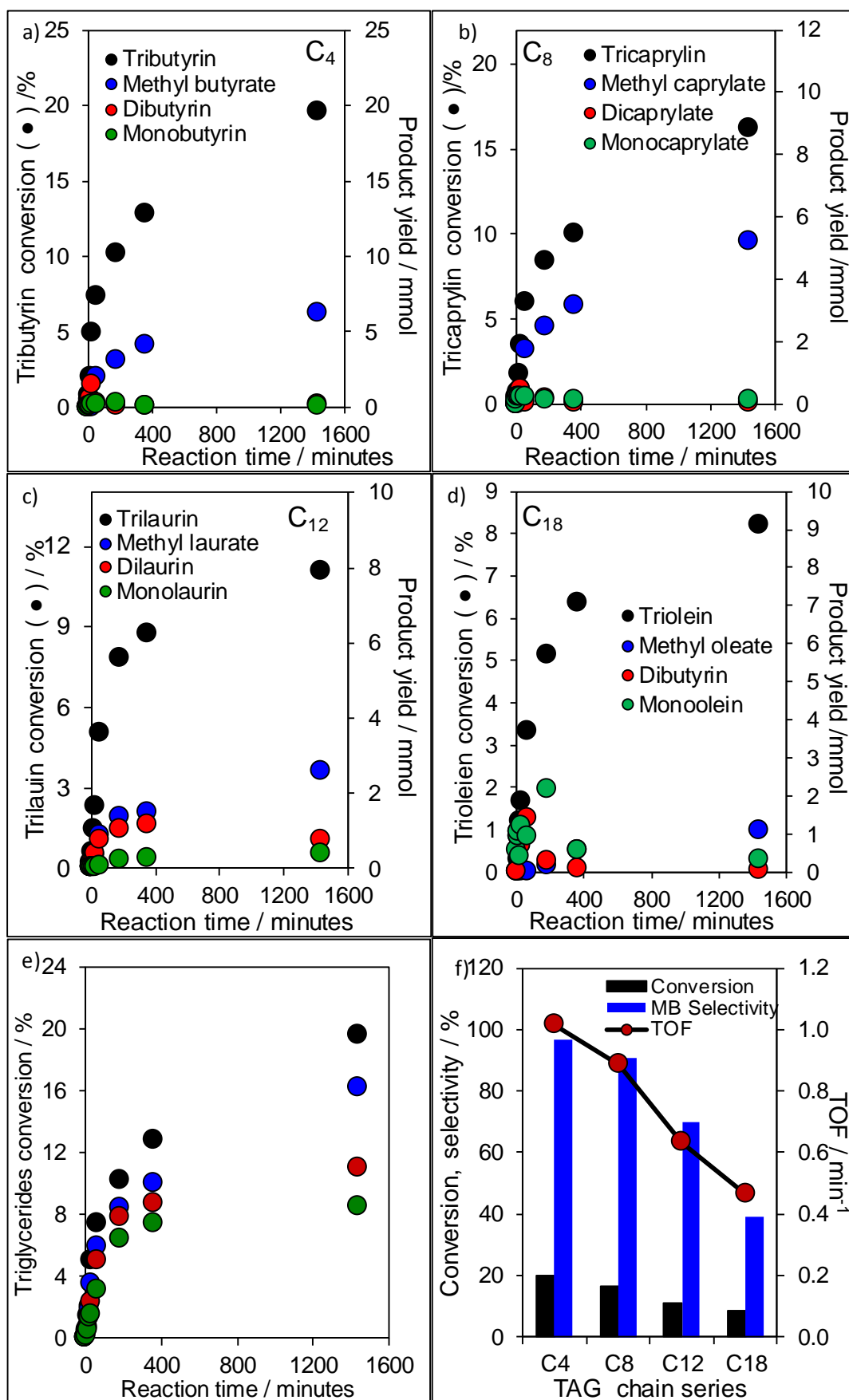


Figure 3.32 Conversion profiles of C4-C18 TAG on Zn:Al_{3.33}:1HTM (a-e) and TOF (f).

Tributyrin, C₄ is the shortest TAG chain used here and has the highest conversion and yield (Figure 3.32a). On moving to a bulkier TAG (C₈-C₁₈), slower initial rates have been observed in the first 400 min throughout the reactions (compared to C₄) indicating diffusion limitation is a problem (Figure 3.32b-d). This factor also has a significant impact on conversion, selectivity and TOF value, where those values decreased as well. The phenomenon indicating sterically hindered triglycerides has limited the reaction to occurred simultaneously. As the initial rates of TAG conversion decrease the observation of intermediates (dibutyrin and monobutyrin) increases, which may be attributed to these bulkier species being more weakly bound to the surface allowing them to desorb rather than react. For a better insight, a comparison of conversion and TOF of C₄-C₁₈ are summarised in **Figure 3.32e-f**. These studies demonstrate that as the TAG chain was increased from lower to higher (C₄-C₁₈), diffusion limitation occurred due to the steric hindrance of triglycerides. Increasing the TAG chain suppresses the accessibility of interlayer OH⁻ anions, as the diffusion of TAG molecules becomes harder, leading to a decreased turnover frequency (TOF) of transesterification⁷⁴.

3.4.6 Leaching Test of ZnAl HTM

To check the stability of the catalyst under reaction conditions a leaching test was conducted with the Zn:Al3.33:1HTM catalyst, with the catalyst removed from the reactor by hot filtration after 3h of reaction. As illustrated by the reaction profile in **Figure 3.33a**, the conversion of tributyrin was abruptly stopped after removal of the catalyst at 3h and gave 28 % of conversion. Moreover, the composition of the products did not change after filtering. These results confirm that catalysis was associated with the solid phase material, meaning no homogeneity of the catalyst involved here. To further confirm if there any changes in the functional group before and after the catalyst was removed, DRIFTS study has been done on the biodiesel solution at T0, T3h and T24h. Results are shown in **Figure 3.33b**. Meanwhile the band wavelength is presented in **Table 3.9**.

DRIFTS spectra showed no significant changes of the functional groups present at or near the surface.. At T0, the vibration of νO-H (3327 cm⁻¹) was detected from methanol used. Around 3500 cm⁻¹ is assigned to an olefin vibration. Ester groups (ν_{as}C=O and ν_{as}C-O) have been detected at 1748 cm⁻¹ and 1163 cm⁻¹ in all T0, T3h and T24h indicating that no leaching has occurred.

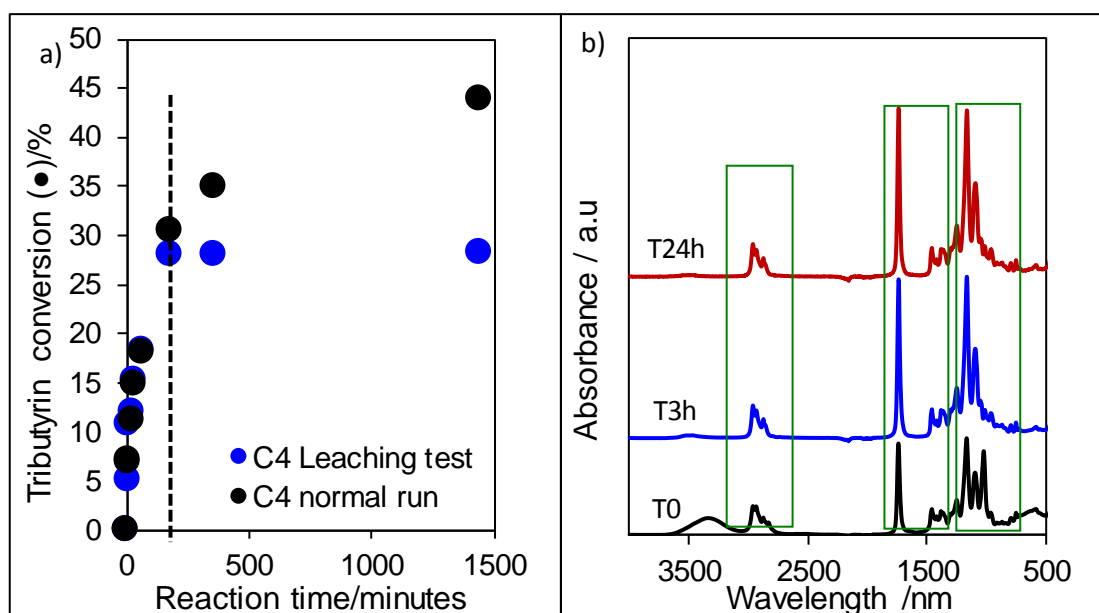


Figure 3.33 Leaching profile of for transesterification of tributyrin with methanol using ZnAl HTM catalyst (ratio 3.33:1) (a). DRIFT spectra of biodiesel solution taken at T0, T3h and T24h(b). Reaction conditions: 100 mg catalyst, 4.98 ml tributyrin, 24.4 ml methanol and 1.18 ml dihexyl ether.

Table 3.9 Band wavelength of biodiesel reaction of C₄ obtained by DRIFTS.

Band/cm ⁻¹	Assignment
3327	vO-H
2925	v _{as} CH ₂
2854	v _s CH ₂
1748	v _{as} C=O
1163	v _{as} C-O

To further measure the content of Zn and Al in the residues filtered off, ICP-OES was used. The method used that as described in Chapter 2. ICP detected a very low concentration of metal ions in the solutions (**Table 3.10**). Only 1.84 % of the catalyst was found leached after the reaction. Somehow, this tiny amount seems to not affect the conversion value during transesterification reaction and is, therefore, negligible. This further confirmed leaching could be disregard here.

Table 3.10 The concentration of Zn and Al (3.33:1) in leaching tests as determined by ICP-OES.

Sample/ time taken	Mass concentration / %		Total ZnAl leaching / %
	Zn	Al	
Before filter	0.298	0.121	
After filter	1.560	0.700	
Leaching	1.262	0.579	1.84

3.4.7 Reusability Study of ZnAl HTM

The Zn:Al_{3.33}:1HTM catalyst was reused three times **Figure 3.34a** to further assess the stability. During the test, the catalyst was retaining its activity for at least three cycles in tributyrin with minimal loss in activity and Zn:Al ratio is almost the same (**Table 3.11**). Further characterisation by ICP showed Zn atomic content has also reduced from 31.53 % to 25.93 %. This further confirmed may be active sites of Zn has been reduced throughout the recycles times as the Zn atomic weight decreased after the third cycles. Meanwhile, CHNS shows an increase in carbon content after the third cycle. This could probably explain the relative loss of Zn and Al content as due to carbon formation on the third recycle, which probably built up from incomplete calcination process) which has also affected the activity of the recycled catalyst. Conversion, selectivity and the initial rates hence decreased accordingly (**Figure 3.34b**).

The retained structure of ZnAl HTM was confirmed by PXRD in which we can see no shift of 003 reflections occurred in all patterns (**Figure 3.35**). This indicates no changes occurred in the interlayer spacing either resulting from intercalation of substrates or products. Somehow, the d(003) intensity has dropped from fresh to the third cycle brings the purity of reconstructed ZnAl LDH from 78.4 % to 66.5 % respectively. PXRD patterns also depicted a different reflection especially from d(101) onwards. This has proven that the lamellar structure has been affected by each cycle, thus decreasing the purity of the catalyst. The crystalline structure now has turned to amorphous like after third cycles.

Table 3.11 The atomic weight of Zn and Al on fresh and third cycles determined by ICP-OES and the carbon content from CHNS on Zn:Al_{3.33}:1HTM catalyst.

Sample	Atomic concentration / %		Total ratio	C content from CHNS / %
	Zn	Al		
Fresh	31.53	10.36	3.15	1.45
Third cycle	25.93	8.32	3.11	1.72

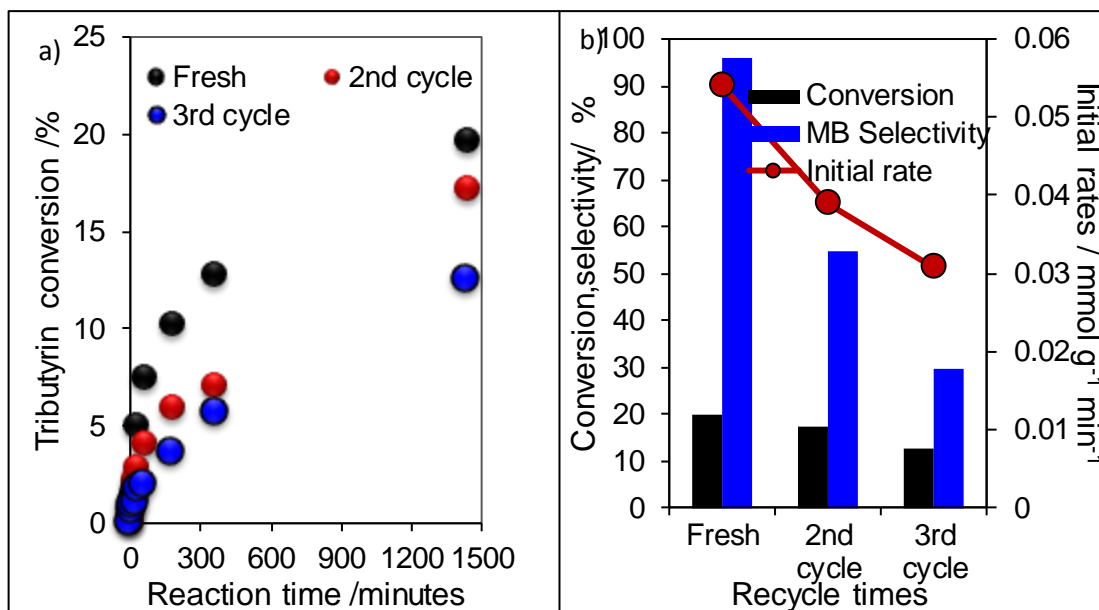


Figure 3.34 Catalyst recyclability study involved Zn:Al_{3.33}:1HTM for three cycles involved fresh, and spent catalysts (2nd and 3rd cycle).

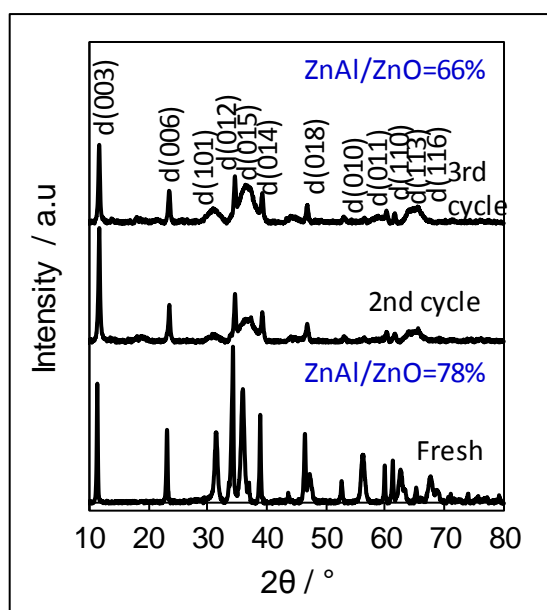


Figure 3.35 PXRD patterns of fresh and spent catalysts (2nd and 3rd cycle). The intensity ratio of ZnAl HT/ZnO is denoted in percentage value.

3.5 Conclusion

This study makes several noteworthy contributions to the application of hydrothermally reconstructed ZnAl LDH materials which are as follows:

i) The alkali-free co-precipitation (ppt) method that has been adapted for this ZnAl LDH synthesis for the first time has shown a superior base sites density and also overcomes the common leaching problem obtained from alkali co-ppt method.

ii) Reconstruction of ZnAl LDH via hydrothermal methods outdone the performances of the gas and liquid-phase rehydration methods in all scopes especially in regards to the textural parameter and catalytic reaction.

iii) Hydrothermally reconstructed ZnAl LDH materials show remarkable promising avenue in model chain triglycerides in transesterification reaction matter. These results could be extended and adapted for use in the real oil if further improvement of catalyst active site accessibility could be improved. Enlargement of pores such as through macroporous-mesoporous study could help overcomes diffusion limitation of higher TAG and aids the reactivity.

Based on both results in leaching and reusability studies, it is now affirmed ZnAl LDH is a heterogeneous catalyst which leaching is almost negligible. The result from recycling study shows a potential reduction of active sites happened in each cycle due to the Zn content has found to be reduced after third cycles.

3.6 References

- (1) Rodriguez-Chiang, L.; Llorca, J.; Dahl, O. *Bioresour. Technol.* **2016**, *218*, 84–91.
- (2) Zhang, J.; Li, Y.; Zhou, J.; Chen, D.; Qian, G. *J. Hazard. Mater.* **2012**, *205–206*, 111–117.
- (3) Li, D.; Lu, M.; Aragaki, K.; Koike, M.; Nakagawa, Y.; Tomishige, K. *Appl. Catal. B Environ.* **2016**, *192*, 171–181.
- (4) Hu, Q.; Yang, L.; Fan, G.; Li, F. *J. Catal.* **2016**, *340*, 184–195.
- (5) Zhang, X.; Yang, S.; Xie, X.; Chen, L.; Sun, L.; Zhao, B.; Si, H. *J. Anal. Appl. Pyrolysis* **2016**, *120*, 371–378.
- (6) Carja, G.; Husanu, E.; Gherasim, C.; Iovu, H. *Appl. Catal. B Environ.* **2011**, *107*, 253–259.
- (7) Hallett-Tapley, G. L.; Crites, C.-O. L.; González-Béjar, M.; McGilvray, K. L.; Netto-Ferreira, J. C.; Scaiano, J. C. *J. Photochem. Photobiol. A Chem.* **2011**, *224*, 8–15.
- (8) Theiss, F. L.; Ayoko, G. A.; Frost, R. L. *Appl. Surf. Sci.* **2016**, *383*, 200–213.
- (9) Paušová, Š.; Krýsa, J.; Jirkovský, J.; Forano, C.; Mailhot, G.; Prevot, V. *Appl. Catal. B Environ.* **2015**, *170*, 25–33.
- (10) Bunekar, N.; Tsai, T.-Y.; Yu, Y.-Z. *Mater. Today Proc.* **2016**, *3*, 1415–1422.
- (11) Zhang, J.; Li, Y.; Zhou, J.; Chen, D.; Qian, G. *J. Hazard. Mater.* **2012**, *205*, 111–117.
- (12) Coronado, E.; Martí-Gastaldo, C.; Navarro-Moratalla, E.; Ribera, A. *Appl. Clay Sci.* **2010**, *48*, 228–234.
- (13) Yan, L.; Yang, K.; Shan, R.; Yan, T.; Wei, J.; Yu, S.; Yu, H.; Du, B. *J. Colloid Interface Sci.* **2015**, *448*, 508–516.
- (14) Zhong, L.; He, X.; Qu, J.; Li, X.; Lei, Z.; Zhang, Q.; Liu, X. *J. Solid State Chem.* **2017**, *245*, 200–206.
- (15) Chen, Y.; Shui, Z.; Chen, W.; Chen, G. *Constr. Build. Mater.* **2015**, *93*, 1051–1058.
- (16) Kühn, S.; Schumann, J.; Kasatkin, I.; Hävecker, M.; Schlögl, R.; Behrens, M. *Catal. Today* **2015**, *246*, 92–100.
- (17) Birjega, R.; Vlad, A.; Matei, A.; Ion, V.; Luculescu, C.; Dinescu, M.; Zavoianu, R. *Thin Solid Films* **2016**, *614*, 36–41.
- (18) Sturgeon, M. R.; O'Brien, M. H.; Ciesielski, P. N.; Katahira, R.; Kruger, J. S.;

- Chmely, S. C.; Hamlin, J.; Lawrence, K.; Hunsinger, G. B.; Foust, T. D.; Baldwin, R. M.; Bidy, M. J.; Beckham, G. T. *Green Chem.* **2014**, *16*, 824.
- (19) Montañez, M. K.; Molina, R.; Moreno, S. *Int. J. Hydrogen Energy* **2014**, *39*, 8225–8237.
- (20) Tadanaga, K.; Miyata, A.; Ando, D.; Yamaguchi, N.; Tatsumisago, M. *J. Sol-Gel Sci. Technol.* **2012**, *62*, 111–116.
- (21) Mostafa, M. S.; Bakr, A.-S. A.; El Nagggar, A. M. A.; Sultan, E.-S. A. *J. Colloid Interface Sci.* **2016**, *461*, 261–272.
- (22) He, M.; Kang, L.; Liu, C.; Lei, Z.; Liu, Z.-H. *Mater. Res. Bull.* **2015**, *68*, 194–202.
- (23) Bhattacharjee, S.; Anderson, J. A. *J. Mol. Catal. A Chem.* **2006**, *249*, 103–110.
- (24) Dula, R.; Janik, R.; Machej, T.; Stoch, J.; Grabowski, R.; Serwicka, E. M. *Catal. Today* **2007**, *119*, 327–331.
- (25) Giovannelli, F.; Zaghrioui, M.; Autret-Lambert, C.; Delorme, F.; Seron, A.; Chartier, T.; Pignon, B. *Mater. Chem. Phys.* **2012**, *137*, 55–60.
- (26) Liu, Q.; Wang, B.; Wang, C.; Tian, Z.; Qu, W.; Ma, H.; Xu, R. *Green Chem.* **2014**, *16*, 2604.
- (27) Liu, Q.; Wang, C.; Qu, W.; Wang, B.; Tian, Z.; Ma, H.; Xu, R. *Catal. Today* **2014**, *234*, 161–166.
- (28) Meng, Z.; Zhang, Y.; Zhang, Q.; Chen, X.; Liu, L.; Komarneni, S.; Lv, F. *Appl. Surf. Sci.* **2016**.
- (29) Cantrell, D. G.; Gillie, L. J.; Lee, A. F.; Wilson, K. *Appl. Catal. A Gen.* **2005**, *287*, 183–190.
- (30) Bankauskaite, A.; Baltakys, K. *J. Therm. Anal. Calorim.* **2015**, *121*, 227–233.
- (31) Everaert, M.; Warrinnier, R.; Baken, S.; Gustafsson, J. P.; De Vos, D.; Smolders, E. *ACS Sustain. Chem. Eng.* **2016**, *4*, 4280–4287.
- (32) Wiyantoko, B.; Kurniawati, P.; Purbaningtias, T. E.; Fatimah, I. *Procedia Chem.* **2015**, *17*, 21–26.
- (33) F. Cavani, F. Trifiro, A. V. *Catal. Today* **1991**, *2*, 173–301.
- (34) Touahra, F.; Sehailia, M.; Ketir, W.; Bachari, K.; Chebout, R.; Trari, M.; Cherifi, O.; Halliche, D. *Appl. Petrochemical Res.* **2015**.
- (35) Hasan, H. M. I.; Masoud, M. S. **2014**, *12*, 11–22.
- (36) Wang, Q.; Tay, H. H.; Guo, Z.; Chen, L.; Liu, Y.; Chang, J.; Zhong, Z.; Luo, J.; Borgna, A. *Appl. Clay Sci.* **2012**, *55*, 18–26.
- (37) Pavel, O. D.; Zăvoianu, R.; Bîrjega, R.; Angelescu, E.; Costentin, G.; Che, M. *Appl. Clay Sci.* **2015**, *104*, 59–65.
- (38) Melián-Cabrera, I.; López Granados, M.; Fierro, J. L. G. *Phys. Chem. Chem. Phys.* **2002**, *4*, 3122–3127.
- (39) Kooli, F.; Ge, C. D.; Ennaqadi, A.; Roy, A. D. E.; Besse, J. E.; Matriaux, L. D. P.; Cnrs, U. R. A.; Pascal, U. B.; Cedex, A. **1997**, *45*, 92–98.
- (40) Thevenot F; Szymanski R; Chaumette, P. *Clays Clay Miner.* **1989**, *37*, 396–402.
- (41) Shirley Nakagaki, Karen Mary Mantovani, Guilherme Sippel Machado, K. A. D. de F. C. and F. W. *Molecules* **2016**, *21*, 291.
- (42) Carriazo, D.; Arco, M.; García-lópez, E.; Marci, G.; Martín, C.; Palmisano, L.; Rives, V. *Journal Mol. Catal. A, Chem.* **2011**, *342–343*, 83–90.
- (43) Cavani F, T. F. & V. A. *Catal. Today* **1991**, *11*, 173–301.
- (44) Oil, V. **2015**, *8*, 422–433.
- (45) Hosono, E.; Fujihara, S.; Kimura, T.; Imai, H. *J. Colloid Interface Sci.* **2004**, *272*, 391–398.
- (46) Lin, C.-C.; Li, Y.-Y. *Mater. Chem. Phys.* **2009**, *113*, 334–337.
- (47) Reinoso, D. M.; Damiani, D. E.; Tonetto, G. M. *Catal. Sci. Technol.* **2014**, *4*, 1803.
- (48) Debecker, D. P.; Gaigneaux, E. M.; Busca, G. *Chem. – A Eur. J.* **2009**, *15*, 3920–3935.
- (49) Brunauer, S.; Emmett, P. H.; Teller, E. *J. Am. Chem. Soc.* **1938**, *60*, 309–319.
- (50) Wang, S.-H.; Wang, Y.-B.; Dai, Y.-M.; Jehng, J.-M. *Appl. Catal. A Gen.* **2012**,

- 439–440, 135–141.
- (51) Wang, Z.; Lu, G.; Guo, Y.; Guo, Y.; Gong, X.-Q. *ACS Sustain. Chem. Eng.* **2016**, *4*, 1591–1601.
 - (52) Zeng, H.; Feng, Z.; Deng, X.; Li, Y. *Fuel* **2008**, *87*, 3071–3076.
 - (53) Zhao, Y.; Chen, G.; Bian, T.; Zhou, C.; Waterhouse, G. I. N.; Wu, L. Z.; Tung, C. H.; Smith, L. J.; O'Hare, D.; Zhang, T. *Adv. Mater.* **2015**, *27*, 7824–7831.
 - (54) Miyata, S. *Clays Clay Miner.* **1980**, *28*, 50–56.
 - (55) Paulo, M. J.; de Matos, B. R.; Ntais, S.; Fonseca, F. C.; Tavares, A. C. J. *Nanoparticle Res.* **2013**, *15*, 1–14.
 - (56) Abelló, S.; Medina, F.; Tichit, D.; Pérez-Ramírez, J.; Groen, J. C.; Sueiras, J. E.; Salagre, P.; Cesteros, Y. *Chem. – A Eur. J.* **2005**, *11*, 728–739.
 - (57) Meher, S. K.; Justin, P.; Rao, G. R. *ACS Appl. Mater. Interfaces* **2011**, *3*, 2063–2073.
 - (58) Wei, Y. .; Zhang, X. .; Wu, X. .; Tang, D. .; Cai, K. .; Zhang, Q. *RSC Adv.* **2016**, *6*, 39317–39322.
 - (59) Wang, Z.; Lu, G.; Guo, Y.; Guo, Y.; Gong, X.-Q. *ACS Sustain. Chem. Eng.* **2016**, *4*, 1591–1601.
 - (60) Álvarez, M. G.; Chimentão, R. J.; Figueras, F.; Medina, F. *Appl. Clay Sci.* **2012**, *58*, 16–24.
 - (61) Miyazaki, A.; Numata, M.; Etou, M.; Yonezu, K.; Balint, I.; Yokoyama, T. *Colloids Surfaces A Physicochem. Eng. Asp.* **2013**, *420*, 115–121.
 - (62) Van Der Laag, N.; Snel, M.; Mnelagusin, P.; Dewith, G. J. *Eur. Ceram. Soc.* **2004**, *24*, 2417–2424.
 - (63) Alexander V. Naumkin, Anna Kraut-Vass, Stephen W. Gaarenstroom, and C. J. P. NIST Standard Reference Database 20, Version 4.1. <https://srdata.nist.gov/xps> (accessed Oct 8, 2016).
 - (64) Daza, C. E.; Gallego, J.; Moreno, J. A.; Mondragón, F.; Moreno, S.; Molina, R. *Catal. Today* **2008**, *133–135*, 357–366.
 - (65) Teodorescu, F.; Pălăduță, A.-M.; Pavel, O. D. *Mater. Res. Bull.* **2013**, *48*, 2055–2059.
 - (66) Hammoud, D.; Gennequin, C.; Aboukaïs, A.; Aad, E. A. *Int. J. Hydrogen Energy* **2015**, *40*, 1283–1297.
 - (67) Klopprogge, J. T.; Hickey, L.; Frost, R. L. *J. Solid State Chem.* **2004**, *177*, 4047–4057.
 - (68) Woodford, J. J.; Dacquin, J.-P.; Wilson, K.; Lee, A. F. *Energy Environ. Sci.* **2012**, *5*, 6145.
 - (69) Chantrasa, A.; Phlernjai, N.; Goodwin, J. G. *Chem. Eng. J.* **2011**, *168*, 333–340.
 - (70) Liu, Y.; Lotero, E.; Goodwin, J. G.; Mo, X. *Appl. Catal. A Gen.* **2007**, *331*, 138–148.
 - (71) Singh, A. K.; Fernando, S. D. *Energy and Fuels* **2009**, *23*, 5160–5164.
 - (72) Bet-Moushoul, E.; Farhadi, K.; Mansourpanah, Y.; Molaie, R.; Forough, M.; Nikbakht, A. M. *Renew. Energy* **2016**, *92*, 12–21.
 - (73) Olutoye, M. A.; Wong, S. W.; Chin, L. H.; Amani, H.; Asif, M.; Hameed, B. H. *Renew. Energy* **2016**, *86*, 392–398.
 - (74) Wilson, K.; Hardacre, C.; Lee, A. F.; Montero, J. M.; Shellard, L. *Green Chem.* **2008**, *10*, 654.

Chapter 4

Alkali-free NiAl Hydrothermally Reconstructed Layer Double Hydroxide

4.1 Introduction

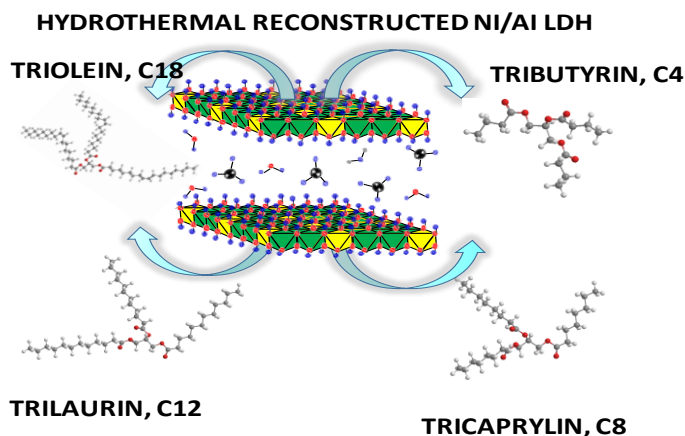
Nano-sized layered double hydroxides (LDHs) have gained great attention and been applied in a variety of applications due to its specialty to reconstruct the collapsed lamellar structure after calcination-rehydration process¹. Recent developments in hydrotalcite HT) synthesis have led to a proliferation of studies on various preparation steps²⁻⁴ and its application in many ways⁴⁻⁶.

Nowadays, metals such as Ni are receiving great interest from researchers due to the promising advantages they possess such as good conductivity, eco-friendliness and inexpensive catalysts, and also having the ability to produce various types of host structure with high proton mobility⁷. In terms of catalytic performance, Ni catalysts are preferable due to their active phase especially in hydrogenation reactions⁸, steam reforming⁹, depolymerisation of lignin¹⁰ and their ability to be applied as electrochemical capacitors⁴ and high-performance supercapacitors¹¹. Nevertheless, the catalytic activity and lifetime of Ni catalysts could vary depending on their physical and chemical properties.

MgAl HT, the common features of Al-based LDH have received huge attention over past decades, which includes the effect of the topotactical study (*Memory Effect-an ability of the lamellar to reconstruct after underwent calcination-rehydration process*)^{3,4,12-17}. For instance, a straightforward lamellar recovered from MgAl mixed oxides via gas-phase rehydration have been widely reported elsewhere^{18,19}. On the other hand, ZnAl mixed oxides are not fully reconstructed due to the formation of Al(OH) or ZnO, which was detected even though the precursor was calcined at a lower temperature (300-400 °C)²⁰. NiAl LDH has been predicted to be hard and challenging to reconstruct due to the formation of rigid mixed oxide after the calcination process^{21,22}. Due to that, a dearth of studies into the reconstruction of NiAl LDH have been reported compared to its mixed oxide (NiO) which has better stability exhibited from the Lewis basic site. Nevertheless, calcined LDH has a drawback which attributes to lower catalytic activity^{1,23}. Rehydration alternatively exhibits Brönsted base OH⁻ species which are highly favourable for base catalysed reactions^{1,19}.

Generally, reconstruction of NiAl LDH is possible yet needs special conditions such as controlling the calcination temperature or the reconstruction time¹. In terms of synthesis methods, some literature reported NiAl LDH were synthesised using a different method such as co-precipitation^{3,7-9,24}, urea hydrolysis^{16,24} or through a sol-gel method^{7,25}. These methods have their own drawbacks such as exhibiting poor crystallinity and poor adherence to the substrate in the catalytic reaction^{7,26}.

In addition to the above reasons, it is important to find an alternative to synthesise and reconstruct NiAl LDH in order to obtain good morphologies, structural properties and at the same time to improve the catalytic performance in the transesterification reaction. In the previous chapter, the ZnAl LDH materials were synthesised and investigated under gas-phase (GP), liquid-phase (LP) and hydrothermal (HTM) reconstructed conditions. From the catalytic results obtained, it was confirmed that HTM ZnAl LDH is more active compared to GP and LP in the transesterification of triglycerides. Inspired from that, again in this chapter, NiAl LDH has been prepared and reconstructed under similar HTM conditions (**Scheme 4.1**).



Scheme 4.1 Illustration of hydrothermally reconstructed NiAl layered double hydroxides (LDHs) applied in a transesterification reaction of triglycerides spanning from C₄ to C₁₈.

4.2 Novelty and contribution to knowledge

Alkali-free NiAl LDH was successfully synthesised for the first time and underwent hydrothermal reconstruction method. Also, for the first time, the application of these alkali-free catalysts in the transesterification of short and long chain triglycerides has been demonstrated.

4.3 Aim

The aims of this work were to develop hydrothermally reconstructed NiAl LDH, to investigate their physicochemical properties, as well as to explore their effects in biodiesel production via transesterification of bulky triglycerides.

4.4 Results and discussion

A family of NiAl HT materials were synthesised with different Ni:Al atomic ratios ranging from 1.5:1 to 4:1 (pH 9.5) via the green free-alkali method according to Woodford

*et al.*²⁷ and Cantrell *et al.*²⁸ except the main metal group was changed to Ni²⁺. NiAl LDH underwent calcination at 350 °C followed by reconstruction under a hydrothermal process. The successful synthesis has been confirmed via a range of characterisation techniques. Catalyst later has been tested in the transesterification reaction involving lower to bulkier TAG (C₄-C₁₈). The catalytic activity of reconstructed NiAl LDH has been studied and thoroughly investigated.

4.4.1 NiAl LDH Materials Characterisation

4.4.1.1 Energy dispersive X-Ray spectroscopy of NiAl LDH

Energy dispersive X-Ray (EDX) analysis was carried out in order to determine the bulk Ni:Al atomic ratio of the hydrotalcite and results are presented in **Table 4.1**. The bulk ratio was found to slightly deviate from the nominal ratio. As the Ni:Al atomic ratio increased from 1.5:1 to 4:1, it was found that Ni²⁺ content was increased, meanwhile, Al³⁺ content was decreased accordingly. The x value, the ratio between a number of Al atoms and sum of Al and Ni atoms (Al/(Al+Ni)), is also in good agreement with the Al³⁺ content. An EDX spectrum revealed that only Ni, O and Al atoms were present in the materials, as can be seen in **Figure 4.1**. No other alkali has been detected, proving the successful synthesis of the alkali-free NiAl LDH.

Table 4.1 The nominal and actual bulk of NiAl LDH atomic ratio.

Nominal atomic Ni:Al ratio	Ni at% bulk (EDX)	Al at% bulk (EDX)	Bulk atomic Ni:Al ratio (EDX)	$x=(Al/(Al+Ni))$
1.5:1	19.3	11.2	1.7 ± 0.1	0.37
2:1	20.7	8.7	2.4 ± 0.2	0.30
3:1	21.9	8.3	2.6 ± 0.1	0.27
4:1	22.7	5.9	3.9 ± 0.1	0.21

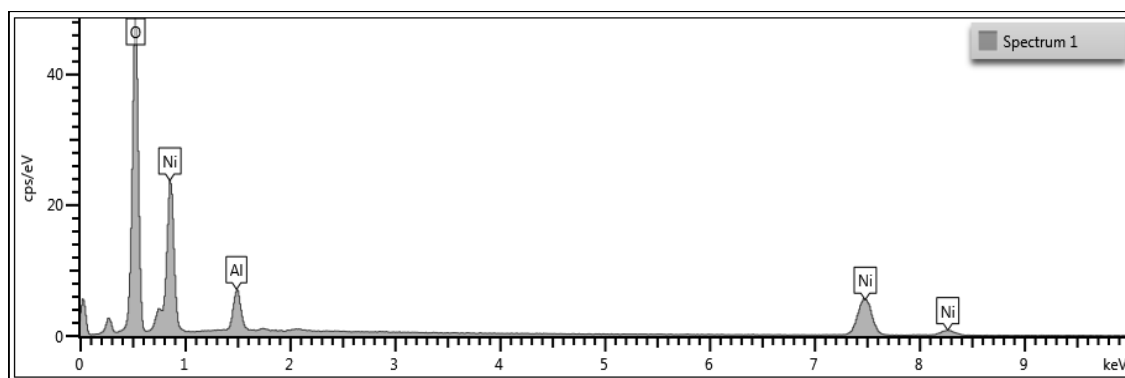


Figure 4.1 EDX spectra of Ni:Al3.85:1 LDH precursor.

4.4.1.2 Thermogravimetric analysis-Mass spectrometry of NiAl LDH

The results from thermal dehydration/decomposition of NiAl LDH precursor in the temperature range from 40-800 °C are shown in **Figure 4.2i-ii**. The profiles show two typical steps of weight loss of hydrotalcite. The first transition associated with loss of water from the interlayer occurred up to 149 °C (11-14 %) attributed to the removal of intercalated water molecules (**Table 4.2**).

The second weight loss was due to a dehydroxylation of LDH layers along with the decarbonation process and correlated with the MS analysis shown on peak $m/z = 44$. This transitions occurred around 261-355 °C with 9-12 % weight loss. Total weight loss of around 20-24 % is known as a common total weight loss of hydrotalcite²⁷. These data are correlated with NiAl LDH formula as shown in **Table 4.2**. As the Ni loading increased, the interlayer tends to expand more as the interlayer basal spacing value increases (will be further discussed in the sub-chapter 4.4.1.3). Thus the structure of Ni:Al3.85:1 exhibits more opportunity for H₂O to bind to the interlayer space which also contributes to higher weight loss compared to less Ni ratio in the series.

The NiAl LDH structural formula was determined by a combination of EDX and Thermogravimetric analysis (TGA) weight loss analysis using the formula previously mentioned in Chapter 3; $[M(II)_{1-x}M(III)_x(OH)_2]^{x+}(A^{n-}_{x/n}) \cdot mH_2O$ where $m = 0.81 - x$ ²⁹. This result correlated with a number of carbonate compounds deposits in the interlayer where it decreased with an increase of water amount. The measured amount of CO₃²⁻ and OH⁻ are also a reflection of the presence interlayer anions needed to compensate the divalent and trivalent of Ni²⁺ and Al³⁺ cations. Differential Scanning Calorimetry (DSC) profiles of Ni:Al LDH prepared from 1.72:1 to 3.85:1 showed heat flow steps at 45-232 °C are attributed to the absorbed water and dehydroxylation of water in the interlayer. Another

heat flow was observed at 270-350 °C is attributed to the loss of carbon dioxide from the interlayer anion.

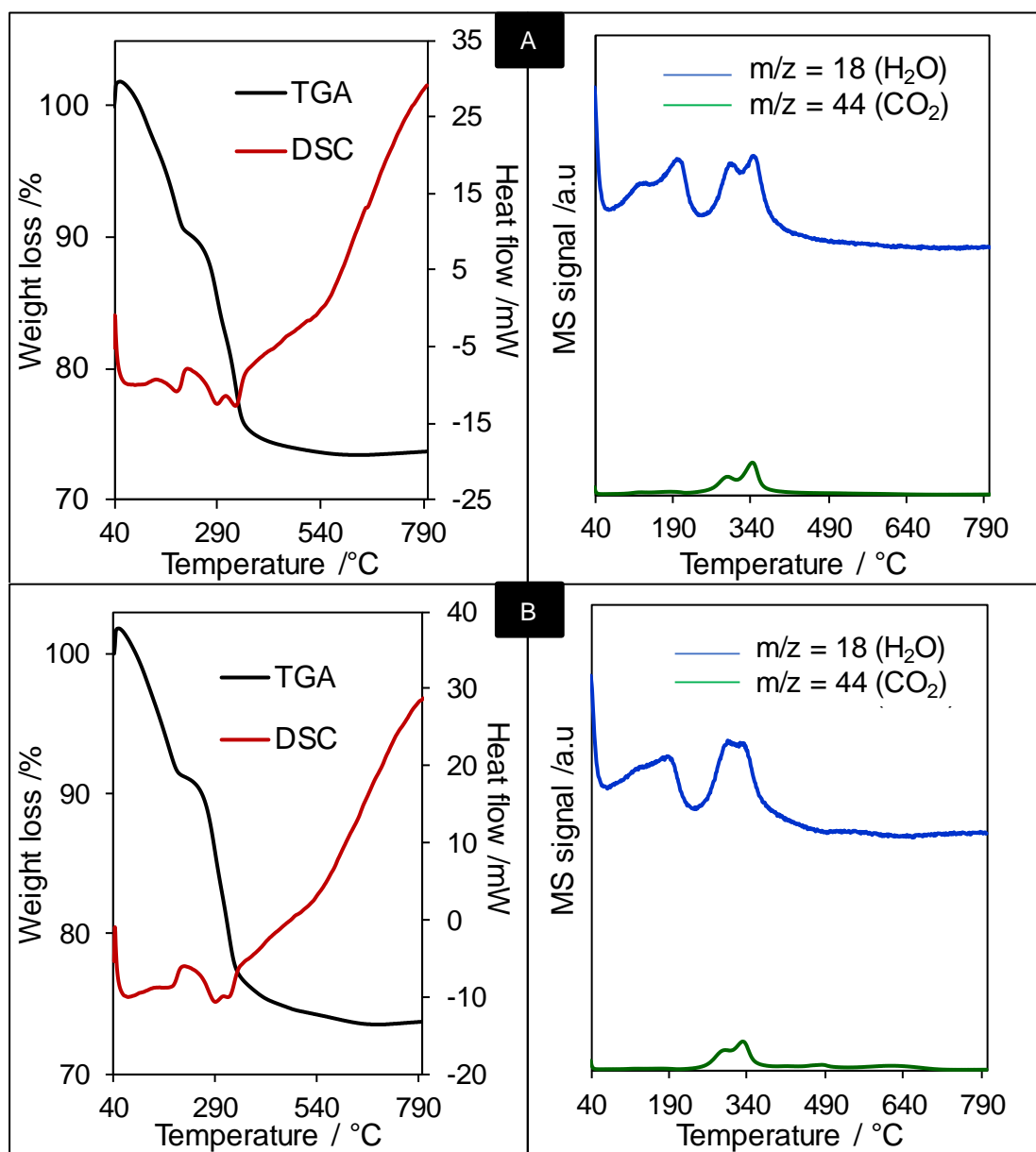


Figure 4.2i TGA/DSC with MS profiles during thermal decomposition of NiAl LDH from 40-800 °C on Ni:Al1.72:1 (A) and Ni:Al2.37:1 (B).

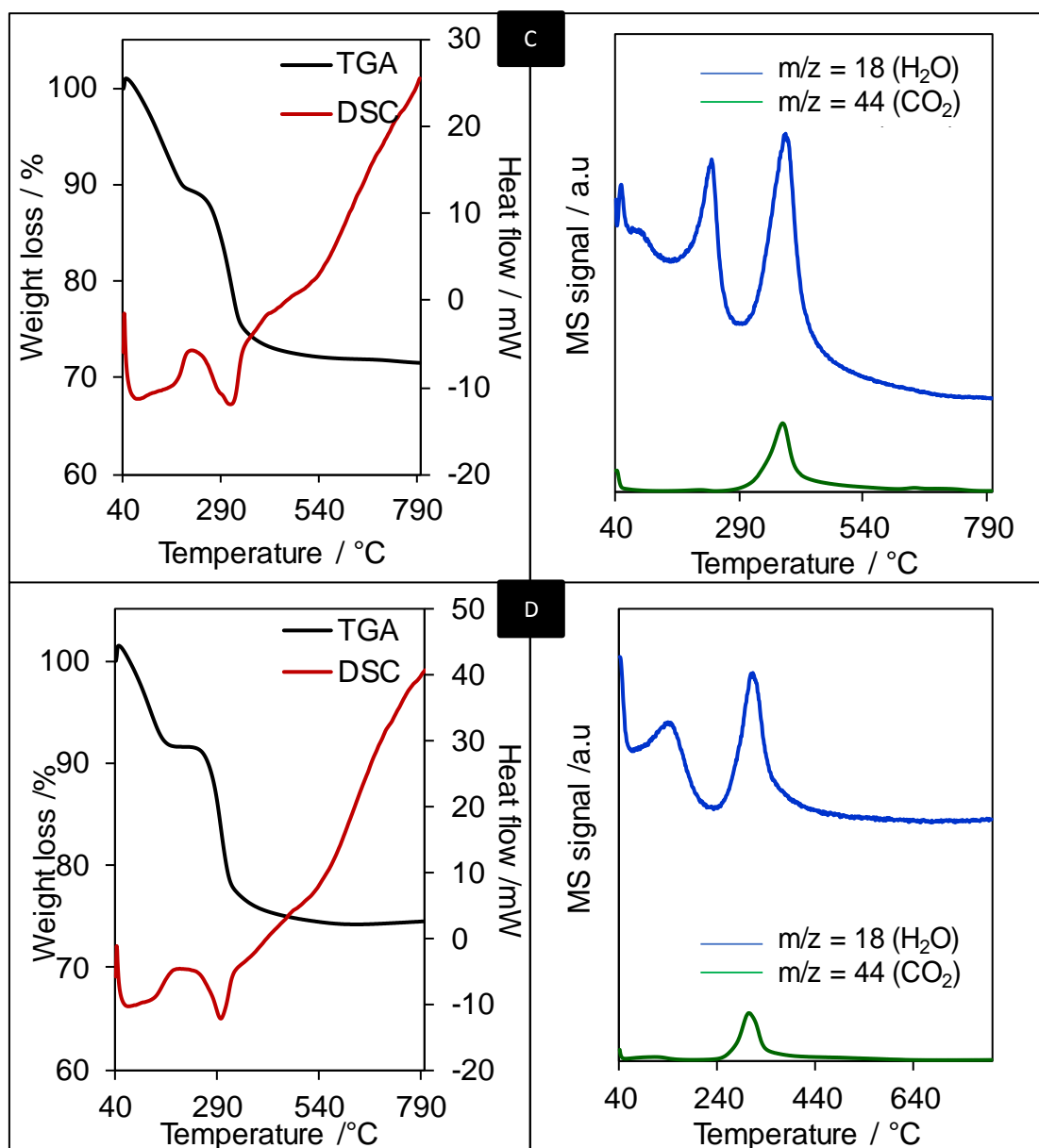


Figure 4.2ii TGA/DSC with MS profiles during thermal decomposition of NiAl LDH from 40-800 °C on Ni:Al_{2.64}:1 (C) and Ni:Al_{3.85}:1 (D).

Table 4.2 Comparison of water and carbonates in experimental and theoretical weight loss of NiAl LDH.

LDH catalyst/ weight loss	Experimental Weight loss / %			Theoretical weight loss /%			NiAl LDH Formula
	H ₂ O exp	CO ₃ exp	Total Weight loss/ %	H ₂ O theory	CO ₃ theory	Total Weight loss / %	
Ni:Al1.72:1	11.0	9.1	20.1	10.1	10.8	20.9	[Ni _{0.63} Al _{0.37} (OH) ₂].(CO ₃) _{0.18} 0.56H ₂ O
Ni:Al2.37:1	11.1	10.2	21.3	10.3	9.0	19.3	[Ni _{0.70} Al _{0.30} (OH) ₂].(CO ₃) _{0.15} 0.57H ₂ O
Ni:Al2.65:1	11.3	12.5	23.6	10.4	8.4	18.8	[Ni _{0.73} Al _{0.27} (OH) ₂].(CO ₃) _{0.14} 0.58H ₂ O
Ni:Al3.85:1	14.1	10	24.1	13.0	6.0	19.0	[Ni _{0.79} Al _{0.21} (OH) ₂].(CO ₃) _{0.10} 0.72H ₂ O

4.4.1.3 Powder X-ray diffraction of NiAl LDH

The as-synthesised, calcined and rehydrated NiAl LDH (ratio 1.72:1 to 3.85:1) were analysed by XRD to confirm the formation of pure hydrotalcite (**Figure 4.3a-d**). From the results obtained, it can clearly be seen NiAl LDH precursor possesses definite diffraction patterns appearing at 11.4° , 23.2° , 36.4° , 39.3° , 47° , with doublets at 60.1° and 62.7° (**Figure 4.3a**). Results are matched with data from the Joint Committee on Powder Diffraction Standards (JCPDS) catalogue: 15-0087 resembling a takovite structure³⁰. This confirmed that NiAl hydrotalcite has been successfully synthesised.

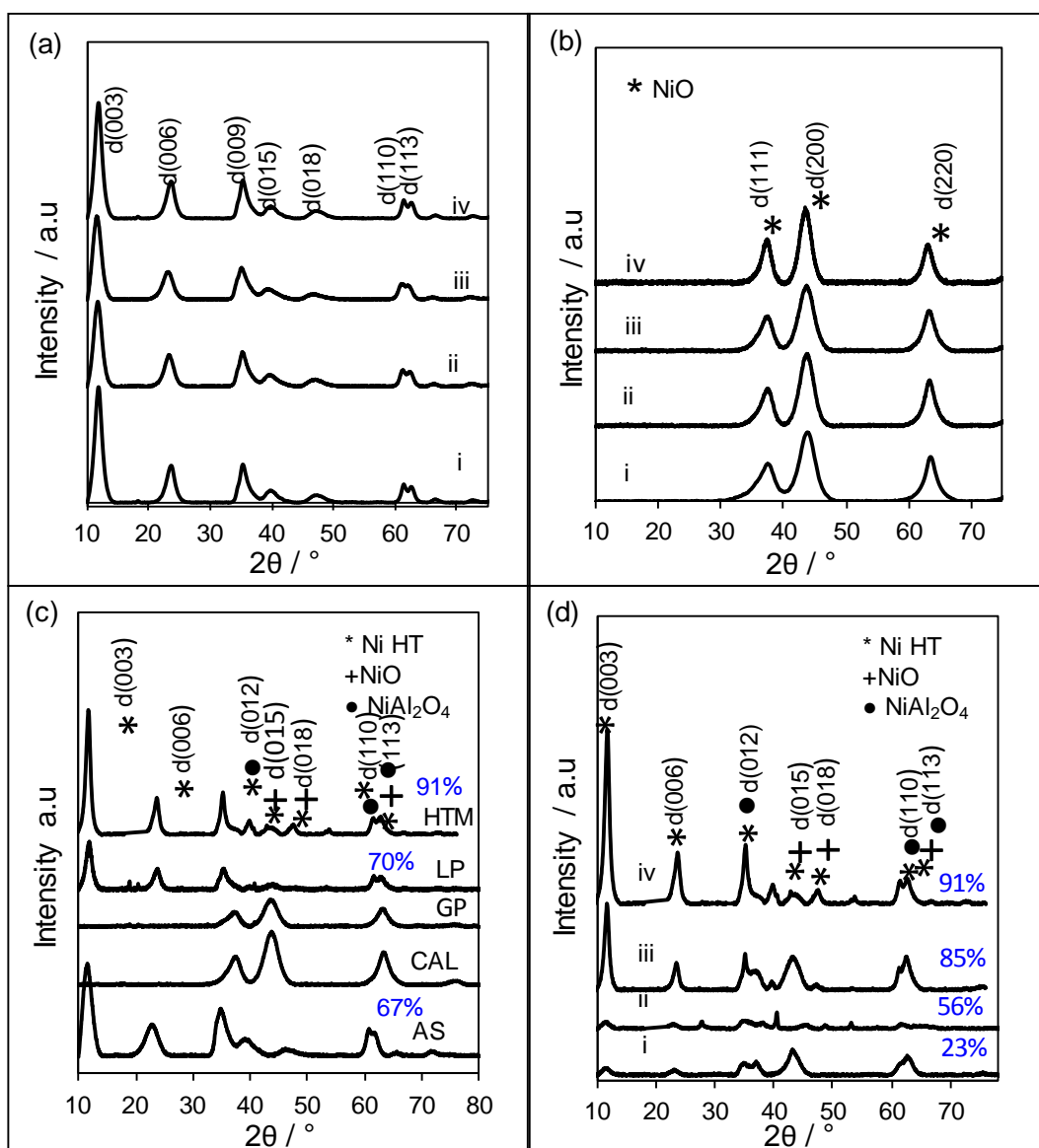


Figure 4.3 Offset wide-angle XRD patterns of as-synthesised NiAl LDH (a), calcined (b), comparison on as-synthesised, calcined, gas-phase, liquid-phase and hydrothermal reconstructed method on ratio 3.85:1 (c) and NiAl LDH hydrothermal series (d). Ni:Al1.72:1, Ni:Al2.37:1, Ni:Al2.64:1 and Ni:Al3.85:1 are denoted as i, ii, iii and iv respectively. The intensity ratio of NiAl HT/NiO is denoted in percentage value.

NiAl LDH was calcined at 350 °C following dehydroxylation and decarboxylation temperature in TGA-MS. During the calcination, this material shows diminishing peaks of hydrotalcite as it gets converted to mixed oxides and an appearance of NiO (bunsenite) at 37.4°, 43.9° and 63.3° (JCPDS:04-835) were detected (**Figure 4.3b**). These diffraction patterns matched most of the published findings in the literature^{31,32}. No formation of NiAl₂O₃ has been observed and detected in these calcined series.

It has been reported that NiAl hydrotalcite reconstruction is rarely occurring due to the formation of a rigid spinel after the calcination above 500 °C²². Factors that contribute to successful rehydration/reconstruction have been discussed in **Chapter 1 (1.1.4)**. Reconstruction of NiAl LDH via gas-phase failed as can be seen from the data in **Figure 4.3c**. This is due to the rigid formation of NiO formed during calcination process. To improve it, NiO was rehydrated in a liquid phase and rehydration was found to be successful and only 69.5 % was able to reconstruct. This amount is nearly the same as in the precursor where rehydration did not occur fully. These results inspired subsequent efforts to improve the crystallinity and purity of hydrotalcite by attempting reconstruction under hydrothermal techniques. Hydrothermal treatment improved the reconstruction towards 90.8 % purity of Ni HT/ NiO. The HTM reconstruction method over NiAl LDH gives comparatively higher purity of HT phase in comparison with the same method on ZnAl LDH (Chapter 3).

Alkali-free NiAl LDH series underwent successful hydrothermal treatment at mild temperatures (100 °C) as can be seen in **Figure 4.3d**. Incomplete reconstruction was observed at lower Ni content (ratio of 1.72 and 2.37) where the basal spacing of 003 is hardly formed. Thus, the intensity ratio of NiAl LDH over NiO is really low (23.4 and 56.3 %). Further increases of atomic ratio increased the purity of HTM formed toward 90.8 % as the d(003) basal spacing increased and the intensity peak got stronger. This shows hydrothermal reconstruction is influenced by the Ni and Al content in LDH where the ordered LDH was reformed. NiAl₂O₄ were also detected in the hydrothermal structure where previously it could not be detected in calcined samples as shown in XRD.

The effect of changing the hydrothermal Al content (x value) on basal spacing d(003), crystallite size and lattice parameter (a and c), can be seen in **Table 4.3** and **Figure 4.4a-b**. Basal spacing d(003) decreases with increasing Al content, or increases with Ni content as discussed earlier. Crystallite size, the value of average cation-cation distance a, and the thickness of the brucite c, are increased as the Ni content were increased. These results are correlated with the previous ZnAl LDH presented in sub-chapter 3.4.1.3. The reason behind this is due to increased cation content which increases the electrostatic attraction between the positive cation and negative anion in

the interlayer, thus interlayer distance will be expanded and crystallite size will be increased³³. Overall, hydrothermal techniques improved the textural parameter of NiAl LDHs compared to the as-synthesised materials.

Table 4.3 The textural parameter of basal spacing $d(003)$, lattice parameter and crystallite size of NiAl LDH precursor and hydrothermal.

Parameter / catalyst	d003 / nm	^a Lattice parameter / nm		^b Crystallite size / nm
		<i>a</i>	<i>c</i>	
<i>NiAl LDH precursor</i>				
Ni:Al 1.72:1 AS	0.74±0.01	0.302±0.016	2.26±0.13	5.0±0.3
Ni:Al 2.37:1 AS	0.74±0.01	0.302±0.017	2.24±0.06	5.1±0.3
Ni:Al 2.65:1 AS	0.74±0.02	0.303±0.017	2.26±0.03	5.5±0.2
Ni:Al 3.85:1 AS	0.75±0.02	0.305±0.018	2.29±0.08	5.8±0.4
<i>NiAl LDH hydrothermal</i>				
Ni:Al 1.72:1 HTM	0.73±0.01	0.300±0.016	2.25±0.12	4.1±0.3
Ni:Al 2.37:1 HTM	0.74±0.01	0.301±0.018	2.29±0.01	5.6±0.2
Ni:Al 2.65:1 HTM	0.74±0.01	0.302±0.018	2.29±0.05	8.7±0.2
Ni:Al 3.85:1 HTM	0.77±0.05	0.304±0.017	2.32±0.17	9.1±0.3

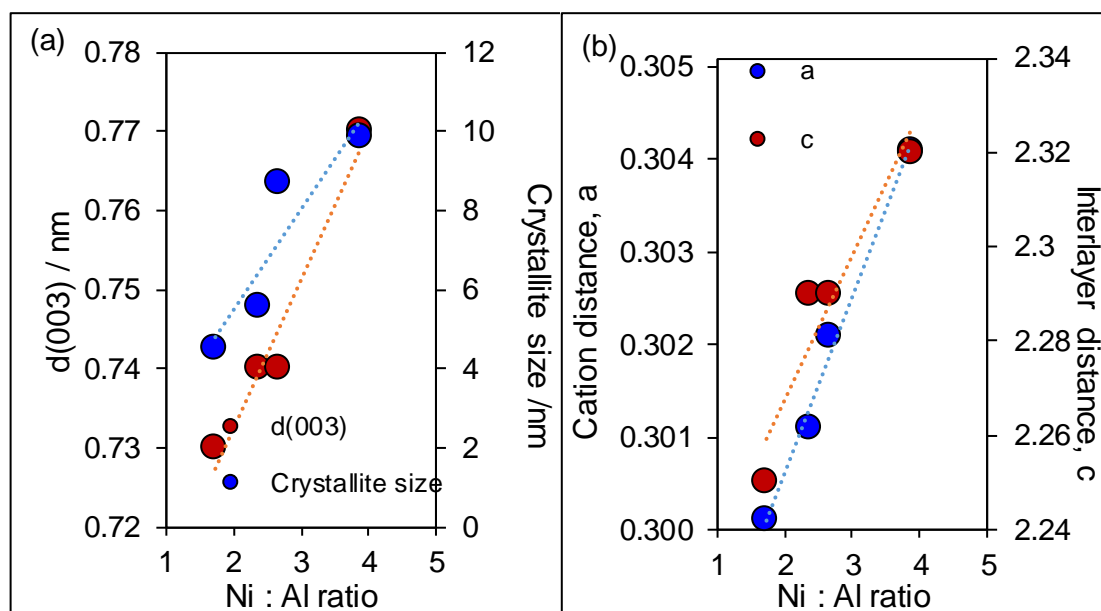


Figure 4.4 Effect of Al content on basal spacing $d(003)$, crystallite size and lattice parameter (*a* and *c*).

4.4.1.4 Nitrogen porosimetry of NiAl AS and NiAl HTM

All eight NiAl compilation isotherms (precursor and hydrothermal) are plotted in **Figure 4.5a-b**. The data show Type II isotherms with H3 hysteresis loops based on the IUPAC classification³⁴. Figures were offset for clarity. Narrow loops again have been observed in most of the samples and are more pronounced in the hydrothermal samples. This contributes to the higher surface area as depicted in **Table 4.4**. Generally, no trend of increasing or decreasing surfaces area has been observed across the series of hydrothermal samples. This concludes NiAl loading does not influence the surface area. Somehow, the surface area of ratio 1.72:1 and 3.85:1 were slightly higher after hydrothermal treatment. The reason behind this is might be due to the increased growth and expansion of crystal as being induced by water and heat from the hydrothermal process at the same time.

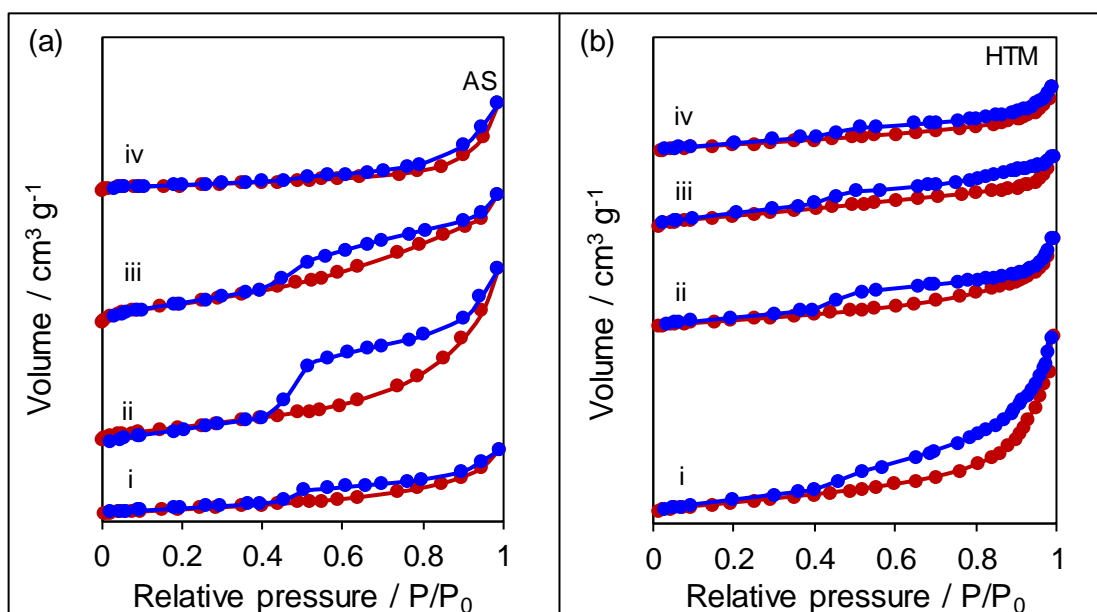


Figure 4.5 Stacked adsorption-desorption isotherms of NiAl LDH precursor and hydrothermal series. i-iv are the ratio of Ni:Al synthesised from 1.72:1, 2.37:1, 2.65:1 and 3.85:1.

The effect of rehydration under hydrothermal time has been studied by Kovanda *et al.*³⁵ via alkali-precipitation method. They observed the effect of different hydrothermal time (2 h, 4 h and 20 h) on the synthesis of NiAl LDH. They found that BET surface area was increased 17 m²/g from the original value after a short (4 h) hydrothermal treatment. Somehow, the BET surface area was decreased after a longer (20 h) hydrothermal treatment, which is in agreement with Kovanda *et al.*³⁶ and Saiah *et al.*³⁷. This could be explained by the unambiguous process of dissolution of Ni(Al)O and NiAl LDH recrystallisation that occurred under longer hydrothermal exposures^{1,35}. However, in our experiments, it is hard to prove how rehydration time could influence the

surface area as we are not measuring that particular parameter specifically. Another possible reason that could decrease the BET surface area might be due to pore blockage as Ni tends to form agglomerates when the Ni loading was increased⁸.

Table 4.4 BET surface area (S_{BET}) for NiAl precursor and hydrothermal LDH.

Ni:Al ratio	BET Surface area / m ² /g
<i>NiAl LDH precursor</i>	
1.72	123±25
2.37	154±11
2.65	236±13
3.85	77±20
<i>NiAl LDH hydrothermal</i>	
1.72	177±5
2.37	152±4
2.65	207±6
3.85	129±5

Again, a more accurate pore has been measured by DFT method³⁴ using QuantaChrome Autosorb instrument (under N₂ at 77 K) and results are presenting in **Figure 4.6a-b**. The plot for NiAl HTM clearly exhibits at 3.5 nm (**Figure 4.6a**) corresponding to mesopores with attributes that include internal void and interlayer spacing^{38,39}. These results are also in agreement with those reported by Meher *et al.*³⁸ and Wei *et al.*³⁹ where the cumulative pore volume of the mesoporous samples~2.4-3.7 nm. The fitted and measured pore volumes are identical as can be seen in **Figure 4.6b**. As NiAl LDH exhibits high surface area, the pathway of mass transport in transesterification reaction is permissible.

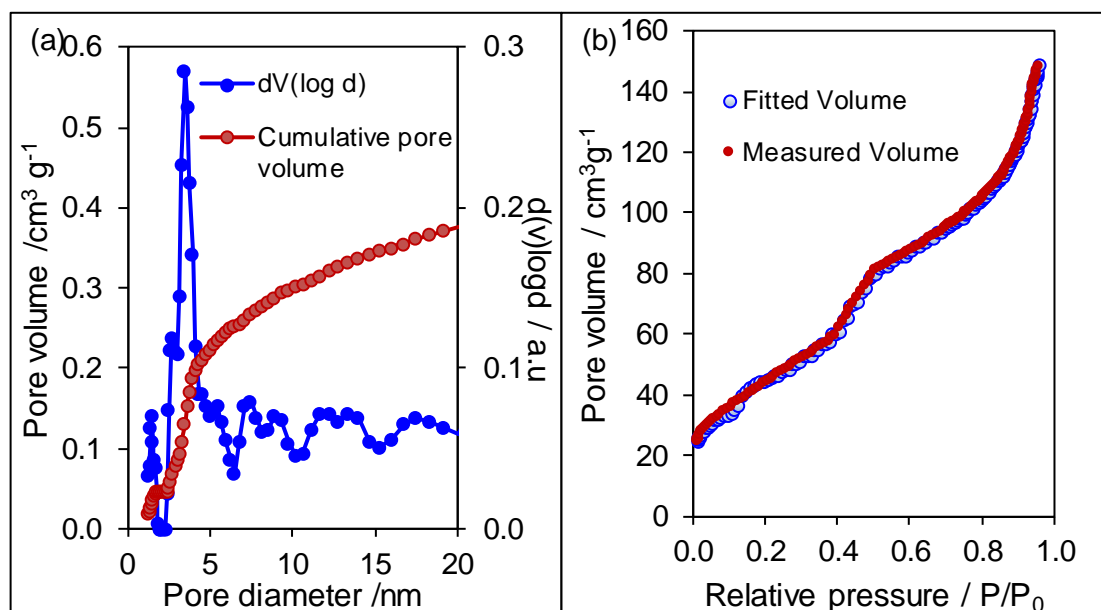


Figure 4.6 Pore size distribution and fitting plot for NiAl LDH.

4.4.1.5 Scanning electron microscopy of NiAl LDH

The morphologies of catalyst were further characterised by SEM (**Figure 4.7**).

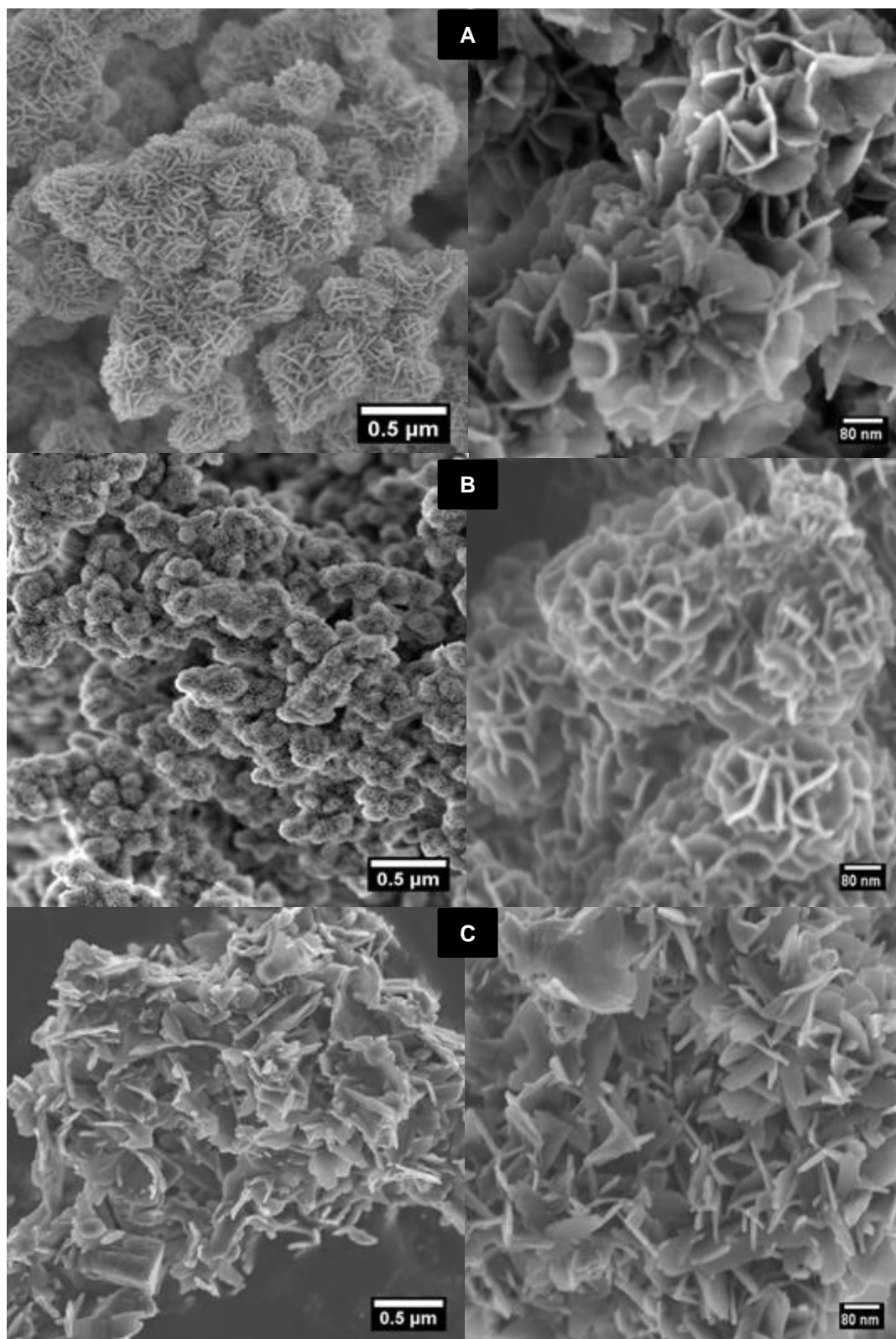


Figure 4.7 SEM images NiAl LDH (ratio 3.85:1) at different stages; the precursor (A) undergone calcined (B) and hydrothermal reconstruction (C) respectively.

SEM images of NiAl HT showed morphology was changed upon calcination and rehydration processes, yet the hexagonal structure remains intact. HTM images showed the '*Memory Effect*' of NiAl LDH has been regained.

4.4.1.6 High-resolution scanning transmission electron microscopy of NiAl LDH

Samples were subsequently analysed by HR-STEM to screen the morphology of precursor and HTM as depicted in **Figure 4.8**.

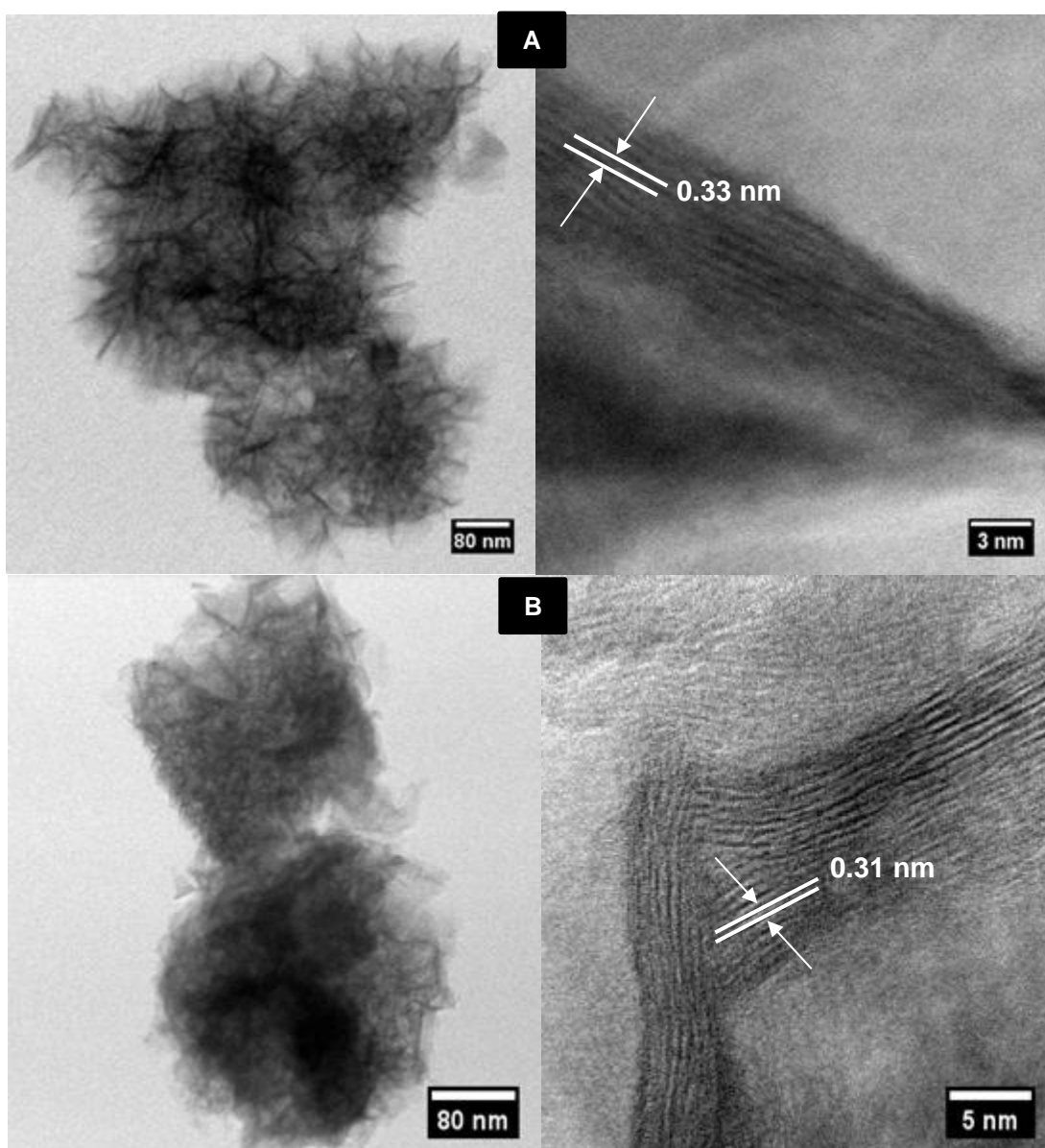


Figure 4.8 HR-STEM images of NiAl LDH with comparison with as-synthesised (A) and after hydrothermal (B) reconstruction techniques on Ni:Al3.85:1 catalyst.

The assemblies of the whisker-like structure were observed on the precursor. According to Nishimura *et al.*¹⁵, these features are due to the initial crystallisation of nuclei prior to the formation of hexagonal LDH structures. Lattice fringes on the precursor show that 0.33 nm corresponding to d(110) is slightly higher than data obtained from XRD on lattice parameter, *a* but still in the range of hydrotalcite lattice fringes. Lattice fringes of Ni/Al HTM at 0.31 nm are in the same agreement of lattice parameter *a*.

4.4.1.7 Solid-state Al-NMR of NiAl LDH

Al MAS-NMR spectra of fresh, calcined and hydrothermal reconstructed structure are presented in **Figure 4.9**. The main peak observed at 9.7 ppm representing a characteristic of octahedral aluminium (Al^{VI})^{1,40} where this peak does not change over calcined-rehydration techniques. Calcination has induced the formation of tetrahedral alumina, Al^{IV} (NiAl_2O_4) at 65 ppm, which somehow has not been detected by XRD. This peak reappeared with low intensity after hydrothermal reconstruction. These data affirmed that NiAl_2O_4 was present in calcined samples and remains after reconstruction via hydrothermal treatment as proven by XRD.

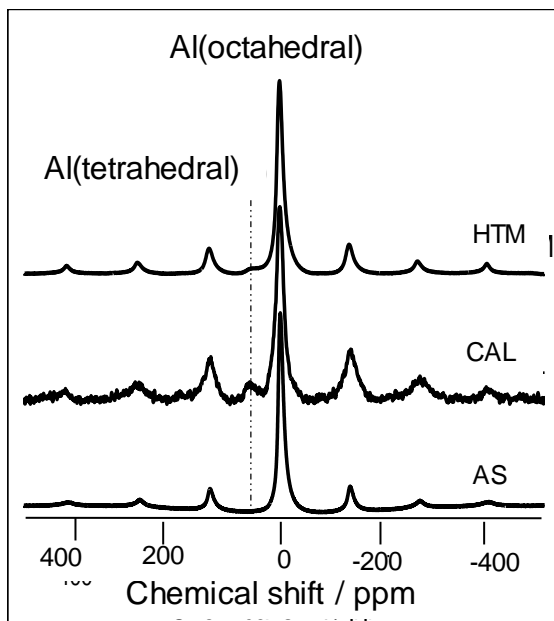


Figure 4.9 ^{27}Al MAS NMR spectra of Ni:Al3.85:1 hydrotalcite obtained at different stages approaches using 9.4 T magnet spectrometer with 14 kHz spin rates.

4.4.1.8 Diffuse reflectance infrared Fourier transform spectroscopy of NiAl AS and NiAl HTM

DRIFTS spectra of NiAl LDH series are presented in **Figure 4.10a-b**. The broad band around 3540 cm^{-1} is attributed to the stretching vibration of the O-H groups both in hydroxyl layers and interlayer water molecules⁴¹. Another weak bending mode of water is observed approximately around 1640 cm^{-1} . The difference between as synthesised and hydrothermal spectra can clearly be seen at OH functional group where the broad peaks were detected in the precursor compared to in hydrothermal treatment. This is possibly due to the amount of OH in the precursor are greater compared with a hydrothermal which underwent calcination process prior to that.

Calcination removed the water content during dehydration and dehydroxylation process. Upon rehydration, less than 100 % of the morphology has been recovered in the interlayer (proven by XRD whereby LDH were not fully reconstructed), hence the OH⁻ vibration detected by DRIFTS were significantly weaker compared to the precursor. A stretching of carbonate ions is observed as a sharp band at 1353 cm^{-1} . Bidentate carbonates are observed around 1443 cm^{-1} . The small peaks found around 750 cm^{-1} confirmed the presence of some nickel hydroxide.

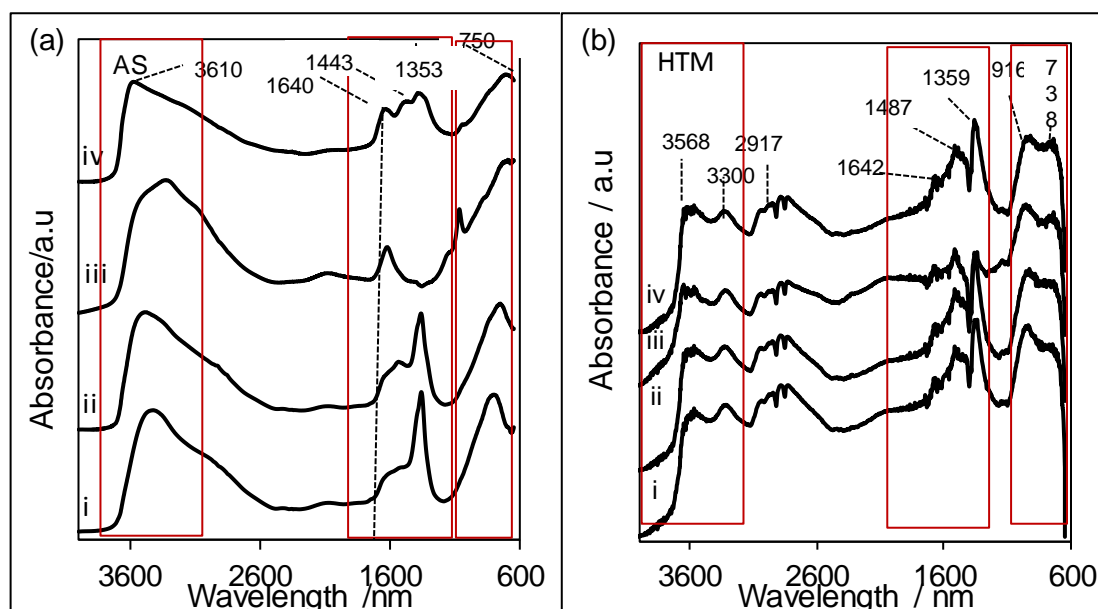


Figure 4.10 Stacked DRIFTS spectra of NiAl AS (a) and NiAl HTM (b) where i-iv represents the Ni:Al ratio from 1.72:1 to 3.85:1 respectively.

4.4.1.9 Temperature-programme desorption of CO₂ of NiAl HTM

In order to probe the basicity of the samples, temperature programmed desorption (TPD) profiles of the hydrothermal NiAl LDH are illustrated in **Figure 4.11**. From this profile, we can clearly see only one distinctive region detected on NiAl hydrotalcite samples. No bicarbonates group (weakly basic) detected on the catalyst at low temperature (100-200 °C). Bidentate carbonates are detected at a medium temperature from 201-380 °C. Meanwhile, the interaction of strong CO₂ in unidentate was found from 390 °C onwards. This indicates reconstructed hydrotalcite consists of two types of interactions which are Ni-O (bunsenite) and Ni₂AlO₄ which still remain after rehydration under hydrothermal conditions (proved by XRD).

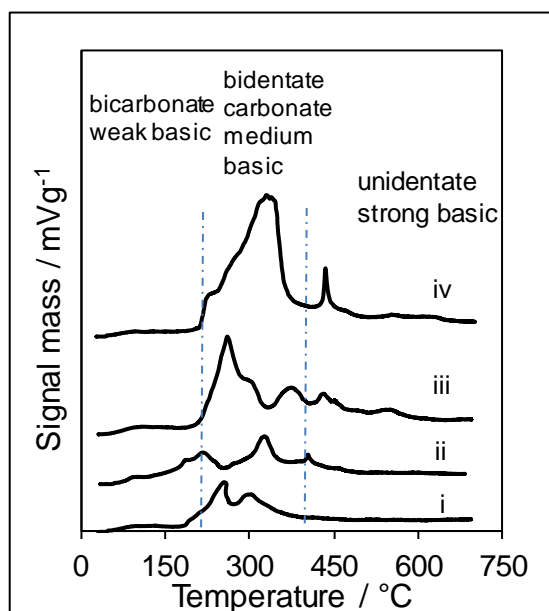


Figure 4.11 CO₂-TPD profile of NiAl hydrothermal reconstructed hydrotalcite series from 1.72-3.85 (i-iv).

There is no desorption peak observed at 450 °C which indicates that NiAl LDH only contained a medium basic site. Somehow, a bump of unidentate was observed in sample iv (3.85:1) might represent an amount of unidentate exists in this sample which correlated to the highest basicity among the series. This also proved that basic strength is increased with Ni/Al content. The basicity strength definitely will have an impact towards transesterification reaction as the reaction is favoured by a strong basic site catalyst. Basicity gradually increased as the Ni content increased as tabulated in **Table 4.5**. A comparison with precursor active sites is also included in this table.

Table 4.5 The amounts of basic sites in NiAl LDH samples.

Sample	Number of active sites ^a / mmol g ⁻¹	Base site density ^b / molecules g ⁻¹
<i>NiAl LDH precursor</i>		
Ni:Al1.72:1AS	0.014	8.6 x 10 ¹⁸
Ni:Al2.37:1 AS	0.010	6.2 x 10 ¹⁸
Ni:Al2.64:1 AS	0.074	4.5 x 10 ¹⁹
Ni:Al3.85:1 AS	0.023	1.4 x 10 ¹⁹
<i>NiAl LDH hydrothermal</i>		
Ni:Al1.72:1HTM	0.062	3.7 x 10 ¹⁹
Ni:Al2.37:1HTM	0.066	4.0 x 10 ¹⁹
Ni:Al2.64:1HTM	0.072	4.4 x 10 ¹⁹
Ni:Al3.85:1HTM	0.099	6.0 x 10 ¹⁹

^{a,b}Determined by CO₂ pulse chemisorption

4.4.1.10 X-ray photoelectron spectroscopy of NiAl HTM

XPS was employed to probe the surface structural information⁴² of NiAl hydrothermal reconstructed LDH. All spectra have been energy calibrated to adventitious carbon at 284.6 eV and background subtracted. Ni/Al HTM series were successfully synthesised and have been compared with pure Ni(OH)₂ standard sample (JCPDS 380715) and using NIST standard XPS database^{43,44}. Many kinds of literature are reported Ni 2p spectra appears as a mixture of NiO and Ni(OH)₂ from the region of 853.7 to 855.7 eV and making it harder to distinguish them due to these three major reasons^{45–47}: multiple splitting from complex structures of Ni 2p spectra^{48–50}, shake-up satellites and plasmon loss structure^{50–52} due to the probability of interaction between photoelectron and other electrons. Somehow, these assumptions have been denied and proven by Biesinger *et al.*⁵³ that those two NiO and Ni(OH)₂ possess different binding energies and spectra as can be seen in **Scheme 4.2**.



Scheme 4.2 Comparison of NiO and Ni(OH)₂ XPS spectra obtained from <http://xpssimplified.com/elements/nickel.php>.

The spectra depicted shifted regions between Ni 2p_{3/2} and Ni 2p_{1/2} peaks. A clear multiplet split of Ni 2p_{3/2} and Ni 2p_{1/2} can be seen on NiO spectra around 855 and 875 eV respectively. Meanwhile, no multiplet was detected on Ni(OH)₂ on both Ni 2p_{3/2} and Ni 2p_{1/2} peaks. Thus in here, we choose Ni(OH)₂ as the standard to be compared with our NiAl LDH catalyst. Even though XRD measurement detected NiO in the reconstruction phase, due to its multiplet split peak, as shown above, deconvolution of its spectra would be a real challenge⁵³.

The resulting Ni 2p, Al 2p and O1s spectra are shown in **Figure 4.12a-c**. XPS results from Ni 2p spectra reveals that Ni(OH)₂ is mainly governed at the surface. Ni 2p (**Figure 4.12a**) spectra displayed four spectra with the main peak at 872 and 854 eV indicating the core binding energy of Ni 2p_{1/2} and Ni 2p_{3/2} regions^{45,54}. Their satellites were detected at 879 and 860 eV respectively. The split spin-orbit component is found to be 18 eV in the range of common Ni 2p spectra (17.3 eV). Reconstruction of NiAl layered is affirmed by the intense peak of Ni 2p_{3/2}. Meanwhile, the successful re-cooperation of Ni in the interlayer can be confirmed by formation of a lower Ni 2p_{1/2} peak. NiAl LDH intensity was found to increase with the increasing Ni content on the surfaces.

Two peaks of Al 2p spectra were depicted in **Figure 4.12b** with two convoluted peaks found at 74 eV corresponding to Al octahedral and Al tetrahedral respectively. Al octahedral was detected at 74 eV representing the Al 2p binding energy of Al-O interaction. Meanwhile, Al-tetrahedral was detected at lower binding energy (73.6 eV). This finding is correlated with Al-MAS NMR results which found higher Al intensity in octahedral structure instead of tetrahedral.

From the deconvolution of O 1s spectra (**Figure 4.12c**), two main binding energy were detected at the region of 531 and 533 eV. These correlate to the existence of O in CO₃²⁻ and O in OH⁻ in the interlayer. Again, the intensity was increased as the Ni content increased.

Figure 4.13 shows the linear relationship between surface and bulk NiAl LDH as determined by XPS and EDX respectively. As the content was increased, the ratio of Ni/Al in the surface and bulk were increased accordingly. Somehow, the ratio in the surface was found to be lower compared to the ratio of Ni/Al detected in the bulk. This result is expected as XPS is a surface sensitive, thus it only recognised atom on the surface instead of in the bulk.

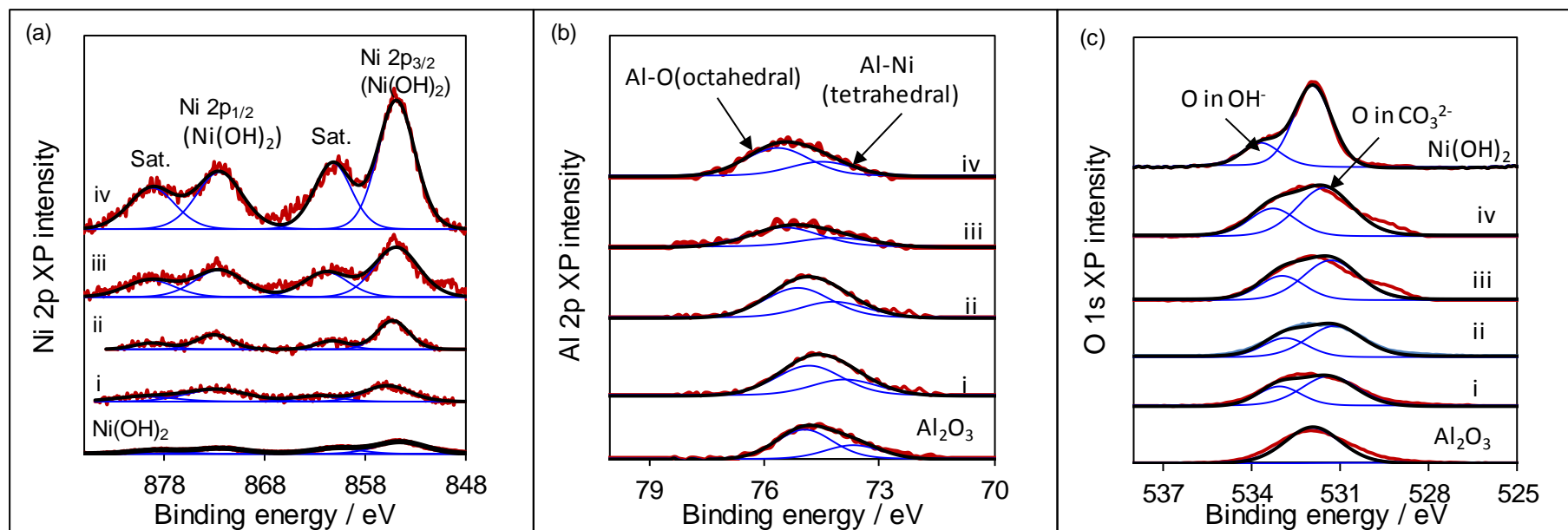


Figure 4.12 XPS spectra of NiAl HTM represents (a) Ni 2p, (b) Al 2p and (c) O 1s. The lower to a higher ratio of Ni:Al is denoted as i-iv respectively.

— denoted as envelope, — raw data and — HT component.

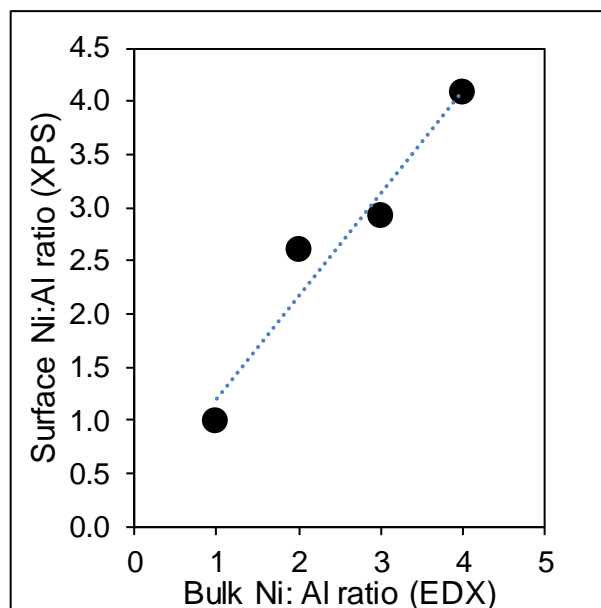


Figure 4.13 Ni surface to bulk ratios determined by XPS and EDX analysis for NiAl HTM LDH.

4.4.2 Kinetic transesterification of tributyrin over NiAl HTM

4.4.2.1 Effect of ratio on NiAl HTM

To observe the effect of NiAl HTM ratio in the transesterification of triglycerides, reactions have been run on lower TAG chain (C_4). Results of a profile reaction at different loading at 110 °C are shown in **Figure 4.14a-b**. As the Ni content was increased from 1.72-3.85, the conversion increased simultaneously (**Figure 4.14a**). The data in **Figure 4.14b** reveals the relationship of NiAl HTM loading with initial rates and TOF. A significant correlation can be recognised between composition and basicity; once the amount (ratio) of Ni^{2+} increases, the basic strength increases significantly^{23,55}. Thus, enhancement of catalytic reaction occurred simultaneously throughout the series.

Our CO_2 -TPD results also confirmed that the strength of basic sites is interrelated with Ni:Al ratio. It is worth remarking that changing the elemental composition of the cation or anion, positively alters the bulk structure of NiAl LDH, thus it correlates with their basicity and influence on catalytic activities¹. These data confirmed that conversion of tributyrin strongly depends on Ni content in the same manner as reported by Liu *et al.*⁵⁶.

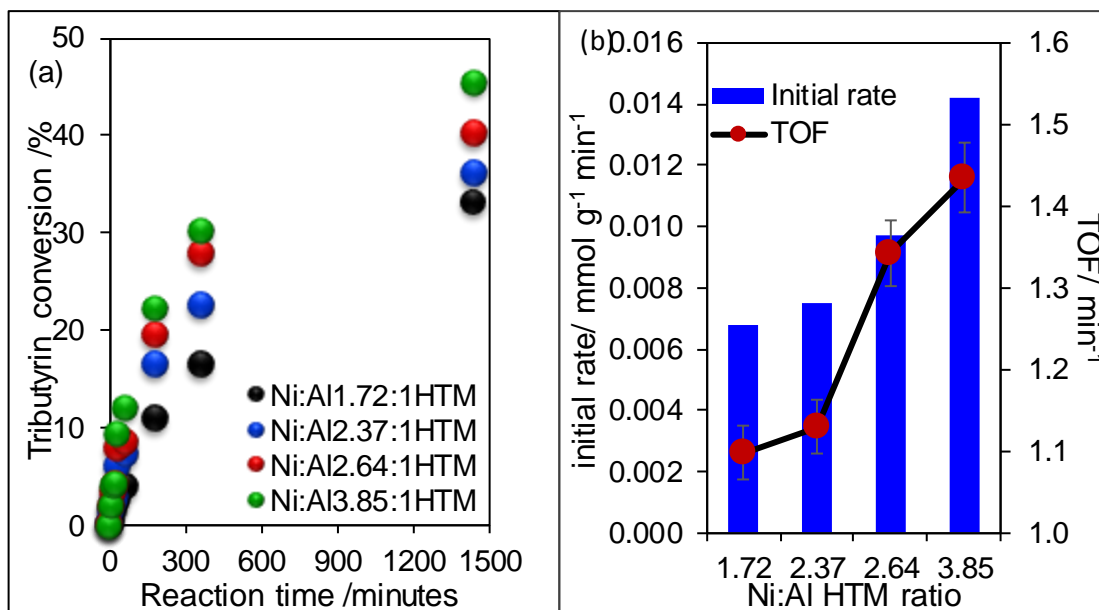


Figure 4.14 Tributyrin conversion using NiAl HTM at different ratios (a). Effect of catalytic activity on Ni:Al ratio of hydrothermal reconstructed hydrotalcite. (b). The reaction involved 100 mg catalyst, at 110 °C, 30:1 methanol: tributyrin ratio, 650 rpm for 24 hours.

4.4.2.2 Effect of temperature on NiAl HTM

Effect of temperature on reaction condition has been investigated and results are depicted in **Figure 4.15a**. Initially, reactions were carried out in a normal round bottom flask at 65 °C (using 3.85:1 catalyst), gave a higher conversion compared to a reaction at 80 °C, somehow the selectivity observed was relatively low (6.1 %). (**Figure 4.15b**). Hence, the temperature has been increased from 65 °C to 80 °C, 90 °C and 110 °C in a pressure flask following results discussed in **Chapter 3 (3.3.4.3)**. Selectivity increased tremendously in a pressure flask where reactions were done at 80 °C, 90 °C and 110 °C. Results show a relative temperature dependence here. The selectivity value reached a near plateau at 89 % in this temperature range. Meanwhile, conversion and TOF increased linearly with increasing temperature. As the molecules were heated, the average speed of collision will be increased, thus increasing the activation energy.

The activation energy was calculated and depicted in **Figure 4.15c**. The activation energy of NiAl HTM is 46 kJ/mol, much higher than the activation energy of ZnAl HTM (38 kJ/mol) discussed in **sub-chapter 3.3.4.4**. This value is still in the range of solid base catalyst especially layered double hydroxide^{17,57,58}, as low as 38 kJ/mol for MgAl HT⁵⁷ to the highest of 222 kJ/mol with the addition of polystyrene in NiAl LDH¹⁷ which is normally found in the transesterification reaction.

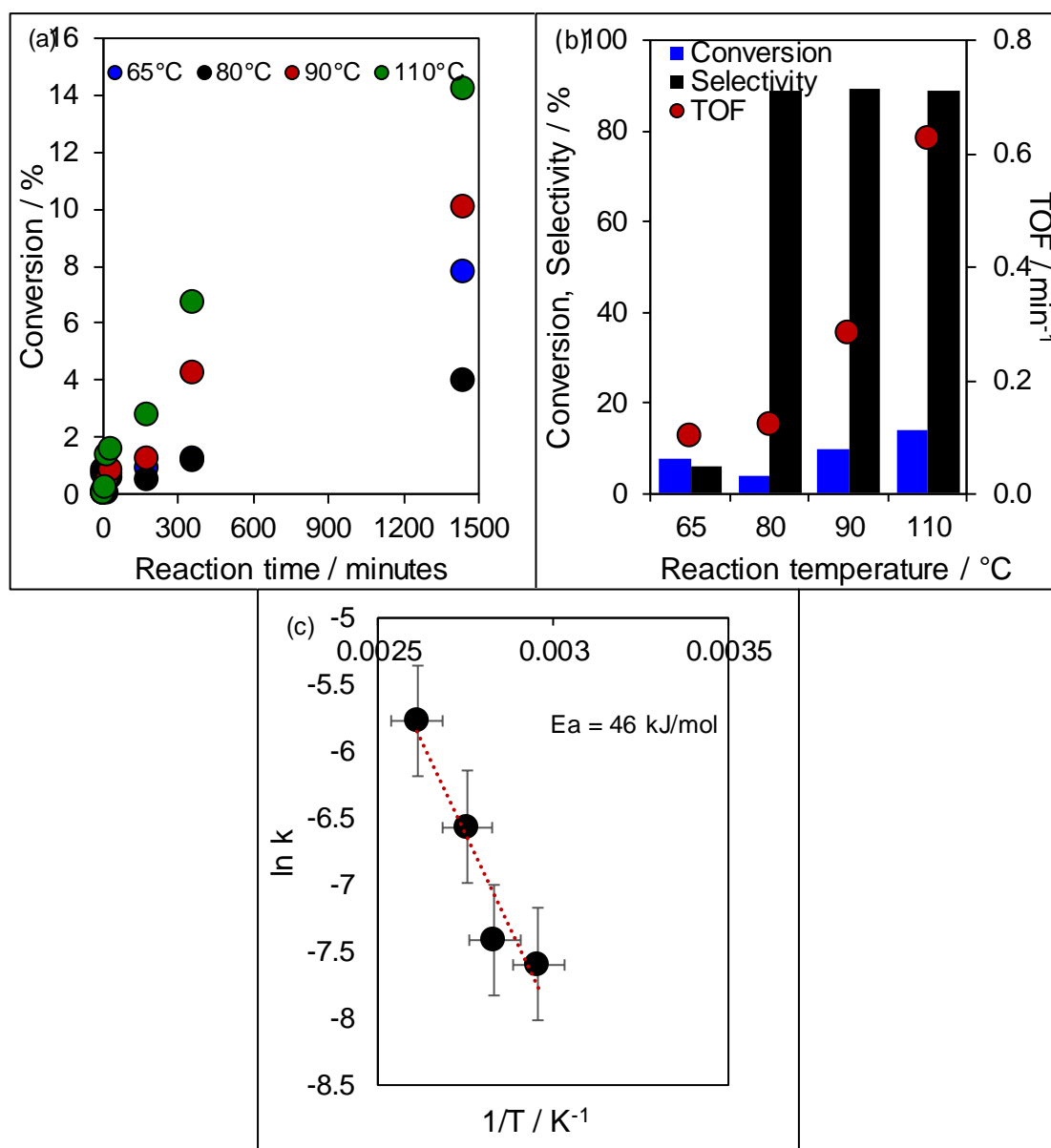


Figure 4.15 Dependence of rate on temperature using Ni:Al_{3.85}:1 catalyst; (a) Conversion profiles of tributyrin using NiAl HTM at a different temperature, (b) Effect of temperature on TOF and selectivity and (c) Arrhenius plot for transesterification of tributyrin.

4.4.2.3 Effect of catalyst weight on NiAl HTM

Effect of catalyst weight on the catalytic performance of transesterification of tributyrin is given in **Figure 4.16**. Results revealed that conversion increased with catalyst amount added in the reaction. At 25 mg and 50 mg, only 13.8 % and 14.2 % tributyrin were converted respectively. When the catalyst loading was increased to 100 mg, 45.3 % conversion was obtained. This also proven that catalyst amount has a significant impact on the rate of reaction, thus the initial rates improved significantly. As

this reaction has been done at a higher temperature (110 °C), the selectivity was maintained around 88 %.

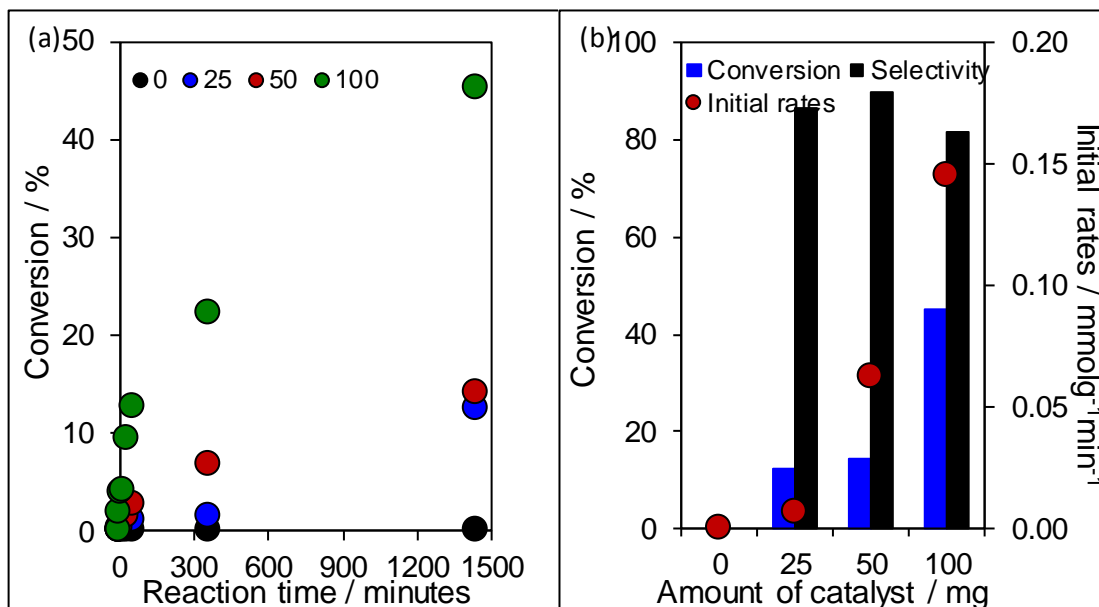


Figure 4.16 Tributyrin conversion using NiAl hydrothermal at different catalyst weight (a). Effect of conversion, selectivity and initial rates by ranging the catalyst amount (b). Conditions: 110 °C in pressure flask, different catalyst weight, 650 rpm and 24 h reaction.

4.4.3 Transesterification of model compound triglycerides

4.4.3.1 C₄-C₁₈ TAG reactions

In accordance with the above results, this section will demonstrate the compilation of TAG conversion, yield, selectivity and TOF of a TAG series involved in this study; spanning from C₄ to C₁₈. Only Ni:Al3.85:1HTM will be presented here. It is useful to note that all reactions took place with the addition of butanol in order to enhance the catalytic activity, especially on the bulkier TAG as discussed in the previous chapter. Formation of reactant, product, intermediate (dibutyrin and monobutyrin) and internal standard can be seen in the GC chromatogram as shown **Figure 4.17**. Meanwhile, glycerol normally is not detected in the GC indicating very small (or none) of the substrate has been converted to glycerol. The effect of TAG chain from C₄-C₁₈ on transesterification reaction can be seen in **Figure 4.18a-e**. The effect of Ni ratio on C₄ has been presented in **sub-chapter 4.4.2.1** and here the conversion profile under the best catalyst is depicted in **Figure 4.18a**. A similar trend of all TAG series has been discovered on NiAl HTM and is the same as in ZnAl HTM.

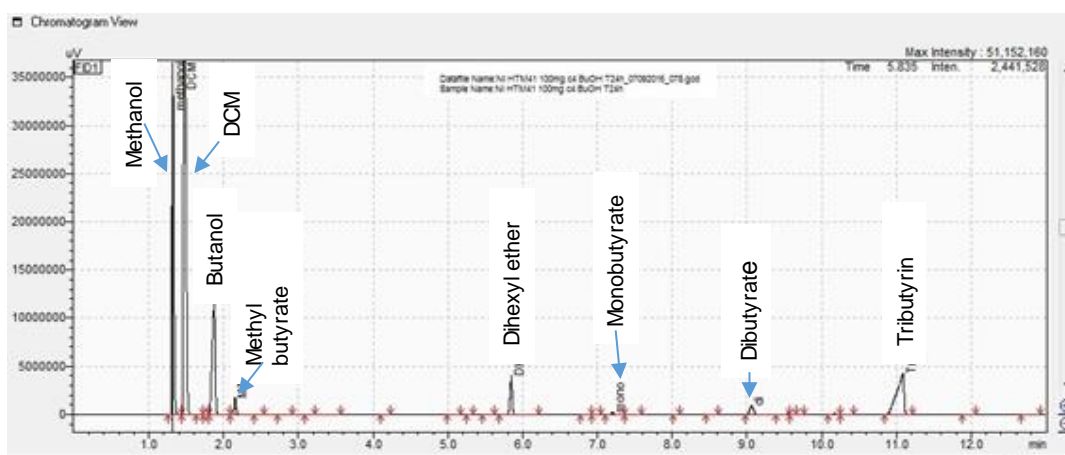


Figure 4.17 GC chromatogram from transesterification of tributyrin using NiAl HTM catalyst with C₄ triglycerides at 110 °C.

Among all, C₄ TAG produces the highest conversion, yield, selectivity and TOF value as those tabulated in **Figure 4.18**. Tributyrin reaction has been converted around 45.3 % with 12.3 mmol of yield and 81.8 % selectivity. TOF is calculated by dividing initial rates ($\text{mmol g}^{-1} \text{min}^{-1}$) over a number of active sites (mmol g^{-1}). To assess the catalytic activity in bulkier TAG, transesterification reaction proceeded in C₁₂ and C₁₈ TAG (**Figure 4.18c and d**). A small conversion (13.5 %) is observed with C₁₂ and no conversion has been observed with C₁₈ TAG. As previously mentioned, solid base catalysts are very effective for transesterification reactions, unfortunately, in NiAl LDH cases, they cannot transesterify fatty acids of triolein to FAME⁵⁹ and it was noticed that a rapid deactivation occurred here. As the TAG series was increased from C₄ to C₁₂, conversion and selectivity were decreases accordingly. Interestingly, there is no conversion/ selectivity observed on C₁₈. As mentioned earlier, the increment of the TAG length will significantly reduce the conversion and selectivity value. Bulkier TAG will limit the mass diffusion transfer of the catalyst, thus affecting the yield and conversion in the end. These findings further support the action that transesterification using NiAl HTM only favours lower TAG and we postulate that the reaction would be even more difficult if attempted with the real oil. There was a significant correlation between TAG series and conversion, selectivity, initial rates and TOF.

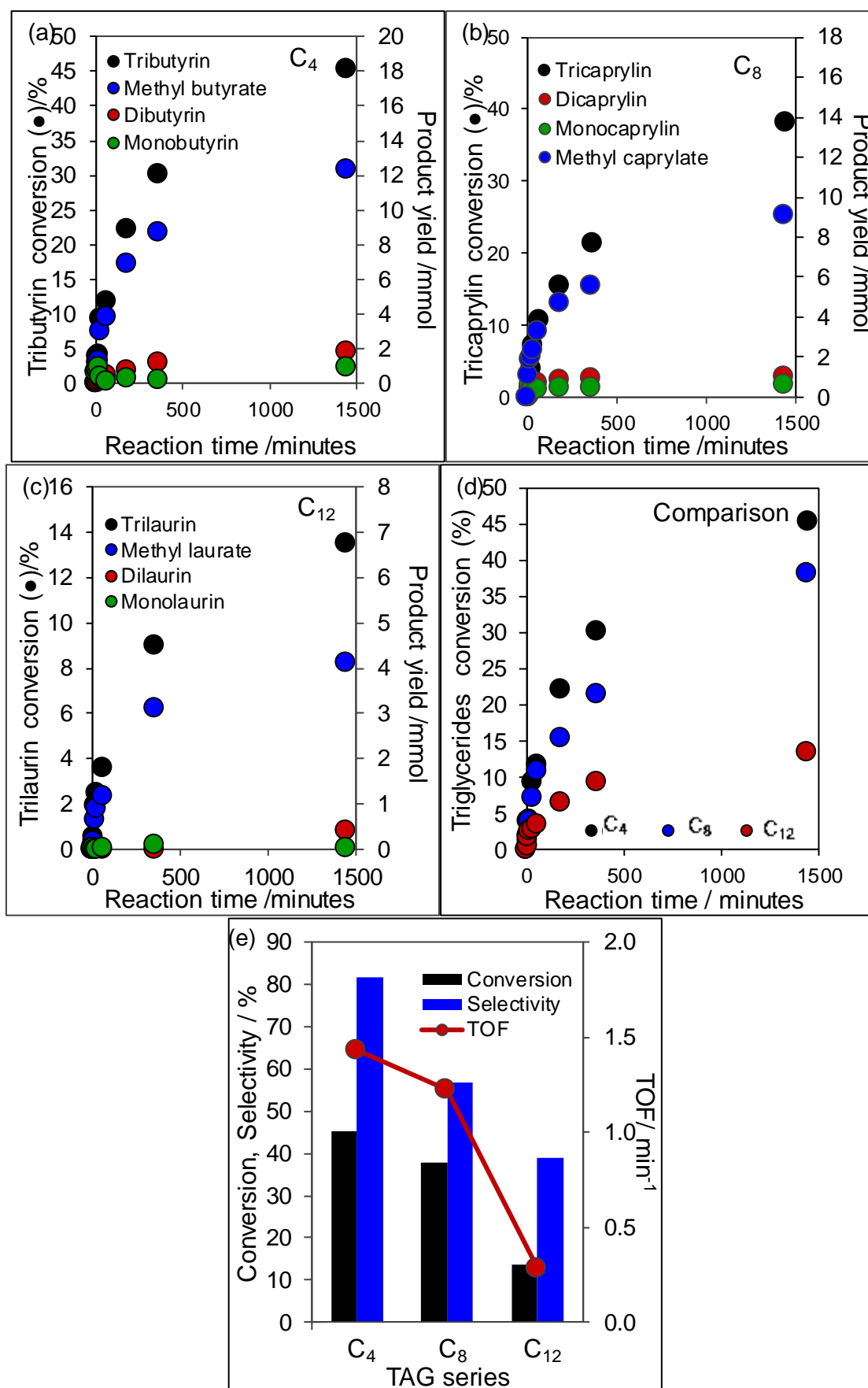


Figure 4.18 Comparison of conversion, selectivity and TOF from C₄-C₁₈ using Ni:Al3.85:1 catalyst. Conditions: 110 °C in pressure flask, 650 rpm and 24 h reaction.

4.4.4 Leaching study of NiAl HTM

To test the heterogeneity of the NiAl HTM catalyst in the system, a leaching test was undertaken⁶⁰ (**Figure 4.19a-b**). At a reaction time 3 h, the catalyst was isolated by filtration and washed with methanol. The reaction was resumed immediately afterward.

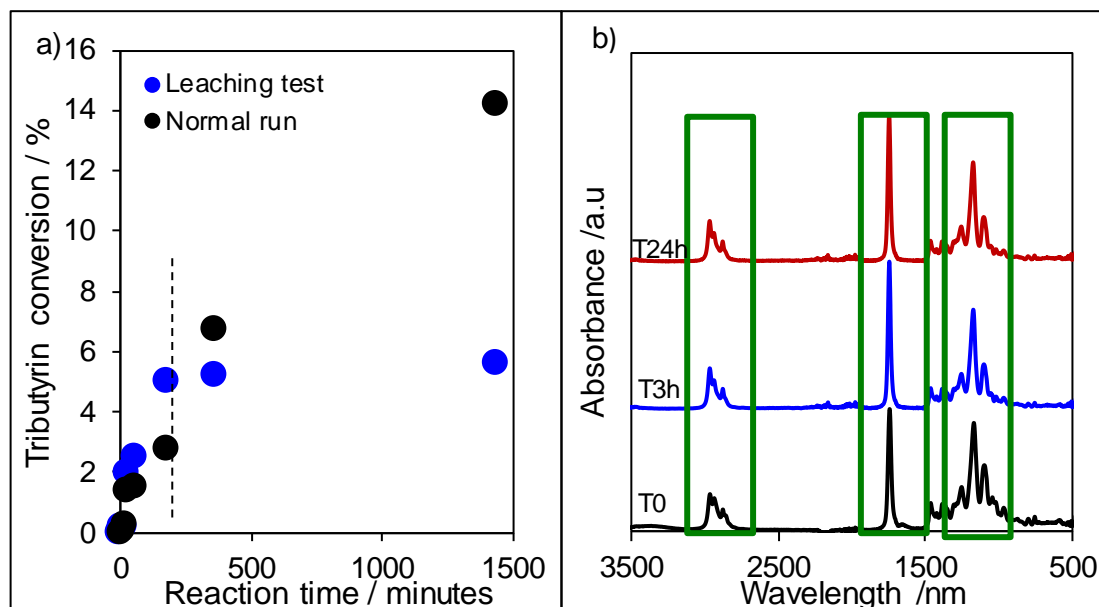


Figure 4.19 Leaching profile of the transesterification of tributyrin with methanol using Ni:Al3.85:1 HTM catalyst (a). FTIR spectra of biodiesel solution taken at T0, T3h and T24h (b). Reaction conditions: 100 mg catalyst, 4.98 ml tributyrin, 24.4 ml methanol and 1.18 ml dihexyl ether.

Figure 4.19a shows the reaction profile of a normal run and a comparison profile of a leaching study of the 24 h reaction. The tributyrin profile shows constant conversion around 5 % after the catalyst was removed from the system. No significant difference of the functional group was detected by Fourier transform infra-red (FTIR) indicating no changes have occurred in the solution after the removal of the catalyst (**Figure 4.19b**). In this study, biodiesel supernatant was governed by three major functional groups which were detected around 2874 cm^{-1} (CH_2 vibration), 1736 cm^{-1} (C=O vibration) and 1167 cm^{-1} (C-O asymmetric vibration).

Furthermore, NiAl content was determined by ICP-OES analysis in both the T0 and T24 h solutions. Results showed very low leaching occurred (0.22 %) after the catalyst was removed by filtration which means that leaching could be disregarded (data not shown). Somehow, this amount is still acceptable and depends on its stability in a reusability experiment.

4.4.5 Reusability study of NiAl HTM

A reusability study (**Figure 4.20a-b**) was conducted to test the stability of the catalyst towards reproducibility over multiple reactions without having any significant loss of its content or structure⁶⁰. **Figure 4.20a** depicts the reaction profile of the transesterification reaction over three-time cycles. Results show an expected significant loss in each cycle. Conversion, selectivity and TOF were decreased simultaneously with the increasing number of reusability times (**Figure 4.20b**). This could be because the Brönsted sites of the catalyst are being poisoned by the reaction medium such as glycerol, alcohol or methyl ester⁶¹, thus decreasing the activity in each cycle.

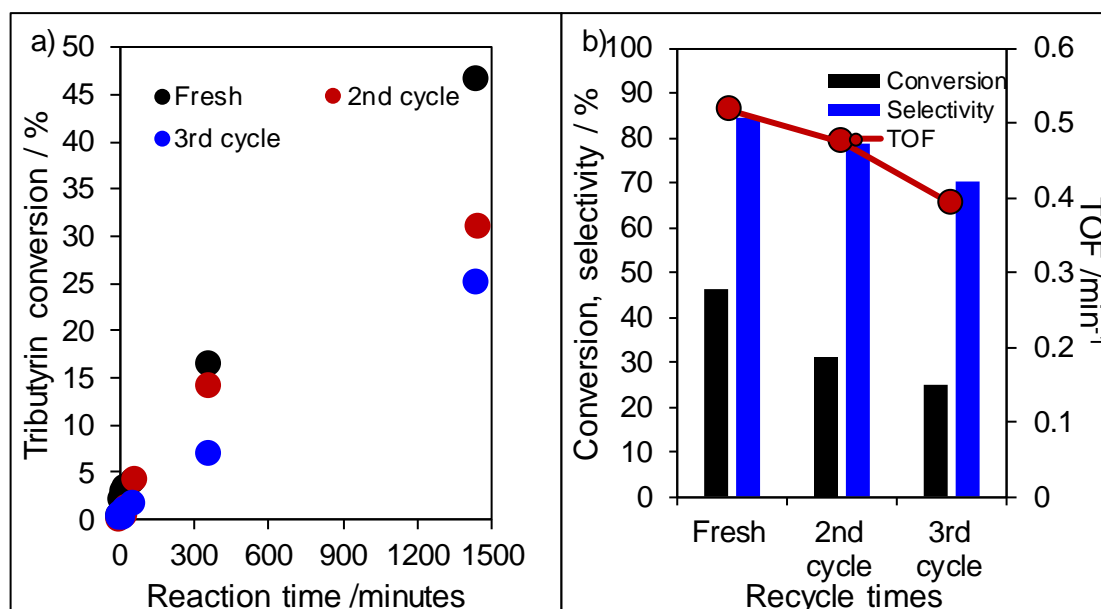


Figure 4.20 Catalyst recyclability study involving Ni:Al_{3.85}:1HTM for three cycles. Conditions: 110 °C in pressure flask, 650 rpm and 24 h reaction.

Apart from that, the decreasing activity after the third cycles could be explained by some changes observed in PXRD diffraction patterns (**Figure 4.21**). PXRD affirmed no significant shift in d(003) basal spacing indicating no inter-lamellar changes occurred. However, the crystallinity of the catalyst has been affected after the third cycles, which later promotes to the more amorphous-like structure. ICP-OES confirmed a minimal loss of Ni and Al content after the third cycles as can be seen in **Table 4.6**. This also proves that hydrotalcite is a heterogeneous catalyst and recyclable as reported by Lal *et al.*⁶¹.

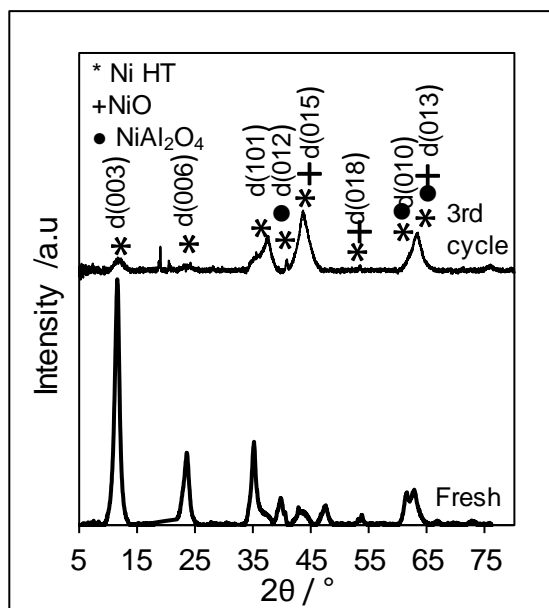


Figure 4.21 PXRD patterns of fresh and spent catalysts (3rd cycle).

Table 4.6 Atomic weight of Ni and Al on first and third cycles determined by ICP-OES.

Sample	Atomic concentration / %		Total ratio
	Ni	Al	
Fresh	64.96	15.80	3.96
Third cycles	55.84	13.71	3.37

4.5 Conclusion

In this chapter, alkali-free NiAl LDH was successfully synthesised for the first time and underwent the hydrothermal reconstructed process. The catalysts have been used in the transesterification of C_4 - C_{18} . Hydrothermal approaches have displayed changes in the textural and morphology properties of the catalyst. Even though the basal spacing was increased after undergoing hydrothermal treatment, there were no substantial changes observed in lattice parameter a , and only slightly changes in the crystallite size. Hydrothermal NiAl HT also active in transesterification reaction, due to it having a positive correlation with basicity, which gave the substrate more chances to interact in the transesterification reaction. The reactions were optimised under temperature, ratio and catalyst weight variables, where active conversion and TOF were highly reported at optimum conditions. Tributyrin (C_4) reached about 45.3 % conversion. Though the basic strength has increased via the hydrothermal reconstruction method, no conversion has been observed in C_{18} reaction. This indicates that basic strength is not the only parameter needed in this reaction, but more improvement of pore architecture is required to enable the macroporous catalyst to enhance activity. A very small amount of leaching (0.22 %)

has been observed in this study and is almost negligible. NiAl LDH showed stable durability over three recycles periods, which also proves the reproducibility of the catalyst.

4.6 References

- (1) Takehira, K. *Appl. Clay Sci.* **2017**, 136, 112–141.
- (2) Wang, H.; Liu, Y.; Chen, Z.; Wu, B.; Xu, S.; Luo, J. *Nat. Publ. Gr.* **2016**, 6:22748, 1–8.
- (3) Theiss, F. L.; Ayoko, G. A.; Frost, R. L. *Appl. Surf. Sci.* **2016**, 383, 200–213.
- (4) Li, R.; Hu, Z.; Shao, X.; Cheng, P.; Li, S.; Yu, W. *Nat. Publ. Gr.* **2016**, 6:18737, 1–9.
- (5) Sharma, Y. C.; Singh, B.; Korstad, J. *Fuel* **2011**, 90, 1309–1324.
- (6) Fan, G.; Li, F.; Evans, D. G.; Duan, X. *Chem. Soc. Rev.* **2014**.
- (7) Birjega, R.; Vlad, A.; Matei, A.; Ion, V.; Luculescu, C.; Dinescu, M.; Zavoianu, R. *Thin Solid Films* **2016**, 614, 36–41.
- (8) Manikandan, M.; Venugopal, A. K.; Prabu, K.; Jha, R. K.; Thirumalaiswamy, R. *J. Mol. Catal. A Chem.* **2016**, 417, 153–162.
- (9) Li, D.; Lu, M.; Aragaki, K.; Koike, M.; Nakagawa, Y.; Tomishige, K. *Appl. Catal. B Environ.* **2016**, 192, 171–181.
- (10) Sturgeon, M. R.; O'Brien, M. H.; Ciesielski, P. N.; Katahira, R.; Kruger, J. S.; Chmely, S. C.; Hamlin, J.; Lawrence, K.; Hunsinger, G. B.; Foust, T. D.; Baldwin, R. M.; Biddy, M. J.; Beckham, G. T. *Green Chem.* **2014**, 16, 824.
- (11) Nguyen, V. H.; Shim, J. J. *Electrochim. Acta* **2015**, 166, 302–309.
- (12) Rahul, R.; Satyarthi, J. K.; Srivinas, D. *Indian J. Chem.* **2011**, 50A, 1017–1025.
- (13) Hosoglu, F.; Faye, J.; Mareseanu, K.; Tesquet, G.; Miquel, P.; Capron, M.; Gardoll, O.; Lamonier, J.-F.; Lamonier, C.; Dumeignil, F. *Appl. Catal. A Gen.* **2015**, 504, 533–541.
- (14) Delidovich, I.; Palkovits, R. *J. Catal.* **2015**, 327, 1–9.
- (15) Nishimura, S.; Takagaki, A.; Ebitani, K. *Green Chem.* **2013**, 15, 2026.
- (16) Montañez, M. K.; Molina, R.; Moreno, S. *Int. J. Hydrogen Energy* **2014**, 39, 8225–8237.
- (17) Sinha, M. K.; Pugazhenth, G. *Adv. Mater. Res.* **2013**, 747, 23–26.
- (18) Kikhtyanin, O.; Lesnik, E.; Kubička, D. *Appl. Catal. A Gen.* **2016**, 525, 215–225.
- (19) Lee, G.; Kang, J. Y.; Yan, N.; Suh, Y.-W.; Jung, J. C. *J. Mol. Catal. A Chem.* **2016**, 423, 347–355.
- (20) Liu, Q.; Wang, B.; Wang, C.; Tian, Z.; Qu, W.; Ma, H.; Xu, R. *Green Chem.* **2014**, 16, 2604.
- (21) Sampieri, A.; Fetter, G.; Villafuerte-Castrejon, M. E.; Tejeda-Cruz, A.; Bosch, P. *Beilstein J. Nanotechnol.* **2011**, 2, 99–103.
- (22) Benito, P.; Guinea, I.; Labajos, F. M.; Rives, V. *J. Solid State Chem.* **2008**, 181, 987–996.
- (23) Sharma, S. K.; Parikh, P. A.; Jasra, R. V. *Appl. Catal. A Gen.* **2010**, 386, 34–42.
- (24) Wu, X.; Du, Y.; An, X.; Xie, X. *Catal. Commun.* **2014**, 50, 44–48.
- (25) Zhang, H.; Wang, J.; Xu, X. *J. Fuel Chem. Technol.* **2015**, 43, 81–87.
- (26) Tadanaga, K.; Miyata, A.; Ando, D.; Yamaguchi, N.; Tatsumisago, M. *J. Sol-Gel Sci. Technol.* **2012**, 62, 111–116.
- (27) Woodford, J. J.; Dacquin, J.-P.; Wilson, K.; Lee, A. F. *Energy Environ. Sci.* **2012**, 5, 6145.
- (28) Cantrell, D. G.; Gillie, L. J.; Lee, A. F.; Wilson, K. *Appl. Catal. A Gen.* **2005**, 287, 183–190.
- (29) Wang, Q.; Tay, H. H.; Guo, Z.; Chen, L.; Liu, Y.; Chang, J.; Zhong, Z.; Luo, J.; Borgna, A. *Appl. Clay Sci.* **2012**, 55, 18–26.

- (30) Ranran Wang, Q. L. • N. D.; Lu, Tao Zhang, H. *Res Chem Intermed* **2015**, 41, 7899–7914.
- (31) Jinesh, C. M.; Antonyraj, C. A.; Kannan, S. *Catal. Today* **2009**, 141, 176–181.
- (32) Abelló, S.; Bolshak, E.; Gispert-Guirado, F.; Farriol, X.; Montané, D. *Catal. Sci. Technol.* **2014**, 4, 1111.
- (33) Leont'eva, N. N.; Cherepanova, S. V.; Drozdov, V. A.; Bel'skaya, O. B.; Tsybulya, S. V.; Stepanova, L. N. *Theor. Exp. Chem.* **2012**, 48, 1–5.
- (34) S, L.; E Joan, S.; Martin A, T.; Thommes, M. *Characterization of Porous Solids and Powders: Surface Area, Pore Size and Density*; Springer Netherlands, 2004.
- (35) Kovanda, F.; Rojka, T.; Bezdička, P.; Jiráťová, K.; Obalová, L.; Pacultová, K.; Bastl, Z.; Grygar, T. *J. Solid State Chem.* **2009**, 182, 27–36.
- (36) Kovanda, F.; Koloušek, D.; Cílová, Z.; Hulínský, V. *Appl. Clay Sci.* **2005**, 28, 101–109.
- (37) Saiah, F. B. D.; Su, B.-L.; Bettahar, N. *J. Hazard. Mater.* **2009**, 165, 206–217.
- (38) Meher, S. K.; Justin, P.; Rao, G. R. *ACS Appl. Mater. Interfaces* **2011**, 3, 2063–2073.
- (39) Wei, Y.; Zhang, X.; Wu, X.; Tang, D.; Cai, K.; Zhang, Q. *RSC Adv.* **2016**, 6, 39317–39322.
- (40) Reinholdt, M.; Brendlé, J.; Tuilier, M.-H.; Kaliaguine, S.; Ambroise, E. *Nanomaterials* **2013**, 3, 48–69.
- (41) Liji Sobhana, S. .; Mehedi, R.; Malmivirta, M.; Paturi, P.; Lastusaari, M.; Dîrtu, M. M.; Garcia, Y.; Fardim, P. *Appl. Clay Sci.* **2016**, 132, 641–649.
- (42) Fairely, N. CasaXPS Manual: Introduction to XPS and AES. Casa Software Ltd, 2009, 1–177.
- (43) Lee, A. Y.; Blakeslee, D. M.; Powell, C. J.; Rumble, J. R. *Data Sci. J.* **2002**, 1–12.
- (44) Naumkin, A. V.; Kraut-Vass, A.; Gaarenstroom, S. W.; Cedric J, P. NIST Standard Reference Database 20, Version 4.1. <https://srdata.nist.gov/xps> (accessed Oct 8, 2016).
- (45) Biesinger, M. C.; Payne, B. P.; Lau, L. W. M.; Gerson, A.; Smart, R. S. C. *Surf. Interface Anal.* **2009**, 41, 324–332.
- (46) Fadley, C. S. *J. Electron Spectros. Relat. Phenomena* **2010**, 178–179, 2–32.
- (47) Mårtensson, N.; Söderstrom, J.; Svensson, S.; Travníkova, O.; Patanen, M.; Miron, C.; Sæthre, L. J.; Børve, K. J.; Thomas, T. D.; Kas, J. J.; Vila, F. D.; Rehr, J. J. *J. Phys. Conf. Ser.* **2013**, 430, 12131.
- (48) Yin, H.; Li, H.; Wang, Y.; Ginder-Vogel, M.; Qiu, G.; Feng, X.; Zheng, L.; Liu, F. *Chem. Geol.* **2014**, 381, 10–20.
- (49) Heß, V.; Matthes, F.; Bürgler, D. E.; Monakhov, K. Y.; Besson, C.; Kögerler, P.; Ghisolfi, A.; Braunstein, P.; Schneider, C. M. *Surf. Sci.* **2015**, 641, 210–215.
- (50) Pauly, N.; Yubero, F.; García-García, F. J.; Tougaard, S. *Surf. Sci.* **2016**, 644, 46–52.
- (51) Politano, A.; Chiarello, G.; Spinella, C. *Mater. Sci. Semicond. Process.* **2016**.
- (52) Katić, J.; Metikoš–Huković, M.; Peter, R.; Petravić, M. *J. Power Sources* **2015**, 282, 421–428.
- (53) Biesinger, M. C.; Payne, B. P.; Grosvenor, A. P.; Lau, L. W. M.; Gerson, A. R.; Smart, R. S. C. *Appl. Surf. Sci.* **2011**, 257, 2717–2730.
- (54) Chen, X.; Ma, Y.; Wang, L.; Yang, Z.; Jin, S.; Zhang, L.; Liang, C. *ChemCatChem* **2015**, 7, 978–983.
- (55) Zeng, H.-Y.; Xu, S.; Liao, M.-C.; Zhang, Z.-Q.; Zhao, C. *Appl. Clay Sci.* **2014**, 91, 16–24.
- (56) Liu, D.; Lau, R.; Jia, X.; Borgna, A.; Yang, Y. In *Developments in Catalysis*; Elsevier, 2013; pp. 297–352.
- (57) Chantrasa, A.; Phlernjai, N.; Goodwin, J. G. *Chem. Eng. J.* **2011**, 168, 333–340.
- (58) Ho, W. W. S.; Ng, H. K.; Gan, S.; Tan, S. H. *Energy Convers. Manag.* **2014**.
- (59) Wilson, K.; Lee, A. F. *Catal. Sci. Technol.* **2012**, 2, 884–897.

- (60) Gruber-Woelfler, H.; Radaschitz, P. F.; Feenstra, P. W.; Haas, W.; Khinast, J. G. *J. Catal.* **2012**, 286, 30–40.
- (61) Lal, J.; Sharma, M.; Gupta, S.; Parashar, P.; Sahu, P.; Agarwal, D. D. *J. Mol. Catal. A Chem.* **2012**, 352, 31–37.

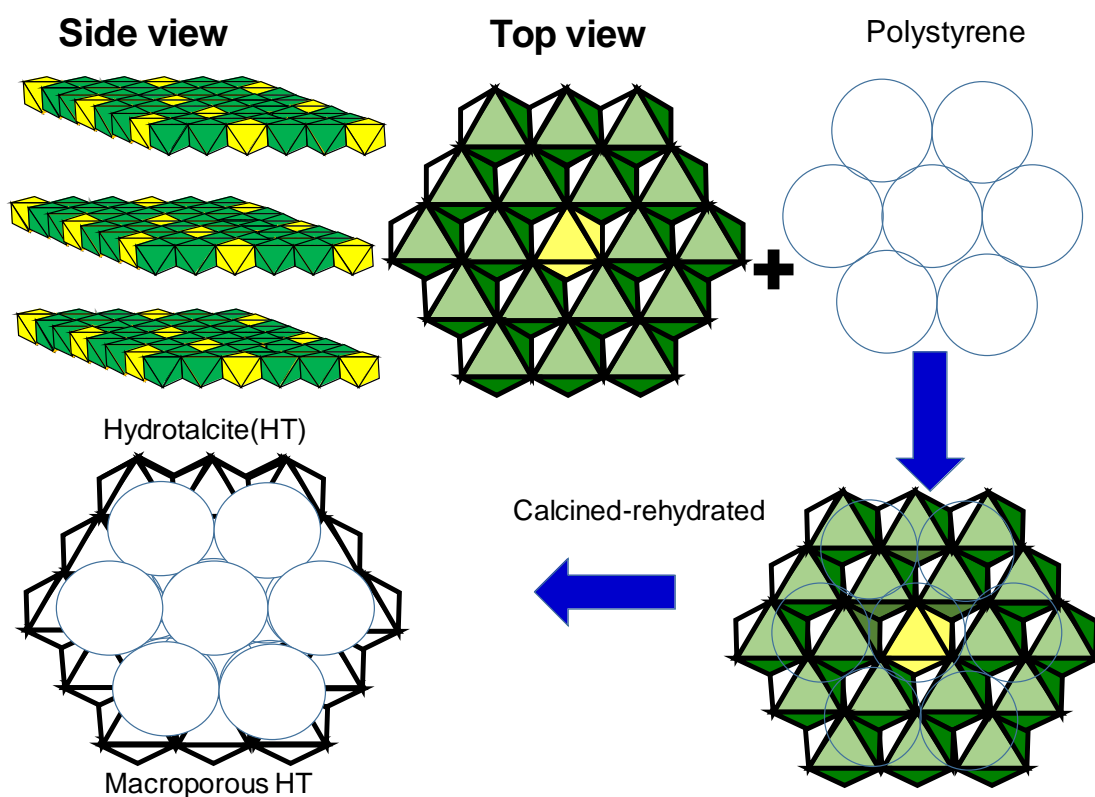
Chapter 5

***Conventional
versus
Macroporous of
MgAl LDH and
ZnAl LDH***

5.1 Introduction

In Chapter 3 and 4, we have portrayed how to overcome the mass transport limitation in triglycerides (TAG) transesterification via changing the textural properties, morphology and basicities of layered double hydroxide (LDH) through hydrothermal reconstructed method. Although the outcomes were dramatic in terms of the catalytic enhancement, further improvement is still required in order to overcome the limitation of rates, especially in C18 TAG. With this considered, the development of macroporous LDH could possibly be the best solution to the mass transfer limitation of bulkier TAG.

There are a number of methods of synthesising macroporous LDH materials that have been previously reported, which and are listed in **Table 5.1** along with the advantages and disadvantages associated with each method. Our macroporous synthesis is based on the work from Woodford *et al.*¹ where they modified the method from Géraud *et al.*². Polystyrene (PS) has been chosen for the production of macroporous MgAl hydrotalcite due to the facile synthesis and scale up (emulsifier-free method)¹ whilst simultaneously being easy to remove by dissolution or calcination². The large diameter of polystyrene (around 350¹ nm for the conditions chosen in this work) empowers it to be used as a macroporous template (**Scheme 5.1**).



Scheme 5.1 Polystyrene templating route to transform ordinary layered double hydroxide into a macropore network.

Table 5.1 Collection of methodologies implemented for the synthesis of macroporous LDH materials.

Synthesis type	Method used	Advantages	Disadvantages	References
Mesoporous-macroporous MgAl HTs	Combination of paraffin emulsion, surfactant and sol-gel transition	Well-defined hierarchical mesoporous-macroporous exhibited high specific surface areas and pore volumes	Emulsion droplets caused unordered packed on the slit-like shape mesopores, also entrapped the paraffin droplets in macropores	3
Macroporous MgAl HTs	Alkali-free and polystyrene templated	Enhances the diffusion of bulkier TAG (C18) in transesterification reaction	-Base sites accessibility towards different TAGs series remains challenging -Direct measurement of intrapore molecular diffusion coefficients is extremely difficult.	1
Macroporous MgAl HTs	Used 'inverse opals method' with polystyrene beads	Could be used to overcome diffusions limitation in reactions.	Not successfully removed PS by dissolution method as proven by IR spectrometer	2
Macroporous perovskite-type complex oxide catalysts of $\text{La}_{1-x}\text{K}_x\text{Co}_{1-y}\text{Fe}_y\text{O}_3$	Combination of organic ligation of ethylene glycol and methanol	High catalytic activities for diesel soot combustion	Depend on the amount of methanol added. Macroporous tend to collapse if amount of methanol is not adequate	4

Woodford *et al.*¹ have reported that macroporous HT offered nearly 10-fold rate enhancement over the bulkier TAG, C₁₈ where a thin-walled mixed oxide framework was created containing large macropore voids via PS hard sphere templating. This remarkable outcome has motivated us to study and apply the same concept in ZnAl LDH. The aim of this section is to investigate and compare the catalytic activities of conventional HT and macroporous HT of both MgAl and ZnAl hydrotalcites.

5.2 Novelty and contribution to knowledge

In this chapter, all conventional catalysts (MgAl LDH and ZnAl LDH) were synthesised using the alkali-free method as mentioned before. We report the novel synthesis of macroporous ZnAl LDH (later will be referred as MacroZnAl) using the alkali-free method according to the methodology by Woodford *et al.*¹ to be compared with conventional ZnAl LDH (later will be referred as ConvZnAl) as previously discussed in Chapter 3. Alkali-free conventional MgAl LDH (later will be referred as ConvMgAl), and macroporous MgAl LDH (later will be referred as MacroMgAl), also were synthesised according to the same method. The relative abilities of MgAl and ZnAl conventional and macroporous LDH for the transesterification reaction of lower to bulkier (C₄ to C₁₈) triglycerides are significantly novel, especially towards the enhancement and understanding of the diffusion efficiency.

5.3 Aim

The major objective of this chapter is to investigate the differences between conventional and macroporous LDHs synthesised from the alkali-free method. The impact of macroporous LDH on the physicochemical properties and catalytic activities for the transesterification of TAGs to produce biodiesel are also explored, with particular focus towards the enhancement of bulkier TAGs which suffer diffusion limitation within conventional LDH systems due to the intrinsic narrow pore size.

5.4 Results and discussion

5.4.1 Characterisation of Conventional MgAl HTs

5.4.1.1 Energy dispersive X-Ray spectroscopy of ConvMgAl LDH

Bulk elemental analysis of the MgAl series was determined by EDX as tabulated in **Table 5.2**. In general, the bulk ratios obtained from EDX deviate slightly compared to the nominal ratio, potentially due to changes in the pH of the system during the synthesis⁵. The hydrotalcite was synthesised in the nominal range of $0.23 < x < 0.35$, within the limit of pure hydrotalcite⁶.

Table 5.2 The nominal and actual bulk of MgAl HT atomic ratio.

Nominal Mg:Al ratio	Mg wt% bulk (EDX)	Al wt% bulk (EDX)	Bulk Mg:Al ratio	x value (Al/(Mg+Al))
1.5:1	19.73	11.94	1.83	0.35
2:1	20.97	10.01	2.06	0.33
3:1	28.5	15.2	2.17	0.32
4:1	66.2	8.6	3.31	0.23

5.4.1.2 Thermogravimetric analysis mass spectrometry of ConvMgAl HT

Figure 5.1(i-ii) represents ConvMgAl HT TGA-MS profiles and show a two-step weight loss. The first transition is credited to water weight loss and the second transition is ascribed to carbonates weight loss. The first dehydration step of water has occurred between 46 - 170 °C with a small amount of water weight loss (4.08 – 8.76 %), followed by a dehydroxylation water weight loss happened around 163 – 221 °C (5.00 – 8.15 %). This brings the total experimental water weight loss to 10.25 – 14.5 % as can be seen in **Table 5.3**.

Second transition step attributes to dehydroxylation and decarbonation steps which occurred around 240 - 432 °C (5.7 – 12.5 % of weight loss). The pattern of Differential Scanning Calorimetry (DSC) and Mass Spectroscopy (MS) curves were found to be identical and in agreement with TG/DSC data. The total experimental and theoretical weight losses are comparable with both amounts weight loss being around 17.5 – 23.9 % in a range with common HT weight loss⁷. DSC profiles of ConvMg:Al1.83:, ConvMg:Al2.06:1, ConvMg:Al2.17:1 and Conv3.31:1, showed two heat flow around 45 °C and 230°C which are ascribed to the absorbed water and dehydroxylation of water in the interlayer. Another heat flow was observed around 400 °C is attributed to the loss of carbon dioxide from the interlayer anion.

The chemical formulation of the prepared HTs was determined experimentally from a combination of EDX and TGA-MS with the inorganic components obtained from EDX spectroscopy and H₂O content obtained from percentage mass loss calculated from TGA-MS. To calculate the theoretical formula of LDH, a general formula for HTs; $[M(II)_{1-x}M(III)_x(OH)_2]^{x+}(A^{n-}_{x/n}) \cdot mH_2O$ where $m = 0.81 - x$, has been applied throughout. Mg content was found to gradually increase across the series, incrementally increasing with an increase in the nominal Mg:Al ratio. Simultaneously, Al mass percentages were seen to exhibit the expected decrease associated with an increasing ratio of Mg:Al. As the

ratio increased, more water was found to have been incorporated into the interlayer and the amount of carbonate within the complex was determined to diminish.

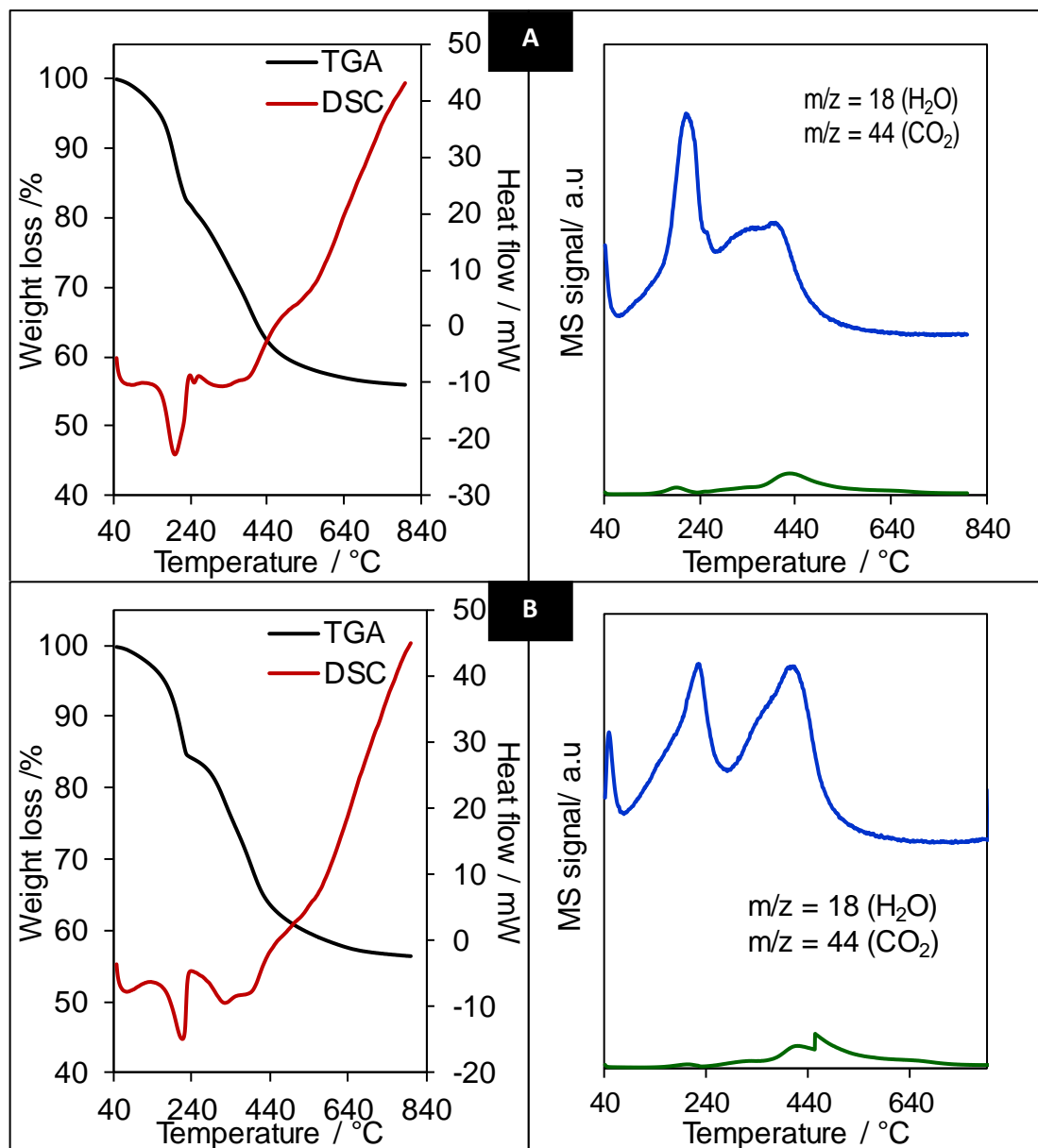


Figure 5.1i TGA-MS patterns of thermal ConvMgAl LDH of ratio 1.83 (A) and 2.06 (B).

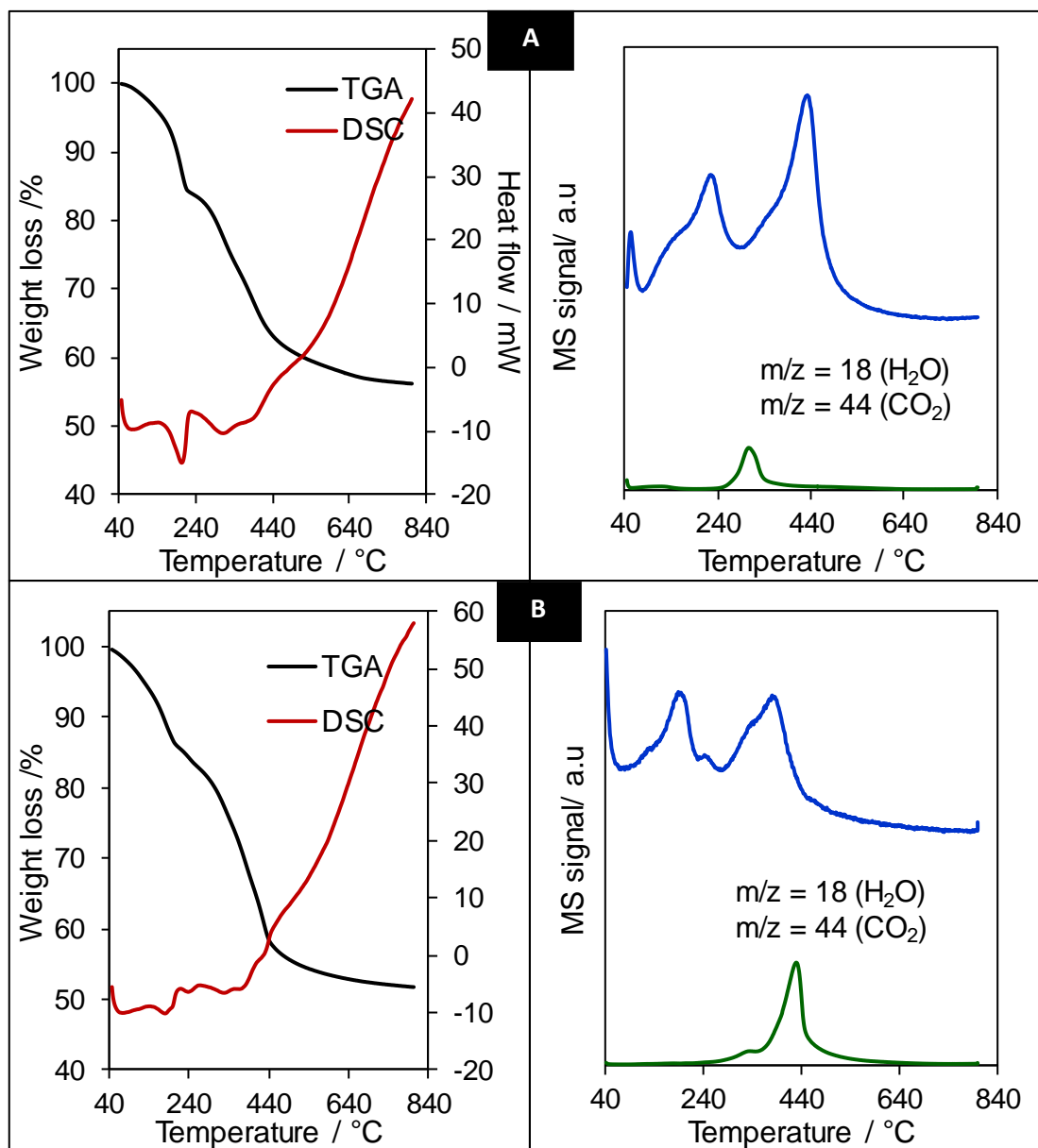


Figure 5.1ii TGA-MS patterns of thermal ConvMgAl LDH of ratio 2.17 (A) and 3.31 (B).

Table 5.3 Comparison of water and carbonate in experimental and theoretical weight loss of ConvMgAl HT as obtained from TGA-MS and EDX.

LDH catalyst/ weight loss	Experimental Weight loss / %			Theoretical weight loss /%			ConvMgAl HT Formula
	H ₂ O exp	CO ₃ exp	Total Weight loss/ %	H ₂ O theory	CO ₃ theory	Total Weight loss / %	
Mg:Al 1.83:1	11.6	12.3	23.9	5.0	16.2	21.2	[Mg _{0.65} Al _{0.35} (OH) ₂].(CO ₃) _{0.18} 0.46H ₂ O]
Mg:Al 2.06:1	12.2	10.2	22.4	7.4	12.0	19.4	[Mg _{0.67} Al _{0.33} (OH) ₂].(CO ₃) _{0.17} 0.48H ₂ O]
Mg:Al 2.17:1	10.6	12.5	22.8	8.8	9.6	18.4	[Mg _{0.68} Al _{0.32} (OH) ₂].(CO ₃) _{0.16} 0.49H ₂ O]
Mg:Al 3.31:1	14.5	5.7	20.2	10.3	7.2	17.5	[Mg _{0.77} Al _{0.23} (OH) ₂].(CO ₃) _{0.12} 0.58H ₂ O]

5.4.1.3 Scanning electron microscopy of ConvMgAl HT

To further understand the morphology of the ConvLDH, SEM analysis was undertaken over the parent catalyst (**Figure 5.**). SEM showed a characteristic of sand roses morphology⁸, a common feature of hydrotalcite which has been observed for all samples.

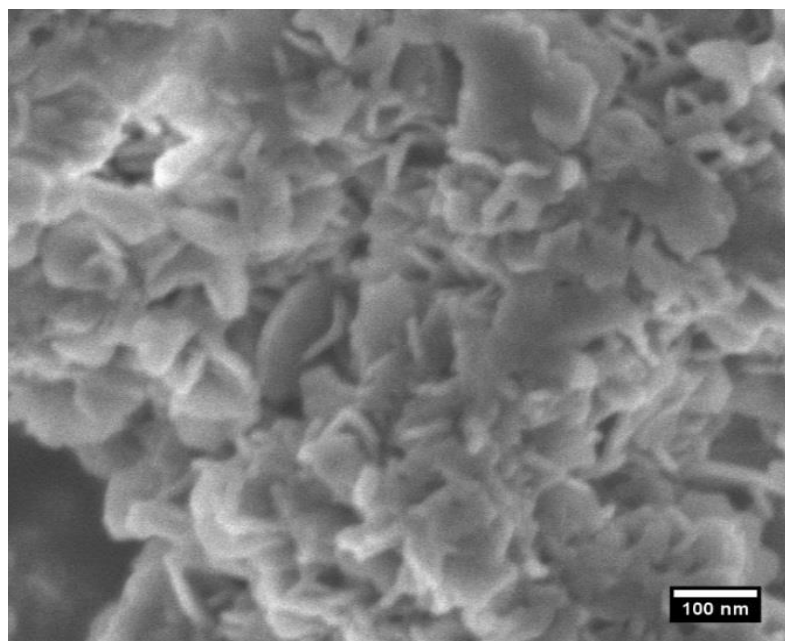


Figure 5.2 SEM micrograph of parent ConvMgAl LDH.

5.4.1.4 Powder X-ray diffraction of ConvMgAl LDH

As-synthesised (AS), calcined (calc) and hydrothermally rehydrated (HTM) hydrotalcite series have been analysed by X-ray Diffraction (XRD) to confirm formation, deformation and reformation of hydrotalcite (**Figure 5.3**). These patterns revealed the same definite pattern of hydrotalcite with different ratios spanning from 1.83 to 3.31 as found in the previous literatures^{9–11}.

Lower diffraction angles at 11.6°, 23.4° and 35° with sharp intense peaks are attributed to diffraction by planes of d(003), d(006) and d(009) respectively (**Figure 5.3a**) while the broader, less intense peaks at 39.6°, 47.1°, and 61.1° are ascribed to diffraction by planes d(015), d(018) and d(110), which complete the characteristic set of diffraction peaks associated with MgAl HTs¹². The presence of CO₃²⁻ anion is confirmed by a basal spacing of d(003)= 0.76 nm compared to 0.78 nm which has been reported by Ref¹³. A very weak pattern also observed at d(116) is negligible.

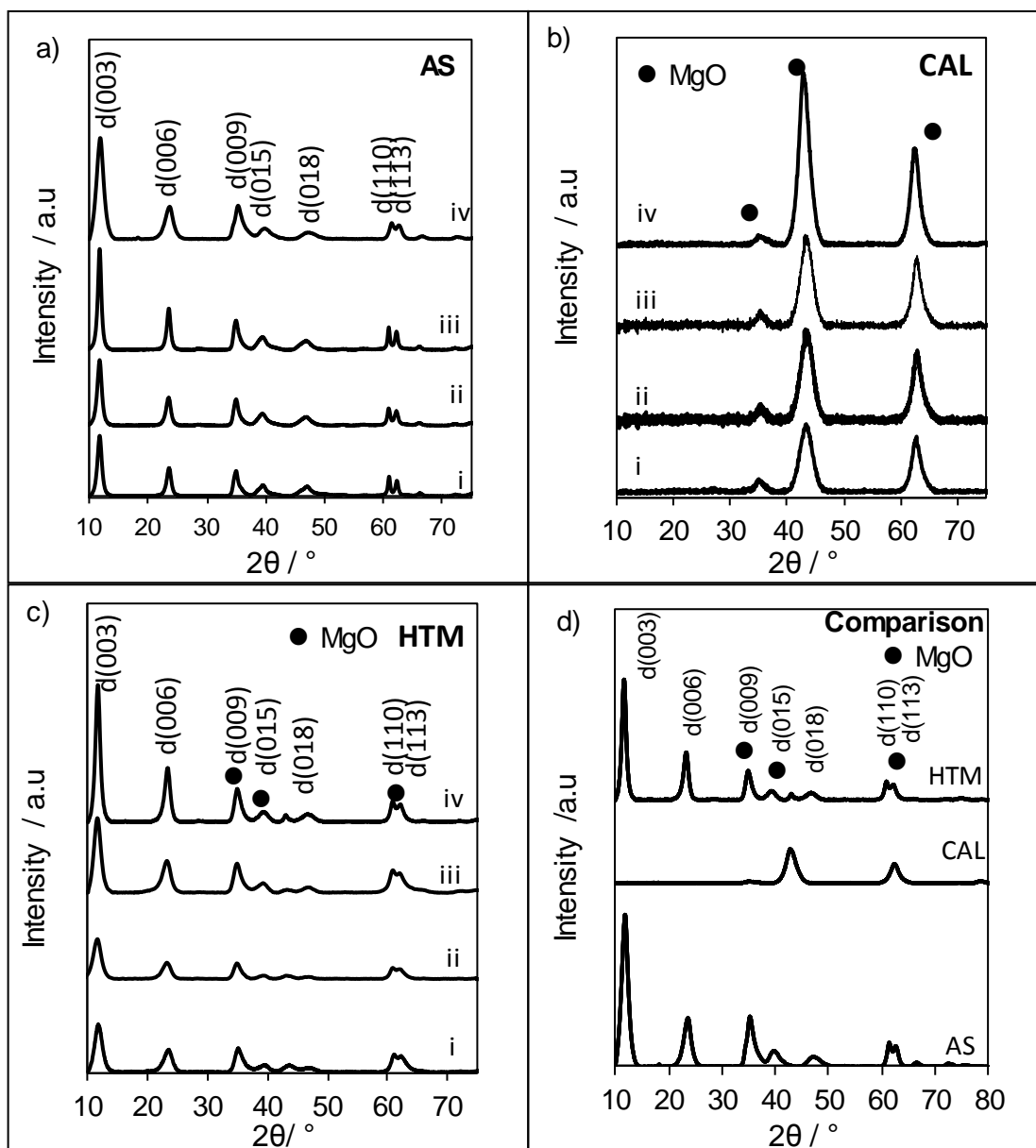


Figure 5.3 XRD patterns of the precursor, calcined, hydrothermal rehydrated and comparison of the as-synthesised (AS), calcined (CAL), hydrothermal (HTM) MgAl HTs, and comparison of all (d). a-d denoted for ConvMgAl HT ratio spanning from 1.83:1, 2.06:1, 2.17:1 and 3.31:1.

During calcination, decomposition of the hydrotalcite occurs resulting in the formation of a crystalline MgO phases. XRD patterns confirm the formation of the mixed oxides phases as displayed in **Figure 5.3b**. The patterns revealed a mixed oxide containing the MgO periclase structure as has been previously reported by Alvarez *et al.*¹⁴ on MgAl HT materials. In these PXRD patterns, there is clear evidence of the basal spacing of d(003) and d(006) reflection diminishing greatly, indicative of the destruction of the hydrotalcite structure during the calcination process. It has been previously reported that calcination below 450 K removed water molecules while calcination from

525 K to 723 K removed carbon dioxide and water¹⁴. In this study, the calcination at 450 °C produces mixed oxide structures.

The XRD pattern of rehydrated (reconstructed) hydrotalcite under hydrothermal is represented in **Figure 5.3c**. Eight diffraction peaks were observed at basal plane d(003), d(006), d(009), d(015), d(018), d(110), d(113) and d(116) confirmed the layers are regained after the rehydration process. **Figure 5.3d** displays the comparison of as synthesised, calcined and reconstructed hydrotalcite. Following rehydration, by means of the so-called ‘*Memory Effect*’, the hydrotalcite-type structure is reconstructed^{11,15,16}. The effect of ratio and hydrothermal rehydration on the basal spacing, lattice parameter and crystallite size are clearly seen in **Table 5.4**. Firstly, lattice parameters, *a* were calculated using d(110) peak, where $a = 2d(110)$. As the ratio increased, the interlayer distance d(003) increased due to the greater incorporation of Mg in the framework which combined with the fact that Mg²⁺ cation is larger than Al³⁺ cation, explains the expansion in the lattice parameter *a*.

Table 5.4 The textural parameter of basal spacing d(003), lattice parameter and crystallite size for MgAl HT.

Parameter/ catalyst	d(003)	^a Lattice parameter / nm		^b Crystallite size / nm
		<i>a</i>	<i>c</i>	
<i>MgAl LDH precursor</i>				
Mg:Al 1.83:1 AS	0.73±0.06	0.310±0.026	2.20±0.03	7.2±0.2
Mg:Al 2.06:1 AS	0.73±0.05	0.312±0.011	2.20±0.03	7.5±0.1
Mg:Al 2.17:1 AS	0.73±0.03	0.316±0.012	2.20±0.03	10.8±0.2
Mg:Al 3.31:1 AS	0.74±0.09	0.316±0.013	2.23±0.01	14.7±0.7
<i>MgAl LDH hydrothermal</i>				
Mg:Al 1.83:1 HTM	0.73±0.03	0.313±0.007	2.20±0.03	6.4±0.3
Mg:Al 2.06:1 HTM	0.74±0.12	0.316±0.016	2.24±0.02	6.4±0.3
Mg:Al 2.17:1 HTM	0.74±0.05	0.315±0.005	2.22±0.02	9.7±0.2
Mg:Al 3.31:1 HTM	0.74±0.10	0.316±0.013	2.23±0.02	13.5±0.1

^afrom Bragg equation and ^bfrom Scherrer formula

Secondly, lattice parameter *c* corresponds to three-times the interlayer spacing, *d* between the layers which calculated as $c = d(003) + 2d(006) + 3d(009)$. Thus the *c* value increases linearly as the *d* spacing value increased. Furthermore, the effect of rehydration on MgAl crystalline structure can be seen in the above figures. Hydrothermal rehydration has enhanced the crystallinity of the sample, as can be seen by the increased intensity and definition of the peaks. A previous study has proven that during the rehydration process, the Gibbs free-energy becomes more thermodynamically favourable at higher Mg:Al ratio, consequently increasing the rate of formation and hence forming a more crystalline structure¹⁷. Sharma *et al.* have proven crystallite size and crystallinity of hydrothermal treatment HTs were significantly increased compared to the precursor¹⁸. The HTMs produced in this work did not exhibit a large enhancement in

terms of crystallite size, however, there was a definite systematic trend of increasing crystallite size across the loading series as evidenced by peak sharpening within the diffractograms. The XRDs also exhibit pure HT phases, without formation of any unexpected impurities such as MgO or brucite layers¹⁹.

5.4.1.5 Temperature-programmed desorption of CO₂ of ConvMgAl LDH

CO₂-TPD of all ConvMgAl series can be seen in **Figure 5.4**. Figures have been offset for clarity. The CO₂-TPD profiles consist of multiple desorption peaks. The lowest temperature (below 200 °C) desorption peak can be attributed to a bicarbonate species interacting on weakly basic OH groups which have been removed after treatment at 100 °C as has been shown in Section 5.4.1.2 by the water loss observed in TGA analysis. At moderate temperature (300-350 °C), the medium strength bicarbonates are observed bound to interlayer anions of hydrotalcite. While at a higher temperature (above 350 °C) shows unidentate carbonates attached to strong basic sites of hydrotalcite compound.

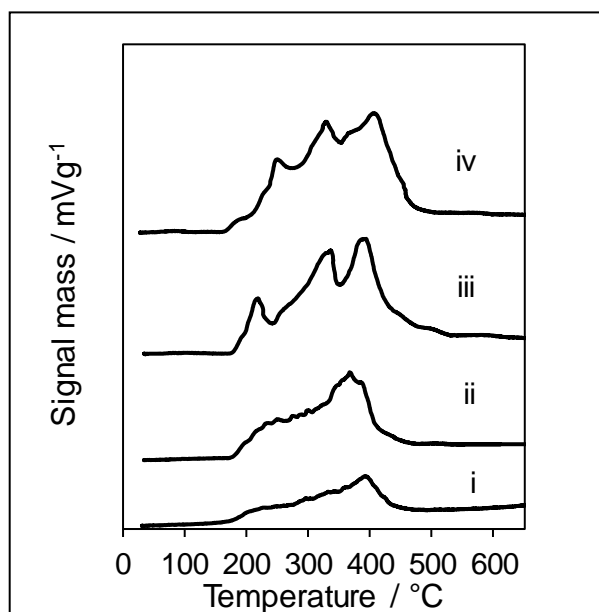


Figure 5.4 CO₂-TPD profile of ConvMgAl HT series from 1.83:1, 2.06:1, 2.17:1 and 3.31:1 (i-iv).

Unidentate formed on strongly basic surfaces of O²⁻ anions and remain adsorbed even after higher treatment at 350 °C. As the Mg:Al ratio increases, the CO₂ desorption peak temperature increases respectively. The number of active sites and base site density are tabulated in **Table 5.5**. Basicity progressively increases as the Mg content increases which could also be suggested by an increased surface concentration of Mg²⁺ and O²⁻ to be measured by XPS.

Table 5.5 The amounts of basic sites in ConvMgAl HT samples.

Sample	Number of active sites ^a / mmol g ⁻¹	Base site density ^b / molecules g ⁻¹ x 10 ¹⁹
<i>ConvMgAl HT</i>		
Mg:Al1.83:1HTM	0.007±0.009	4.1±1.7
Mg :Al2.06:1HTM	0.007±0.006	4.3±1.7
Mg:Al2.17:1HTM	0.007±0.004	4.4±1.7
Mg:Al3.31:1HTM	0.010±0.019	5.8±0.2

^{a,b}Determined by CO₂ pulse chemisorption

5.4.1.6 X-ray photoelectron spectroscopy of ConvMgAl LDH

XPS was employed to probe the surface of ConvMgAl series. The resulting Mg 2s XP, Al 2p XP and O 1s XP spectra are shown in **Figure 5.5** respectively. Spectra were energy referenced to adventitious carbon at 284.6 eV and all spectra were fitted with a Shirley background, whilst peaks were fit with a Gaussian-Lorentz peak shape, prior to background subtraction alongside pure alumina and MgO reference compounds¹⁹. Spectral fitting was performed using CasaXPS software.

The Mg 2s spectra (**Figure 5.5a**) were fitted at 88.1 eV according to the NIST spectral database^{20,21}. These spectra exhibit a single broad peak which indicates a single chemical environment. The Mg²⁺ contents are shown to increase across the series demonstrating a higher concentration of Mg on the surfaces as the loading increases.

Both Al 2p and O 1s spectra were fitted into two distinct chemical environments (NIST standard)²² as shown in **Figure 5.5 b** and **c**. In Al 2p spectra, all spectra were fitted to 74.5 eV according to an experimentally determined standard of Al₂O₃. Octahedral Al was detected at a higher energy binding (74.9 eV), whilst, the tetrahedral Al exists at a lower binding energy (73.1 eV). O 1s spectra were fitted at 532 eV and two main binding energies were detected at 531 eV and 533 eV which correspond to the existence of O in CO₃²⁻ and O in OH⁻ in the interlayer respectively. The intensity of O²⁻ increased with the Mg content loading, which indicates the strength of basic sites increased with Mg content⁸.

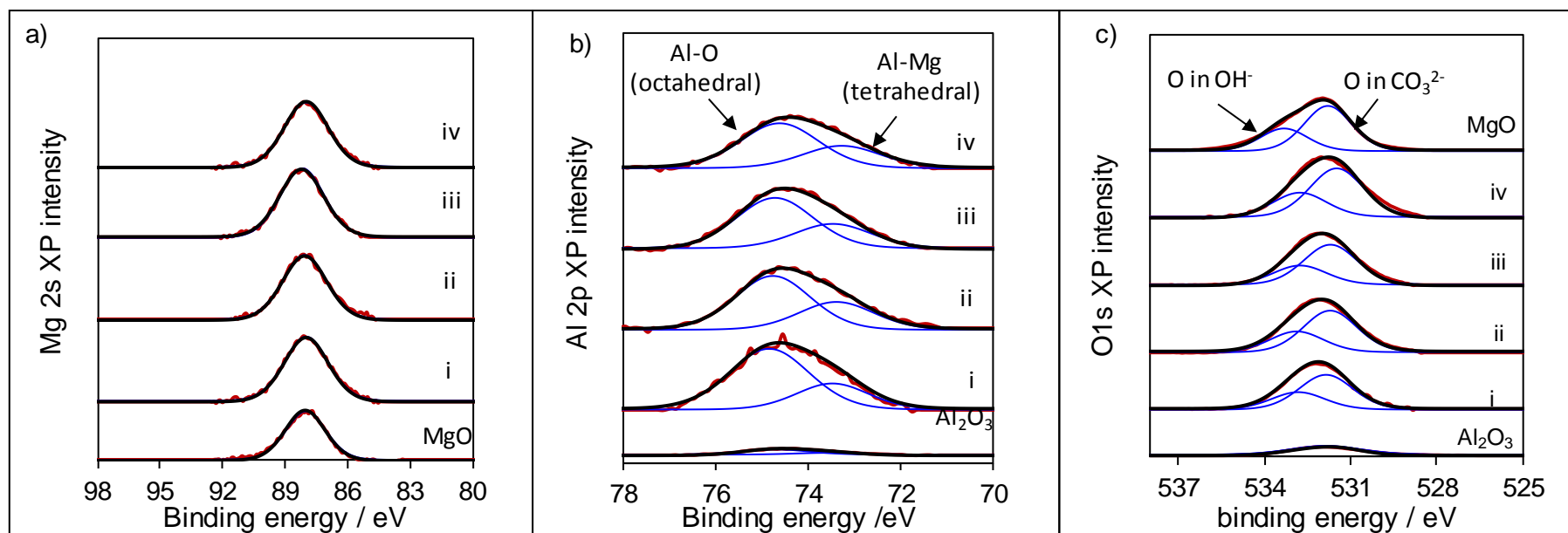


Figure 5.5 Stacked Mg 2s XP (a), Al 2p XP (b) and O 1s XP (c) on ConvMgAl HT series spanning from 1.83:1 to 3.31:1 (i-iv in each series). — denoted as envelope, — raw data and — HT component.

Quantitative analysis of the XP spectra combined with the EDX analysis enabled the correlation between bulk and surface Mg to be determined, which is presented in **Figure 5.6**. The results show a good correlation between both surface and bulk elemental analysis, whereby the surface Mg wt. % increased in a linear fashion with the bulk Mg content, suggesting no spatial changes to the elemental composition within the hydrotalcite¹. Surface loading obtained from XPS analysis reports a much a lower value compared with EDX analysis due to the attenuation of the photoelectron signal of the oxide sample through an outer layer of carbon contaminant present in all powder XPS.

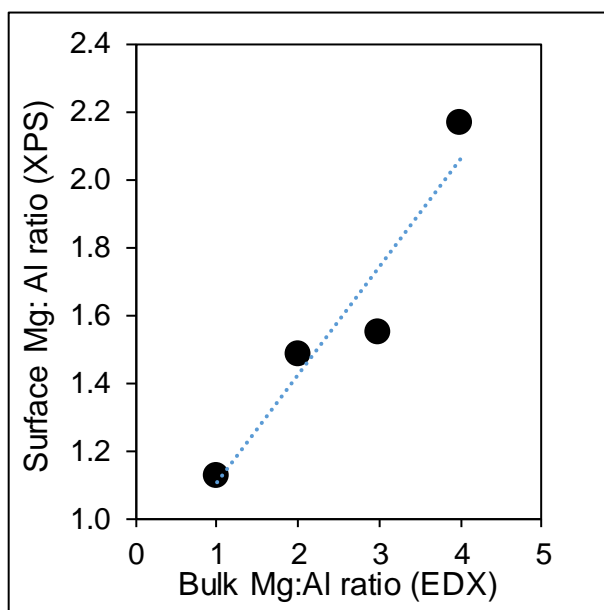


Figure 5.6 Mg surface wt % as a function of Mg:Al atomic ratio determined by XPS and EDX analysis respectively for ConvMgAl HT series.

5.4.2 Characterisation of polystyrene spheres

5.4.2.1 Scanning electron microscopy of polystyrene beads

Polystyrene (PS) beads were prepared as described in Section 2.1.2. SEM imaging was used to confirm the success of PS beads and also to quantify their size distribution^{23–25}. The image confirmed the beads existed in a purely spherical morphology and the mean bead diameters were found to be 375 (\pm 46) nm¹ (**Figure 5.7**).

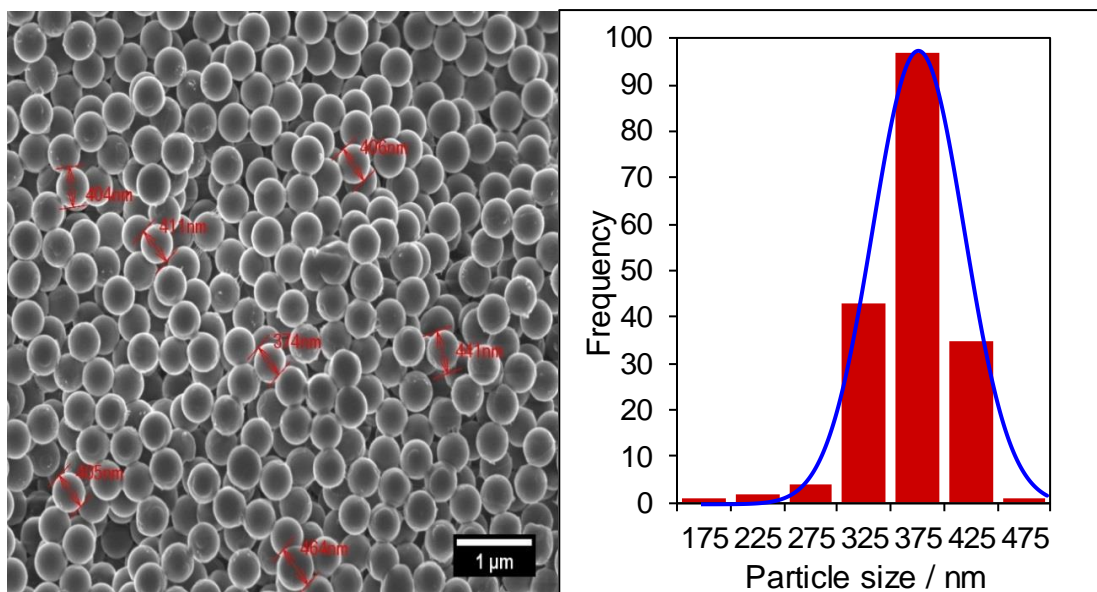


Figure 5.7 Representative SEM image of polystyrene spheres and associated particle size distribution.

5.4.3 Characterisation of conventional and macroporous reconstructed MgAl and ZnAl LDHs

Conventional ZnAl LDH and NiAl LDH have been previously discussed in Chapters 3 and 4. In this subchapter, a series of conventional and macroporous MgAl and ZnAl LDH were prepared according to a modified procedure (described in Section 2.1 – 2.1.3) from Woodford *et al.*¹. We were unable to synthesise MacroNiAl LDH after many rigorous trials. It was found that MacroNiAl LDH does not entirely form nor reconstruct to the anticipated HT layered structure. XRD analysis indicated a non-hydroxalcite structure, producing an unknown diffraction pattern for which no corresponding literature could be identified. Potentially, the high pH and ratio used (4:1) could be uncondusive for the formation of MacroNiAl LDH, as evidenced by a large degree of amorphous material detected by XRD analysis. It was noted that during the synthesis process, a blue solution was formed instead of the typical green colour expected from Ni²⁺ once polystyrene had been introduced. For this reason, further work on this catalyst has been discarded. In future work, it might be the possible to synthesise MacroNiAl LDH at ratio lower than 4. Herein, a ConvLDH and MacroLDH version of MgAl and ZnAl have been synthesised to be compared with M²⁺:Al³⁺ ratios of 4:1, as this ratio has been previously shown to exhibit excellent catalytic activity as discussed in previous chapters. The successful synthesis of all materials has been confirmed by a range of characterisation techniques.

5.4.1.1 Elemental analysis of ConvLDH and MacroLDH

A series of conventional and macroporous alkali-free MgAl and ZnAl LDH at a nominal ratio of 4 were synthesised and further analysed by EDX and XPS to quantify the actual bulk and surface compositions (**Table 5.6**). For both the MgAl and ZnAl materials, the recorded bulk ratio of $M^{2+}:Al^{3+}$ in the macroporous samples are lower than that of the corresponding conventional LDH. This is vital to consider when comparing subsequent reactivity differences, to separate enhancements originating from the morphology or structural effects from those arising from their elemental composition or intrinsic basicity^{1,19}.

Table 5.6 Bulk $M^{2+}: Al^{3+}$ ratio determined by EDX and XPS for conventional and macroporous LDH.

Catalysts Nominal ratio	$M^{2+}:Al^{3+}$ ratio determined by EDX			
	Conventional LDH		Macroporous LDH	
	EDX / $M^{2+}: Al^{3+}$ ratio	XPS / $M^{2+}: Al^{3+}$ ratio	EDX / $M^{2+}: Al^{3+}$ ratio	XPS / $M^{2+}: Al^{3+}$ ratio
Mg:Al4:1	3.31	1.02	2.42	1.15
Zn:Al4:1	3.33	2.28	1.45	1.02

5.4.1.2 Powder X-ray diffraction of ConvLDH and MacroLDH

Both the ConvLDH and MacroLDH versions of MgAl and ZnAl catalysts have been analysed by X-ray Diffraction (XRD) as a core technique to confirm the formation of the anticipated hydrotalcite structure²⁶. The first section will discuss the MgAl HT. Both diffraction patterns of ConvLDH and MacroLDH of MgAl depicted in **Figure 5.8a** and **5.8b (AS)** revealed the same definite pattern of hydrotalcite as found in literatures^{1,26–28}. Diffraction angles at $2\theta = 11.6^\circ, 23.4^\circ, 35^\circ, 39.6^\circ, 47.1^\circ, 61.1^\circ$ and 62.3° , characteristic of MgAl hydrotalcite, confirmed the successful preparation of the desired material^{26–28}.

During calcination of both ConvLDH and MacroLDH Mg/Al, the brucite layers collapsed and the phase shifted to that of periclase MgO, as evidenced by the resulting peaks at $2\theta = 35.9^\circ, 43.5^\circ$ and 63.5° representing the d(111), d(200) and d(220) planes respectively (**Figure 5.8a-b, CAL**). This was accompanied by the associated disappearance of the basal spacings of d(003) and d(006) reflection, affirming that the hydrotalcite structure was mainly destroyed during the calcination process⁸.

Following the rehydration process, diffraction patterns observed at basal plane $d(003)$, $d(006)$, $d(009)$, $d(015)$, $d(018)$, $d(110)$, $d(113)$ and $d(116)$ reappeared, thus confirming the successful rearrangement of the structure back to the LDH form following the rehydration process^{30,31} (**Figure 5.8a-b, HTM**). Hydrothermal MgAl reconstructed has increased the conventional and macroporous crystallinity from 76 % (AS) to 81 % (HTM) and from 83 % to 85 % respectively as determined by peak integration and comparison with a fitted baseline representing the amorphous constituent.

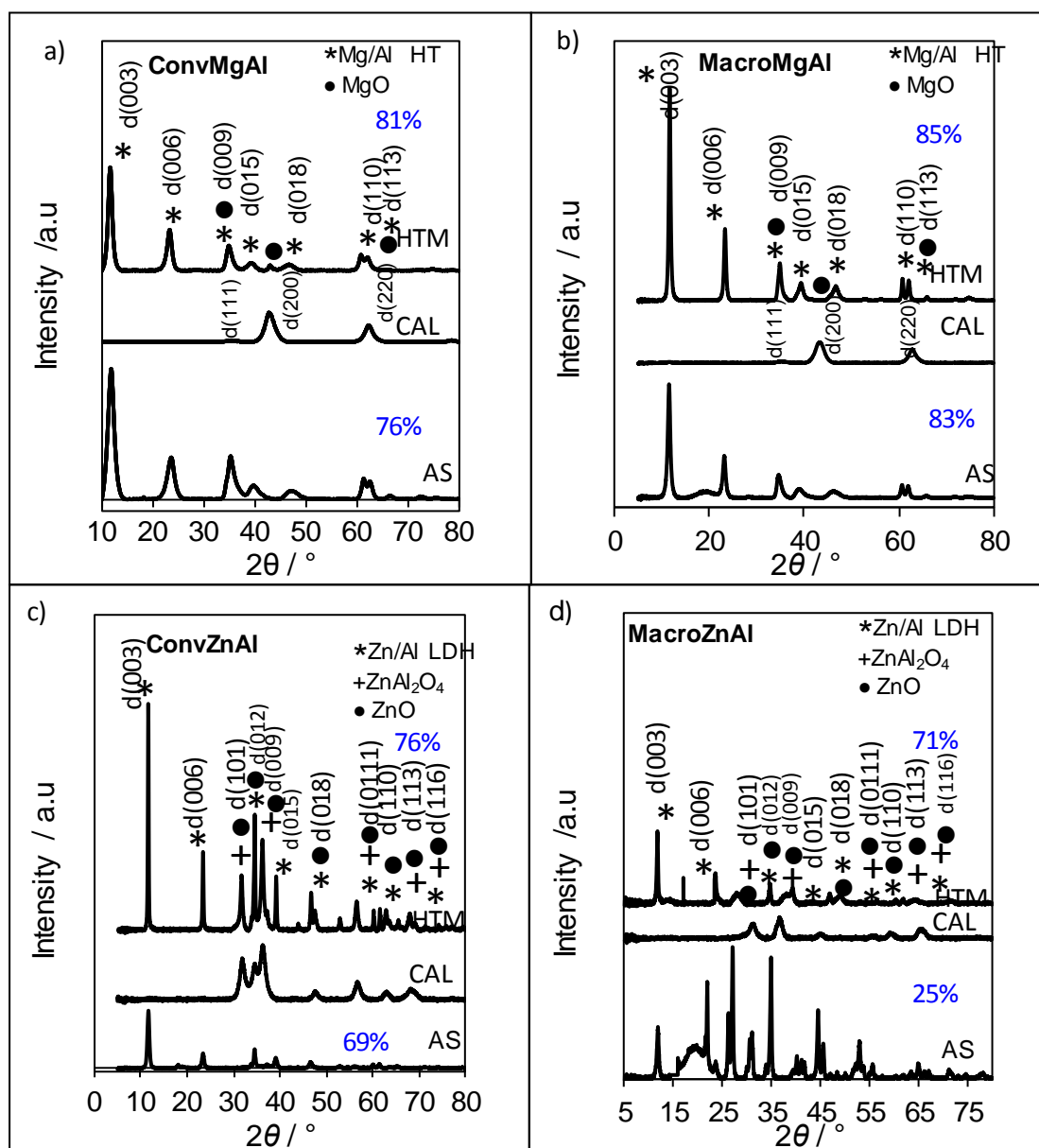


Figure 5.8 XRD diffraction patterns of conventional and macroporous MgAl and ZnAl LDH. The intensity ratio of HT over mixed oxide is denoted by the percentage values.

The successful synthesis of both ConvLDH and MacroLDH forms of the ZnAl LDH was also determined through the use of X-ray diffraction, the results of which have been depicted in **Figure 5.8c** and **5.8d** respectively. The XRD patterns of as-synthesised

(AS) samples exhibit the characteristic of ZnAl LDH which appeared at d(003), d(006), d(012), d(015), d(018), d(0111) and d(110)¹⁶. As with the previous material, a peak appeared at 20° can be seen in the AS (**Figure 5.8d**), representative of the polymer template. The disappearance of this peak upon calcination is suggestive of removal of the polymeric species². ZnO and ZnAl₂O₄ phases were detected after calcination at temperatures as low as 250 °C (Section 3.4.2.1) hence as these samples have been calcined at 350 °C we can expect to see these phases in similar amounts.

MgAl LDH, whether it in the form of ConvLDH or MacroLDH benefit from facile reconstruction, however, the ZnAl LDH materials have been found to suffer a more difficult reconstruction process. This finding agrees with previous literature for ConvZnAl LDH materials in which the formation of ZnO and ZnAl₂O₄ has been detected following a similar calcination process^{32,33}. Diffraction patterns in **Figure 5.8c** and **5.8d** revealed an increase in crystallinity from 69 % (AS) to 76 % (HTM) of ConvLDH and from 25 % (AS) to 71 % (HTM) of MacroLDH upon reconstruction. Calculation of the lattice parameter, *a* and *c* of the Macr MgAl LDH found an increased upon introduction of PS templates and subsequent reconstruction, evident of an increased crystallite size (**Table 5.7**).

Table 5.7 The textural parameter of conventional and macroporous MgAl and ZnAl LDH including the basal spacing d(003), lattice parameter and crystallite size.

Parameter/ catalyst	d003 / nm	^a Lattice parameter /nm		^b Crystallite size / nm
		<i>a</i>	<i>c</i>	
<i>MgAl LDH</i>				
CConvLDH	0.74±0.02	0.304±0.033	2.23±0.41	12.6±0.9
MMacroLDH	0.75±0.03	0.305±0.040	2.28±0.04	24.1±0.2
<i>ZnAl LDH</i>				
CConvLDH	0.74±0.02	0.308±0.041	2.29±0.09	33.8±0.3
MMacroLDH	0.76±0.04	0.306±0.040	2.30±0.04	19.6±0.2

^a were determined by Bragg equation and ^b were determined by Scherrer equation

Interestingly, regarding the ZnAl LDH material, the MacroHT form has brought about a diminished lattice parameter *a* and *c*, and also a reduction in the crystallite size. This has been ascribed to a potential formation of ZnO, ZnAl₂O₄ and PS, intruding into the interlayers, thus severely affecting the reformation of the layer, shrinking the lattice parameter and furthermore, reducing the crystallite size.

5.4.1.3 Nitrogen porosimetry of ConvLDH and MacroLDH

N₂ adsorption-desorption isotherms of ConvLDH and MacroLDH forms of MgAl and ZnAl can be seen in **Figure 5.9a-b** respectively. Figures were offset for clarity. The textural properties of the ConvLDH and MacroLDH families are summarised in **Table 5.8**. The isotherms from ConvLDH of MgAl and ZnAl have type II classifications and exhibit hysteresis loops H2 based on the IUPAC classification³⁴ indicating the catalysts are composed of mesopores with an ‘ink-bottle’ structure³⁵. We postulate restricted pore accessibility in ConvLDH compared with MacroLDH due to the narrow neck bottle shape unveiled in ConvLDH¹. Meanwhile, the MacroLDH of both MgAl and ZnAl exhibit the combination of type II and type IV isotherms with H3 hysteresis loops, marking the presence of unified mesopore/macropores structures³⁵. This also indicates the existences of slit-type pores which arrises from plate-like morphology³⁵.

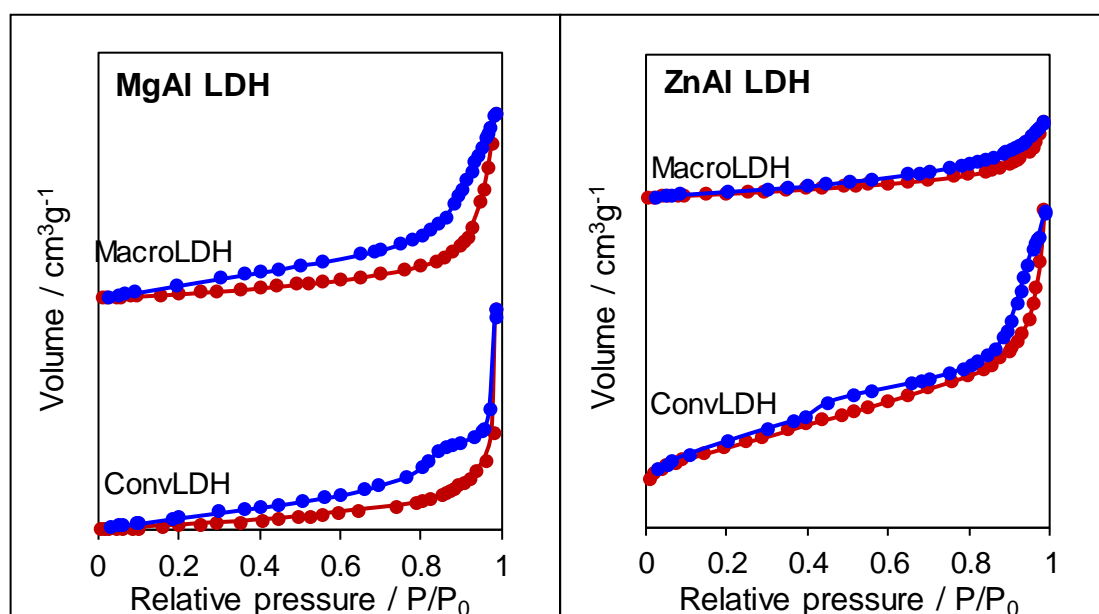


Figure 5.9 Stacked adsorption-desorption isotherms of conventional (a) and macroporous (b) MgAl, and ZnAl LDH.

Table 5.8 BET surface area (S_{BET}) and mercury intrusion pore diameter for conventional and macroporous MgAl and ZnAl LDH.

LDH catalyst	BET Surface area / m ² /g	Mercury intrusion pore diameter/ cm ³ /g ⁻¹
MgAl LDH		
CConvLDH	13±4	31
MMacroLDH	17±3	146
ZnAl LDH		
ConvLDH	256±23	25
MacroLDH	24±6	106

To further evaluate and examine the pore network, mercury intrusion analysis was undertaken. Both ConvLDH (MgAl and ZnAl) possess a pore diameter in the range of typical mesoporous structures (31 and 25 nm) which attributes to interparticulate spacings. Meanwhile, MacroHT forms of both formulations exhibit macroporous voids, with measured pore diameters of 146 and 106 nm respectively (**Figure 5.10**), in agreement with previous studies^{35,36}. The reason behind this is due to the incorporation of PS templates enlarging the inter-particulate spacings between hydrotalcite clusters, hence significantly increase accessibility of the basic catalyst. A number of previous studies on mercury intrusion porosimetry pore size distribution of hydrotalcite have reported centred around a range of 100-200 nm^{35,36}. Pore size distribution profiles of both ConvLDH and MacroLDH show a unimodal pore diameter, with a narrow distribution for all samples except in MacroMgAl LDH material, which possesses a broader distribution. This is further evidence of the successful synthesis of a macroporous ZnAl hydrotalcite for the first time.

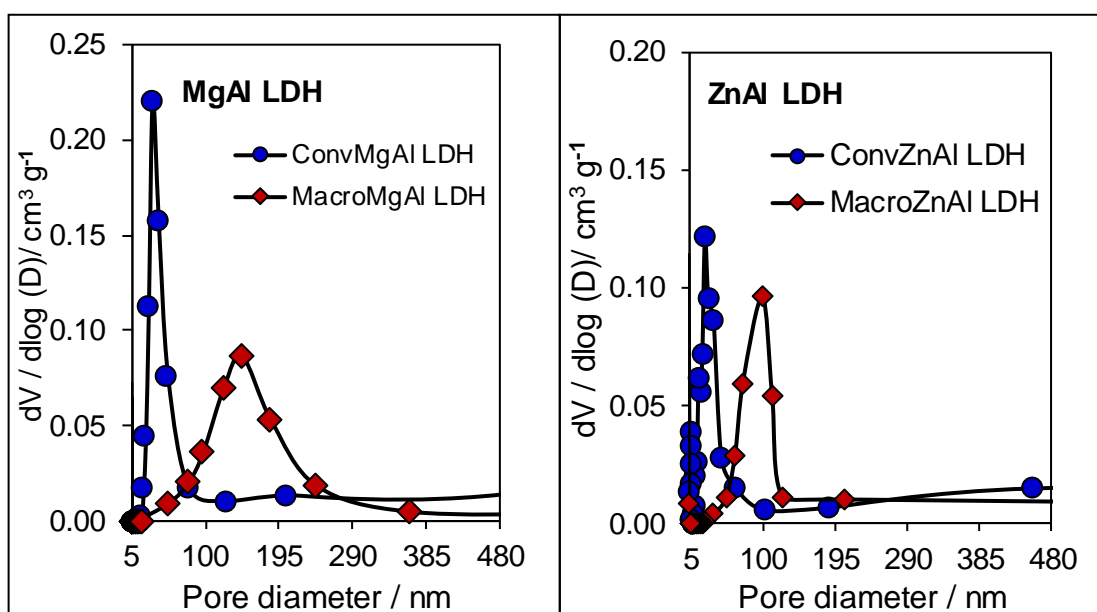


Figure 5.10 The pore size distribution of ConvLDH and MacroLDH on MgAl HT (left) and ZnAl HT (right) obtained from mercury intrusion porosimetry.

5.4.1.4 Scanning electron microscopy of ConvLDH and MacroLDH

In order to first probe the morphological differences between conventional and macroporous LDH, SEM images were taken of both catalysts, displayed in **Figure 5.11**. ConvMgAl LDH possesses the traditional sand-roses morphology as previously discussed in Section 5.4.1.3. Meanwhile, in ConvZnAl LDH, hexagonal platelets with plate-plate overlapping has been observed, which can be reasoned as to the higher

surface area associated with ConvZnAl LDH materials³⁷. The macropore network is clearly visible in the MacroLDH form of both of MgAl and ZnAl. The average diameters of the macropores within MacroMgAl LDH and MacroZnAl LDH are 316 ± 26 and 270 ± 35 nm, respectively. These values are slightly lower than the measured diameter of the PS bead templates (375 ± 46 nm), likely due to the shrinkage of beads occurring during the calcination process.

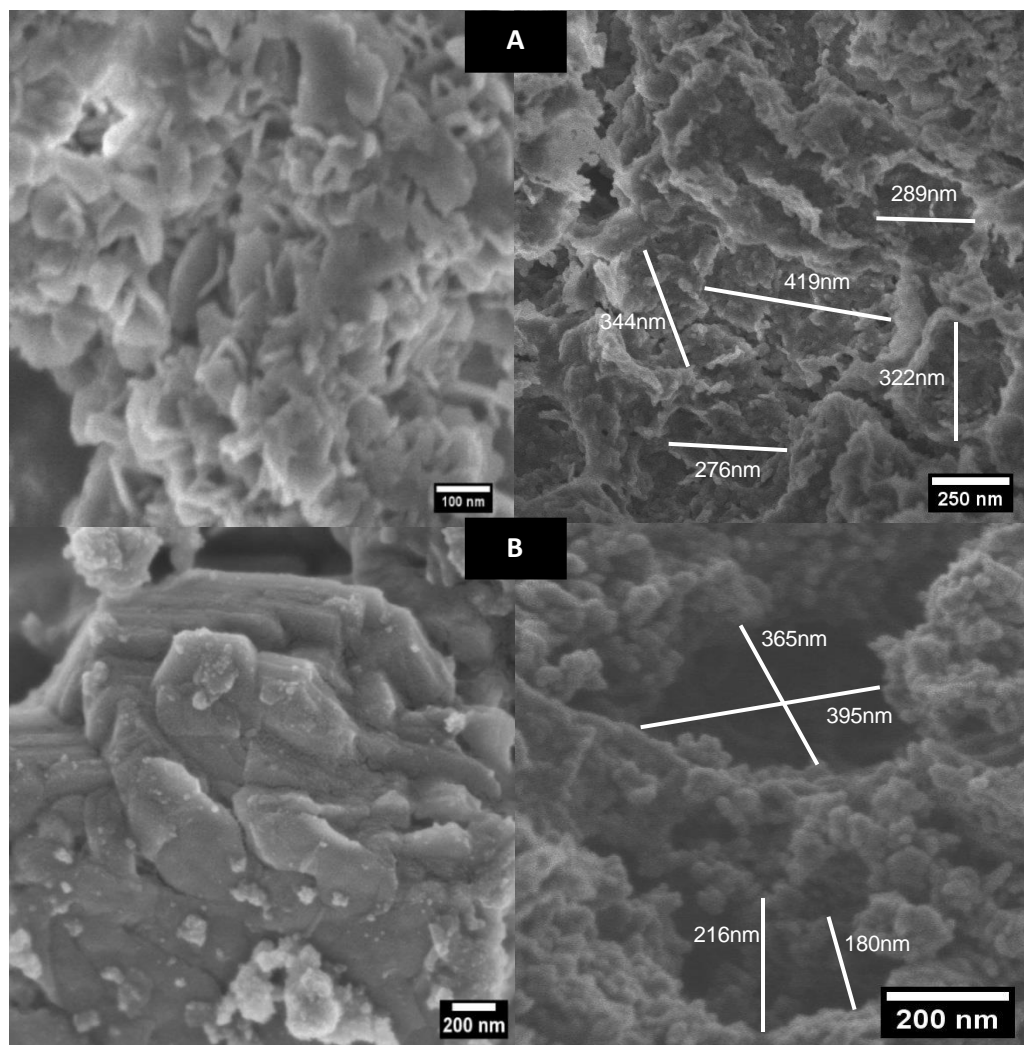


Figure 5.11 SEM images of conventional (left) and macroporous (right) MgAl LDH(A) and ZnAl LDH (B).

Figure 5.12 displays the morphology of MacroLDH of MgAl and ZnAl after calcination and rehydration processing. These SEM images further demonstrate the successful incorporation of macropores into the hydrotalcite framework, which is in agreement with the pore distributions obtained from mercury intrusion porosimetry. Calcination was done under O_2 to remove the PS beads, leaving clearly visible voids within the structure. Rehydration has regained the layer as proven by XRD due to the 'Memory Effect' of the materials.

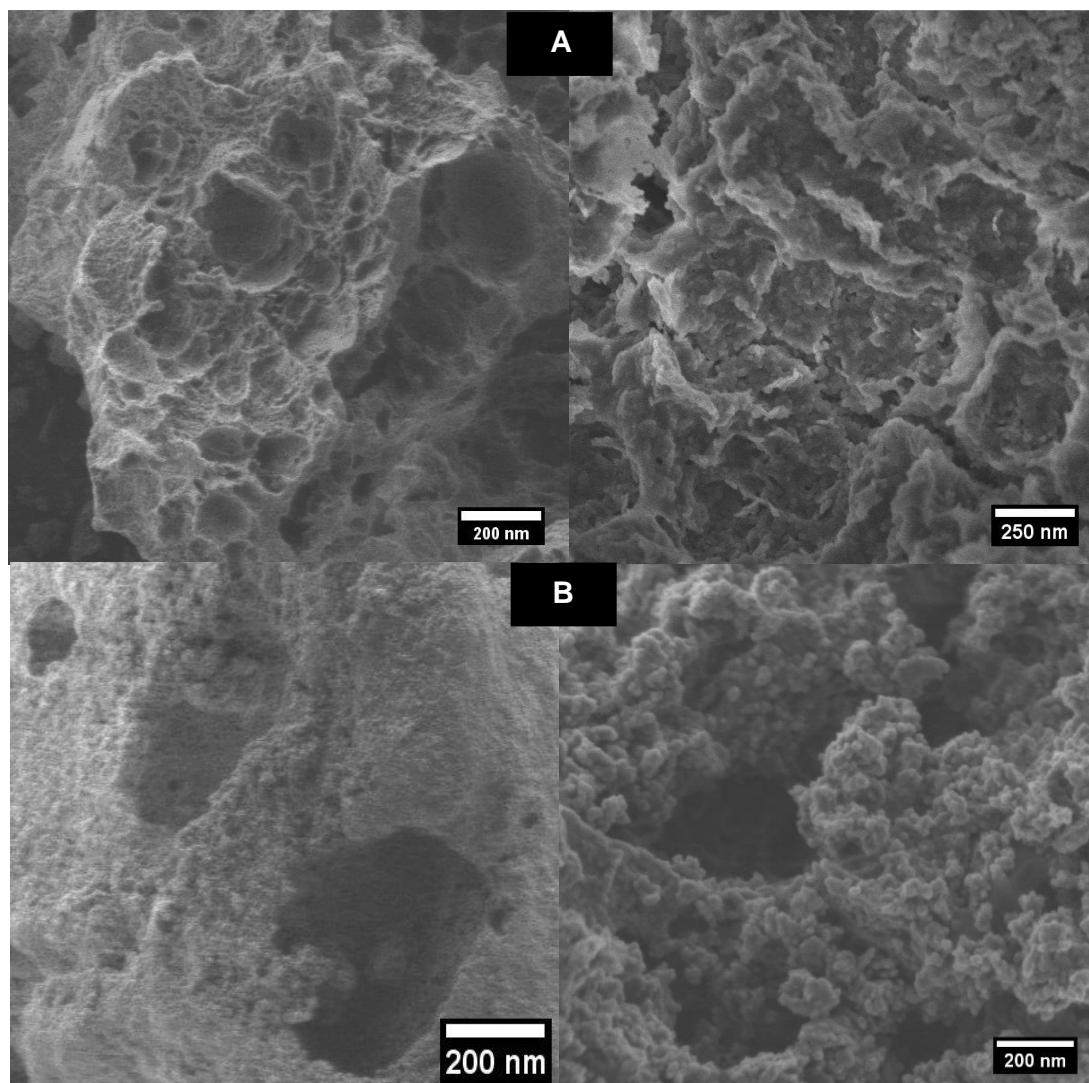


Figure 5.12 Calcined (left) and rehydrated (right) MacroMgAl LDH (A) and MacroZnAl LDH (B).

5.4.1.5 High-resolution scanning transmission electron microscopy of MacroLDH

HR-STEM analysis was undertaken on MacroLDH (MgAl and ZnAl) and the images from the high-angle annular dark field are shown in **Figure 5.13**. The images reveal ordered thin walled macropores introduced from PS template removal following the calcination-rehydration process. The average pore diameter of MacroMgAl LDH is 299 ± 12 nm which is in the range of the PS and consistent with the SEM analysis. Macropore shrinkage is a common phenomenon to be observed in PS bead templated macropore networks due to contraction during the calcination phase¹. These results are consistent with the work done by Woodford *et al.*¹ wherein they found the mean pore diameter of MacroMgAl HT to be 310 nm formed from a PS bead diameter of 350 nm.

As both MacroMgAl studies involved nominal ratio 4:00:1 (actual ratio ~2.00:1), the materials can be considered comparable.

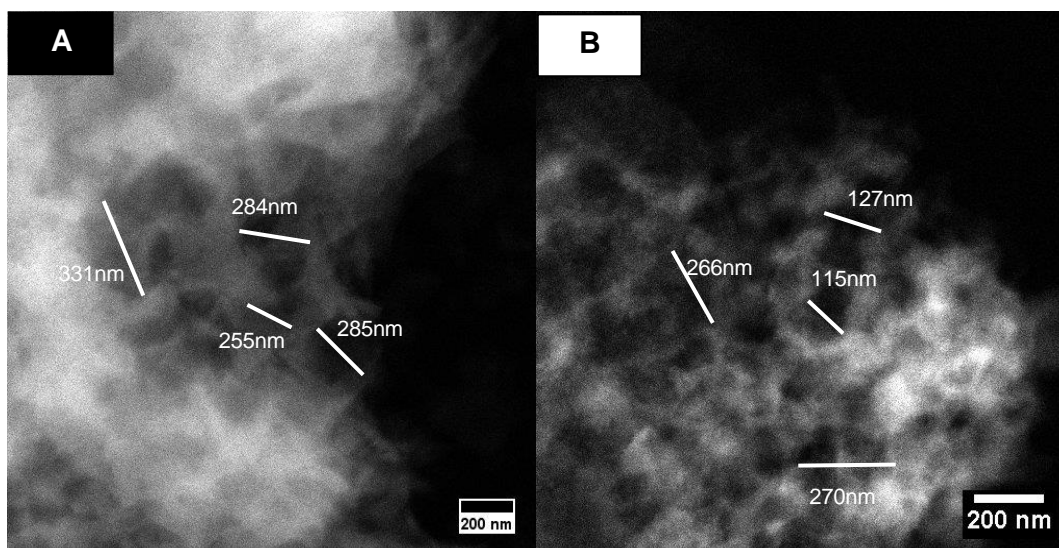


Figure 5.13 HR-STEM images of the MacroMgAl LDH (A) and MacroZnAl LDH (B).

TEM images of MacroZnAl LDH clearly shown a non-uniform macropore with non-rigid images of framework reflecting the less effective synthesis method of PS incorporation. This could potentially be remedied by switching from a thermal processing method for removal of PS beads to a dissolution methodology such as that reported by Geraud *et al.*³⁸ in which it was reported that PS beads can be removed by a dissolution method via three successive toluene or tetrahydrofuran (THF): acetone (1:1) (1g/10 mL) washes in order to obtain a more ordered framework. The macropores void of MacroZnAl LDH was calculated as 250 nm (**Figure 5.13b**), a slightly lower than that SEM data (270 nm) and likely due to the less clear boundaries visible in the STEM images.

5.4.1.7 Diffuse reflectance infrared Fourier transform spectroscopy of ConvLDH and MacroLDH

Figure 5.14 illustrates the DRIFTS spectra of ConvLDH and MacroLDH series respectively. Generally, three distinctive regions can be seen in DRIFTS analysis for common hydrotalcite samples³⁹. The first region at around 3000 to 3800 cm^{-1} indicates the surface OH stretching mode and also corresponds to water absorbed within hydrotalcite lamellar structure. This can also be seen as a bending mode of water molecules appearing at around 1600 cm^{-1} . According to the literature of MgAl HT, the common OH stretching vibration visible at 3700 cm^{-1} indicates the hydroxyl groups located on the corner or edges of MgO structure³⁹. In this case, both ConvLDH and

MacroLDH of MgAl revealed one broad peak at 3773 cm^{-1} and one sharp peak 3711 cm^{-1} for ConvLDH and MacroLDH respectively. This is further evidence of the conversion of LDH to MgO during the calcination process, which is later reversed during the rehydration procedure as seen by XRD analysis. Rehydration also increases the amount of water incorporated in the structures as represented by broad water stretching mode at this region. This theory also is supported by the XRD wherein the amount of material rehydrated is higher than the precursor.

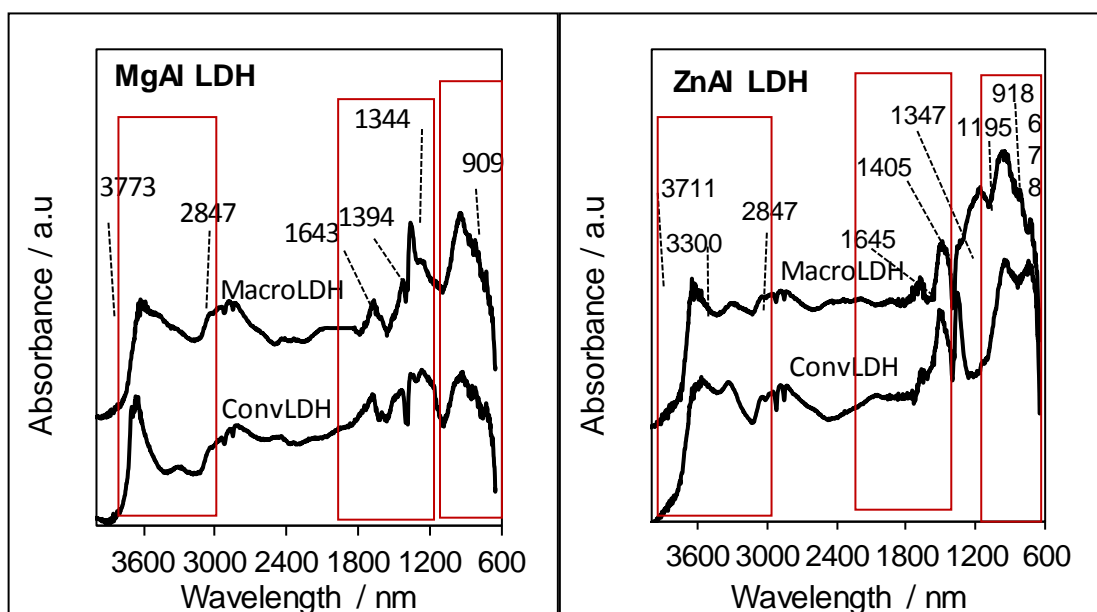


Figure 5.14 DRIFTS spectra of MgAl LDH and ZnAl LDH with indicates spectra for ConvLDH and MacroLDH respectively.

C-O vibration is detected at 2847 cm^{-1} in all samples. Overlapping infrared bands were observed on all hydrotalcite series in the $1700\text{--}1300\text{ cm}^{-1}$ region. Carbonate bonding is detected at around $1400\text{--}1665\text{ cm}^{-1}$ and is mainly comprised of unidentate ($1488, 1347\text{ cm}^{-1}$) and bidentate ($1645, 1347\text{ cm}^{-1}$) bonding modes. Meanwhile, Mg bonded to carbonates are detected at 1405 cm^{-1} . Hydrotalcite formation also can be assured of the existence of a Mg-O vibration at $950\text{--}700\text{ cm}^{-1}$ ¹¹³.

Typically, ZnAl hydrotalcites exhibit similar infrared spectra to that of MgAl HT with the exception of a few bands which are slightly different. For instance, a shoulder at around 3300 cm^{-1} was detected for both ZnAl samples (ConvLDH and MacroLDH) corresponding to the weak vibration of a hydroxyl group (related to main OH vibration at 3700 cm^{-1}) and furthermore indicative the OH bonding⁴⁰. Tania *et al.*⁴⁰ also suggested in one of their studies, that the peak at 3778 cm^{-1} corresponds to tetrahedral Al bonded to OH ($\text{Al}_{\text{IV}}\text{OH}$), meanwhile, the octahedral Al ($\text{Al}_{\text{VI}}\text{OH}$) is reportedly found at 3733 cm^{-1} with the main band at 3695 cm^{-1} . Somehow, it is hard to distinguish between these tetrahedral

and octahedral Al peaks as they have the potential to be superimposed on the same wavelength.

5.4.1.8 Thermogravimetric analysis mass spectrometry of ConvLDH and MacroLDH

Figure 5.15(a-b) and **Figure 5.16(a-b)** represents ConvLDH and MacroLDH of MgAl and ZnAl TGA-MS profiles respectively. The profiles show a characteristic two-step weight loss suggestive of an LDH in which the first transition is ascribed to water weight loss and the second transition is attributed to carbonates weight loss.

The first transition from 42 - 170 °C is associated with dehydration step. Further dehydroxylation steps occurred from 190 - 340 °C. In most cases, two transition steps of water weight loss have been observed except in for the MacroZnAl HT sample where only one major weight loss was observed. The result from the TGA reveals a small water weight loss occurred during dehydration step (3.5 %) followed by a huge weight loss during dehydroxylation step (13.8 %) corresponding to eliminating of interlayer water⁴¹, bringing the total water loss to 17.3%. Total water weight loss on other samples (ConvMgAl, MacroMgAl and ConvZnAl) were only found to be in the range of 11.5 - 14.5 % (**Table 5.9**). This confirmed that the density of interlayer H₂O in MacroZnAl sample is higher⁴² than the other three samples.

The second transition is due to dehydroxylation and decarboxylation of brucite-like layers appeared from 232 °C onwards. Around 4.3 - 10.0 % total mass loss due to dehydroxylation of brucite-like layers occurred on all samples bringing the total weight loss in up to the range of 20.2- 22.1 %. This value is in great agreement with a common mass loss of HT and in line with previous studies of Author⁴³. The pattern of DSC and MS curves were found to be identical in which the MS show two major weight losses of water at around 40-190 °C and 340 °C. Carbon dioxide is evolved at 340 °C, also in agreement with TG/DSC data.

Differential Scanning Calorimetry (DSC) profiles of ConvLDH and MacroLDH of MgAl LDH and ZnAl LDH are presented in Figure 5.15 and 5.16 respectively. ConvMgAl LDH showed two heat flow steps around 45 °C and 320 °C which are attributed to the absorbed water and dehydroxylation of water in the interlayer. The later heat flow was attributed to the loss of carbon dioxide from the interlayer anion. DSC profiles of MacroMgAlLDH, ConvZnAlLDH and MacroZnAlLDH showed first two heat flow steps around 40 °C and 200 °C which are attributed to dehydroxylation of absorbed water in the interlayer. Heat flow of decarboxylation was detected around 300-490 °C.

To calculate the theoretical and experimental weight loss including the formula of LDH, a general formula for HTs; $[M(II)_{1-x}M(III)_x(OH)_2]^{x+}(A^{n-}_{x/n}) \cdot mH_2O$ where $m = 0.81 - x$, has been applied. Based on this formula, both theoretical and experimental weight loss of all HT samples can be derived (**Table 5.9**). **Figures 5.17** depicted more experimental weight loss occurred compare to the theoretical ones on both ConvLDH and MacroLDH samples. Although these results are in slight contradiction to those previously reported by Woodford *et al.*¹, the total weight loss of both experimental and theory are in good agreement.

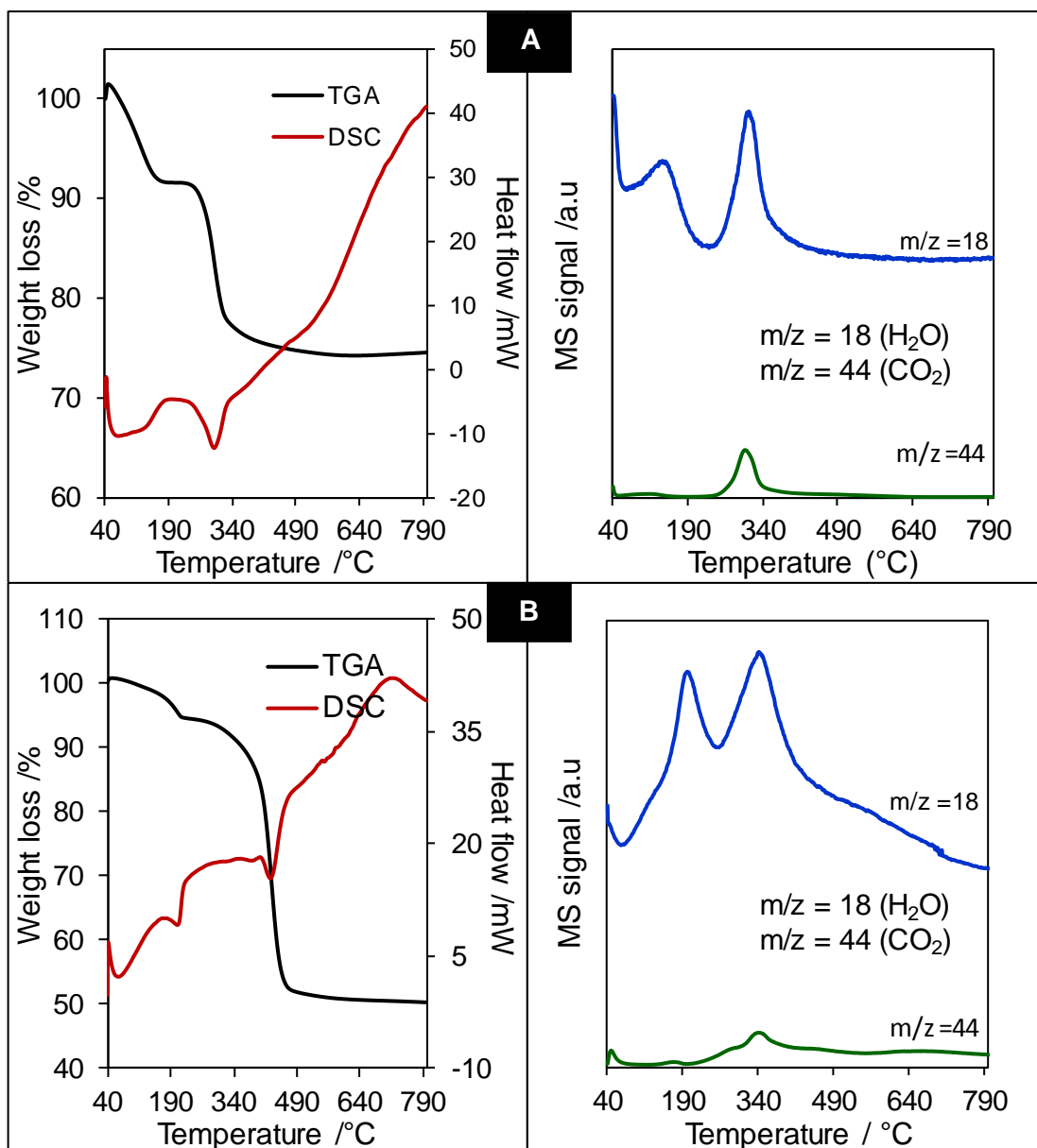


Figure 5.15 TGA-MS patterns of thermal conventional (A) and macroporous (B) MgAl LDH.

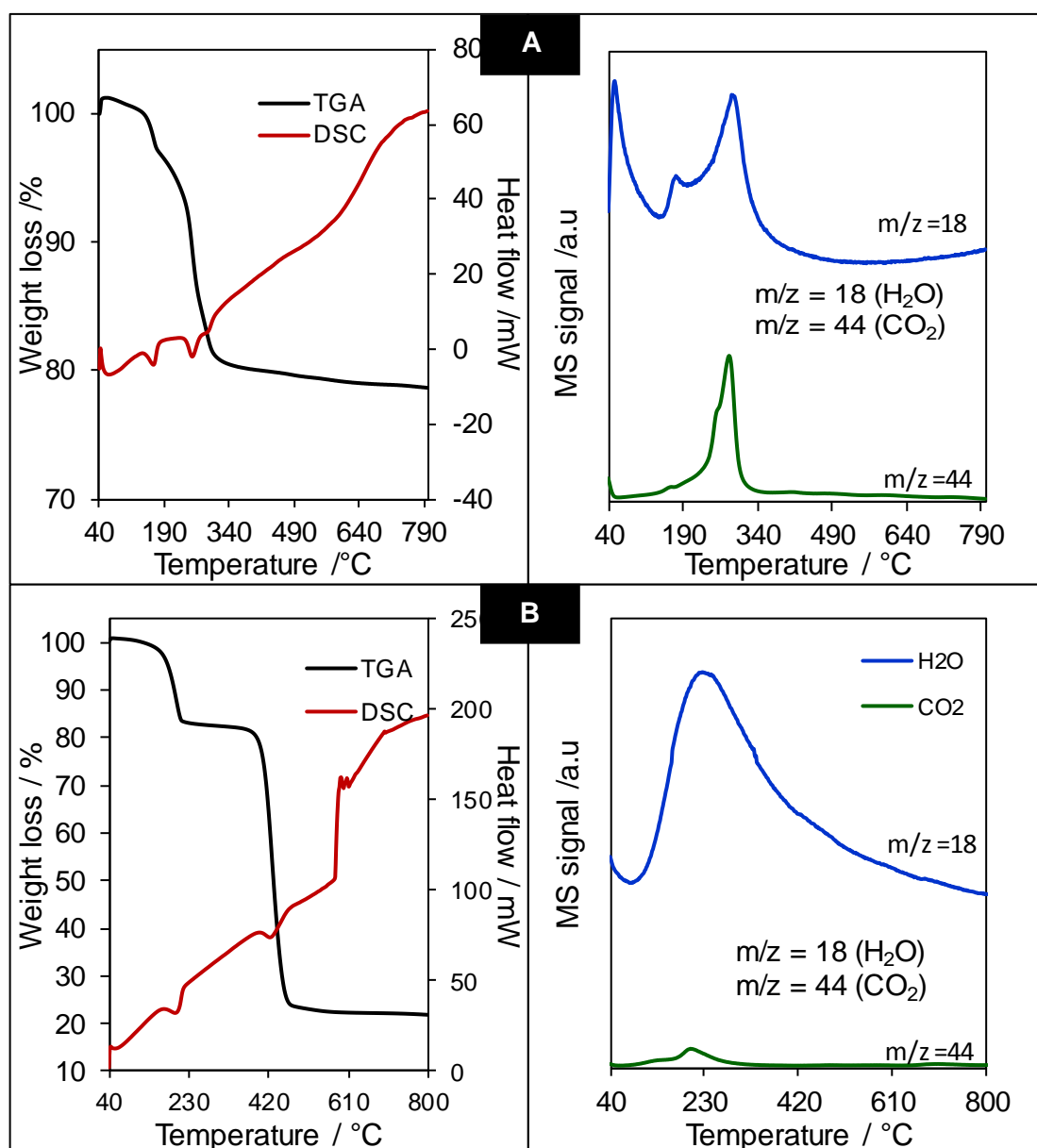


Figure 5.16 TGA-MS patterns of thermal conventional (A) and macroporous (B) ZnAl LDH.

Table 5.9 Experimental and theoretical weight loss and the LDH formula obtained from TGA-MS and EDX.

Experimental Weight loss / %				Theoretical weight loss /%			LDH formula
LDH catalyst/ weight loss	H ₂ O exp	CO ₃ exp	Total Weight loss/ %	H ₂ O theory	CO ₃ theory	Total Weight loss / %	
Conventional LDH							
MgAl	14.5	5.7	20.2	9.4	7.2	16.6	[Mg _{0.77} Al _{0.23} (OH) ₂].(CO ₃) _{0.12} 0.57H ₂ O
ZnAl	12.1	9.0	22.1	10.4	7.2	17.6	[Zn _{0.77} Al _{0.23} (OH) ₂].(CO ₃) _{0.12} 0.58H ₂ O
Macroporous LDH							
MgAl	11.5	9.8	21.2	9.4	9	18.4	[Mg _{0.71} Al _{0.29} (OH) ₂].(CO ₃) _{0.15} 0.52H ₂ O
ZnAl	17.3	4.3	21.6	10.8	12.6	23.4	[Zn _{0.59} Al _{0.41} (OH) ₂].(CO ₃) _{0.21} 0.60H ₂ O

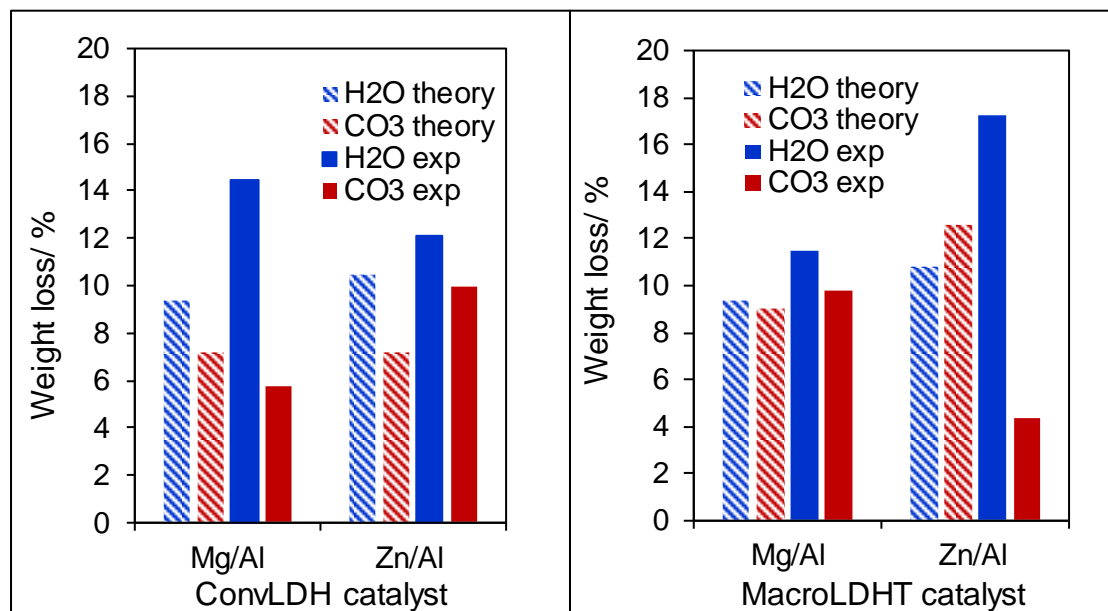


Figure 5.17 Theoretical and experimental weight loss of water and carbonates over ConvLDH and MacroLDH MgAl and ZnAl.

5.4.1.9 Temperature-programme desorption of CO₂ of ConvLDH and MacroLDH

CO₂-TPD of all hydrotalcite series (ConvLDH and MacroLDH) can be seen in **Figure 5.18**. Figures have been offset for clarity. The CO₂-TPD profiles consist of at least two desorption peaks in MgAl HT (conv and macro) and a single, sharp intense peak for the ZnAl LDH series. A combination of medium (temperature between 300-450 °C) and strong basic strength (temperature above 450 °C) is observed in the MgAl HT series. Meanwhile, bidentate carbonates which attached on medium basic sites of hydrotalcite compound was more pronounced in ZnAl HT series⁴⁴. The number of active sites and base site densities are tabulated in **Table 5.10**. In both LDH series, basicity was found to be retarded with the introduction of macroporosity. This might be due to acidic contents from PS reducing the basicity of MacroHT.

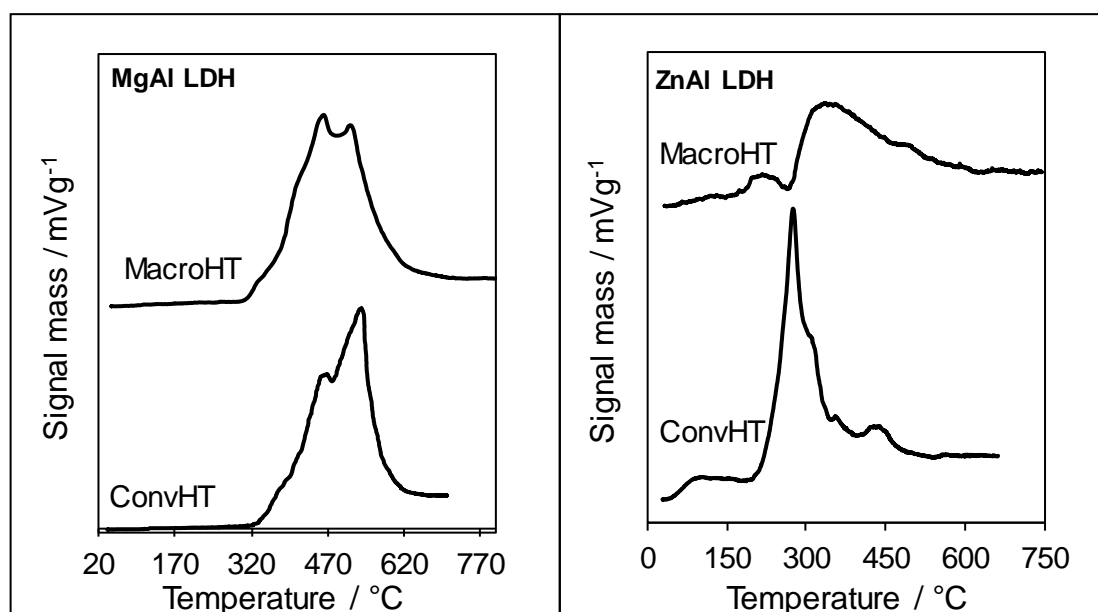


Figure 5.18 Stacked CO₂-TPD profiles of conventional and macroporous of MgAl LDH (A) and ZnAl LDH.

Table 5.10 Base site characterisation obtained via CO₂ chemisorption/TPD.

Sample	Number of active sites/ mmol g ⁻¹	Base site density / molecules g ⁻¹ (10 ⁻¹⁹)
MgAl LDH		
ConvLDH	0.057±0.012	3.4±0.2
MacroLDH	0.045±0.024	2.7±0.3
ZnAl LDH		
ConvLDH	0.100±0.054	6.0±1.2
MacroLDH	0.046±0.023	2.8±0.3

5.4.1.10 X-ray photoelectron spectroscopy of ConvLDH and MacroLDH

The surface composition of MgAl materials was subsequently analysed by XPS in order to understand the surface / near-surface chemical states of C, Mg, Al and O. **Figure 5.19a-d** depicts the C 1s, Mg 2s, Al 2p, O 1s spectra respectively. The C 1s peak of adventitious carbon was used to calibrate spectra using a binding energy of 284.6 eV (**Figure 5.19a**). Mg 2s spectra depicted in **Figure 5.19b** consist of one main peak at 90 eV⁸ indicative of a strong interaction between Mg atoms with the oxide⁴⁵.

Al 2p spectra (**Figure 5.19c**) were deconvoluted into two components; those of octahedral Al (Al-O interaction) at 74.8 eV and tetrahedral Al (Al-Mg) at 72.7 eV respectively. This finding is correlated with Al-MAS NMR in which a slightly more pronounced amount of octahedral Al was detected on MgAl HTM instead of tetrahedral Al.

Figure 5.19d shows O 1s spectra of conventional MgAl HTM. The parent state appears at 530 eV are in the same agreement with literatures^{8,45}. Peak deconvolution revealed two well-defined components. The highly intense peak corresponds to oxygen bonded to carbon species (CO_3^{2-}) (531 eV) while the less intense peak (533 eV) indicates oxygen species in OH^- structures. O^{2-} intensity increases in a linear trend with increasing Mg^{2+} content in MacroLDH.

XPS was subsequently employed to probe the surface of ZnAl LDH materials. The resulting C 1s, Zn 2p XP, Al 2p XP and O 1s XP spectra are shown in **Figure 5.19e-h** respectively. Again, C 1s peak of adventitious carbon was calibrated at the same binding energy (284.6 eV) (**Figure 5.19e**). The Zn 2p spectra (**Figure 5.19f**) were fitted at 1020 and 1042 eV according to the NIST spectral database^{20,21} which corresponding to the spin-orbit split Zn $2p_{3/2}$ and $2p_{1/2}$ states respectively.

Al 2p spectra (**Figure 5.19g**) were fitted at 74.5 eV²², consist two components revealing octahedral Al (Al-O interaction) at 74.0 eV and tetrahedral Al (Al-Zn) at 71.8 eV respectively. O 1s spectra at were fitted at 532 eV^{8,45} (**Figure 5.19h**) and peak deconvolution revealed two well-defined components. The high intense peak corresponds to oxygen bonded to carbon species (CO_3^{2-}) (530 eV) while the less intense peak (533 eV) indicates oxygen species in OH^- structures. The intensity of O^{2-} decreased with on macroporous, which indicates the strength of basic sites decreased with Zn content⁸ as proven by CO_2 -TPD.

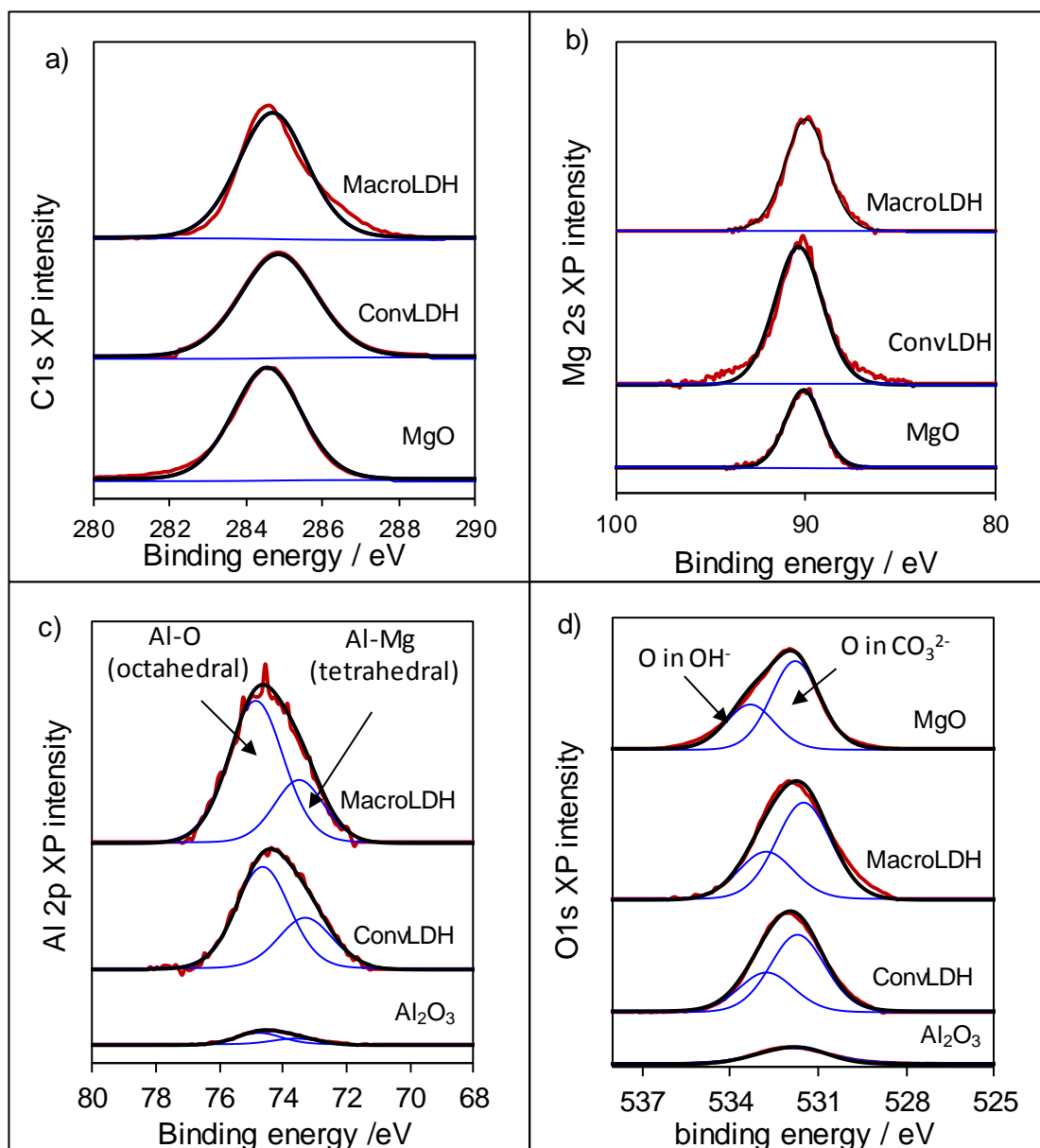


Figure 5.19 a-d XPS spectra ConvLDH and MacroLDH of MgAl for C1s, Mg 2s, Al 2p and O 1s XP . — denoted as envelope, — raw data and — HT component.

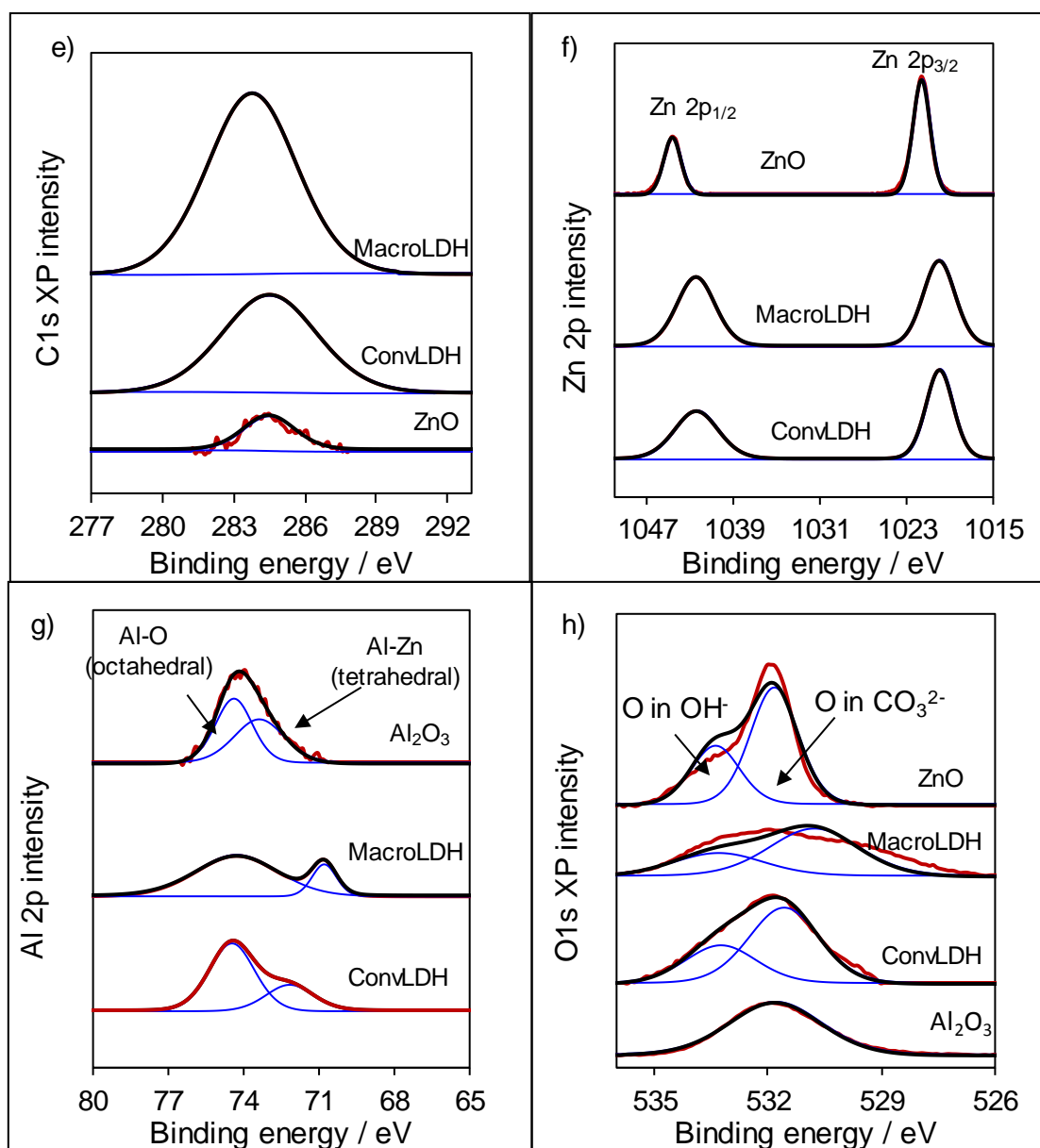


Figure 5.19 e-h XPS spectra ConvLDHLDH and MacroHT of ZnAl for C1s, Zn 2p, Al 2p and O 1s XP. — denoted as envelope, — raw data and — HT component.

5.4.4 Catalytic activity of ConvLDH versus MacroLDH

5.4.4.1 C₄-C₁₈ TAG reactions

The efficiency of ConvLDH and MacroLDH catalysts for FAME production were further examined through their ability to perform transesterification reactions in methanol under similar conditions as adopted in previous chapters (110 °C, 650 rpm for 24 h reactions). C₄-C₁₈ TAGs were subsequently evaluated to assess the enhancement to mass diffusion as a function of sterics. Initial rates have been calculated from the first 60 min of linear conversion reaction profiles. FAME selectivity was calculated as $\{[FAME]/([MAG]+[DAG]+[FAME]+[GLY])\} \times 100$ where MAG, DAG and GLY are the monoglycerides, diglyceride and glycerol respectively. Turnover frequency (TOF) is determined from normalising initial rates by base site density obtained from CO₂-TPD.

Figure 5.20 displays the reaction profiles for the conversion of a series of TAGs over MgAl and ZnAl in the form of ConvLDH and MacroLDH. From the graph, it can be seen that the introduction of macroporosity enhances conversion in all cases remarkably. This augmentation in catalytic activity has been postulated as the result of an enhancement in the mass transport of bulkier TAG components, hence explaining the increased improvement in activity with increased chain length^{1,46}. Both MacroHT incorporation in MgAl and ZnAl systems delivered a striking enrichment in rates of FAME, thus increasing the conversion, yield (**Figure 5.21**) and TOF (**Figure 5.22**).

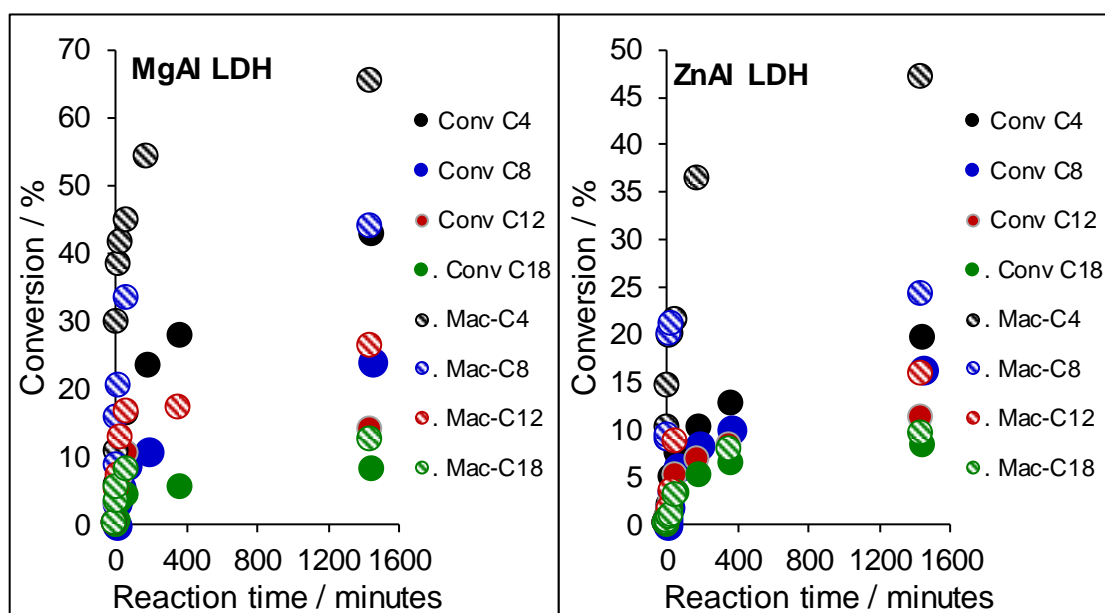
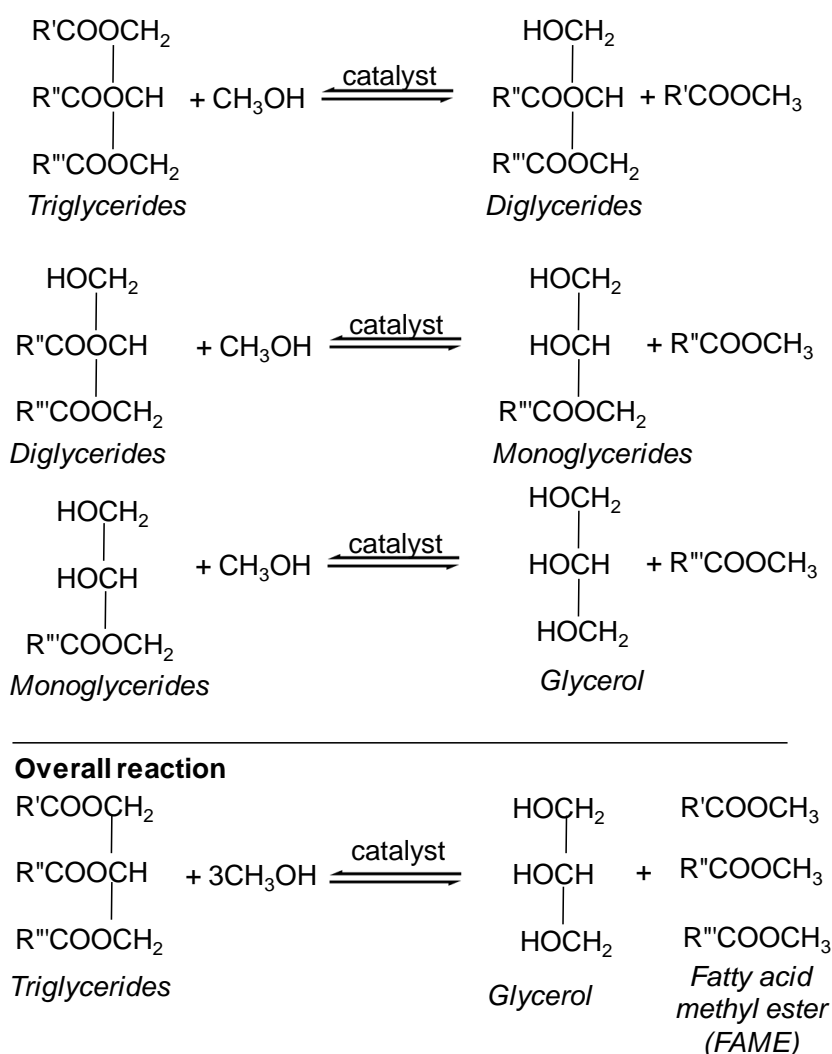


Figure 5.20 Reaction profile C₄-C₁₈ for conventional and macroporous of MgAl LDH (left) and ZnAl LDH (right).

As the chain length of TAGs were increased from smaller towards bulkier, the effective enhancement (due to the introduction of macroporosity) is seen to hold greater weight, with smaller chain TAGs finding a smaller enhancement compared with the large chain TAGs, likely due to decreased mass transport limitation through the interlayer spacings. The enhancement is especially pronounced when considering the diminished surface area and base site density associated with macropore introduction⁴⁶.

Further evidence of the MacroLDH enhancement can be seen in the increasing formation of intermediates, particularly dibutyryl and monobutyryl formation, compared with the ConvLDH (**Figure 5.21**). The selectivity of the MacroLDH catalysts are adequate enough that before the reaction has been completed, the amount of the intermediates dibutyryl and monobutyryl reach a peak and begin to decrease, as these intermediates themselves are converted to the FAME product as can be explained in Equation 5.1.



Equation 5.1 Transesterification reaction of triglycerides showing the intermediates of diglycerides and monoglycerides have been converted to glycerol and FAME during the reaction.

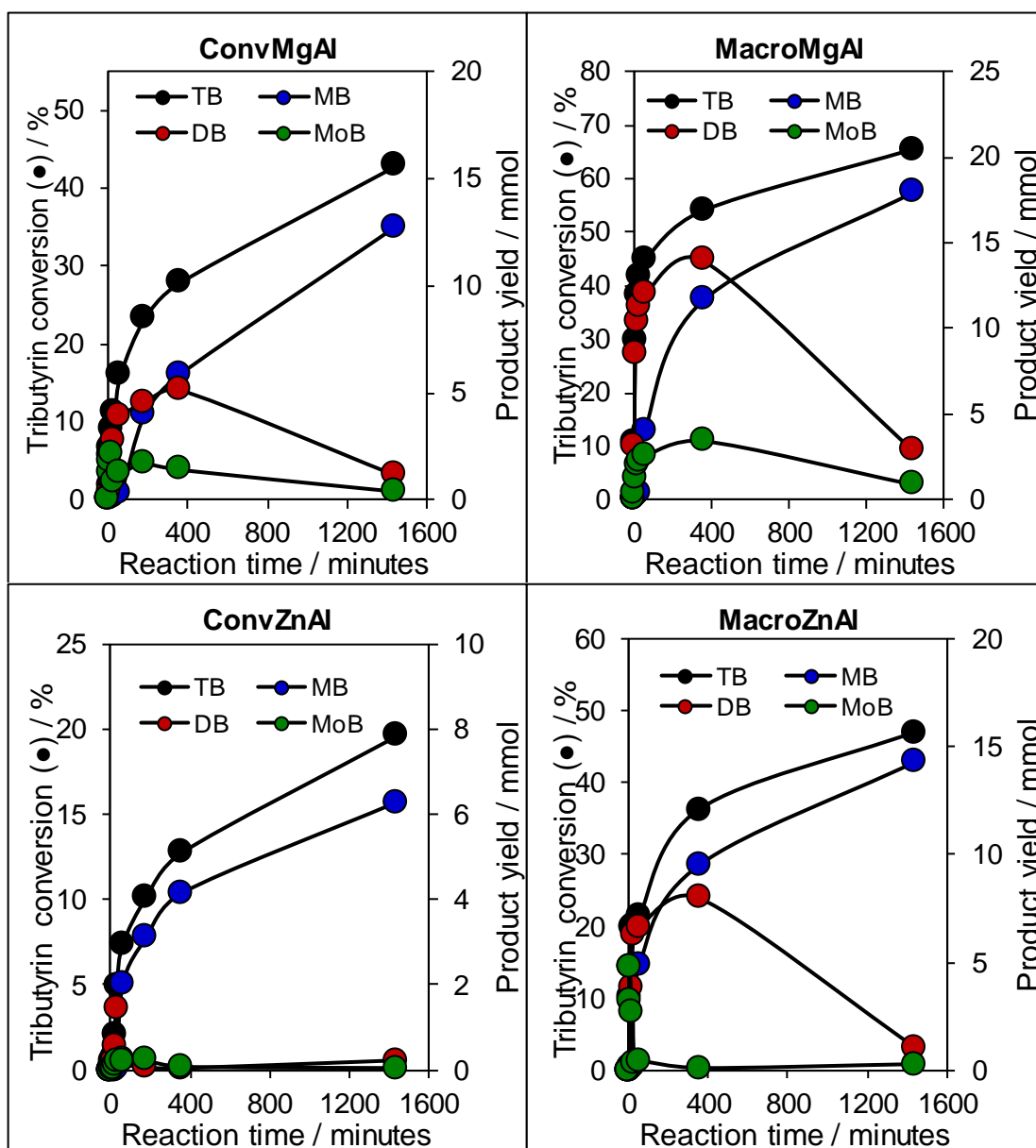


Figure 5.21 Reaction profile of ConvLDH and MacroLDH for both MgAl and ZnAl LDH in transesterification over C_4 . Reaction conditions: 110 °C, 650 rpm for 24 h reactions.

The TOFs of each reaction on the different pore frameworks are reported in **Figure 5.22**. As the TAG chain length is increased, there is an increase in associated diffusion limitation and hence subsequently, we see a significantly diminished TOF. Induction of macropores into the MgAl LDH framework has increased the TOF nearly ~20 fold compared with ConvMgAl. Macropore introduction has evidently enhanced the catalytic performance of transesterification reaction on model chain triglycerides from C_4 - C_{18} to a remarkable degree and could have potentially huge benefits in the transesterification of real oil feedstocks. TOFs of MgAl LDH are found to be much higher

in comparison to ZnAl LDH in both cases, either in ConvLDH or MacroLDH due to the rate of diffusion through MgAl LDH is much higher compared to ZnAl LDH. Both SEM and TEM revealed the MgAl MacroLDH exhibits a bigger pore size diameter compared to ZnAl MacroLDH. Bigger pore provides a bigger ‘highway’ for diffusion to happen, thus reducing the limitation of diffusion which occurs in bulky TAG.

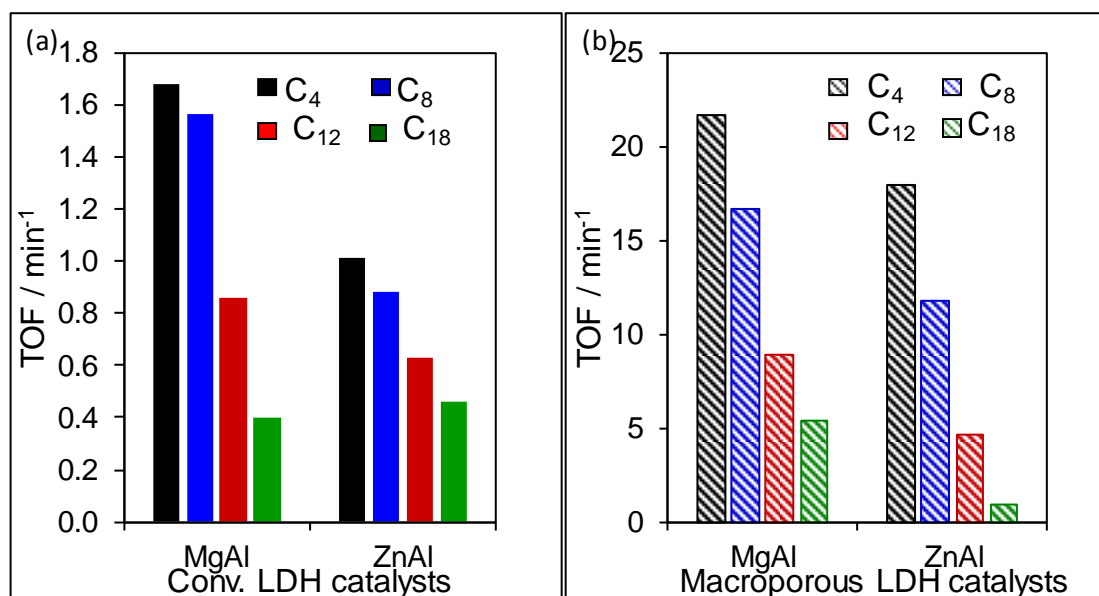


Figure 5.22 TOF profile C₄-C₁₈ for conventional and macroporous of MgAl LDH (a) and ZnAl LDH.

In order to compare MacroMgAl results with the previous work performed by Woodford *et al.*¹, both datasets have been tabulated in **Table 5.11**. Results reveal the conversion and initial rate are much higher with ~3.5 fold of TOF increment. Other conditions used in both work are similar, except for catalyst loading and temperature on MacroMgAl LDH were different where 100 mg of catalyst was used in our instead of 50 mg and reaction have been done at 110 °C instead of 60 °C. This temperature (110 °C) was chosen because to be set as a standardise temperature for all TAGs ranging from lower to bulkier. Hence comparison on this dataset is quite unfair here.

Table 5.11 Comparison of catalytic performance on transesterification using MacroMgAl LDH.

Work was done by	Mg:Al ratio / EDX	TAG conversion after 24h / %	Initial rates / mmol min ⁻¹	TOF / min ⁻¹
Macro MgAl LDH				
Woodford <i>et al.</i> ¹	2.02	41.4	0.040	6.27
Our work	2.42	65.3	0.098	21.67

5.5 Conclusion

Physicochemical properties of the MacroLDH including surface area, pore diameter and base site density are shown to have a pronounced effect on the catalytic performance of C₄-C₁₈ transesterification reaction. Diffusion limitation in bulkier TAGs has been overcome by enhancing the pore network of LDHs via macroporous structure. The incorporation of PS has enlarged the inter-void between hydrotalcite clusters, thus created a macroporosity and relatively enhance the catalytic performance.

The MacroLDH morphology was confirmed by SEM and TEM analysis. The average diameter of MacroMgAl LDH and MacroZnAl LDH were recorded by SEM as 316 nm and 270 nm, respectively. TEM displayed a lower diameter; 299 nm and 250 nm for MacroMgAl LDH and MacroZnAl LDH, respectively. Both values are in good comparable with a previous study done by Woodford *et al.*¹. This also proven incorporation of macroporous on HT framework were successfully done here.

5.7 References

- (1) Woodford, J. J.; Dacquin, J.-P.; Wilson, K.; Lee, A. F. *Energy Environ. Sci.* **2012**, 5, 6145.
- (2) Géraud, E.; Prévot, V.; Leroux, F. *J. Phys. Chem. Solids* **2006**, 67, 903–908.
- (3) Petrolini, D. D.; Urquieta-González, E. A.; Pulcinelli, S. H.; Santilli, C. V.; Martins, L. *Microporous Mesoporous Mater.* **2017**, 240, 149–158.
- (4) Zhang, G.; Zhao, Z.; Liu, J.; Xu, J.; Jing, Y.; Duan, A.; Jiang, G. *J. Rare Earths* **2009**, 27, 955–960.
- (5) Wang, Q.; Tay, H. H.; Guo, Z.; Chen, L.; Liu, Y.; Chang, J.; Zhong, Z.; Luo, J.; Borgna, A. *Appl. Clay Sci.* **2012**, 55, 18–26.
- (6) Cavani F, T. F. & V. A. *Catal. Today* **1991**, 11, 173–301.
- (7) Wang, Q.; Tay, H. H.; Guo, Z.; Chen, L.; Liu, Y.; Chang, J.; Zhong, Z.; Luo, J.; Borgna, A. *Appl. Clay Sci.* **2012**, 55, 18–26.
- (8) Cantrell, D. G.; Gillie, L. J.; Lee, A. F.; Wilson, K. *Appl. Catal. A Gen.* **2005**, 287, 183–190.
- (9) Zeng, H.-Y.; Xu, S.; Liao, M.-C.; Zhang, Z.-Q.; Zhao, C. *Appl. Clay Sci.* **2014**, 91–92, 16–24.
- (10) Zeng, Y.; Zhang, T.; Xu, Y.; Ye, T.; Wang, R.; Yang, Z.; Jia, Z.; Ju, S. *Appl. Clay Sci.* **2016**, 126, 207–214.
- (11) Wang, Z.; Lu, G.; Guo, Y.; Guo, Y.; Gong, X.-Q. *ACS Sustain. Chem. Eng.* **2016**, 4, 1591–1601.
- (12) Nishimura, S.; Takagaki, A.; Ebitani, K. *Green Chem.* **2013**, 15, 2026.
- (13) Pramod K. Sahu, Praveen K. Sahu, S. K. G. and D. D. A. *Catal. Sci. Technol.* **2013**, 3, 1520.
- (14) Sánchez-Cantú, M.; Galicia-Aguilar, J. A.; Santamaría-Juárez, D.; Hernández-Moreno, L. E. *Appl. Clay Sci.* **2016**, 121, 146–153.
- (15) Álvarez, M. G.; Chimentão, R. J.; Figueras, F.; Medina, F. *Appl. Clay Sci.* **2012**, 58, 16–24.
- (16) Pavel, O. D.; Zăvoianu, R.; Bîrjega, R.; Angelescu, E.; Costentin, G.; Che, M. *Appl. Clay Sci.* **2015**, 104, 59–65.
- (17) Bravo-Suárez, J. J.; Páez-Mozo, E. A.; Oyama, S. T. *Quim. Nova* **2004**, 27, 574–581.
- (18) Sharma, S. K.; Kushwaha, P. K.; Srivastava, V. K.; Bhatt, S. D.; Jasra, R. V. *Ind.*

- Eng. Chem. Res.* **2007**, *46*, 4856–4865.
- (19) Creasey, J. J.; Chiericato, A.; Manayil, J. C.; Parlett, C. M.; Wilson, K.; Lee, A. F. *Catal. Sci. Technol.* **2014**, *4*, 861–870.
 - (20) Lee, A. Y.; Blakeslee, D. M.; Powell, C. J.; Rumble, J. R. *Data Sci. J.* **2002**, 1–12.
 - (21) Naumkin, A. V.; Kraut-Vass, A.; Gaarenstroom, S. W.; Cedric J, P. NIST Standard Reference Database 20, Version 4.1. <https://srdata.nist.gov/xps> (accessed Oct 8, 2016).
 - (22) Alexander V. Naumkin, Anna Kraut-Vass, Stephen W. Gaarenstroom, and C. J. P. NIST Standard Reference Database 20, Version 4.1.
 - (23) Capek, I.; Chitu, L. *Chem. Pap.* **2005**, *59*, 41–47.
 - (24) Koriyama, T.; Asoh, T.-A.; Kikuchi, A. *Colloids Surfaces B Biointerfaces* **2016**, *147*, 408–415.
 - (25) Zhang, M.; Zhang, C.; Du, Z.; Li, H.; Zou, W. *Compos. Sci. Technol.* **2017**, *138*, 1–7.
 - (26) Lee, G.; Kang, J. Y.; Yan, N.; Suh, Y.-W.; Jung, J. C. *J. Mol. Catal. A Chem.* **2016**, *423*, 347–355.
 - (27) Zhang, X.; Yang, S.; Xie, X.; Chen, L.; Sun, L.; Zhao, B.; Si, H. *J. Anal. Appl. Pyrolysis* **2016**, *120*, 371–378.
 - (28) Bunekar, N.; Tsai, T.-Y.; Yu, Y.-Z. *Mater. Today Proc.* **2016**, *3*, 1415–1422.
 - (29) J.M. Lopez Nieto, A. Dejoz b, M. I. V. b. *Appl. Catal. A Gen.* **1995**, *135*, 41–59.
 - (30) Teodorescu, F.; Pălăduță, a.-M.; Pavel, O. D. *Mater. Res. Bull.* **2013**, *48*, 2055–2059.
 - (31) Adachi-Pagano, M.; Forano, C.; Besse, J.-P. *J. Mater. Chem.* **2003**, *13*, 1988.
 - (32) Liu, Q.; Wang, B.; Wang, C.; Tian, Z.; Qu, W.; Ma, H.; Xu, R. *Green Chem.* **2014**, *16*, 2604.
 - (33) Kooli, F.; Ge, C. D.; Ennaqadi, A.; Roy, A. D. E.; Besse, J. E.; Matriaux, L. D. P.; Cnrs, U. R. A.; Pascal, U. B.; Cedex, A. **1997**, *45*, 92–98.
 - (34) Thommes, M.; Kaneko, K.; Neimark, A. V.; Olivier, J. P.; Rodriguez-Reinoso, F.; Rouquerol, J.; Sing, K. S. W. *Physisorption of gases, with special reference to the evaluation of surface area and pore size distribution (IUPAC Technical Report)*; 2015; Vol. 87.
 - (35) Jung, J.-S.; Hong, G. H.; Park, J. I.; Yang, E.-H.; Hodala, J. L.; Moon, D. J. *RSC Adv.* **2016**, *6*, 104280–104293.
 - (36) Wang, Y.; Zhang, F.; Xu, S.; Wang, X.; Evans, D. G.; Duan, X. *Ind. Eng. Chem. Res.* **2008**, *47*, 5746–5750.
 - (37) Zeng, H.; Feng, Z.; Deng, X.; Li, Y. *Fuel* **2008**, *87*, 3071–3076.
 - (38) Géraud, E.; Rafqah, S.; Sarakha, M.; Forano, C.; Prevot, V.; Leroux, F. *Chem. Mater.* **2008**, *20*, 1116–1125.
 - (39) Navajas, A.; Arzamendi, G.; Romero-Sarria, F.; Centeno, M. A.; Odriozola, J. A.; Gandía, L. M. *Catal. Commun.* **2012**, *17*, 189–193.
 - (40) Montanari, T.; Sisani, M.; Nocchetti, M.; Vivani, R.; Concepcion Herrera Delgado, M.; Ramis, G.; Busca, G.; Costantino, U. *Catal. Today* **2010**, *152*, 104–109.
 - (41) Navajas, A.; Campo, I.; Arzamendi, G.; Hernández, W. Y.; Bobadilla, L. F.; Centeno, M. A.; Odriozola, J. A.; Gandía, L. M. *Appl. Catal. B Environ.* **2010**, *100*, 299–309.
 - (42) Wu-Liang Huang; Bassett, W. A.; Tzy-Chung Wu. *Am. Mineral.* **1994**, *79*, 683–691.
 - (43) Reyero, I.; Velasco, I.; Sanz, O.; Montes, M.; Arzamendi, G.; Gandía, L. M. *Catal. Today* **2013**, *216*, 211–219.
 - (44) Zhang, Z.; Zhang, Y.; Wang, Z.; Gao, X. *J. Catal.* **2010**, *271*, 12–21.
 - (45) Valente, J. S.; Lima, E.; Toledo-antonio, J. A.; Cortes-jacome, M. A.; Lartundo-rojas, L.; Montiel, R.; Prince, J. *Phys. Chem. Chem. Phys.* **2010**, *114*, 2089–2099.
 - (46) Lee, A. F.; Wilson, K. *Catal. Today* **2015**, *242*, Part, 3–18.

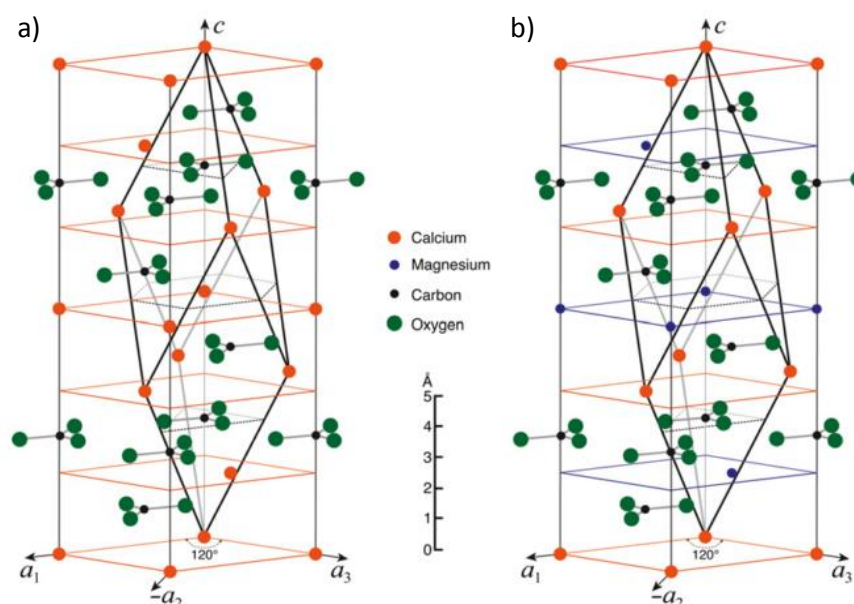
Chapter 6

Commercial catalysts (Dolomite and NanoMgO) for Transesterification Reaction

6.1 Introduction: Dolomite and nanocrystalline MgO

Dolomites and NanoMgO have been proven to play an important role as a solid base catalyst in the transesterification of biodiesel^{1,2}. Solid base catalyst does wonder in transesterification reaction especially for high purity oils with low free fatty acid (FFA) content³.

Dolomite is a basic carbonate mineral mainly consisting of alternating layers of Mg^{2+} , Ca^{2+} cation and balanced by CO_3^{2-} anions. Dolomite represents a rhombohedral structure that is derived from the calcite structure (**Scheme 6.1**)⁴ and adopt a $R\bar{3}$ space group. Calcite, on the other hand, displays $R3c$ space group. Dolomite is normally found in continental and marine sedimentary rocks. Due to it is abundance in nature, using dolomite as a catalyst is very economical and also has been considered as one of environmental friendly mineral (non-toxic)⁵.

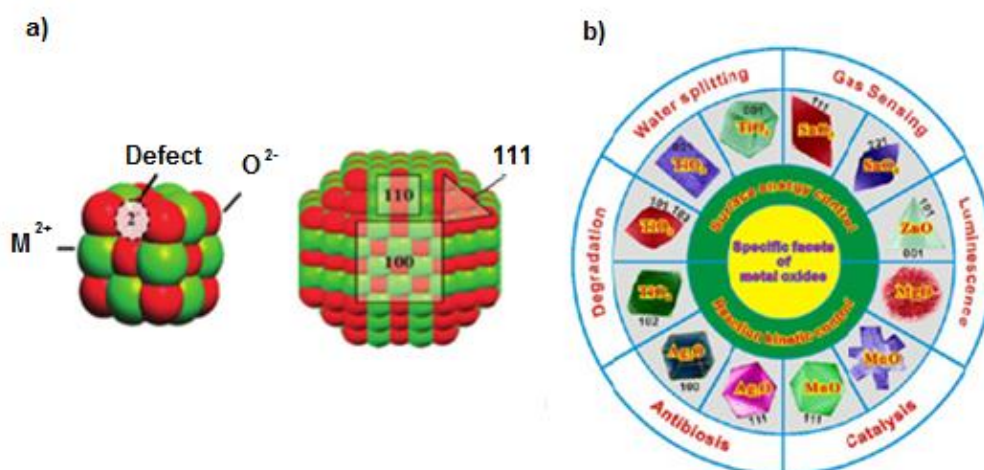


Scheme 6.1 Calcite hexagonal unit cell superimposed onto rhombohedral unit cell (a) and dolomite hexagonal unit cell superimposed onto rhombohedral unit cell (b). Figure adapted from Gregg *et al.*⁴.

NanoMgO is another solid base catalyst that exhibits remarkable catalytic activity in transesterification reaction⁶. There are various applications involving NanoMgO such as in electronics, catalysis, ceramic, petrochemical products, fire retardant, coatings and much more. Physical and chemical properties of crystals normally depend on their specific facets structure which plays a role in thermodynamics, kinetics effect and also has been applied in many applications (**Scheme 6.2a-b**)⁷. NanoMgO exhibits different three common surface facet; (100), (110) and (111) facet. The surface termination has

a direct effect on Lewis basicity of Mg, where the highest number of exposed (111) planes display more basicity sites compared to lower number exposed. Calcination can result in a defect on the surface due to the modification of the coordinate sites of the corner, steps or edge sites. The defects induce the surface towards more polarisable and become more tendency to donate electron than stoichiometric sites, which later subsidies to higher basicity and gives better catalytic performance⁸.

Wilson *et al.*¹ have reported 100 % conversion in the transesterification of tributyrin using dolomite (> 98 % selectivity) but no relationship with the facet structure of dolomite has been reported. Meanwhile, in the other study on NanoMgO, nearly 80 % tributyrin conversion has been observed by Montero *et al.*⁶. They observed different facet - in as-prepared NanoMgo:(100 facet) meanwhile,a vacuum annealed NanoMgO at 700 °C exhibits 110 facet with step edges of cuboid crystal⁹. Changes in facet surfaces have increased the basicity of the Mg^{2+} . Somehow, a significant effect of leaching from the mixed oxide on the surface has not been further studied in the both cases.



Scheme 6.2 Cationic defect on the solid base catalyst of Mg^{2+} - O^{2-} and how crystal facet termination increased the base strength from (100) < (110) < (111) (a), adapted from Ref³ and the application of mixed oxide from different facet (b), adapted from Kuang *et al.*⁷.

Based on the above-reported results, a correlation study between the surface morphology (technically the facet structure), and the basicity which later become the main contributor in transesterification reaction have to be further studied here. Effect of leaching from the mixed oxide compound also has to be further investigated to give an overall outlook on how the surface structure does influence on leaching of the basic site.

6.2 Novelty and contributions to knowledge

This work is an extension work from what have been done by Wilson *et al.*¹, (on dolomite) and Montero *et al.*^{2,6,9}, (on NanoMgO). The main focus of this work is on how the defect surface of mixed oxide sites could influence the leaching in dolomite and NanoMgO. In addition, ex-gasifier dolomite (used to crack tar during the gasification of biomass) has been used as the novel contribution in this study, where it could be a good comparison with commercial dolomite in term of their surface modification via calcination process, would affect on basicity and how they act in the transesterification reaction. This explores whether it would be viable to employ waste dolomite from gasification plants in catalytic applications.

6.3 Aims

The aim of this chapter is to compare the behaviour of the three solid base catalysts obtained from calcined dolomite (commercial and ex-gasifier) and NanoMgO in the transesterification of C₄-C₁₈. The morphology of MgO based nanocrystallite facet will be determined in this study. The leaching study on these catalysts also has been carried out to further understand the effect of the surface defect on Mg/O facet surfaces.

6.4 Results and discussion

6.4.1 Characterisation of the catalysts

6.4.1.1 Energy dispersive X-Ray spectroscopy of Dolomite and NanoMgO

EDX analysis was conducted on parent and calcined solid base catalysts (dolomite and NanoMgO) to quantify the bulk ratio of Ca:Mg and Mg:O as reported in **Table 6.1** and **Table 6.2**. In this study, the dolomite and NanoMgO have been calcined at 900 °C and 500 °C as explained in Chapter 2. The bulk wt % of Ca and Mg in dolomite and Mg in NanoMgO were increased after calcination process. This possibly due to the decomposition of impurities species during calcination which increased the bulk wt% of Ca and Mg respectively. Data also revealed the Ca and Mg content in the ex-gasifier was higher than that of the fresh material, suggesting that loss of carbonate may also occur at the temperatures employed in gasification. **Figure 6.1** reveals both dolomite compounds consist of Mg, Ca, O atom along with impurities such as Fe, Si, Al and Ir. Zn and K were also detected in ex-gasifier dolomite. The presence of such impurities was

expected in dolomite¹⁰. Meanwhile, Mg and O atom are observed in NanoMgO without any impurities were detected.

Table 6.1 Elemental analysis of commercial dolomite and ex-gasifier dolomite NanoMgO determined by EDX.

Sample	Bulk Mg wt% (EDX)	Bulk Ca wt% (EDX)	Bulk atomic Ca:Mg
Commercial dolomite			
Precursor	12.86	13.51	2.02
Calcined	10.56	15.76	2.46
Ex-gasifier dolomite			
Precursor	13.60	17.22	2.09
Calcined	16.91	25.94	2.52

Table 6.2 Elemental analysis of NanoMgO determined by EDX.

Sample	Bulk Mg wt% (EDX)	Bulk O wt% (EDX)	Bulk Mg:O ratio
NanoMgO			
Precursor	34.32	58.45	0.89
Calcined	41.95	53.85	1.18

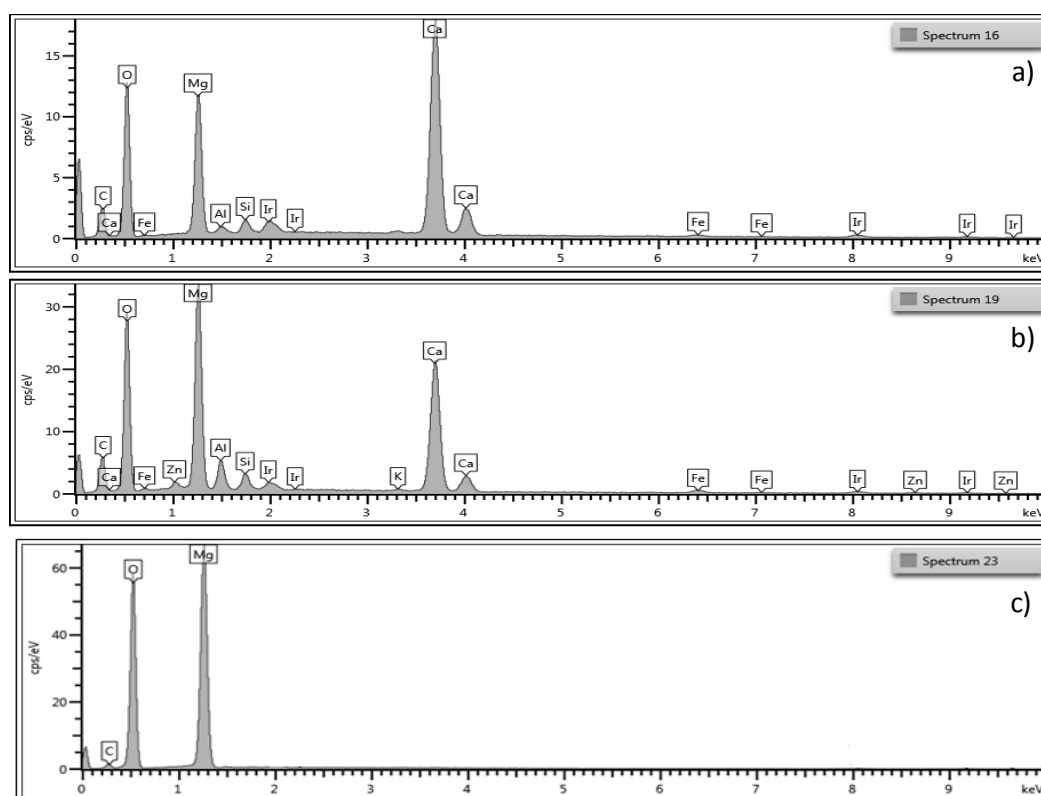
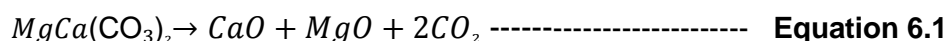


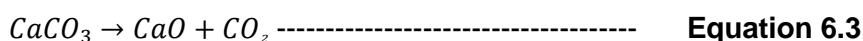
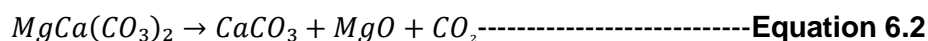
Figure 6.1 EDX spectra of commercial dolomite (a), ex-gasifier dolomite(b) and NanoMgO(c).

6.4.1.2 Thermogravimetric analysis-Mass spectrometry of Dolomite and NanoMgO

Figure 6.2a-c illustrates the thermal decomposition behaviour of dolomite (commercial dolomite (a), ex-gasifier dolomite (b) and NanoMgO (c)). One major weight loss belonging to CO₂ was observed in TGA and MS around 800 °C in both dolomite samples. Fresh dolomite revealed 34.9 % and 12.8 % of CO₂ weight loss in commercial and ex-gasifier dolomite respectively. These data are in correlation with DSC where a sharp peak can be seen in a similar temperature. TGA show only one significant weight loss with can be attributed to this equation (**Equation 6.1**):



The mechanism of dolomite thermal decomposition is the subject of debate,¹¹⁻¹³ with CO₂ partial pressure believed to play an important role. -Valverde *et al.*¹¹ have proven if the partial pressure is below $P \cong 0.1$ atm, a single decomposition as displayed as in **Equation 6.1** is observed. However, if the $P > 0.1$ atm, two decomposition steps might be observed (**Equation 6.2 and 6.3**)¹¹:



In our case, only single decomposition of CO₂ has been observed as shown in **Equation 6.1**. This proven the decomposition process occurred simultaneously at a temperature around 800 °C and no partial decomposition mechanism has taken place here. In-situ XRD has been undertaken by Valverde *et al.*¹¹ where it strongly support the arguments that dolomite was observed decomposed directly into MgO and CaO at a temperature around 700 °C. They also reported that CaO crystal is immediately carbonated as shown in **Equation 6.1**. Ex-gasifier dolomite shown a lesser CO₂ weight loss, emphasise most of the sample have decomposed directly to CaO and MgO as EDX also proven higher wt% on bulk Mg and Ca.

TGA-MS curves of NanoMgO can be seen in **Figure 6.2c**. These data reveal a huge dehydration/decomposition of water near 400 °C which could be reflected Mg(OH)₂ compound. The water weight loss from Mg(OH)₂ is 23.0 %, is reasonably high for decomposition to happened and transformed the compound into MgO as proven by XRD in calcination process. The mechanism can be written as in **Equation 6.4**:



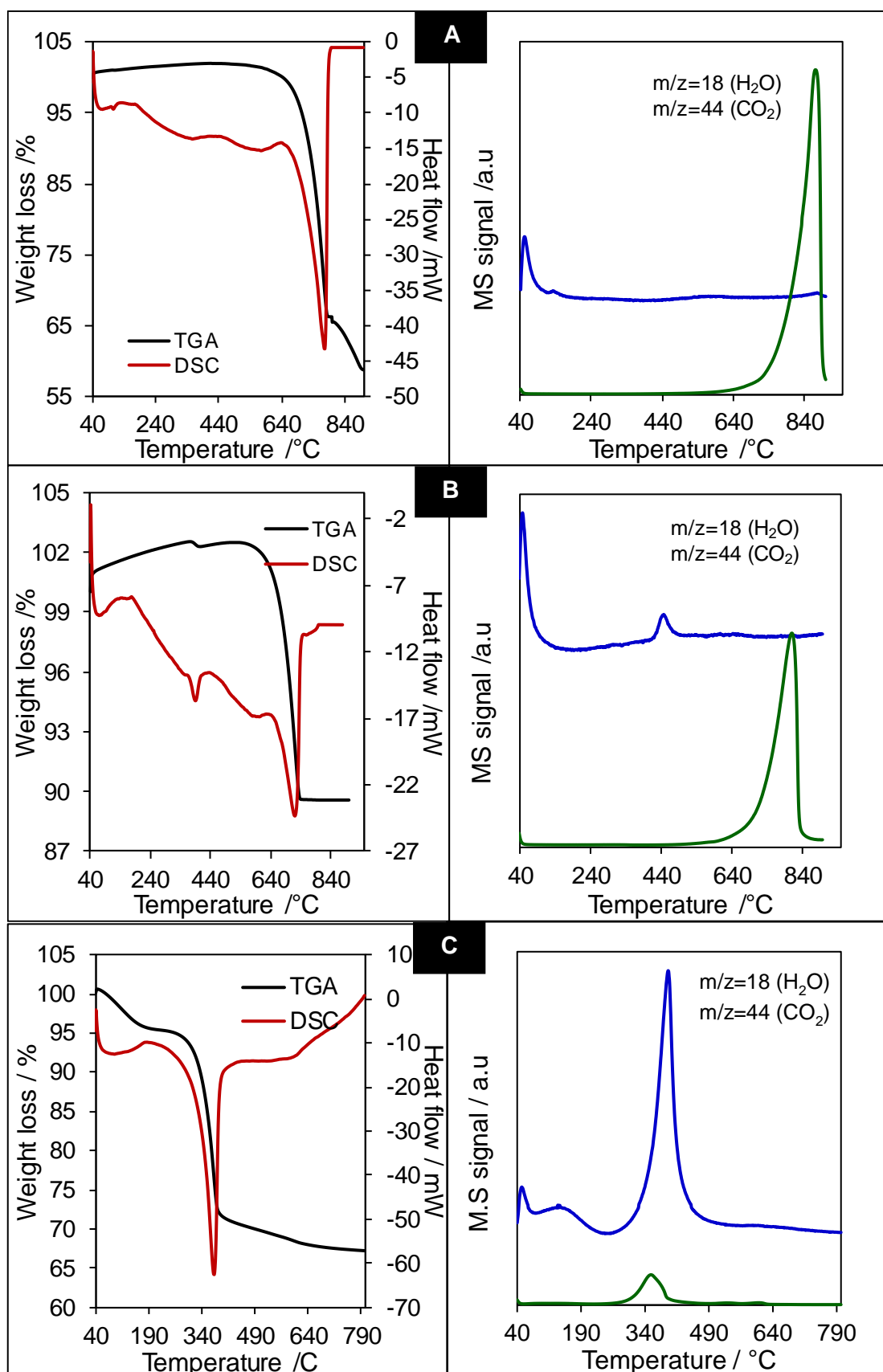


Figure 6.2 TGA/DSC with MS profiles during thermal decomposition of commercial dolomite (A), ex-gasifier dolomite (B) and NanoMgO (C) in N_2 at $10\text{ }^\circ\text{C min}^{-1}$ from $40\text{--}900\text{ }^\circ\text{C}$ (for both dolomite) and from $40\text{--}800\text{ }^\circ\text{C}$ (for NanoMgO).

DSC profiles of commercial dolomite (**Figure 6.2a**) and ex-gasifier dolomite (**Figure 6.2b**) showed two heat flow of absorbed and dehydroxylation of water around 50 and 340 °C. Meanwhile, a heat flow of decarboxylation is observed at around 780 °C is attributed to the loss of carbon dioxide from the interlayer anion. **Table 6.3** shows the carbon dioxide weight loss from dolomite and NanoMgO obtained from EDX.

Table 6.3 Carbon dioxide weight loss from dolomite and NanoMgO obtained from EDX.

Catalysts	CO ₂ weight loss / %
Commercial dolomite	34.9
Ex-gasifier dolomite	12.8
NanoMgO	23.0

6.4.1.3 Powder X-ray diffraction of Dolomite and NanoMgO

In fresh dolomite sample (**Figure 6.3a**), most of the diffraction patterns can be attributed to calcite (CaCO₃) and dolomite (MgCa(CO₃)₂) phases. Calcite phases were observed at 26.59°, 34.82°, 41° and 46.33°. Meanwhile, dolomite phases were observed at 30.94°, 37.30°, 42.90° and 51.14° respectively. Calcined samples exhibit Ca(OH)₂ (18°, 21°.13°, 26°.59°, 34.29°, 50.53°, 64° and 66.79°), CaO (28.71°, 37.6° and 54.1°) and MgO (43.97° and 62.5°) which also indicates the disappearance of calcite and dolomite phases. These reflections are in the same agreement as found in literature^{1,4,14}.

Contrary to commercial dolomite, the fresh ex-gasifier sample (**Figure 6.3b**) exhibits a combination of MgCa(CO₃)₂ (29.35°, 31.12°, 37.56° and 48.72°), CaCO₃ (26.74° and 32.36°), Ca(OH)₂ (18.53° and 21.27°), MgO (43.48° and 62.54°) and CaO (54.1°) multi-phases. As the samples were obtained from a post waste collection in the gasifier and possibly have been extensively employed in pyrolysis gasification processes, hence these phases (calcite and dolomite) are expected to be found in this ex-gasifier sample. Calcined samples exhibit most of the dolomite phases have been eliminated except at 37.4° which reflected a strong intensity of dolomite. The second highest intensity peak was reflected by MgO at 43.11° and followed by CaO reflected at 54.12°. The rest of the reflection w governed by CaCO₃ and Ca(OH)₂.

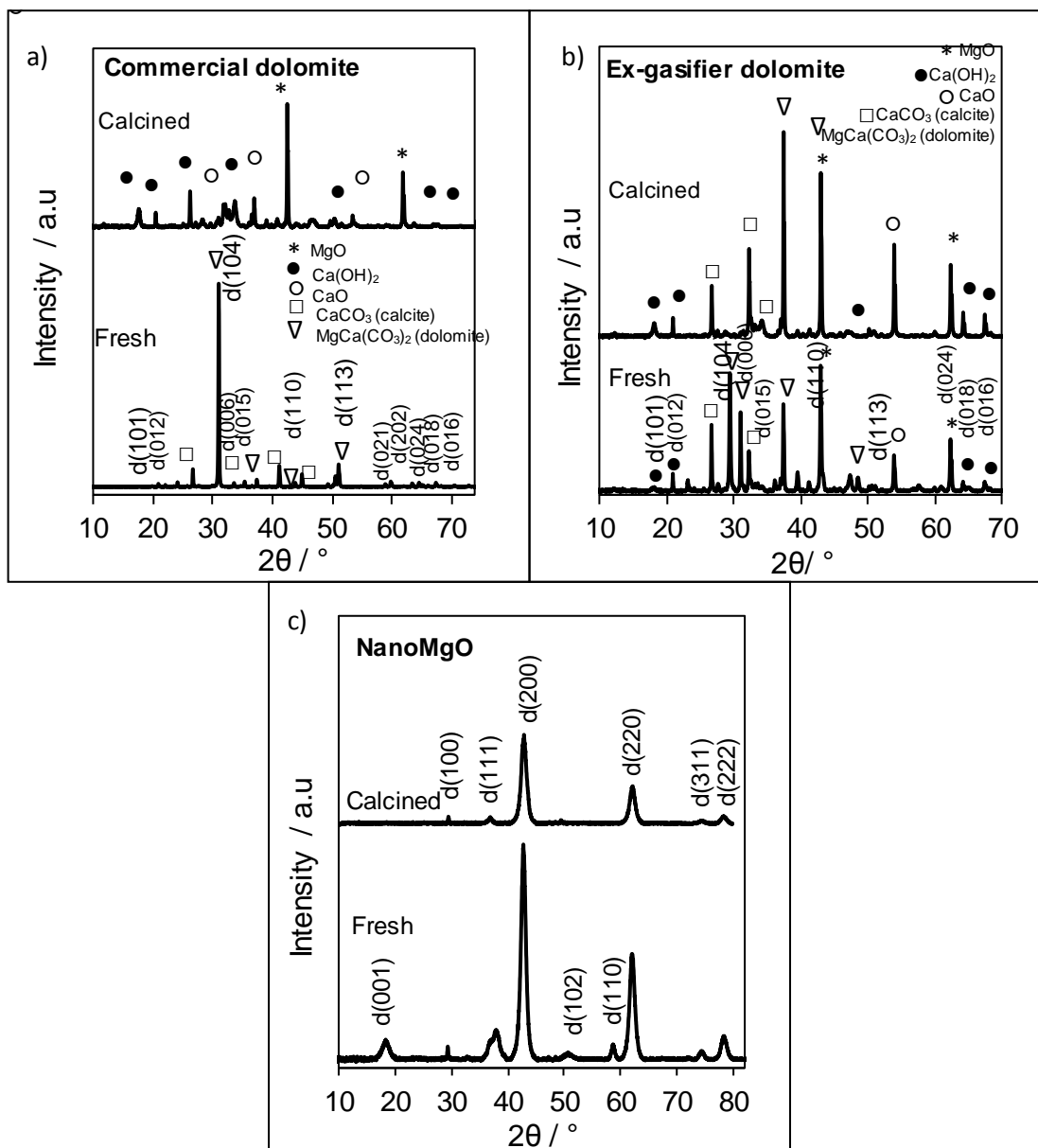


Figure 6.3 XRD patterns of commercial dolomite, ex-gasifier dolomite and NanoMgO. Dolomite samples were calcined at 900 °C, meanwhile, NanoMgO was calcined at 500 °C.

Fresh NanoMgO (**Figure 6.3c**) shows the reflections attributed to mixed crystalline phase in this samples. The diffraction patterns at $d(001)$, $d(102)$ and $d(110)$ resembles the hexagonal structure of $\text{Mg}(\text{OH})_2$ (JCPDS: 7-239)¹⁵. The diffraction peak of $\text{Mg}(\text{OH})_2$ at $d(001)$ indicates the peak from hydroxyl compound as proven by TGA-MS. Calcined NanoMgO at 500 °C has eliminated most of the amorphous hexagonal phase resulting from a cubical crystal of MgO ⁹ which assigned as $d(100)$, $d(111)$, $d(200)$, $d(220)$ and $d(311)$ ¹⁶. Some reported this material exhibits icosahedral geometry¹⁷ while other predicted it might be formed as quasicrystalline in nature¹⁶.

Table 6.4 summarises the crystallite size of catalysts used in this study. Overall, results shown are in good agreement with literature^{2,9}. It has been reported crystallite size of dolomite is around 50-60 nm. Meanwhile, the crystallite size of NanoMgo for calcination at 500 °C and lower, is reported <10 nm.

Table 6.4 Comparison of crystallite size of commercial dolomite, ex-gasifier dolomite and NanoMgO.

Catalyst	Crystallite size / nm
Commercial dolomite	
Fresh	59
Calcined	50
Ex-gasifier dolomite	
Fresh	45
Calcined	50
NanoMgO	
Fresh	7.7
Calcined	8.5

6.4.1.4 Nitrogen porosimetry of Dolomite and NanoMgO

N₂ adsorption-desorption isotherms for commercial dolomite, ex-gasifier dolomite and NanoMgO are displayed in **Figure 6.4**. Samples were degassed prior to analysis. The adsorption-desorption isotherms of both commercial and ex-gasifier dolomites (**Figure 6.4a-b**) exhibit type IV isotherms and type H1 hysteresis loops indicates microporous-mesoporous material with narrow-slit pore¹⁸. These also associated with solids consisting of nearly cylindrical channels or agglomerates or compacts of near-uniform spheres⁷. Similarly, Nano MgO catalyst exhibits type IV isotherms with H₂ hysteresis loops (**Figure 6.4c**).

Calcination at 900 °C (dolomites) and 500 °C (NanoMgO) have increased the BET and BJH surface area of dolomites and NanoMgO compared to the precursor, respectively (**Table 6.5**). Yoosuk *et al.*¹⁹ have reported the expansion of surface area is related to the changes of the morphology triggered by the expulsion of CO₂ occurred during calcination process. Although the surface area is slightly increased after the hydration and dehydration steps, no significant changes have been detected on pore volume of dolomites. The pore diameter of dolomite was slightly decreased but still in the same range of the parents' materials.

Table 6.5 The textural parameter of surface area, pore volume and pore diameter of the precursor and calcined dolomite and NanoMgO.

Catalysts/Parameter	BET Surface area / m ² /g	BJH Pore volume / cc/g	BJH Pore diameter / nm
Commercial dolomite			
Precursor	14	0.05	2.2
Calcined	19	0.05	1.5
Ex-gasifier dolomite			
Precursor	8	0.04	2.5
Calcined	13	0.04	2.0
NanoMgO			
Precursor	145	0.42	6.7
Calcined	150	0.42	6.7

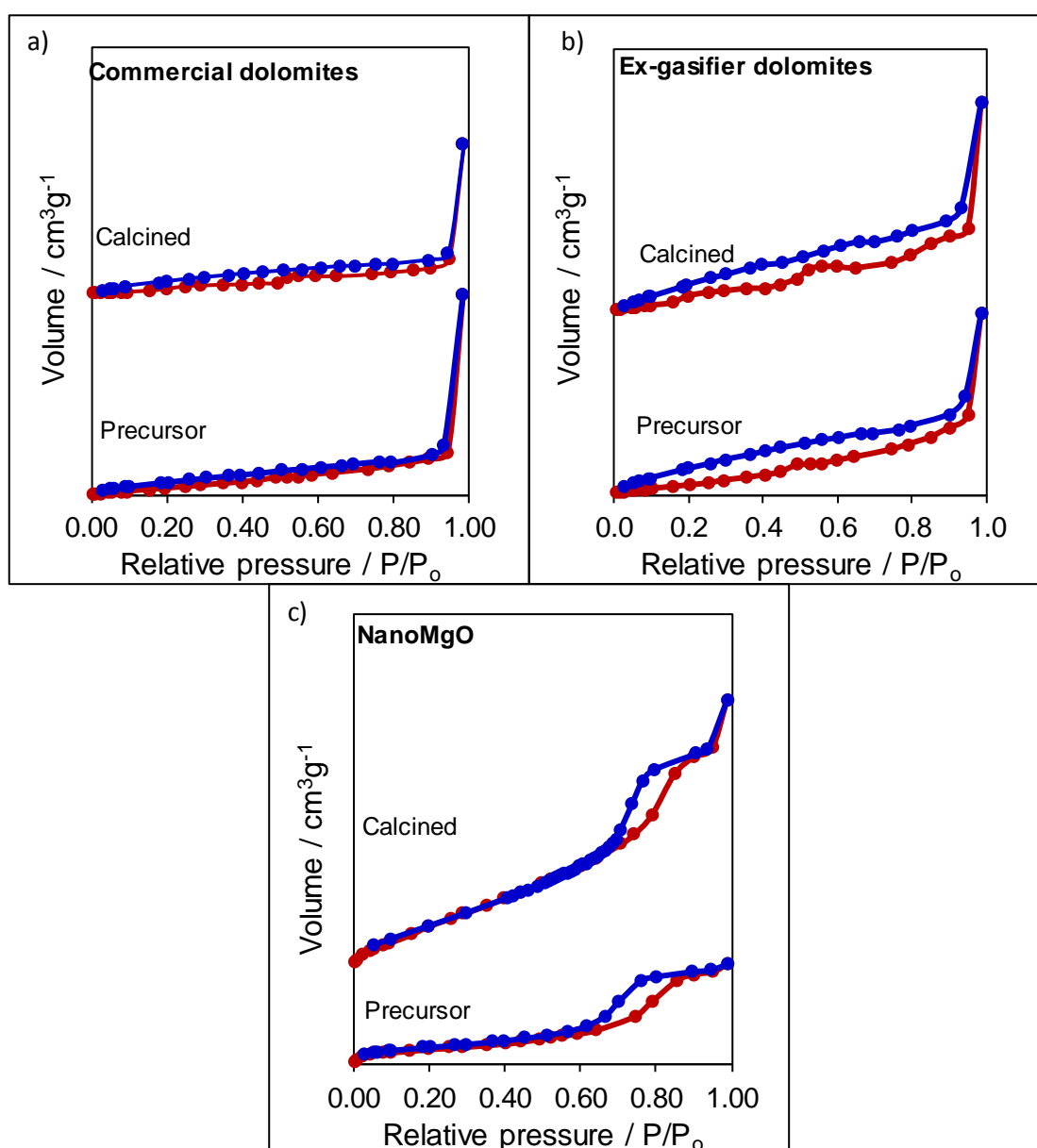


Figure 6.4 A stack of adsorption-desorption isotherms of commercial dolomite (a), ex-gasifier dolomite (b) and Nano MgO (c).

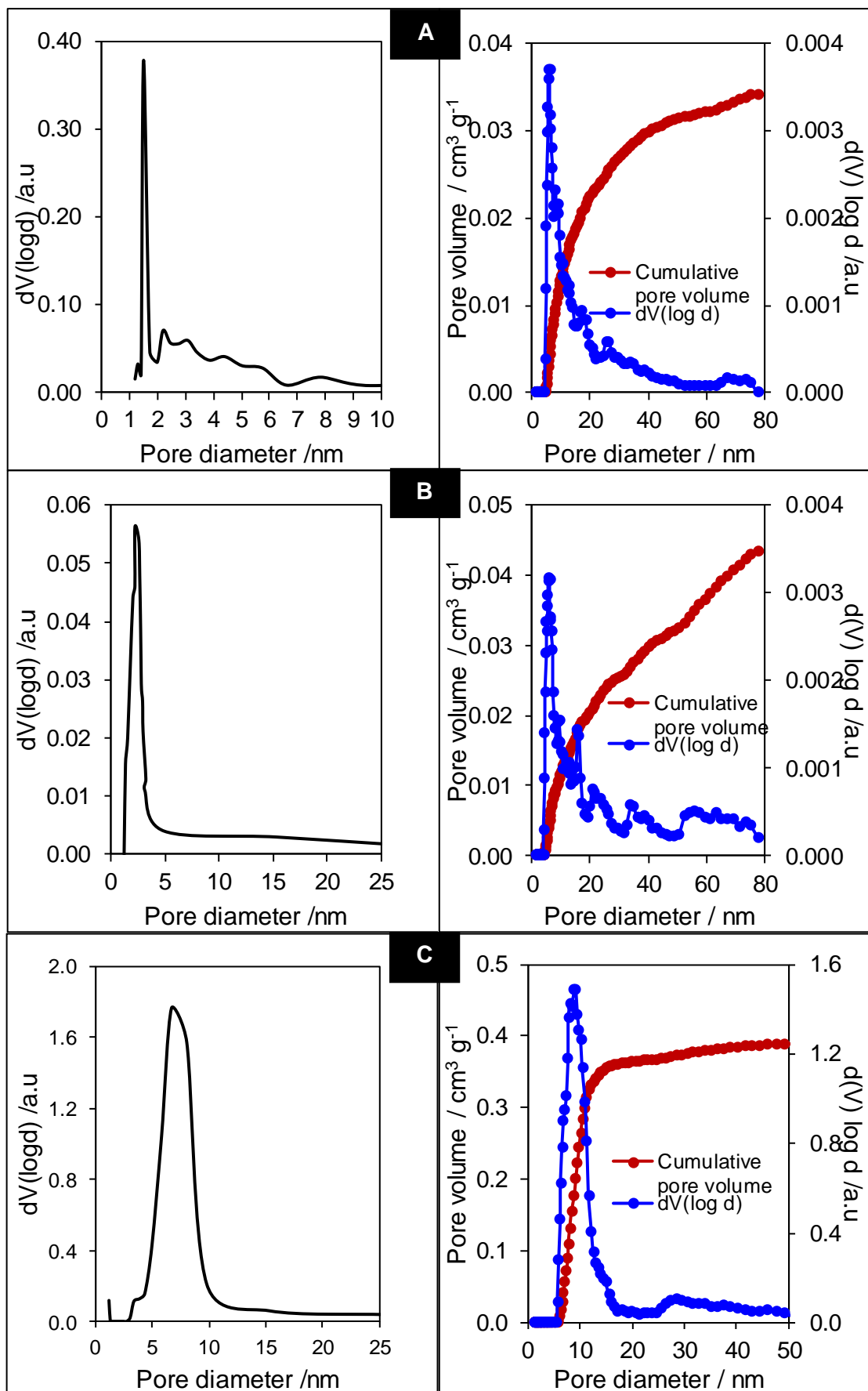


Figure 6.5 BJH pore size distribution (left) and DFT pore size distribution (right) of commercial dolomite (A), ex-gasifier dolomite (B) and Nano MgO (C).

NanoMgO exhibits increment in surface area compared to dolomite, thus increased the pore volume and pore diameter simultaneously. BJH pore distribution of dolomites and NanoMgO are in the range of 1-3 nm and 6-12 nm respectively as depicted in **Figure 6.5a-c (left)**. To further confirm this, a DFT method has been conducted (**Figure 6.5a-c (right)**). Both dolomites reveal mean pore diameter around 5.6 nm, whereas the NanoMgO displays a slightly higher pore diameter i.e, 9.1 nm.

6.4.1.5 Scanning electron microscopy of Dolomite and NanoMgO

SEM images in **Figure 6.6** reflected the differences of surface morphologies on the dolomites (commercial and ex-gasifier) and NanoMgO catalysts. Images on commercial dolomites appear as smooth planes or regularly faceted steps exposing high crystallinity of the catalyst¹ in well-correlated agreement with XRD data (**Table 6.2**).

In contrast with ex-gasifier dolomites, images of flattened flakes or saddle-like flakes have been visualised. This could indicate the low crystallinity of the catalyst as proven by XRD due to the sintering process produced from calcination. Sintering promoted more segregated compound of Mg and CaO grains¹¹. EDX also has proven the Mg and Ca content were increased in dolomite and NanoMgo after calcination processes.

SEM images of NanoMgO reveals the non-symmetry morphology, with some of the particles, resemble icosahedron with non-convex form, are in good agreement with XRD data and also agreed with Jeevanandam *et al.*¹⁷.

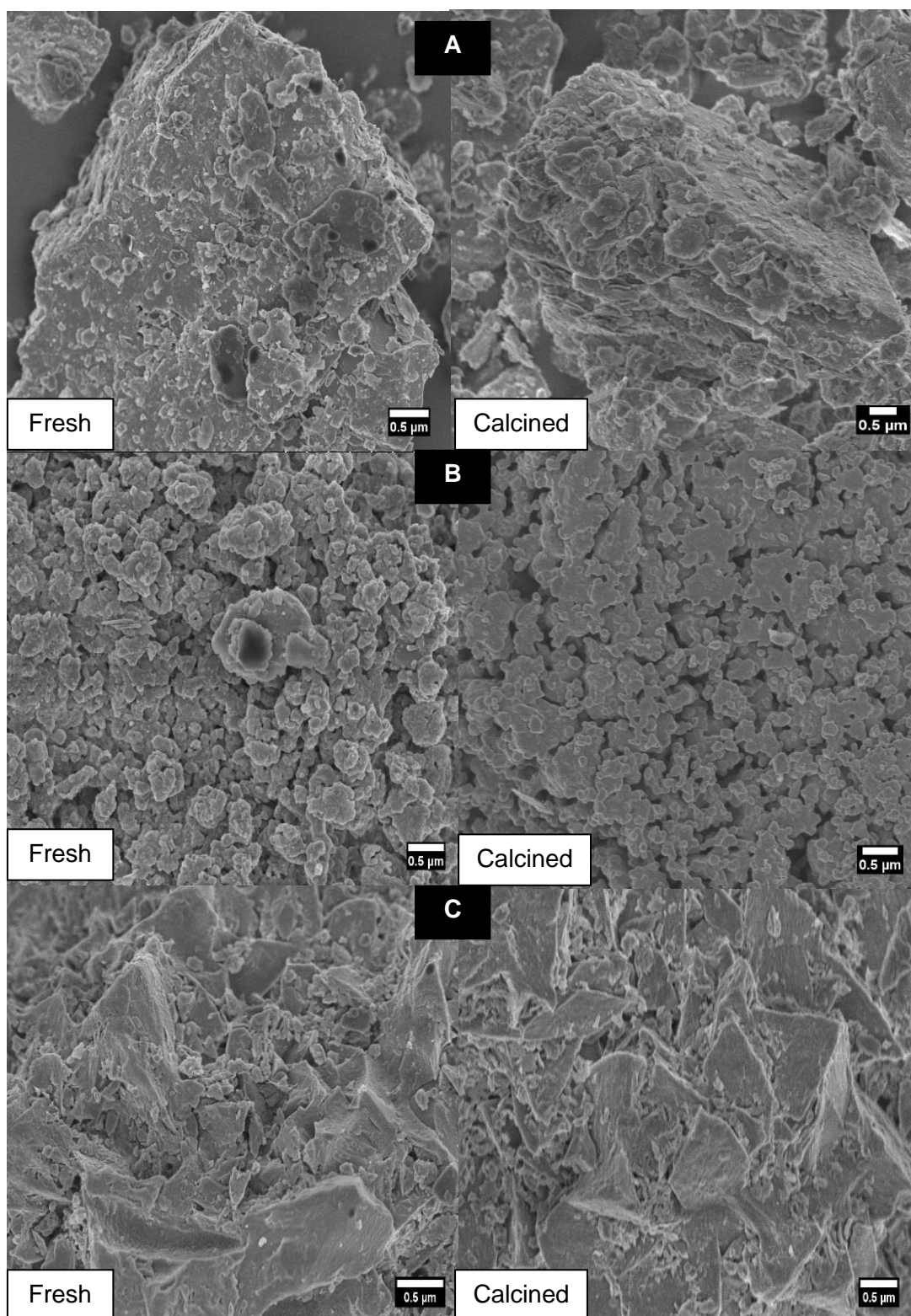


Figure 6.6 SEM images of commercial dolomite (A), ex-gasifier dolomite (B) and NanoMgO (C).

6.2.1.6 High-resolution scanning transmission electron microscopy of Dolomite and NanoMgO

Figure 6.7 shows representative STEM images of commercial dolomite, ex-gasifier dolomite and NanoMgO. STEM images of commercial dolomite (**Figure 6.7a**) show a rhombohedral structure with lattice string of 0.215 nm. According to XRD, this value is correlated to diffraction at 42.8° attributed to (110) spacing (0.210 nm). Meanwhile, the STEM images of ex-gasifier dolomite (**Figure 6.7b**) reveals a spherical or curved crystal face common known as saddle dolomite²⁰. HRTEM exposed the lattice string of 0.200 nm reflected to the XRD d spacing value of 0.209 nm which attributes to 110 diffraction pattern.

A cubic attribute to MgO nanocrystalline with defect has been observed in **Figure 6.7c**. Lattice string was calculated as 0.184 nm in similar agreement obtained from XRD data which attributes to 110 facets. Our result is in a good agreement with a work from Janine *et al.*^{6,21} (**Scheme 6.3**).



Scheme 6.3 The (100), (110) and (111) facets of MgO. Source: ²²

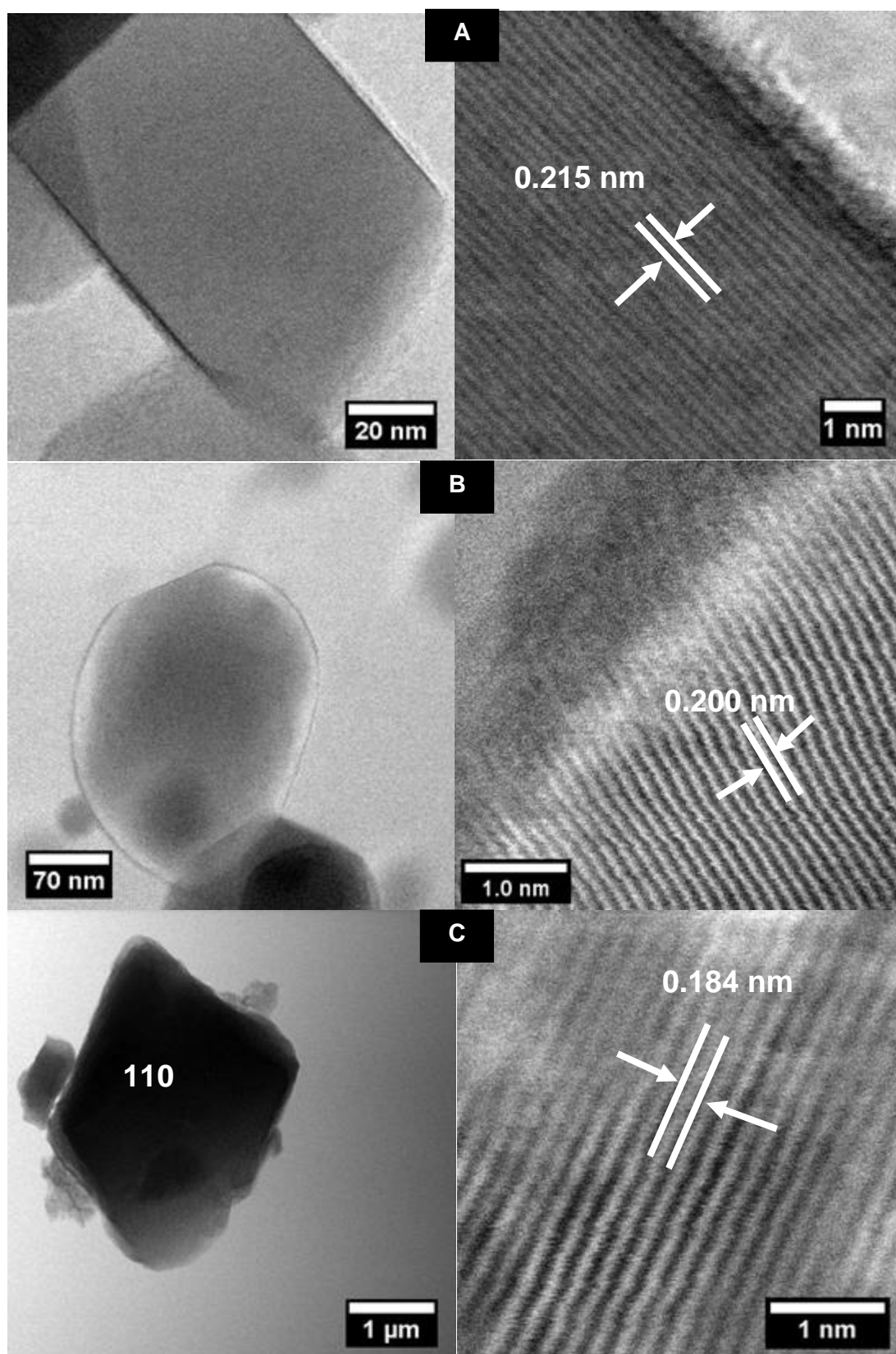


Figure 6.7 Representative bright STEM images of commercial dolomite (A), ex-gasifier dolomite (B) and NanoMgO (C).

6.2.1.7 Temperature-programme desorption of CO₂ of Dolomite and NanoMgO

CO₂-TPD profile of the precursor and calcined dolomites (both commercial and ex-gasifier) and NanoMgO catalysts are shown in **Figure 6.8**. Effect of basicity strength on calcined temperature on dolomites has been studied by Ilgen²³ where he found basicity increased with calcined temperature hence simultaneously affect the catalytic activity of transesterification reaction. He also showed that calcination of dolomites at below 700 °C did not lead the materials to be able to catalyse the transesterification reaction due to weak basic strength. Meanwhile, calcination from 800–900 °C increased the basicity up to ~3 fold (in Hammett basicity H_{18.4}). Their study shown calcination at 800 °C gave the highest FAME yield (92 %) compared to only 83 % yield were produced at 900 °C due to it exhibited strong base site density.

Table 6.6 summarises the number of basic sites and base site density of all catalysts used in this study including the before and after calcination. Data reveals the increment number of active sites and base site density in both dolomites (commercial and ex-gasifier). The desorption of strong basic sites in fresh dolomites mostly governed around 600 °C is might be associated to the carbonates from calcite (CaCO₃²⁻) along with pulse chemisorption of CO₂ from TPD. Calcination has changed the morphology due to the segregation and increased the surface area which later significantly increase the basicity.

It can be clearly seen that NanoMgO samples shown a single desorption peak in both fresh and calcined sample around 430 °C which is attributed to CO₂ interaction with medium base strength site. Based on the data collected, the basicity of these materials can be listed in a sequence as follows: commercial dolomite > ex-gasifier dolomite > NanoMgO. The reason behind this is due to dolomite mostly governed by mixing of a base compound such as CaO, Ca(OH), CaCO₃²⁻ and Mg which attributes to higher base site density. Meanwhile, NanoMgO only exhibits basic sites from MgO.

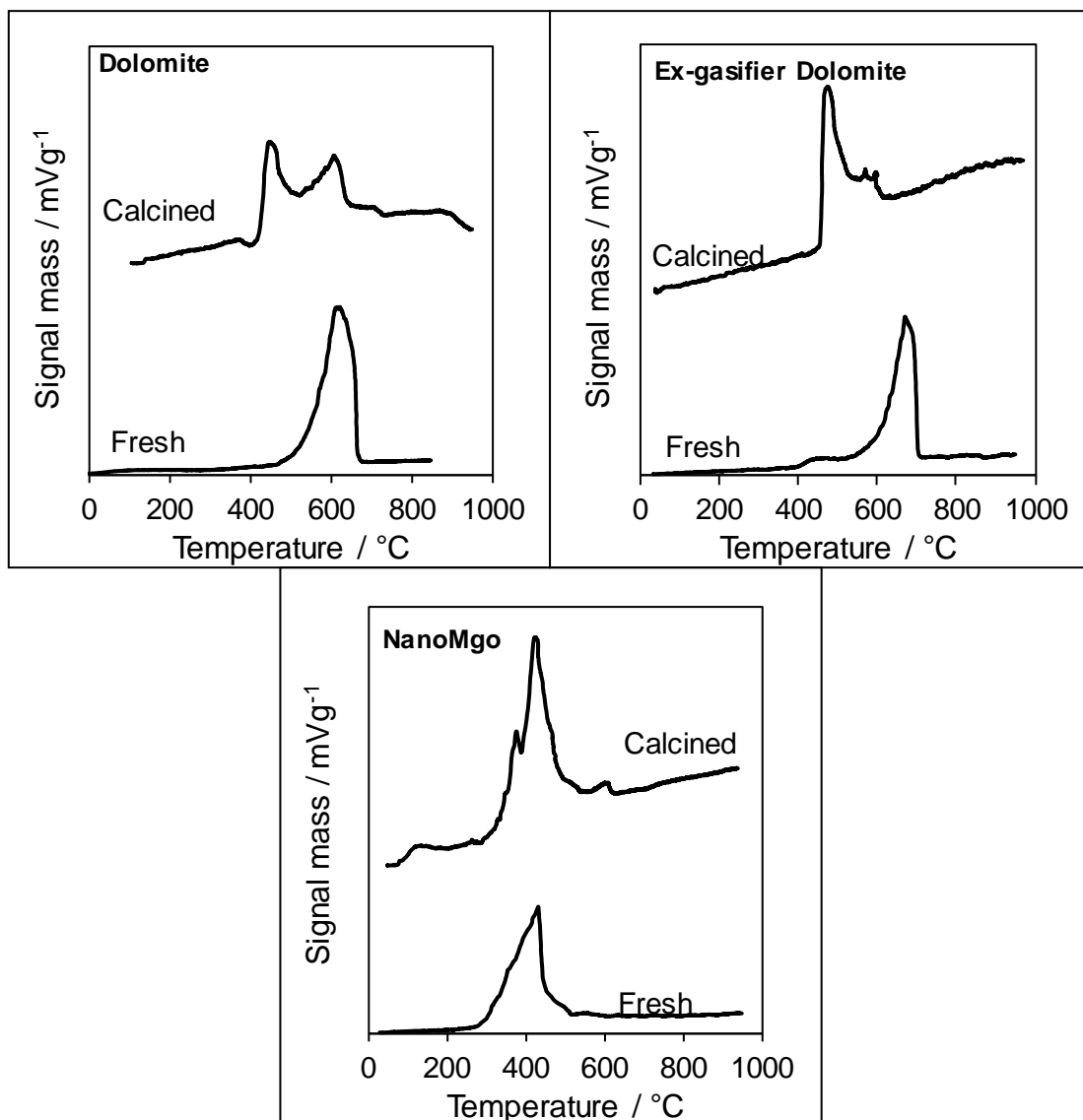


Figure 6.8 CO₂ desorption profiles of precursor and calcined dolomites, spent dolomite and NanoMgO.

Table 6.6 The amounts of basic sites in dolomites (commercial and ex-gasifier) and NanoMgO

Sample	Base site loading ^a / mmol g ⁻¹	Base site density ^b / molecules g ⁻¹ (x 10 ¹⁹)
Commercial dolomite		
Fresh	0.034	2.0
Calcined	0.076	4.6
Ex-gasifier dolomite		
Fresh	0.036	2.2
Calcined	0.054	3.3
NanoMgO		
Fresh	0.031	1.9
Calcined	0.035	2.1

^{a,b}Determined by CO₂ pulse chemisorption

6.2.1.8 Diffuse reflectance infrared Fourier transform spectroscopy

DRIFTS spectra of commercial dolomites, ex-gasifier dolomites and NanoMgo are shown in **Figure 6.9**. Similarities of bands between the fresh and calcined samples have been observed. Commercial dolomite stretching bands are detected at 1470, 874 and 737 cm^{-1} in commercial ones. Literature^{1,24,25} reports the main stretching band of dolomite to be normally detected around 730 cm^{-1} .

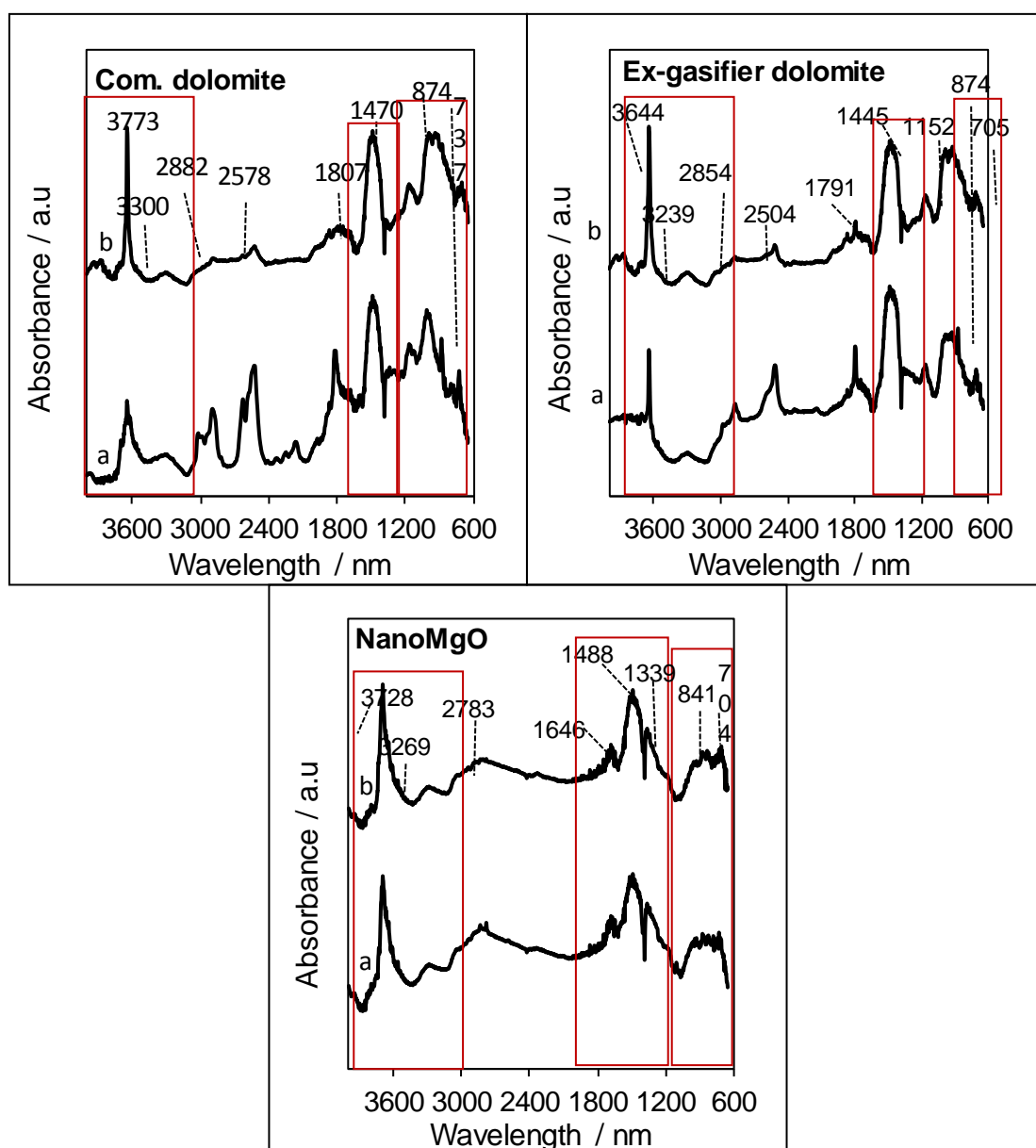


Figure 6.9 DRIFTS spectra of commercial dolomites, ex-gasifier dolomites and NanoMgO. a and b are denoted for fresh and calcined catalysts respectively.

The ex-gasifier sample shows a similar band peaks except at 705 cm^{-1} that might be attributed to calcite compound²⁵. This data is in agreement with XRD where diffraction pattern of calcite is more pronounced compared to dolomite in ex-gasifier. This is probably due to sample has been extensively used in gasifier thus reduced the composition of dolomite inside the compound. In both commercial and ex-gasifier dolomite, the hydroxyl stretching region (around $3600\text{--}3700\text{ cm}^{-1}$) is expected to be seen in FTIR bands due to the humidity of the sample⁵. A shoulder peak of OH^- stretching was later observed around 3000 cm^{-1} .

NanoMgO reveals most likely similar regions as observed in dolomite samples and another solid base catalyst such as in hydrotalcite. Strong peaks have been observed at 3728 cm^{-1} , 1488 cm^{-1} and $841\text{--}704\text{ cm}^{-1}$ attributed to vibration of O-H molecules, C-O and Mg-O respectively⁶. The CO_2 vibration also has been detected at 2783 cm^{-1} and has a similar agreement as reported by Correia *et al.*⁵.

6.2.1.8 X-ray photoelectron spectroscopy of Dolomite and NanoMgO

To further characterise the surface and electronic properties on the catalysts used, XPS analysis has been undertaken⁶. The C 1s spectra of all catalysts are corrected at 284 eV to the adventitious carbon.

Fresh and calcined spectra of commercial and ex-gasifier dolomite are depicted in **Figure 6.10**. A singlet spectre of Mg 2p is centred at 49.56 eV. Ca 2p spectra exhibits doublet peak of Ca $2p_{1/2}$ and Ca $2p_{3/2}$ which corresponds to Ca in OH^- and Ca in CO_3^{2-} respectively.

O1s spectra exhibit doublet at 531 and 532 eV with attributed to O in CO_3^{2-} O and in OH^- respectively.. Wilson *et al.*,¹ postulated these could be formed due to the presence of adventitious CO_2 as proven by the appearance in DRIFTS.

The fresh and calcined NanoMgO spectra of C 1s, Mg 2p and O 1s can be seen in **Figure 6.11**. Mg 2p spectra of NanoMgO (**Figure 6.11**) presents a singlet environment peaks centred at 49.3 eV corresponded to Mg^{2+} and Mg-O respectively. Meanwhile, analysis of the O1s region depicted three environments peaks attributed to O^{2-} (528.7 eV), O in CO_3^{2-} (530.4 eV) and O in OH^- (533.2 eV) respectively (**Figure 6.11c**)

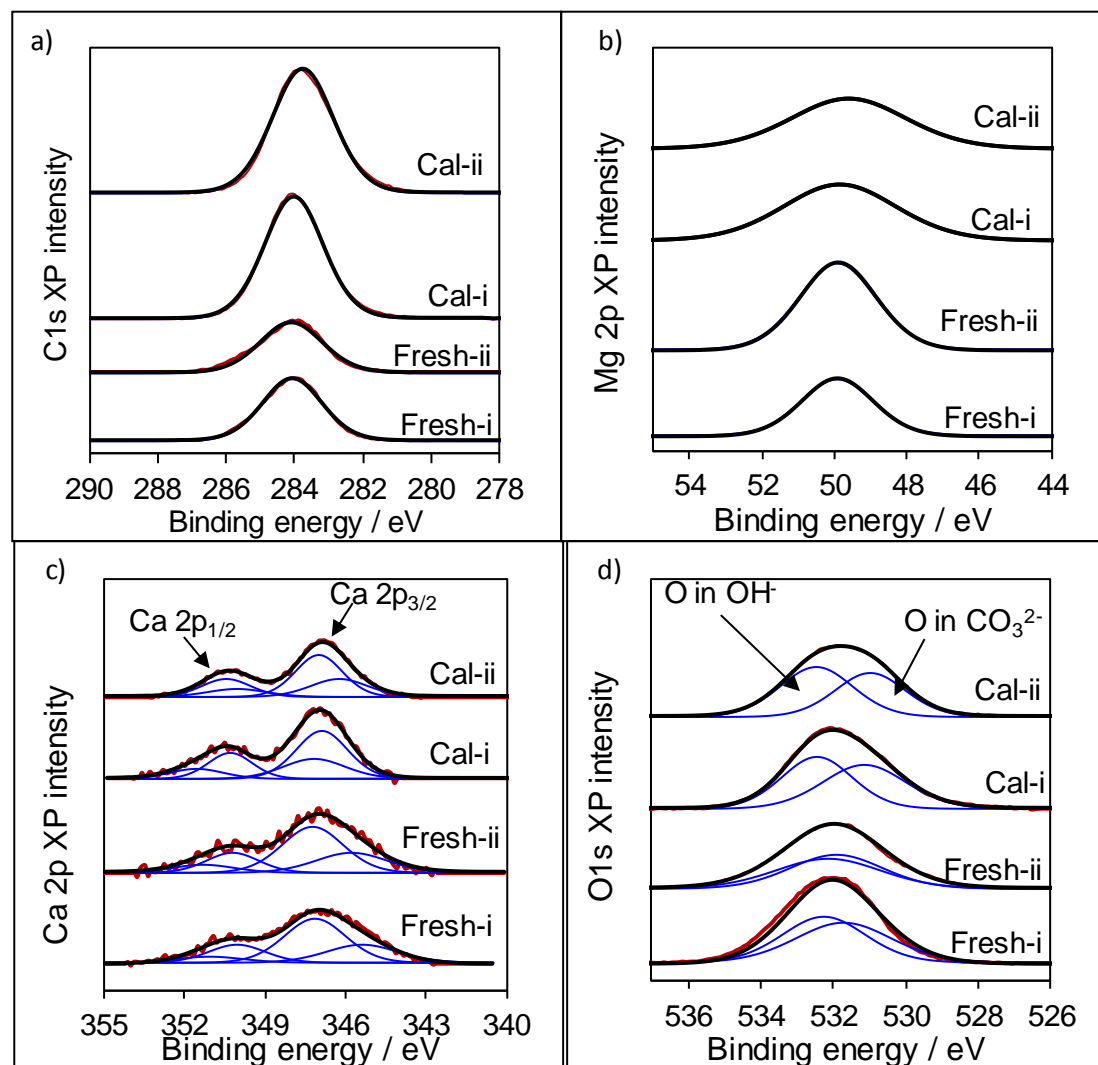


Figure 6.10 C1s (a), Ca 2p (b), Mg 2p (c) and O1s (d) obtained from fresh and calcined of commercial dolomite (i) and ex-gasifier dolomite (ii).

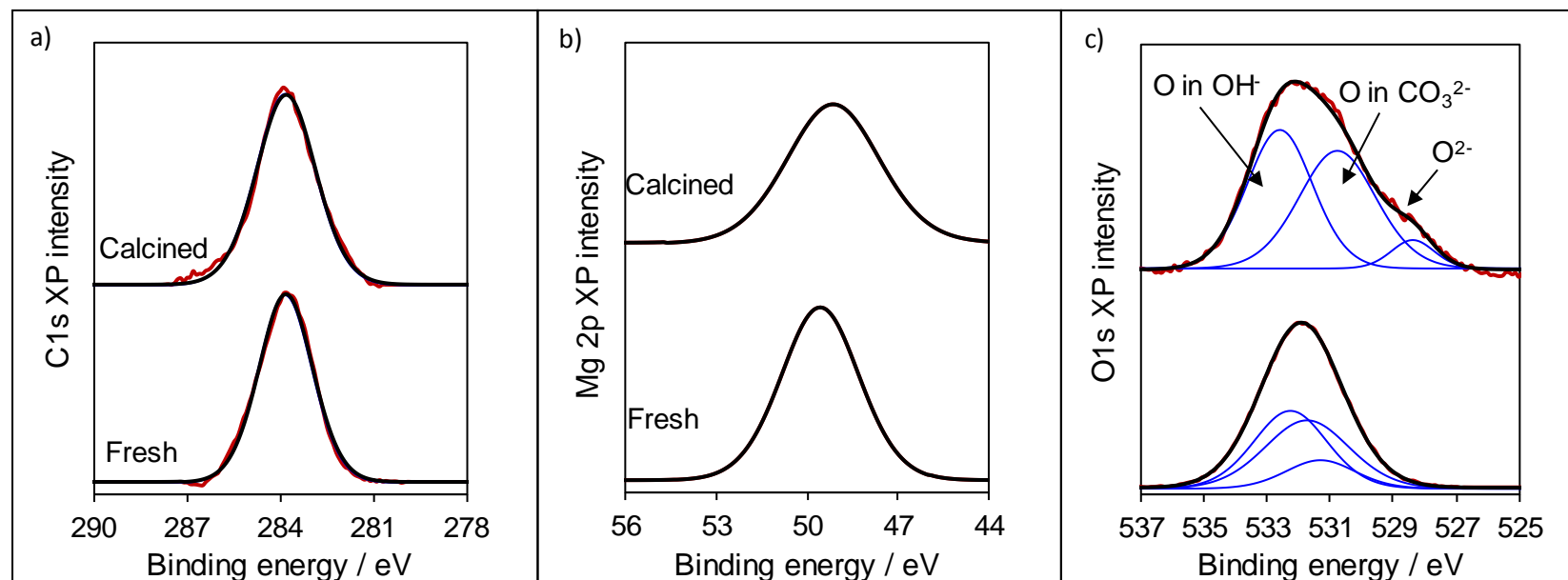


Figure 6.11 C1s (a), Mg 2p (b) and O1s(c) spectra obtained from fresh and calcined NanoMgO sample.

Table 6.7 shows the corresponding elemental and surface analysis of catalysts used in this study. Both data from EDX and XPS show in good agreement. The surface atomic ratio shows a little bit lower compared to bulk but still in the same range of the bulk catalysts.

Table 6.7 Elemental and surface analysis of commercial dolomite, ex-gasifier dolomite and NanoMgO.

Catalyst	Bulk atomic Ca:Mg (EDX)	Surface atomic Ca:Mg (XPS)
Commercial dolomite	2.46	2.21
Ex-gasifier dolomite	2.52	2.51
Catalyst	Bulk atomic Mg:O (EDX)	Surface atomic Mg:O (XPS)
NanoMgO	1.18	0.98

6.3 Catalytic Transesterification reactions of Dolomite and NanoMgO

6.3.1 C₄-C₈ TAG

In order to test the applicability of the solid base catalyst on transesterification reaction, commercial dolomite, ex-gasifier dolomite and NanoMgO were screened on triglycerides (TAG) ranging from C₄ to C₁₈. This reaction has been conducted under mild conditions; 65 °C, 650 rpm, 24 h in methanol.

In this study, fresh dolomite (non-calcined) shows no activity in the transesterification reaction. We obtained only 0.005 mmol yields with 1 % conversion after 3 h reaction (data not included). This result correlates with a study that has been done by Wilson *et al.*¹. They also reported no activity observed in transesterification reaction using non-calcined sample due to lack of basicity sites¹. Ngamcharussrivichai *et al.*²⁶ have reported calcined dolomites at a temperature below 800 °C are inactive for transesterification. They reported calcined dolomite at 800 °C produced the highest conversion (98.6 %) compared to calcined dolomite at 900 °C which produced a lower conversion (81.2 %). They believed increasing the temperature to 900 °C has enhanced the decarboxylation of dolomite to some extent but the reason behind it still remains unclear.

However, Wilson *et al.*¹ again emphasised higher calcination temperature applied will enhance the surface area and basicity sites of dolomite due to segregation

of Mg happened as CaO/(OH) is dispersed on MgO surface. By this, we believed higher temperature (900 °C) is the optimum calcination temperature of dolomites. TGA-MS also proved samples starts to decompose at 900 °C.

Segregation arising from calcination generates very fine powders, provided a higher surface area, accelerates the mass transport and significantly increased the reaction rates and yield. C₄-C₁₈ conversion profiles of commercial dolomite, ex-gasifier dolomite and NanoMgO are illustrated in **Figure 6.12** and tributyrin yield can be found in **Figure 6.13**. Data shows 99.9 % conversion of C₄ was obtained from calcined commercial dolomite at 900 °C and 99.0 % conversion of C₈ using the same catalyst. It achieves 100 % selectivity in C₄ but selectivity reduced to 91.4 % in C₈. As a higher TAG series was introduced (C₁₂ and C₁₈), conversion and selectivity were reduced accordingly. This finding confirms the association between higher TAG compound limits the diffusion efficient due to steric hindrance of TAG suppress the catalytic performance throughout the transesterification process¹.

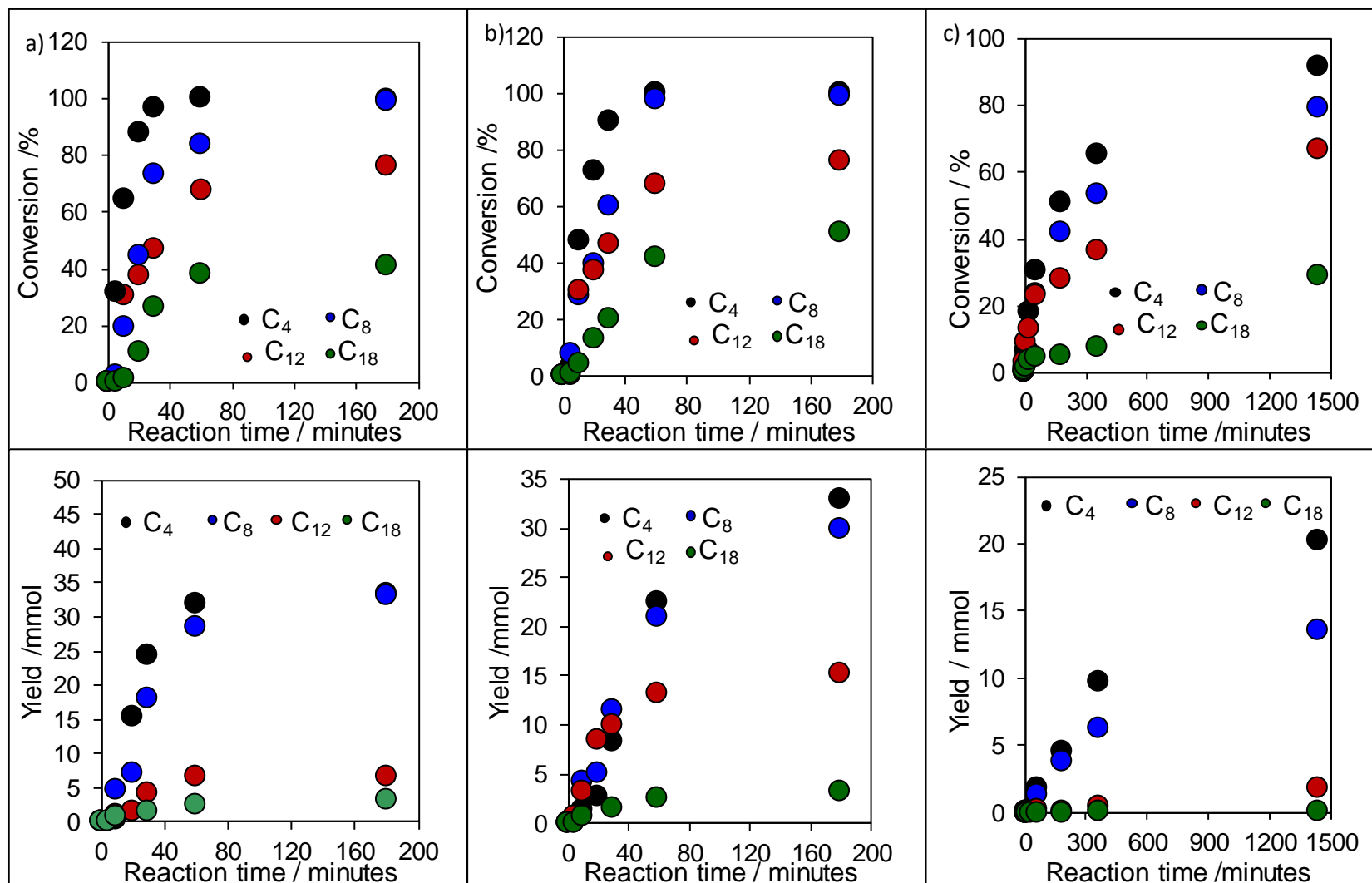


Figure 6.12 C_4 - C_{18} conversion and yield profiles of calcined commercial dolomite (a), ex-gasifier dolomite (b) and NanoMgO (c).

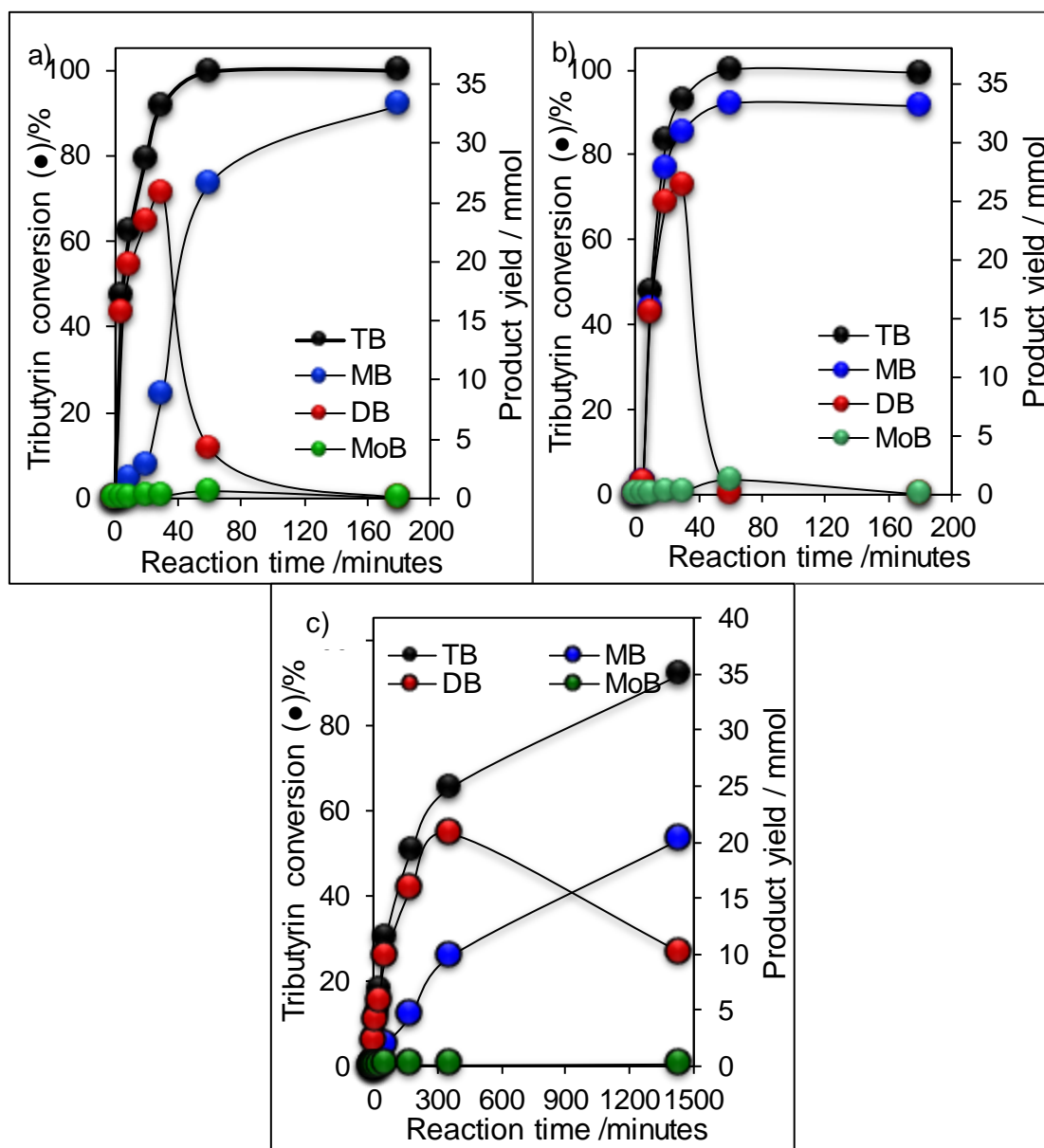


Figure 6.13 Reactant and product profiles of tributyrin (C_4) on commercial dolomite (a), ex-gasifier dolomite (b) and NanoMgO (c). TB, MB, DB and MoB are denoted for tributyrin, methyl butyrate, dibutyrate and monobutyrate respectively.

Again, the same trend has been observed; as the chain length of the TAG series were increased from C_4 - C_{18} , we found the conversion, selectivity, initial rates and TOF decreased significantly. These findings are in a good agreement with the previous experiment that has been done by Wilson *et al.*¹ NanoMgO exhibits (110) facet with defects were observed, which is attributed to lower surface energy²¹, thus slowing down the reaction rates significantly.

The turnover frequency (TOF) of all catalysts used in this reaction is shown in **Figure 6.14**. TOF was found to decrease as the TAG were increased to a bulkier chain which indicated the diffusion limitation of the substrate on the catalyst surface. Both commercial and ex-gasifier dolomite exhibit nearly the same TOF value. C₄ reveals TOF value of 121 min⁻¹ in commercial dolomite and 113 min⁻¹ in ex-gasifier dolomite. These values are lower from what has been reported before¹.

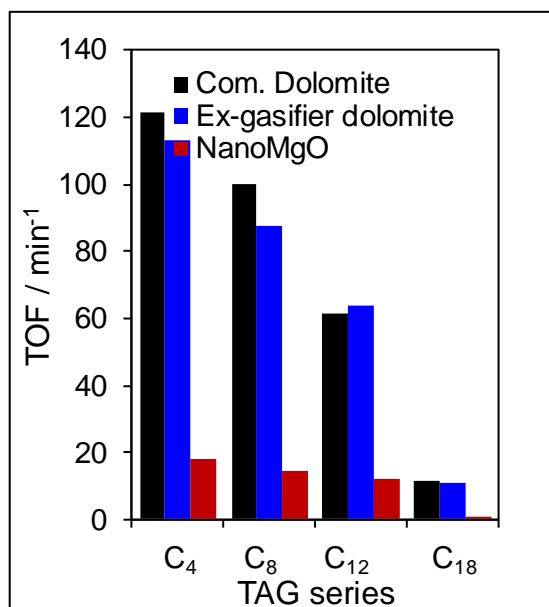


Figure 6.14 Comparison of TOF obtained from C₄-C₁₈ using the commercial dolomite, ex-gasifier dolomite and NanoMgO.

Meanwhile, NanoMgO showed a much lower TOF for the whole TAG applied and has been overwhelmed by dolomite. This is due to higher basic strength sites presents in dolomite (shown earlier in CO₂-TPD) such as from CaO, Ca(OH)₂, CaCO₃ and MgO have influences on the basicity of the sample, hence greatly enhanced the catalytic activity compared to NanoMgo that shown a lower basicity. Wilson *et al.*¹ also reported, high calcination temperature has induced to segregation on the surface, thus increased the surface area and basicity of the catalyst.

6.4 Leaching and reusability study of Dolomite and NanoMgO

To test the leaching content on these heterogeneous catalysts, follow reaction have been undertaken; In a round bottom flask, 20 mL of methanol has been added with 50 mg catalyst and heated up for 24h with stirring. The catalyst then was filtered off, washed and dried in the oven and later was analysed by ICP. By taking only 12.3 ml of methanol from the heated vessel, 0.59 ml dihexyl ether was added with 2.9 ml tributyrin.

No catalyst has been added in this case and reactions were proceeded for 60 minutes. Reaction profiles of leaching and normal run were compared in **Figure 6.15**.

No leaching has been recorded in commercial dolomite as no increase in the reaction conversion profile was observed (**Figure 6.15a-c**). A small leaching of 3.5 % conversion has been observed after 6 h in ex-gasifier dolomite. This data is in good agreement with ICP where it detected 4.2 % of total leached. Which could be attributed from calcite. NanoMgO reveals a constant leaching of 1 % from 10 minutes to 30 minutes of the reaction and increased to 6.1 % after 1-hour reaction. ICP further confirms 11.0 % leaching of Mg (**Table 6.8**). This could possibly be due to the defect observed on 110 facet as proven by TEM.

To observe the reusability and durability of the solid base catalysts used, catalysts were reused for three times and results are depicted in **Figure 6.15d**. Commercial dolomite and ex-gasifier dolomite demonstrated a slightly higher durability throughout the cycles compared to NanoMgO. This could be attributed from the calcium-based catalyst as reported by Lee *et al.*²⁷ which it exhibits higher durability in biodiesel transesterification. MgO showed a lower reusability in each cycle probably due to metal oxides has been poisoned by the adsorption of methanol or another reaction medium such as glycerol or methyl ester during transesterification of TAG²⁷. TEM and XRD proved NanoMgO exhibits (110) facet which represents the lower surface energy due to the formation of defects²¹, thus could be the reason for low durability of the catalyst.

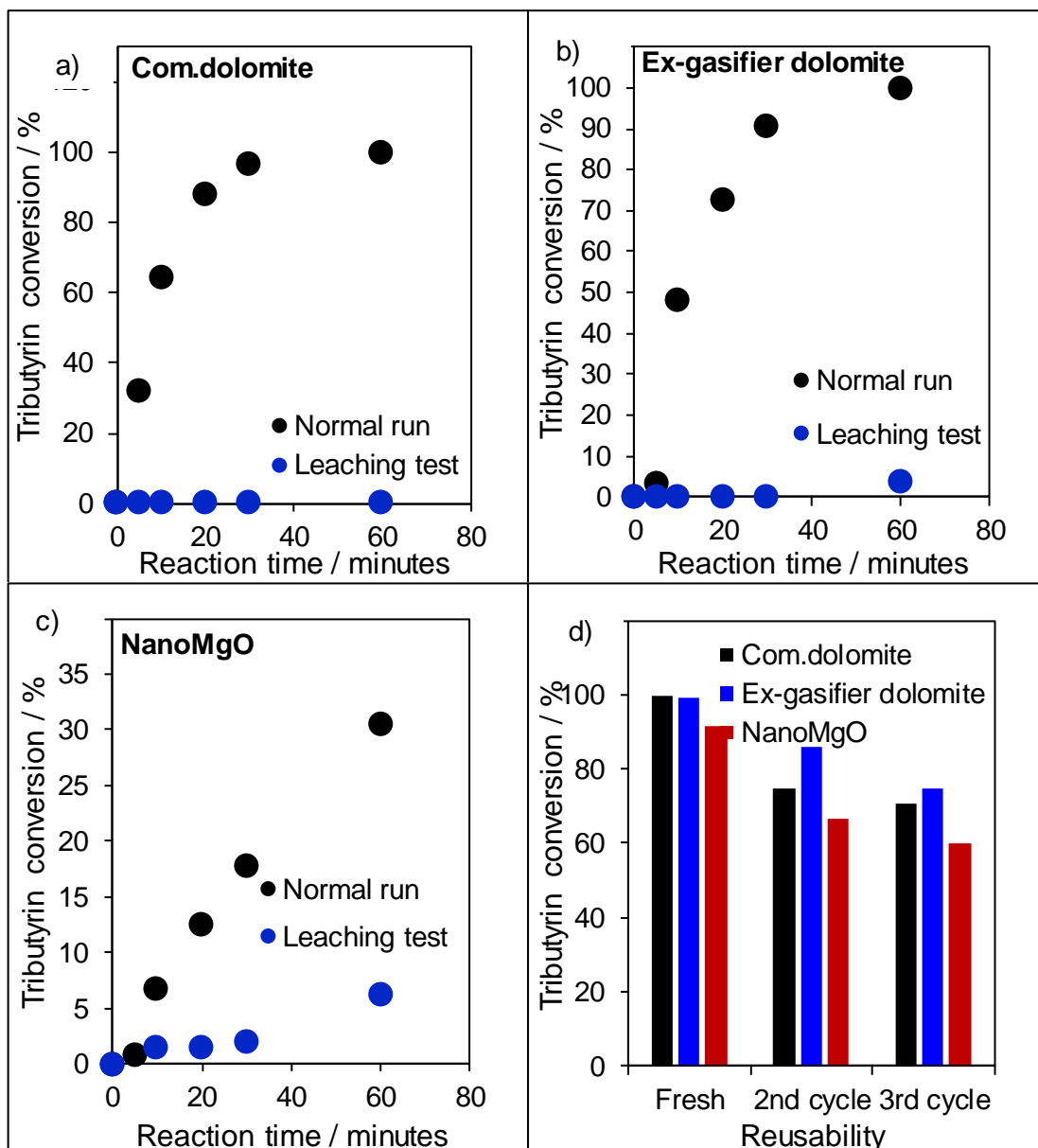


Figure 6.15 Leaching profile (a-c) and reusability (d) of solid base catalyst for transesterification of tributyrin with methanol using commercial dolomite, ex-gasifier dolomite and NanoMgO.

Table 6.8 Before and after filtered mass concentration of the catalysts to evaluate the leaching test as determined by ICP-OES.

Sample	Mass concentration / %		Total leaching / %
	Before filter	After filter	
Com.dolomite (Mg, Ca)	6.6	6.6	Nil
Ex-gasifier dolomite (Mg, Ca)	14.7	18.9	4.2
NanoMgO (Mg)	0.8	11.8	11.0

6.5 Conclusion

In summary, the solid base catalysts specifically dolomite (commercial and ex-gasifier) and NanoMgO have been tested in transesterification reaction of C₄-C₁₈ model compounds. It was demonstrated that high temperature of calcination has segregated the morphology, triggered the surface changes to 110 facet as proven by TEM. The segregation induced towards the higher surface area and basicity and later enhanced the catalytic performance. In NanoMgO, it also attributes to the formation of a Lewis base of MgO formed after calcination.

In terms of catalytic activity, both calcined dolomite catalyst (commercial and ex-gasifier) outperformed calcined NanoMgO in transesterification reaction due to dolomite exhibits higher basicity induced from 110 facet and also could possibly attribute from CaO presence in the compound. Leaching is pronounced in ex-gasifier dolomite and NanoMgO where it might be attributed to calcite formed in calcined dolomite and MgO respectively. NanoMgO demonstrated a lower durability compared to commercial dolomite and ex-gasifier dolomite probably due to the surface of MgO has been poisoned by methanol or any reaction medium.

6.6 References

- (1) Wilson, K.; Hardacre, C.; Lee, A. F.; Montero, J. M.; Shellard, L. *Green Chem.* **2008**, *10*, 654.
- (2) Montero, J. M.; Isaacs, M. A.; Lee, A. F.; Lynam, J. M.; Wilson, K. *Surf. Sci.* **2016**, *646*, 170–178.
- (3) Wilson, K.; Lee, A. F. *Catal. Sci. Technol.* **2012**, *2*, 884–897.
- (4) Gregg, J. M.; Bish, D. L.; Kaczmarek, S. E.; Machel, H. G. *Sedimentology* **2015**, *62*, 1749–1769.
- (5) Correia, L. M.; de Sousa Campelo, N.; Novaes, D. S.; Cavalcante, C. L.; Cecilia, J. A.; Rodríguez-Castellón, E.; Vieira, R. S. *Chem. Eng. J.* **2015**, *269*, 35–43.
- (6) Montero, J. M.; Brown, D. R.; Gai, P. L.; Lee, A. F.; Wilson, K. *Chem. Eng. J.* **2010**, *161*, 332–339.
- (7) Kuang, Q.; Wang, X.; Jiang, Z.; Xie, Z.; Zheng, L. *Acc. Chem. Res.* **2014**, *47*, 308–318.
- (8) Wang, J. A.; Novaro, O.; Bokhimi, X.; Lopez, T.; Gomez, R.; Navarrete, J.; Llanos, M. E.; Lopez-Salinas, E. *J. Phys. Chem. B* **1997**, *101*, 7448–7451.
- (9) Montero, J. M.; Gai, P.; Wilson, K.; Lee, A. F. *Green Chem.* **2009**, *11*, 265–268.
- (10) Debure, M.; Montes-hernandez, G.; Lerouge, C.; Debure, M.; Montes-hernandez, G.; Lerouge, C.; Mad, B. *Procedia Earth Planet. Sci.* **2017**.
- (11) Valverde, J. M.; Perejon, A.; Medina, S.; Perez-Maqueda, L. A. *Phys. Chem. Chem. Phys.* **2015**, *17*, 30162–30176.
- (12) Mohammed, M. A. A.; Salmiaton, A.; Wan Azlina, W. A. K. G.; Mohamad Amran, M. S.; Taufiq-Yap, Y. H.; Mohammed, M. A. A.; Salmiaton, A.; Wan Azlina, W. A. K. G.; Mohamad Amran, M. S.; Taufiq-Yap, Y. H. *J. Energy* **2013**, *2013*, 1–8.
- (13) Robert A. W. Haul, H. H. *Natl. Chem. Res. Lab. Sotuh Africa Counc. Sci. Ind. Res.* **1951**, 165–178.

- (14) Elbaba, I. F.; Williams, P. T. *Fuel* **2013**, *106*, 528–536.
- (15) Ding, Y.; Zhang, G.; Wu, H.; Hai, B.; Wang, L.; Qian, Y. *Chem. Mater.* **2001**, *13*, 435–440.
- (16) Layek, K.; Chakravarti, R.; Kantam, L.; Maheswaran; Vinu, A. *Green Chem.* **2011**, *13*, 2878–2887.
- (17) Jeevanandam, P.; Klabunde, K. J. *Langmuir* **2002**, *18*, 5309–5313.
- (18) Thommes, M.; Kaneko, K.; Neimark, A. V.; Olivier, J. P.; Rodriguez-Reinoso, F.; Rouquerol, J.; Sing, K. S. W. *Physisorption of gases, with special reference to the evaluation of surface area and pore size distribution (IUPAC Technical Report)*; 2015; Vol. 87.
- (19) Yoosuk, B.; Udomsap, P.; Puttasawat, B. *Appl. Catal. A Gen.* **2011**, *395*, 87–94.
- (20) Searl, A. *Mineral. Mag.* **1989**, *53*, 547–555.
- (21) Kato, K.; Dang, F.; Mimura, K.; Kinemuchi, Y.; Imai, H.; Wada, S.; Osada, M.; Haneda, H.; Kuwabara, M. *Adv. Powder Technol.* **2014**, *25*, 1401–1414.
- (22) Cadigan, C. A.; Corpuz, A. R.; Lin, F.; Caskey, C. M.; Finch, K. B. H.; Wang, X.; Richards, R. M. *Catal. Sci. Technol.* **2013**, *3*, 900–911.
- (23) Ilgen, O. *Fuel Process. Technol.* **2011**, *92*, 452–455.
- (24) Breen, C.; Clegg, F.; Herron, M. M.; Hild, G. P.; Hillier, S.; Hughes, T. L.; Jones, T. G. J.; Matteson, A.; Yarwood, J. *J. Pet. Sci. Eng.* **2008**, *60*, 1–17.
- (25) Ji, J.; Ge, Y.; Balsam, W.; Damuth, J. E.; Chen, J. *Mar. Geol.* **2009**, *258*, 60–68.
- (26) Ngamcharussrivichai, C.; Nunthasanti, P.; Tanachai, S.; Bunyakiat, K. *Fuel Process. Technol.* **2010**, *91*, 1409–1415.
- (27) Lee, H. V.; Juan, J. C.; Binti Abdullah, N. F.; Nizah Mf, R.; Taufiq-Yap, Y. H. *Chem. Cent. J.* **2014**, *8*, 1–9.

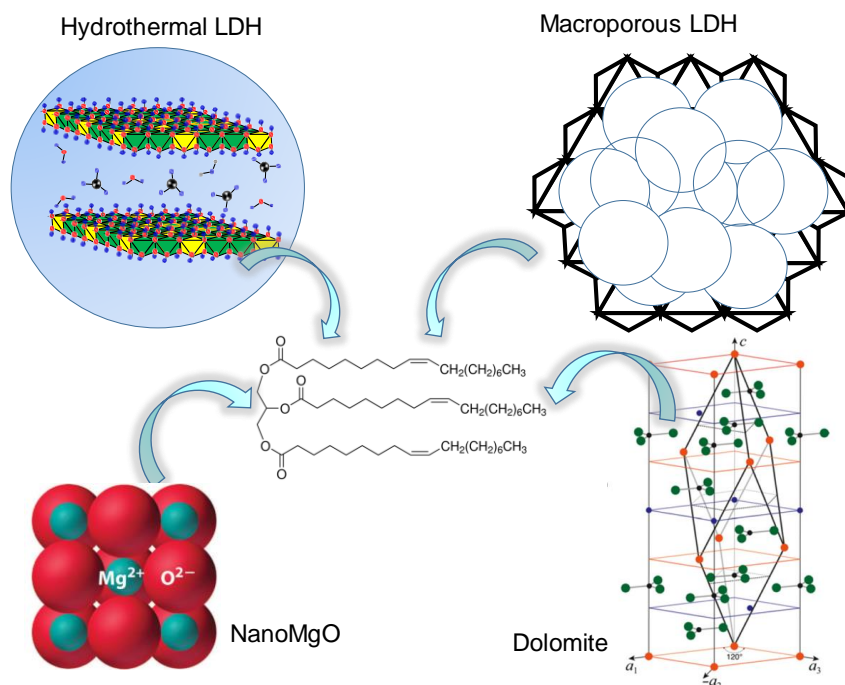
Chapter 7

Conclusion and Future Work

7.1 Conclusions

The objectives of this research were clearly underlined in each chapter along with their novelty and contribution to knowledge. Overall, the goal of this project was to overcome the diffusion limitation problem that normally arises in the transesterification of bulkier triglycerides (TAG) when using solid base catalysts. Solid base catalysts are preferable over solid acid catalysts in transesterification due to they are non-corrosive, environmentally benign, and present fewer disposal problems^{1,2}. Various families of solid base catalysts have been exploited and reported in transesterification reactions ranging from mixed oxide, carbonates, transition metal oxide, layered materials or clays such as hydrotalcite and many more^{3,4}.

Each chapter portrayed a different type of solid base catalyst (**Scheme 7.1**), with the different tuning of morphology based on different cation or synthesis method used. In Chapter 3 and 4, hydrothermal (HTM) rehydration techniques have been applied to ConvZnAl and NiAl LDH by using alkali-free method for the first time. The HTM method was proven outbid the performance of gas-phase (GP) and liquid phase (LP) in terms of enhancing the surface architectures; a high surface area with strong basicity and simultaneously increased the catalytic activity. Somehow, the diffusion rates in triolein (C_{18}) are still hampered by the bulky chains and narrow pores.



Scheme 7.1 Solid base catalysts used in this research for the transesterification reactions of model chain TAGs.

To further investigate the effect of providing a bigger pore network, incorporation of the macroporous structure has been carried out by using polystyrene as a template (Chapter 5). The macroporous incorporation method has injected a dramatic pore enlargement as proven by serial characterisation study. The wider pore has elevated the diffusion of the substrate which in the end manage to achieve the goal of eliminating the diffusion limitation issue⁵. Chapter 6 mainly touches on the effect of using different rich-MgO or/and CaO base catalysts on transesterification reaction. Effect of leaching also has been investigated. Leaching is significant in ex-gasifier dolomite and NanoMgO mainly due to the surface of the catalysts being poisoned by methanol during the reaction⁶.

Herein, a comparison on the best performing catalysts has been made and depicted in **Figure 7.1**.

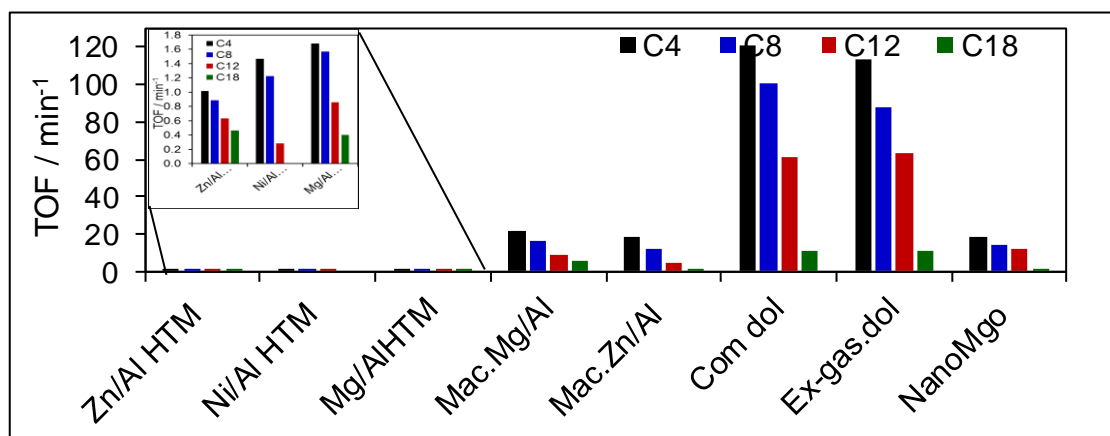


Figure 7.1 Comparison of TOF values in varying chain length triglyceride (C₄, C₈, C₁₂ and C₁₈) transesterification reactions using methanol for the best-performing catalysts from each chapter.

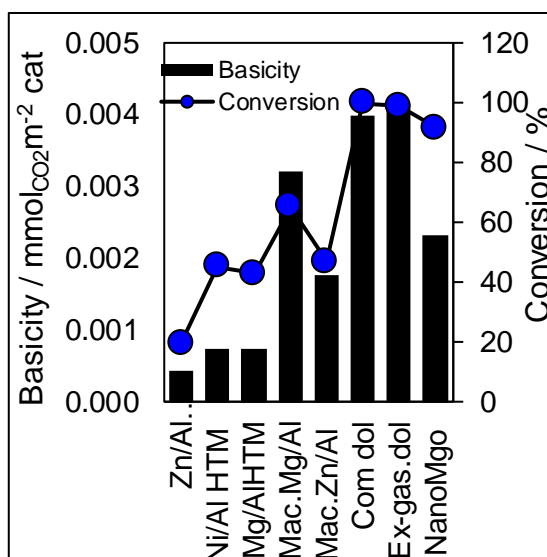


Figure 7.2 Effect of basicity on the solid base catalysts used in this study.

Effect of basicity on conversion of transesterification are so pronounced which be seen in **Figure 7.2**. The sequel relationship can be obtained as follows: conventional LDH < NanoMgO < macroporous LDH < commercial dolomite < ex-gasifier dolomite.

7.2 Recommendation / Future works

As a recommendation, it would probably be nice to have a comparison on NiAl macroporous LDH along with MgAl and ZnAl macroporous LDH in term of their physiochemical properties and catalytic activity in transesterification reactions. In this research, unsuccessful attempted has been made on synthesising macroporous NiAl via PS soft-templated method due to the failure of reconstructing back the layer. A few parameter control has to be taken such as controlling the precipitation pH, the ratio and the calcination temperature possibly would resolve this issue. Also, in order to obtain a more ordered structure of macro LDH, a dissolution method in three successive toluene or tetrahydrofuran (THF): acetone (1:1) (1g/10 mL) has to be applied before calcination-rehydration⁷. This could enhance the formation of ordered sized aggregates particles and give better macroporous morphology. Secondly, a transesterification reaction on a real feedstock such as using any oil (e.g. Jatropha or algae oil) would be highly required in order to further understand how the morphology and basicity would influence on the synergic effect of real biodiesel feedstock.

7.3 References

- (1) Calero, J.; Luna, D.; Sancho, E. D.; Luna, C.; Bautista, F. M.; Romero, A. A.; Posadillo, A.; Verdugo, C. *Fuel* **2014**, 122, 94–102.
- (2) Tan, H. W.; Abdul Aziz, A. R.; Aroua, M. K. *Renew. Sustain. Energy Rev.* **2013**, 27, 118–127.
- (3) Ahmad Tajuddin, N.; Lee, A. F.; Wilson, K. In *Handbook of Biofuels Production*; Woodhead Publishing, 2016; pp. 121–164.
- (4) Woodford, J. J.; Dacquin, J.-P.; Wilson, K.; Lee, A. F. *Energy Environ. Sci.* **2012**, 5, 6145.
- (5) Wilson, K.; Lee, A. F. *Catal. Sci. Technol.* **2012**, 2, 884–897.
- (6) Lee, H. V.; Juan, J. C.; Binti Abdullah, N. F.; Nizah Mf, R.; Taufiq-Yap, Y. H. *Chem. Cent. J.* **2014**, 8, 1–9.
- (7) Géraud, E.; Rafqah, S.; Sarakha, M.; Forano, C.; Prevot, V.; Leroux, F. *Chem. Mater.* **2008**, 20, 1116–1125.

APPENDICES



Appendix 2: Table 1.1 Copyright permission from Elsevier.





Illustration removed for copyright restrictions



Appendix 6: Figure 1.8- Copyright permission from Elsevier.



Appendix 7: Figure 1.11- Copyright permission from Elsevier.



Appendix 8: Figure 1.12- Copyright permission from Elsevier.



Appendix 9: Figure 1.13- Copyright permission from Royal Society of Chemistry.



Appendix 10: Figure 1.14- Copyright permission from Royal Society of Chemistry.



Appendix 11a: Figure 1.15- Copyright permission from Elsevier.



